1-1-2013

Rational Design of Perovskite Based Anode Materials For Solid Oxide Fuel Cells: A Computational Approach

Suwit Suthirakun
University of South Carolina

Rational Design of Perovskite Based Anode Materials for Solid Oxide Fuel
Cells: A Computational Approach

by

Suwit Suthirakun

Bachelor of Science
Chiang Mai University, Chiang Mai (Thailand), 2007

_____

Submitted in Partial Fulfillment of the Requirements

For the Degree of Doctor of Philosophy in

Chemical Engineering

College of Engineering and Computing

University of South Carolina

2013

Accepted by:

Andreas Heyden, Major Professor

John Weidner, Committee Member

Christopher Williams, Committee Member

Hans-Conrad zur Loye, Committee Member

Fanglin Chen, Committee Member

Lacy Ford, Vice Provost and Dean of Graduate Studies

This dissertation is dedicated to my mother Maneerat Pungpiboon for all her love and endless support.

ACKNOWLEDGEMENTS

I would first like to thank my advisor, Professor Andreas Heyden, who has been a fantastic mentor and colleague throughout my time at the University of South Carolina. He gave me the opportunity to attend several meaningful classes that I am interested in, which have greatly benefited my development as a scientist. He also gave me the opportunity to attend many conferences, which helped me improve my presentation skill. He guided me throughout the processes of doing researches and inspired me with his wisdom, patience, and enthusiasm. I would also like to thank my thesis committees: Professors Hans-Conrad zur Loye, Fanglin Chen, John Weidner, and Christopher Williams. The comments provided during the comprehensive exam, pre-defense, and dissertation defense have been very useful and have resulted in a significantly improved dissertation.

I would like to acknowledge all of the members of the Heyden Group. When I started as a PhD student, Dr. Ammal Salai was very patience when she tried to teach me how to run a simple calculation, how to use basic linux commands, and answer every single question with patience. Dr. Jianmin taught me how to run transition state calculations and suggested me some good new programs to view the structures which make my research life much easier. Faheem, Sina, and Sara have both been great friends and colleagues. I have enjoyed learning alongside them and I know that without them working in the office alone would have been a lot more difficult. Their constant hard work has certainly inspired me to work harder on my projects.

I would like to thank all of my colleagues, Fan, Xiaojing Shuai, Tong, Cho, Rahul, Visarn, Chris, Artem, and Elenie, who joined the school at the same time as I did. They all helped me to survive the toughest year of studying I have ever had. Since I did not have a chemical engineering background, they help me understanding materials in classes and tutor me for the qualifying exam. They are also good friends and make my time here more memorable. I also thank all of my Thai friends here, Nok, Trisha, Amie, Gift, and Nikki, whom I share all good and bad times with during my Ph.D. They make this place to be a better place to stay.

The most gratitude goes to my mom, Maneerat Pungpiboon. She is a real giver who never expects anything return. She raised me with love and taught me respect, confidence, and etiquette. She gave me the greatest gift of all, education and the freedom of choice. I would not be who I am today without her support.

ABSTRACT

A key challenge in the development of solid oxide fuel cell (SOFC) technology is related to finding a suitable replacement for Ni-based cermet anodes. Although conventional Ni-based electrodes exhibit excellent catalytic activity and current collection, they suffer from several limitations such as instability upon redox cycling, nickel sintering, and sulfur and carbon poisoning when exposed to practical hydrocarbon fuels. Therefore, alternative anode materials need to be developed for SOFCs. Among the novel anode electrodes, perovskite based materials (ABO_3) are of great interest because they have been shown to satisfy most intrinsic SOFC anode requirements such as high thermodynamic stability in anodic environments and strong resistance to carbon deposition and sulfur poisoning.

In this dissertation, we described how "first principles" modeling can be used to rationally develop a doping strategy to obtain mixed ionic/electronic conductivity in $SrTiO_3$ perovskites under anodic SOFC conditions. First, constrained *ab initio* thermodynamic calculations were employed to evaluate the thermodynamic stability of the doped $SrTiO_3$ phases at synthesized and anodic SOFC conditions. Then, we computed and analyzed the density of states (DOS) of p- and n-doped $SrTiO_3$ to determine the number of charge carriers per unit cell in each phase. In agreement with experimental observations, the computational results reveal that mixed p- and n-doping is an efficient strategy to obtain mixed ionic/electronic conductivity in perovskite oxides such as

SrTiO$_3$. Moreover, we have proven that this strategy is valid independent of p- and n-doping site (A- or B-site) in the perovskite structure. We used La and Nb as n-type dopants and Na and Ga as p-type dopants to replace the A-site and B-site cations in the SrTiO$_3$ perovskite structure, respectively. All p- and n-doped SrTiO$_3$ perovskite oxides exhibit mixed ionic and electronic conductivity in a reducing environment as long as the concentration of p-dopants is significantly below, e.g., half, the concentration of the n-dopant.

Next, we explain how multiscale simulations can help understand the rate / performance limiting steps in SOFCs based on Sr$_2$Fe$_{1.5}$Mo$_{0.5}$O$_{6-\delta}$ (SFM) anodes running on H$_2$. First, we performed constrained *ab initio* thermodynamic simulations to identify the surface phase of SFM (001) under anodic SOFC conditions. Then, we studied the reaction mechanism of the electrochemical H$_2$ oxidation from first principles and developed a microkinetic model that identified the second H transfer step to be rate determining under operating voltage and temperature. As a result, adding a transition metal to the SFM surface such as Ni that facilitates H transfer should improve the overall cell performance. Indeed, experimental observations confirm this predicted SOFC cell behavior.

TABLE OF CONTENTS

CHAPTER 1

INTRODUCTION

1.1.   Introduction

Fuel cell technology is considered an attractive alternative energy system since it exhibits higher energy efficiency and lower emissions of greenhouse gases and conventional pollutants [1-3]. Fuel cells are primarily classified by the electrolyte they employ. This classification determines the kind of chemical reactions that occur in the cell, the kind of catalysts required, the temperature range in which the cell operates, the fuel required, and other factors. There are several types of fuel cells currently being developed; for example, proton exchange membrane fuel cells (PEMFC), phosphoric acid fuel cells (PAFC), molten carbonate fuel cells (MCFC), alkaline fuel cells (AFC), and solid oxide fuel cells (SOFC) [4]. Among these fuel cell technologies, SOFCs are the most energy efficient and display several advantages over other types of fuel cells, such as the use of relatively inexpensive materials, a relatively low sensitivity to fuel impurities, high stability, reliability, durability of operation, and the flexibility of direct utilization of various fuels such as natural gas, liquid fuels, gasified coal, and biofuels [5-10]. As a result, SOFC technology has attracted significant attention as a power generation system over the last years.

From the beginning of SOFC development, several types of materials have been used for SOFC components; for example, $LaMnO_3$-based oxides for the cathode and Ni/YSZ for the anode [4]. The most significant losses of SOFC performance occur at both the cathode and the anode. When hydrogen is used as a fuel, the majority of performance losses arises at the cathode due to the over potential of the oxygen reduction reaction. On the other hand, whenever hydrocarbon fuels are used the most important performance issues occur at the anode since the anode catalyst is easily poisoned by sulfur components and coke formation. As a result, the development of novel materials for the SOFC anode is of great interest and is the topic of this dissertation.

1.2. Scope of the Dissertation

Most of the anode materials for SOFCs are based on Ni supported yttria stabilized zirconia (Ni/YSZ) since it exhibits high electronic and oxide ion conductivity and good catalytic activity for the H_2 or CH_4 oxidation reactions. The oxidation reaction occurs at the three phase boundary of a gas phase, Ni metal, and YSZ oxide-phase. Unfortunately, Ni/YSZ also exhibits some disadvantages. For example, it gets easily poisoned by very small amounts of sulfur contaminations in the fuel gas [11]. Moreover, since Ni itself is also a catalyst for carbon formation from hydrocarbon fuels, the formation of carbon deactivates the catalytic activity [12]. Consequently, alternative SOFC anode materials are currently being developed.

Overall, the candidate materials for the SOFC anode should meet the following requirements: *(i)* the materials should have good chemical and mechanical stability under the cell operation conditions; *(ii)* they should possess high ionic and electronic conductivity and good catalytic activity for the fuel oxidation reaction; *(iii)* finally, the

materials should be tolerant to sulfur impurities and coke formation. In recent years, several alternative anode materials have been developed with fluorite, rutile, tungsten bronze, pyrochlore, perovskite, and spinel structures [13]. Among these materials, perovskite based materials have been shown to satisfy most intrinsic SOFC anode requirements such as high mixed ionic/electronic conductivity, good catalytic activity, and high thermodynamic stability at anodic conditions [14-20]. Furthermore, perovskite based materials possess high resistance to sulfur impurities [21-23] and coke formation [14, 24-26] since both sulfur and carbon species can easily be oxidized at the surface of the perovskite oxide [27].

It is the objective of this dissertation to utilize modern computational tools to obtain fundamental understanding of structure-property-performance relationships of perovskite based anode materials. We further utilize this understanding to rationally design promising novel anode catalysts for SOFCs. In particular, we performed density functional theory (DFT) calculations to study the effects of p- and n-dopants to ionic and electronic conductivity of doped $SrTiO_3$ perovskites. Constrained *ab initio* thermodynamic simulations were carried out to determine phase stability and reducibility of doped structures under synthesized and anodic SOFC conditions. We analyzed the density of states (DOS) of the most dominant structures in the phase diagrams to evaluate the number of charge carriers and degree of electronic conduction of each material. The doped $SrTiO_3$ samples were also experimentally prepared and our experimental partners confirmed our computational predictions.

Furthermore, we aim to study the electrochemical performance of $Sr_2Fe_{1.5}Mo_{0.5}O_{6-\delta}$ (SFM) for the H_2 electro-oxidation reaction under anodic SOFC

3

conditions. Again, we employed constrained *ab initio* thermodynamic calculations to obtain surface models at realistic reaction conditions. We further conducted a microkinetic analysis in conjunction with DFT calculations to precisely predict rate determining steps and the apparent activation energy of the reaction.

1.3.   Organization of the Dissertation

This introduction is followed by Chapter 2 "Literature Reviews", which summarizes the basic knowledge of SOFC operations. The chapter aims to point out the main reasons why we want to develop novel anode catalysts to replace Ni/YSZ cermet electrodes. Advantages and disadvantages of various types of alternative anode materials are explained and discussed. Finally, the chapter thoroughly reviews structural, physical, and electronic properties of perovskite based anode materials. The electrical and electrochemical performance of perovskite anodes studied by various groups is also reviewed.

In Chapter 3, a detailed description of various theoretical methods used throughout the dissertation is provided (primarily Chapters 4, 5, and 6). The chapters themselves contain short method sections, which present important information regarding methodology specific to that particular chapter, as well as references to specific sections within Chapter 3 for further information.

Chapter 4, "DFT Study on the Electronic Structure of p- and n-Doped $SrTiO_3$ in a Reducing Environment", presents the results of our density functional theory calculations of mixed ionic/electronic perovskite conductors. Constrained *ab initio* thermodynamic calculations and density of states analysis have been used to investigate the effects of p- and n-type dopants to the ionic and electronic conductivity of doped $SrTiO_3$ perovskites.

The calculations reveal that mixed ionic/electronic conductivity in perovskite oxides can be obtained using the mixed p- and n-doping approach.

Chapter 5, "Obtaining Mixed Ionic/Electronic Conductivity in Perovskite Oxides under Anodic Solid Oxide Fuel Cell Conditions: A Computational Prediction for Doped $SrTiO_3$" confirms the concepts in Chapter 4 that a mixed p- and n-doping strategy can be used to improve ionic and electronic conductivity in perovskite oxides. The computational tools and models used in the study of this chapter are very similar to that of Chapter 4 so that the calculated results can be compared. The computational results ensure that the p- and n-doping approach is an efficient doping strategy to obtain mixed ionic/electronic perovskite conductors. The results also suggest that this doping approach can be efficiently used independent of the n-doping site.

Chapter 6, "Rational Design of Mixed Ionic and Electronic Conducting Perovskite Oxides for Solid Oxide Fuel Cell Anode Materials: A Case Study for Doped $SrTiO_3$" is motivated by the findings of Chapter 4 and 5 that p-doping can be used to improve the ionic conductivity of the material by increasing the oxygen loss in the structure. Furthermore, n-doping introduces conduction electrons into the lattice and improves the electronic conductivity. In this chapter, we prove unambiguously that the p- and n-doping approach can be used to obtain mixed ionic/electronic conductivity in perovskite materials. Independent of p- and n-doping site, this doping approach can be successfully used to enhance ionic and electronic conductivity of perovskite oxides under anodic SOFC conditions. Our computational predictions are also confirmed by experimental observations.

Chapter 7, "Theoretical Investigation of H_2 Oxidation on (001) $Sr_2Fe_{1.5}Mo_{0.5}O_{6-\delta}$ Perovskite Surfaces" presents a combined DFT and microkinetic modeling study of the H_2 oxidation on the $Sr_2Fe_{1.5}Mo_{0.5}O_{6-\delta}$ surface under anodic SOFC conditions. The surface model used in this study is described in detail. The derived DFT parameters were used to construct a microkinetic model which includes the external environmental conditions. Furthermore, the effect of anode bias potential was included in the model.

Chapter 8 summarizes how the computational tools can be used to rationally design promising perovskite oxide anode materials for SOFCs. The insights gained from the first-principle studies permit us to understand and design a novel anode material. An assessment of how this work has impacted the field of SOFC technology is included. Furthermore, a detailed description of future research directions of this work is outlined.

1.4.   References

[1]   R.J. Kee, H.Y. Zhu, D.G. Goodwin, Proceedings of the Combustion Institute 30 (2005) 2379.
[2]   M.S. Dresselhaus, I.L. Thomas, Nature 414 (2001) 332.
[3]   S. McIntosh, R.J. Gorte, Chemical Reviews 104 (2004) 4845.
[4]   *Perovskite oxide for solid oxide fuel cells*, Springer, New York 2009.
[5]   A. Atkinson, S. Barnett, R.J. Gorte, J.T.S. Irvine, A.J. Mcevoy, M. Mogensen, S.C. Singhal, J. Vohs, Nature Materials 3 (2004) 17.
[6]   N.Q. Minh, Journal of the American Ceramic Society 76 (1993) 563.
[7]   P. Singh, N.Q. Minh, International Journal of Applied Ceramic Technology 1 (2004) 5.
[8]   N.Q. Minh, Solid State Ionics 174 (2004) 271.
[9]   Q.M. Nguyen, T. Takahashi, *Science and technology of ceramic fuel cells*, Elsevier Science, Amsterdam ; New York 1995.
[10]   S.C. Singhal, K. Kendall, *High-temperature solid oxide fuel cells : fundamentals, design, and applicatons*, Elsevier Advanced Technology, New York 2003.
[11]   Y. Matsuzaki, I. Yasuda, Solid State Ionics 132 (2000) 261.
[12]   X. Turrillas, A.P. Sellars, B.C.H. Steele, Solid State Ionics 28 (1988) 465.
[13]   S.W. Tao, J.T.S. Irvine, Chemical Record 4 (2004) 83.
[14]   S.W. Tao, J.T.S. Irvine, Nature Materials 2 (2003) 320.
[15]   Y.H. Huang, R.I. Dass, Z.L. Xing, J.B. Goodenough, Science 312 (2006) 254.

[16] D.P. Fagg, V.V. Kharton, A.V. Kovalevsky, A.P. Viskup, E.N. Naumovich, J.R. Frade, J. Eur. Ceram. Soc. 21 (2001) 1831.

[17] S.Q. Hui, A. Petric, J. Eur. Ceram. Soc. 22 (2002) 1673.

[18] T. Ishihara, H. Matsuda, Y. Takita, J. Am. Chem. Soc. 116 (1994) 3801.

[19] M. Feng, J.B. Goodenough, Eur. J. Solid State Inorg. Chem. 31 (1994) 663.

[20] K.Q. Huang, M. Feng, J.B. Goodenough, M. Schmerling, J. Electrochem. Soc. 143 (1996) 3630.

[21] J. Canales-Vazquez, S.W. Tao, J.T.S. Irvine, Solid State Ionics 159 (2003) 159.

[22] O.A. Marina, N.L. Canfield, J.W. Stevenson, Solid State Ionics 149 (2002) 21.

[23] J. Canales-Vazquez, J.C. Ruiz-Morales, J.T.S. Irvine, W.Z. Zhou, J. Electrochem. Soc. 152 (2005) A1458.

[24] A. Sin, E. Kopnin, Y. Dubitsky, A. Zaopo, A.S. Arico, L.R. Gullo, D. La Rosa, V. Antonucci, J. Power Sources 145 (2005) 68.

[25] P. Vernoux, E. Djurado, M. Guillodo, J. Am. Ceram. Soc. 84 (2001) 2289.

[26] Y.B. Lin, Z.L. Zhan, S.A. Barnett, J. Power Sources 158 (2006) 1313.

[27] L. Aguilar, S.W. Zha, Z. Cheng, J. Winnick, M.L. Liu, J. Power Sources 135 (2004) 17.

CHAPTER 2

LITERATURE REVIEW

2.1 Solid Oxide Fuel Cell Overview

A solid oxide fuel cell (SOFC) is an electrochemical conversion device that produces electricity directly by oxidizing fuel. It operates at very high temperatures, typically between 500 and 1000 ^{o}C, which allows the solid electrolyte and electrode to promote rapid kinetics and leads to an overall high electrochemical activity. Theoretically, the efficiency of a SOFC cell can be as high as 60 percent [1]. Due to the high operating temperature though, only selected materials are stable which again led to the development of low cost ceramic materials that can easily be fabricated.

Unlike most other types of fuel cells, solid oxide fuel cells allow the use of a wide range of fuels. Because of the relatively high operating temperatures, light hydrocarbon fuels including methane, propane and butane can be internally reformed at the anode. The cell can also be fueled by externally reformed hydrocarbons, such as gasoline, diesel, jet fuel or biofuels. The efficiency of the system can be enhanced by harnessing the heat released from the exothermic electrochemical oxidation within the fuel cell for the endothermic steam reforming process.

A solid oxide fuel cell is made up of three major components including the electrolyte, the cathode, and the anode. Hundreds of cells are connected in series to form the SOFC stack. This SOFC stack contains an electrical interconnect, which links individual cells together. The cell operates at a high temperature which allows the ceramic materials to become electrically and ionically conductive.

Next, the electrochemical reactions occurring in the SOFC are discussed and illustrated. At the cathode, oxygen molecules from the air are reduced into oxide ions on the porous surface by electrons. These oxide ions are charge carriers that conduct through the ceramic electrolyte to the fuel rich porous anode where the oxide ions react with the fuel to generate electrons. The electrons travel through the external circuit providing electric power and producing some heat. The reactions at the anode and cathode are shown in equation 1.1 and 1.2. Figure 2.1 shows a schematic diagram of SOFC operation.

Anode: $C_n H_{2n+2} + (3n + 1)O^{2-} \rightarrow nCO_2 + (n + 1)H_2O + (6n + 2)e^-$ (1.1)

Cathode: $\frac{1}{2}O_2 + 2e^- \rightarrow O^{2-}$ (1.2)
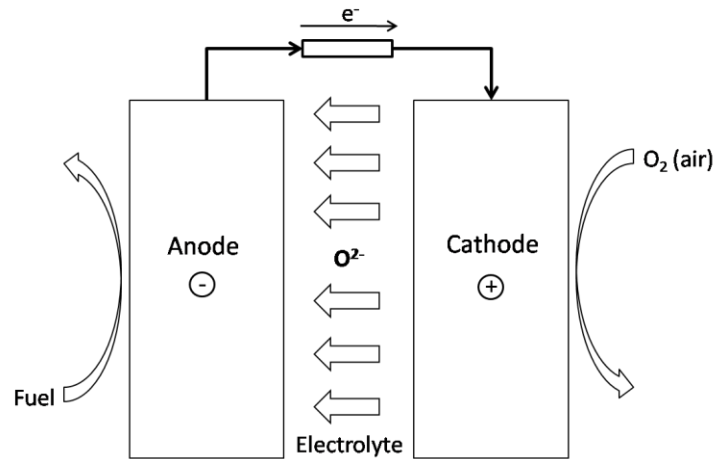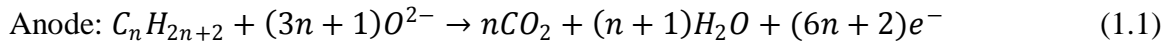
Figure 2.1 Schematic diagram showing the working principle of a solid oxide fuel cell

Typically, SOFCs use solid oxide ceramics as electrolytes. These electrolyte materials must possess high ionic conductivity, be dense in order to separate the air and fuel compartments, and be an electronic insulator [2]. Moreover, the electrolyte must maintain these properties over a wide range of oxygen partial pressure since the partial pressure of oxygen deviates from 1 atm at the cathode to 10^{-20} atm at the anode [3]. In the 1980s, Nernst [4] realized that certain perovskites and stabilized zirconia provide promisingly effective ionic conductivity. Baur and Preis [5] already demonstrated in 1943 that such electrolytes could be used as oxide ion conductors in a fuel cell. Recently, yttrium stabilized zirconia (YSZ) is the most commonly used electrolyte for SOFCs. At a temperature above 700 $^{\circ}$C, YSZ provides high ionic conductivity while exhibiting only minor electronic conductivity [6-8].

To date, YSZ seems to be the material of choice because it is stable at a wide range of pO$_2$, has good mechanical strength, and is inexpensive. However, many research groups continue searching for alternative electrolyte materials in order to improve the overall efficiency of SOFCs (particularly at a lower temperature). One such material is scandium doped zirconia (SDZ). As depicted in Fig. 2.2 [6-8], SDZ exhibits higher conductivity than YSZ under reducing conditions at a lower temperature. Other alternative materials include strontium and magnesium doped lanthanum gallate perovskite materials discovered by Goodenough [9]. These materials can be used at a temperature as low as 600 $^{\circ}$C even on a thick electrolyte. Finally, some oxide compounds such as doped ceria and $La_{0.9}Sr_{0.1}Ga_{0.8}Mg_{0.2}O_{2.85}$ (LSGM) are also considered promising electrolytes because they have higher ionic conductivities [10].
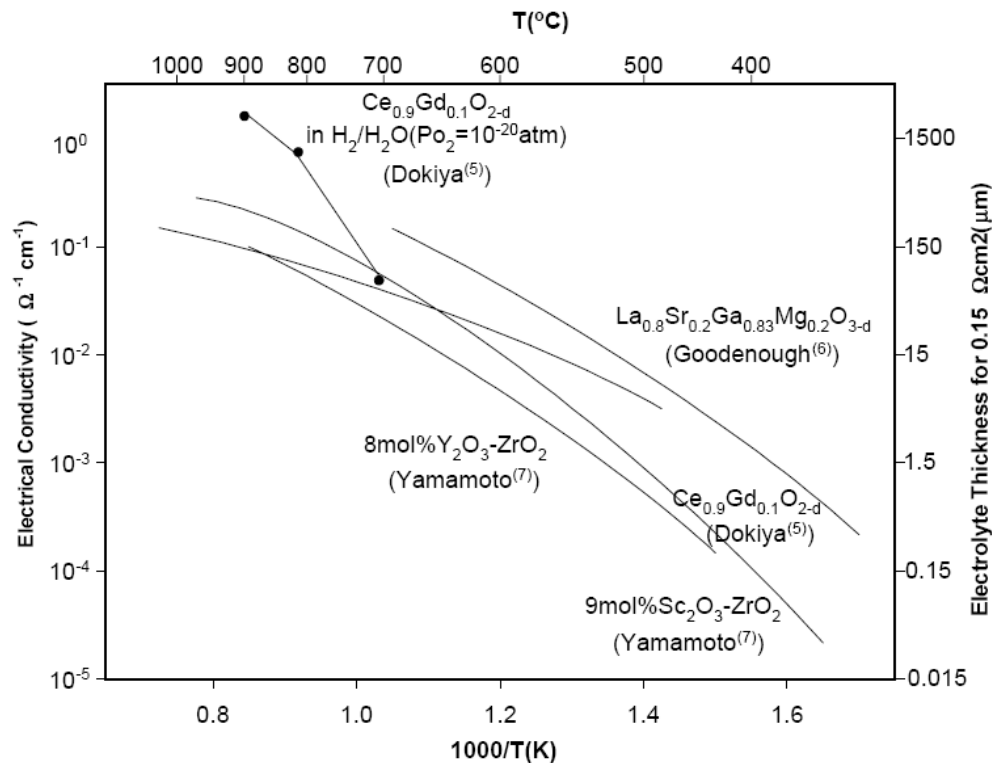
Figure 2.2 Electrolyte conductivity as a function of temperature [6-8]

The cathode materials used in SOFCs must be able to dissociate O_2 and be electronically conductive. Generally, the materials are lanthanum based perovskite materials. Platinum and other noble metals and even magnetite have also been used as cathode materials during the early development of SOFCs [10]. However, due to their chemical and physical instability and incompatibility with most electrolytes, they are no longer employed in SOFCs. Currently, most cathodes are based on perovskite oxide materials such as Sr-doped $LaMnO_3$ (LSM) and mixed ionic-electronic conductors (MIEC), such as $La_{0.6}Sr_{0.4}Fe_{0.8}Co_{0.2}O_3$ [11, 12], $Ba_{0.5}Sr_{0.5}Co_{0.8}Fe_{0.2}O_{3-\delta}$ [13], and $Sm_{0.5}Sr_{0.5}CoO_3$ [14]. The choice of cathode material should be a compromise between a number of factors:

(i)   Chemical stability and relatively low interaction with the electrolyte

(ii) High electronic and ionic conductivity

(iii) Relatively high activity

(iv) Manageable interactions with ceramic interconnects

(v)   Thermal expansion coefficients that match that of the electrolyte

The anode not only functions as the site for electrochemical oxidation of the fuel, but also transfers charge to the material surface. The difference in oxygen chemical potential between anode and cathode is the driving force for oxygen ion migration through the electrolyte and to the anode where they are consumed by the fuel oxidation shown in Eq. 2.1 [2]. A wide range of materials have been considered as anode materials for SOFCs [10] and most studies use a cermet of nickel supported yttrium stabilized zirconia (Ni/YSZ). Early on in the development of SOFC anodes, precious metals as well as pure transition metals such as nickel and iron were used as anode materials. However, the physical and chemical instability of these materials necessitated the testing of other materials. Finally in 1970, Spacil [15] identified that a composite of nickel and YSZ could provide a stable and active anode.

Generally, when H_2 is used as the fuel for the SOFC, the biggest loss of the cell efficiency occurs at the cathode where the oxygen reduction reaction takes place. However, when hydrocarbon fuel is used, the biggest loss is at the anode since the anode catalyst is easily poisoned by coke formation and sulfur poisoning. As a result, the rational design for the anode catalyst is of interest and we review in the next section potential SOFC anode materials and their properties.

2.2 Anode Materials for Solid Oxide Fuel Cells

The development of SOFC anode materials have spanned several years with the goal of developing materials that can replace Ni which exhibits significant disadvantages such as a low tolerance to sulfur [16] and carbon deposition [17] when using hydrocarbon fuels. Moreover, the Ni metal in the cermet tends to agglomerate after operation, causing a reduction in three phase boundary and increasing cell resistance. As suggested by Goodenough and Huang [18], a good candidate for SOFC anode materials should meet five basic requirements:

(i) *Catalytic activity*. The dissociative chemisorption of hydrocarbon fuels must be facilitated by the anode catalyst. This dissociative adsorption needs to be followed by a reaction of dissociative fuel with O^{2-} ions from the electrolyte. If the metal catalyst is used as the anode, the dissociative fuel must be transferred to the three phase boundary (TPB). This TPB consists of a metal catalyst, oxide electrolyte, and fuel in the gas phase. In this case, the chemisorption process involves electron transfer from the fuel to the conduction band of the metal catalyst. On the other hand, if a mixed ionic/electronic conductor (MIEC) is used, O^{2-} ions are transported from the electrolyte directly to the anode surface. Both reactions occur at the material surfaces. The chemisorption involves transfer of electrons to a mixed-valent redox couple of the MIEC. In addition, the anode must not be poisoned by sulfur impurities in the feed gas or by carbonaceous residues if a hydrocarbon fuel is used.

(ii) *Electronic conductivity*. The anode materials must be electronically conductive in order to transfer the electrons from the chemical reaction at the material

surface to an external circuit. A metallic-screen current collector is used to reduce the distance that electrons have to travel in the anode since the surface area of electrolyte is very large. Nonetheless, resistive losses within the anode still have to be minimized by having a material that is active and electronically conductive.

(iii) *Thermal compatibility*. Since a SOFC operates at a high temperature, the thermal expansion of the anode must be matched to that of the electrolyte with which it makes chemical contact, and also to that of the current collect with which it makes physical contact.

(iv) *Chemical stability*. Since the anode must be exposed to a reducing atmosphere and is in contact with the electrolyte, it needs to be chemically stable at the operating temperature. Interface phases that block electron transport from the anode to the current collector must not be formed over time under operating conditions. Furthermore, the anode must be chemically stable next to the electrolyte under the sintering conditions to form a dense ceramic membrane.

(v) *Porosity*. The anode must be fabricated with a porous structure that maintains its physical shape over time of operation. The three phase boundary of the anode or the MIEC surface must make contact with the gaseous fuel over an area as large as possible. In addition, the current collector that makes the physical contact with the anode surface must not cover the entire surface.

Upon these constraints, many research groups reported the advantages and disadvantages of several candidates for anode materials ranging from the traditional Ni/YSZ cermet to alternative oxide anode materials based on the perovskite structure.

14

2.2.1 Ni supported yttria stabilized zirconia cermet anode materials

For both the direct oxidation and steam reforming reaction of fuels, the Ni in the cermet anode plays an important role in facilitating the dissociative chemisorption of the fuel and transferring electrons from the dissociation products to the current collector. The YSZ is known as an effective oxide ion conductor. In addition to its function as a catalyst supporter of the Ni metal [3, 10, 19, 20], the YSZ possesses a thermal expansion coefficient that is compatible with the YSZ electrolyte. As a result, this material fulfills most requirements of an anode. However, the disadvantages of this material are its poor redox stability, low tolerance to sulfur impurities [16], carbon deposition when using hydrocarbon fuels [21-23], and nickel agglomeration after operation.

Several methods have been adopted in order to solve the problem of carbon deposition when using hydrocarbon fuels. Steele [24] suggested that the carbon deposition can be avoided by reducing the operating temperature. They found that carbon arising from the dissociation of methane is not deposited on any materials at temperatures below 750 $^{\circ}$C. Many researchers also reported that the coke formation can be avoided by improving the anode material. The composite anode consisting of Cu-CeO$_2$-YSZ/SDZ has been developed for this purpose and it has been demonstrated that the addition of CeO$_2$ to a Cu-YSZ/SDZ cermet significantly enhances the performance of the cell for hydrocarbon fuels [25, 26]. However, Cu is not as good as an electrocatalyst when compared to Ni, and power densities reported for Cu-based anodes are lower than those of Ni-based anodes. Moreover, Cu has a relatively low melting point and is thus not compatible with high temperature SOFCs.

2.2.2 Fluorite anode materials

Single phase oxide anodes with different structures such as fluorite, perovskite, pyrochlore, tungsten bronze etc. have been proposed as possible SOFC anode materials. In the fluorite structure, the coordination numbers for cations and anions are 4 and 8, respectively [27]. Most SOFC developers used doped ceria as anode materials to lower the operating temperature. Ceramics based on ceria exhibit the cubic fluorite structure (Fig. 2.3) with mixed ionic and electronic conductivity in a reducing atmosphere due to the presence of mixed-valent Ce^{3+}/Ce^{4+}. The introduction of lower valent cations (Ce^{3+}) into the lattice results in the formation of oxygen vacancies, which allows the oxide ions to transfer through the material at a high temperature. It is also believed that the excellent catalytic activity of ceria stems from the oxygen vacancy formation associated with the reversible CeO_2-Ce_2O_3 transition [28, 29]. The electronic conduction of ceria-based materials arises from the reduction of Ce^{4+} to Ce^{3+} and release of electrons at low oxygen partial pressure. Therefore, doped or undoped ceria is a MIEC at low pO_2 and high temperatures.

In addition, it has been reported that ceria based anodes exhibit a high resistance to carbon deposition which permits the use of hydrocarbons as a fuel at the anode [30]. Hibino et al. [31, 32] suggested that a Ru-Ni-GDC ($Ce_{0.9}Gd_{0.1}O_{1.95}$) anode provides excellent catalytic activity for the oxidation of hydrocarbon fuels such as methane, ethane, and propane at 600 ^{o}C. They proposed that the Ru metal plays the main role in the anode reaction. Ruthenium catalysts promote reforming reactions of the unreacted hydrocarbons. Recently, Ye et al. [33] studied the performance of Cu-CeO_2-ScSZ (Scandia stabilized zirconia) composite anode materials for SOFCs that use ethanol fuel.

16

This anode showed a stable performance at 800 $^{\circ}$C for a feed of ethanol and water. Moreover, there was no carbon deposition on the anode surface after operation. Unfortunately, the ethanol oxidation mechanism is still not understood.

Hirabayashi et al. [34] suggested that doped Bi-based oxides are potential anode materials for direct hydrocarbon SOFCs. It has been shown that $(Bi_2O_3)_{0.85}(Ta_2O_5)_{0.15}$ provides a promising candidate at intermediate temperatures. Since the Bi_2O_3 fraction can be reduced to BiO and Bi under the reducing atmosphere, the material achieves a high mixed ionic/electronic conductivity and sufficient catalytic activities to promote complete oxidation of hydrocarbons.
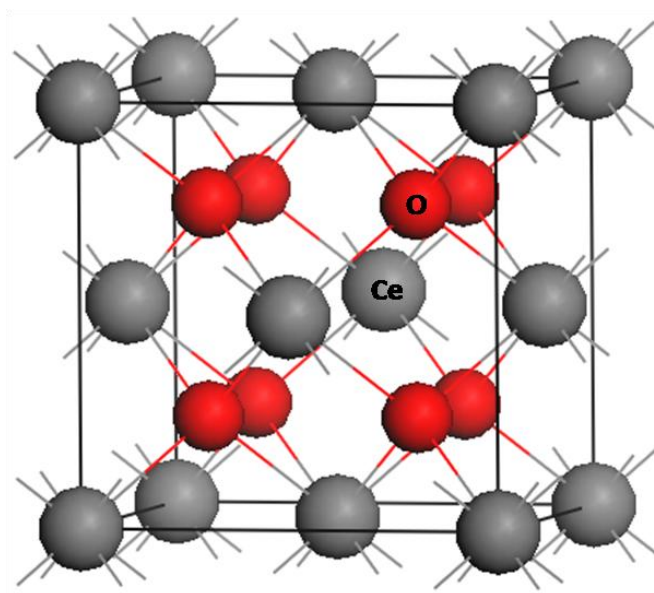
Figure 2.3 Ceria (CeO_2) fluorite structure

2.2.3 Rutile anode materials

The rutile structure is based on a distorted hexagonal close packed anion array with the octahedral sites occupied by cations. Each octahedron shares an edge with the next one, as shown in Fig. 2.4. These edge-sharing octahedrals facilitate the electron

transfer between the octahedral which is related to the high electronic conductivity in materials with a rutile structure. It is hard to find oxygen vacancies in a rutile structure since the octahedra have to be rotated if the produced oxygen vacancies are to jump from one octahedron to the next one. The rotation of edge sharing octahedra in a rutile lattice is much harder than the corner sharing octahedra in the perovskite lattice. As a result, the mobility of oxide ions in the rutile structure is relatively much lower than in lots of other materials. Rutile anode materials, such as Nb_2TiO_7, exhibit quite poor anode performance due to the low ionic conductivity [27]. The thermal expansion coefficient of this material is relatively low compare to that of YSZ. Therefore, the rutile anode materials are not ideal anode materials from the points of thermal expansion and ionic conduction.
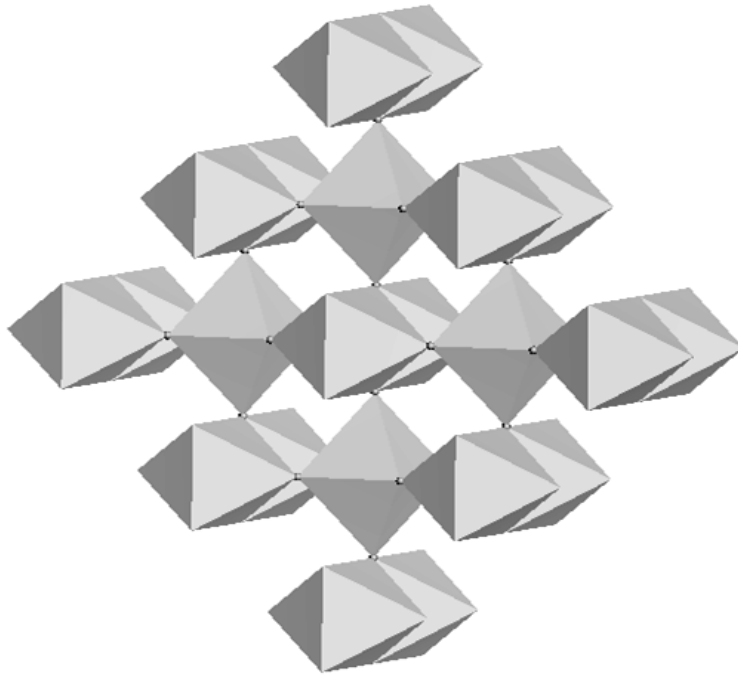
Figure 2.4 The rutile, MO_2 structure

2.2.4 Tungsten bronze anode materials

Tungsten bronze type materials have been considered as potential SOFC anodes. The structure is similar to the perovskite structure. In general, these oxides have the formula $A_2BM_5O_{15}$ (with M = Nb, Ta, Mo, W, and A or B = Ba, Na, etc.) which correspond to a tetragonal tungsten bronze structure (TTB) or an orthorhombic tungsten bronze structure (OTB) [35]. These oxides can be described by a framework of MO_6 octahedra sharing summits, delimiting tunnels of pentagonal, square and triangular sections [2]. The structure of tungsten bronze is illustrated in Fig. 2.5 [27]. The distortion of octahedra means that some M-O bonds are extended and some are shortened. The connection of the short M-O bond length supplies a percolation path for charge transfer, which leads to high electronic conductivity.
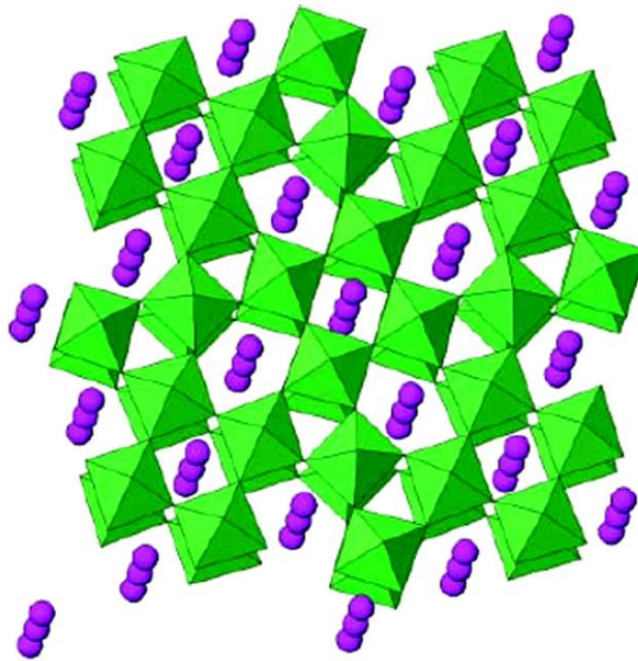
Figure 2.5 The tungsten bronze structure

A wide range of different materials with tungsten bronze structure have been investigated as potential SOFC anodes. The formula $(Ba/Sr/Ca/La)_{0.6}M_xNb_{1-x}O_{3-\delta}$ (M = Mg, Ni, Mn, Cr, Fe, In, Ti, Sn) exhibits high electronic conductivity at low oxygen partial pressure at high temperatures [36]. However, Slater et al. [37, 38] reported that materials with compositions $(Ba/Sr/Ca/La)_{0.6}M_xNb_{1-x}O_{3-\delta}$ (M = Cr, Mn, Fe, Ni, Sn) are not suitable as anode materials because of a poor oxygen exchange kinetics and instability in a reducing atmosphere and high temperature.

2.2.5 Pyrochlore anode materials

Because of the lack of some small A-sites in the pyrochlore, the pyrochlore structure is similar to the tungsten bronze structure, as shown in Fig. 2.6. These oxides have a formula of $A_2B_2O_7$ and can be regarded as a perovskite phase with extra oxygen in the lattice. The structure can also be derived from fluorite, by removing 1/8 of the oxygen sites, ordering the two cations and ordering the oxygen vacancies. Several materials with pyrochlore structure exhibit high ionic conductivity. The anode material with $(Gd_{0.98}Ca_{0.02})_2Ti_2O_7$ provides comparable ionic conductivity to that of YSZ [39]. Moreover, it also exhibits mixed conductivity. Therefore, it could be a potential parent phase for a SOFC anode. Mo-doped $Ga_2Ti_2O_7$ is also considered for use in SOFCs. It was found that this oxide has a very high mixed ionic/electronic conductivity under reducing condition [40]. However, this pyrochlore solid solution is only stable in a certain range of oxygen partial pressure and temperature.
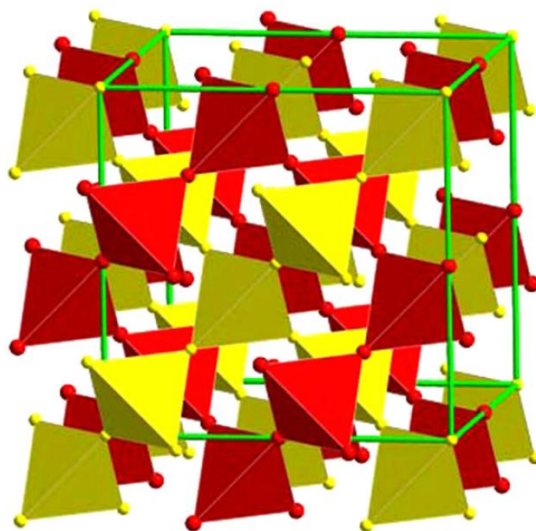
Figure 2.6 The Pyrochlore structure [27]

Finally, it was found that mixed ionic/electronic conductivity may be obtained for zirconates containing cations. $Pr_2Zr_2O_{7-\delta}$ modified by the multivalent cations Mn and Ce on Zr site has been investigated as a potential anode material. However, these pyrochlore phase structures are either redox unstable or poorly conducting. As a result, it seems difficult to find an ideal redox stable mixed conductor in the pyrochlore system.

2.2.6 Perovskite anode materials

The perovskite oxide has the general formula ABO_3 where A is a large cation with a coordination number of 12 and B is a small cation with a coordination number of 6. These materials can accommodate oxygen vacancies; therefore, several perovskites are good oxygen ion conductors. When the overall valence of the A- and B-site cation (n+m) adds up to less than 6, the missing charge is made up by introducing vacancies at the oxygen lattice sites [41]. Figure 2.7 illustrates the typical structure of the cubic perovskite ABO_3. The small B-site in the perovskite allows multivalent transition metal elements to be introduced in the lattice. These elements display mixed-valency under

21

different conditions, which is the source of high electronic conductivity. Good ionic and electronic conductivity is found in several perovskite oxides.
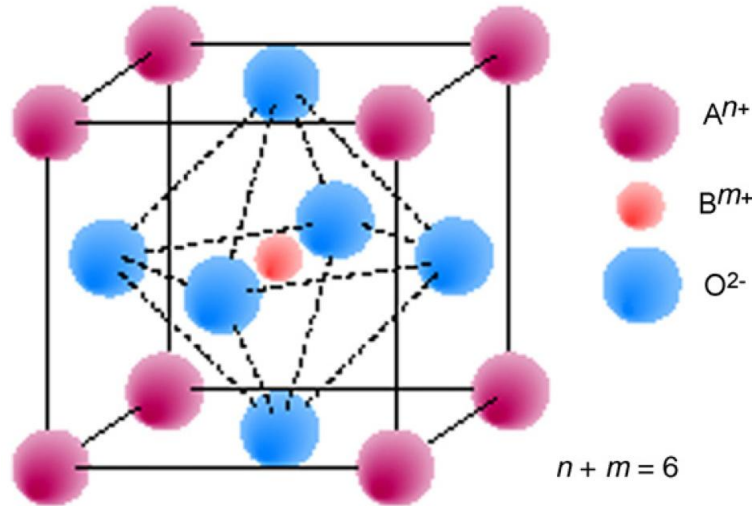
Figure 2.7 Unit cell of the ABO_3 perovskite structure [53]

Materials with the perovskite structure such as Sr- and Mg-doped $LaGaO_3$ (LSGM) exhibit promising good ionic conductivity [42-44]. Recently, many new compounds have been proposed as alternative anode materials in SOFCs. Tao et al. [45] studied an oxygen-deficient perovskite $La_{0.75}Sr_{0.25}Cr_{0.5}Mn_{0.5}O_3$ with comparable electrochemical performance to that of Ni/YSZ and with good catalytic activity for the oxidation of methane at high temperatures. This material was studied as a SOFC anode and found stable in both fuel and air conditions. Moreover, this oxide also has a thermal expansion coefficient that is compatible with that of solid oxide electrolytes. However, this anode material has a low electronic conductivity in the reducing anodic atmosphere and is also not resistant to small amounts of sulfur impurities in the fuel [46].

The perovskite oxide $La_{0.6}Sr_{0.4}Co_{0.2}Fe_{0.8}O_3$ was suggested as a SOFC anode for intermediate temperatures (550-700 ^{o}C) [47]. However, the stability of this anode material is still in doubt in the lower temperature range. The $SrFeCo_{0.5}O_x$ anode exhibits both high electronic and ionic conductivities in air and can be used as a ceramic membrane for gas separation [48]. Although there are still some questions about the exact structure of this material, it is commonly thought to be related to the perovskite structure [49].

Recently, Goodenough et al. [50] reported that the double perovskite $Sr_2Mg_{1-x}Mn_xMoO_{6-\delta}$ can be used with natural gas as a fuel and shows high chemical and physical stability and tolerance to sulfur. This material is oxygen deficient which allows oxide ions to transfer through the material. Thus, it exhibits good ionic conductivity. The mixed valence Mo^{4+}/Mo^{5+} sub-array provides electronic conductivity with an ability to accept electrons from a hydrocarbon. It also promises to be catalytically active for the oxidation of a hydrocarbon fuel since it can accept electrons while losing oxygen, a characteristic of MIEC materials. The ability of accepting electrons while losing oxygen is made possible because Mo^{4+} and Mo^{5+} cations are stable in less than six-fold oxygen coordination, while both Mg^{2+} and Mn^{2+} are stable in four-fold as well as six-fold oxygen coordination [51].

Doped perovskite materials are also promising anode materials. Hui et al. [52] studied the stability and mixed conductivity of yttrium doped $SrTiO_3$ (SYT) as a potential SOFC anode material. They investigated the stability, redox behavior, chemical compatibility with YSZ and LSGM, thermal expansion coefficient, and fuel cell performance. With the optimized composition $Sr_{0.86}Y_{0.08}TiO_{3-\delta}$, the electronic

conductivity was promising at high temperatures. Also, this material has high structural stability over a broad range of temperatures and oxygen partial pressures. Fagged et al. [53] investigated La- and Fe-doped $SrTiO_3$ as an anode material for SOFCs. It was found that the various compositions of La and Fe affect both physical properties and mixed conductivity.

Finally, Marina et al. [30] suggested that $(La,Sr)TiO_3$ doped with several transition metals (Ni, Co, Cu, Cr, and Fe) and Ce provide promising mixed conductivity. The most effective among these dopants is Ce, which significantly decreases the polarization resistance. It was also demonstrated that doped $SrTiO_3$ based anodes are tolerant to an oxygen, carbon and sulfur-containing atmosphere. In addition, it was found that the conductivity of $SrTiO_3$ in a reducing atmosphere can also be improved by replacing Ti with Nb.

2.3 Structure and Properties of Perovskite Oxides

In accordance with the discussion of alternative anode materials for SOFCs, materials with perovskite structures seem to provide promisingly effective mixed ionic/electronic conductivity. A unique feature of mixed oxide compounds is the display of a variety of properties that are partially the result of the variety of the structures such as the mixed electronic and ionic conductivity. In this section, the structure related properties and some applications of these materials are briefly described.

2.3.1 Structure of perovskite oxides

The typical formula of an ideal perovskite structure is ABO_3, where the A-site cations are larger than the B-site cations and similar in size to the oxide anions. Figure 2.8 illustrates that in this structure, the A cations are surrounded by twelve anions and the

B cations are surrounded by six anions in octahedral coordination. The ideal structure adopts the cubic space group where $SrTiO_3$ is commonly regarded as the prototype of cubic perovskites. Even though few compounds have this ideal structure, several oxides exhibit slightly distorted structures with lower symmetry such as, hexagonal and orthorhombic. Moreover, the majority of synthetic simple ABO_3 perovskite group compounds are distorted derivatives which result from: (1) rotation or tilting of distortion-free BO_6 polyhedra; (2) first order Jahn-Teller distortions of the BO_6 octahedra; and (3) second order Jahn-Teller effects on A- and B-cation polyhedra. There are many types of distortions in the perovskite structure that strongly affect their properties, in particular, their ferromagnetic properties.
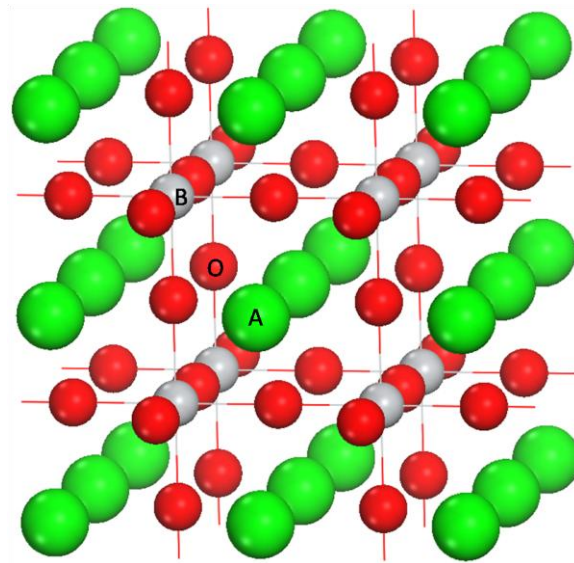
Figure 2.8 The perovskite ABO_3 structure

In order to understand the deviations from the ideal cubic structure, the ABO_3 oxides are regarded as purely ionic crystals. The ideal cubic structure is characterized by the relationship between the ionic radii of the A, B and O ions as shown in the following.

$$r_A + r_O = \sqrt{2}(r_B + r_O) \qquad (1.3)$$

The Goldschmidt tolerance factor [54] t, is used to determine the geometric constraints necessary for the formation of the perovskite structure which can be expressed as:

$$t = (r_A + r_O)/\sqrt{2}(r_B + r_O) . \qquad (1.4)$$

Generally, the value of the tolerance factor of perovskite compounds lies between approximately 0.80 and 1.10. The cubic structure occurs if value of t is close to 1. The observation of the crystal structure related t value reveals that lower values of t will lower the symmetry of the crystal structure; for example, $GdFeO_3$ with $t = 0.81$ is orthorhombic [55] whereas the oxides with $t \leq 0.8$ are characterized as sesquioxide structures such as corundum (α-Al_2O_3) or ilmenite [56]. Furthermore, Giaquinta and zur Loye [56] suggested that the accuracy of structural phase diagram of ABO_3 can be improved by including the bond ionicities of the A and B cations. Figure 2.9 illustrates the structural phase diagram of ABO_3. The axes are the differences in electronegativity of A-O and B-O multiplied by the cation to anion ratio, r_A/r_O and r_B/r_O, respectively.

The formation of superstructures such as double perovskites is reviewed next. Ordered double, triple, or complex perovskites are derivatives of the simple perovskite structure formed when either A- or B-site cations are replaced by combinations of other cations located at specific crystallographic sites. If cations are ordered at only one site the compound are commonly referred to as a double perovskite, whereas if the ordering occurs at both A- and B-site cations they are referred to as complex or quadruple perovskites. Moreover, if the structures exhibit layered ordering of A-site cations with some oxygen vacancies located in the layer (often in the rare-earth layer e.g. $YBaFe_2O_{5+x}$) the structures are referred to as triple perovskites. The majority of ordered

26

perovskites studied are double perovskites with B-site ordering because of their industrial importance and ability to tolerate a wide range of permutation. In general, the B-site ordered perovskites have the general formula $A_2BB'O_6$ where B and B' are different cations in octahedral coordination located at crystallographic distinct sites.
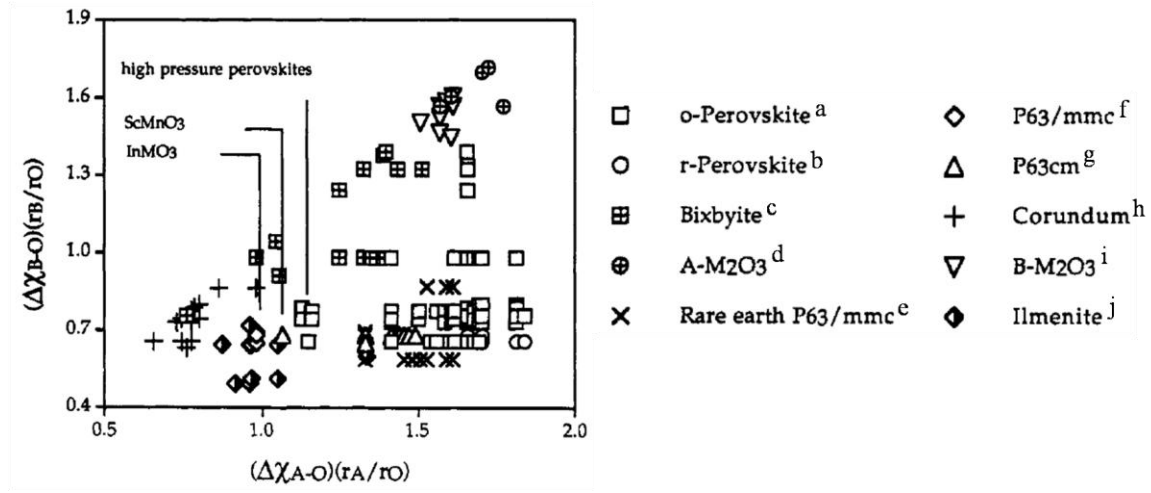
Figure 2.9 Ionicity graph of the ABO_3 phase diagram. [a]Ref [57]. [b]Ref [58]. [c]Ref [59]. [d]Ref [60]. [e]Ref [61]. [f]Ref [62]. [g]Ref[63]. [h]Ref [64]. [i]Ref [60]. [j]Ref [65].

2.3.2 Typical properties of perovskite oxides

Because of the variety of structures and chemical composition, perovskite oxides exhibit several properties related to their structures. The well-known properties of perovskite compounds are ferroelectricity, which is commonly found in $BaTiO_3$-based materials. Moreover, several properties of perovskite oxides are of interest such as, electronic conductivity, ionic conductivity, and catalytic activity especially in oxidation reactions [66]. As a consequence, perovskite oxides are chosen as material for many SOFC components. In this section, typical properties of perovskite compounds are discussed including ferroelectricity, magnetism, superconductivity, catalytic activity and ionic conductivity.

Dielectric properties: A variety of special properties related to dielectric materials such as, ferroelectricity, piezoelectricity, electrostriction, and pyroelectricity, can be found in perovskite oxides. $BaTiO_3$-based compounds display ferroelectric behavior, which is the best-known property of perovskite oxides. This property has a strong relationship with the structure of perovskite materials. Therefore, the crystal structure of $BaTiO_3$ have been studied and reported in detail. $BaTiO_3$ undergoes three phase transformations as the temperature increases (from monoclinic to tetragonal to cubic). The cubic structure is presented at temperatures above 303 K, which does not show ferroelectric behavior. The very high dielectric constant in $BaTiO_3$ can be explained on the basis of the anisotropy of the crystal structure. The crystal structure of $BaTiO_3$ is shown in Figure 2.10 [67]. It is noticed that the large negative potential is localized on the oxygen atoms. When an electric field is applied, Ba^{2+} and Ti^{4+} cations move to the opposite direction to the oxide anions. Hence, a net dipole moment is produced in the unit cell.
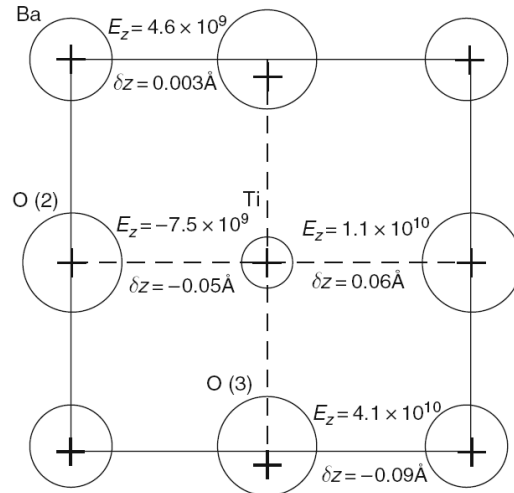
Figure 2.10 Crystal structure of $BaTiO_3$ using the Ewald method and local density of charge [68]

Electrical conductivity and superconductivity: Superconductivity property was first reported by Bednorz and Muller in the La-Ba-Cu-O with K_2NiF_4 structure in 1984 [69]. The presence of square planar sheet of Cu-O was found to be essential for conductivity to occur. High-temperature oxide superconductor of the $YBa_2Cu_3O_7$ perovskite was reported in 1987. The material displays a triple perovskite unit cell where Y and Ba correspond with A-site cations and Cu with B-site cation. The structure contains a 2:1 layered ordering of Ba and Y and additional oxygen vacancies in the Cu layers which lie between the Ba layers [70].

The materials with perovskite structure not only show superconductivity behavior, but also exhibit excellent electronic conductivity. The electronic conductivity of perovskite oxides is comparable with that of Cu metal. Typical examples are $LaCoO_3$ and $LaMnO_3$, which are currently used for the cathode in SOFCs. A-site doped perovskite oxides are also highly effective in enhancing the electronic conductivity because of an increased number of mobile charge carriers generated by the charge compensation.

Catalytic activity: Perovskite oxides have been extensively studied as catalysts for several reactions since the material comprises of various elements and exhibits high chemical stability. There are two types of research trends, which are of interest in the development of perovskite materials as catalysts. The objective of the first trend is to develop oxidation catalysts or oxygen-activated catalysts as an alternative catalyst to replace old-fashioned precious metal catalysts. The second trend's objective is the development of perovskite oxides as a model for active sites. Remarkably, the high catalytic activity of perovskite oxides is based on both high surface activity to oxygen

29

reduction and oxygen activation resulting from a large number of oxygen vacancies presented in the structure.

Perovskite oxides are utilized as environmental catalysts since they display excellent catalytic activity for various reactions such as NO decomposition. Furthermore, it was reported that perovskite oxides consisting of Cu, Co, Mn, or Fe exhibited excellent activity for the direct NO decomposition at higher temperatures [71-73]. It was observed that the key step for NO decomposition ($2NO \rightarrow N_2 + O_2$) is the removal of oxygen molecules from the surface of the catalyst. In addition, it was reported that doping of perovskite oxides can significantly enhance the NO decomposition activity. A relatively high NO decomposition activity was reported for $Ba(La)Mn(Mg)O_3$ perovskites under an oxygen-enriched atmosphere [74].

2.4   Perovskite Oxides for Solid Oxide Fuel Cells

Since perovskite compounds exhibit excellent electronic conductivity, high chemical stability, and high catalytic activity for several reactions, perovskite oxides are considered alternative materials for various components of the SOFC. Mainly, the application of Co- and Mn-containing perovskites as cathodes has been extensively studied because of their high electronic conductivity and catalytic activity for oxygen dissociation.

Several applications of perovskite oxides for SOFC technology have been reported. $LaCrO_3$ is used as a promising interconnect material for tubular-type SOFCs operating at high temperature. $LaCoO_3$ and $LaMnO_3$ are promising SOFC cathodes, and $LaGaO_3$-based oxides have been suggested for the electrolyte. In addition, it has been reported that Cr-based perovskite materials could be potential SOFC anode catalysts.

Therefore, an "all-perovskite SOFC" is currently being considered. In this section, various aspects of perovskite oxides used for SOFCs are briefly discussed.

2.4.1   Oxide ion conductivity in perovskite oxides

Oxides with perovskite structure are well known as effective oxide ion conductors. In order to achieve high oxygen ion conductivity, the introduction of oxygen vacancies by the substitution of a lower valent cation is essential. In the case of perovskite based oxides, when a cation A or B in the ABO_3 structure is partially replaced by a cation M of lower valence, it gives rise to a relatively large number of oxygen vacancies in the lattice to charge compensate the system. Chemical compositions of oxygen deficient perovskite oxides can be expressed as $A_{1-x}M_xBO_{3-\delta}$ in case of A-site doping, or $AB_{1-x}M_xO_{3-\delta}$ in case of B-site doping, where δ is an average number of oxygen efficiencies per unit formula. The oxygen ions can migrate through the crystal lattice with the assistance of oxygen vacancies. In such materials, if the energy barrier of oxygen ion migration is not too high, appreciable ion conduction can be expected at elevated temperatures.

Oxygen ion conduction in perovskite materials was reported for the first time by Stephenson and Flanagan [75]. Later, Takahashi and Iwahara [76] reported very high oxygen ion conductivity in Ti- and Al-based perovskite oxides. Similarly, Al- or Mg-doped $CaTiO_3$ exhibits high conductivity (but still lower than that of YSZ). It was found that in order to achieve excellent oxygen ion conductivity, the rate of oxygen ion migration has to be enhanced. A migrating oxygen ion has to pass through the triangular orifice consisting of two large A- and one small B-site cations in the crystal lattice. As a result, the ionic size of the A-site cations seems to influence greatly the oxygen ion

31

conductivity, whereas the electric or dielectric properties were strongly dependent on B-site cations. It is shown in Fig. 2.11 that the electrical conductivity of $LaAlO_3$ based oxides [43] is improved by increasing the ionic size of the A-site cations. In accordance with these results, a larger unit cell volume is important for higher oxygen ion conductivity because of the larger free volume. Therefore, doping with larger cations for the B-site can improve oxygen ion conductivity. In order to confirm this result, Ga-doped $NdAlO_3$ was investigated. The addition of Ga^{3+}, which is larger than Al^{3+}, to the B-site of $NdAlO_3$ is effective for improving oxygen ion conductivity [77].
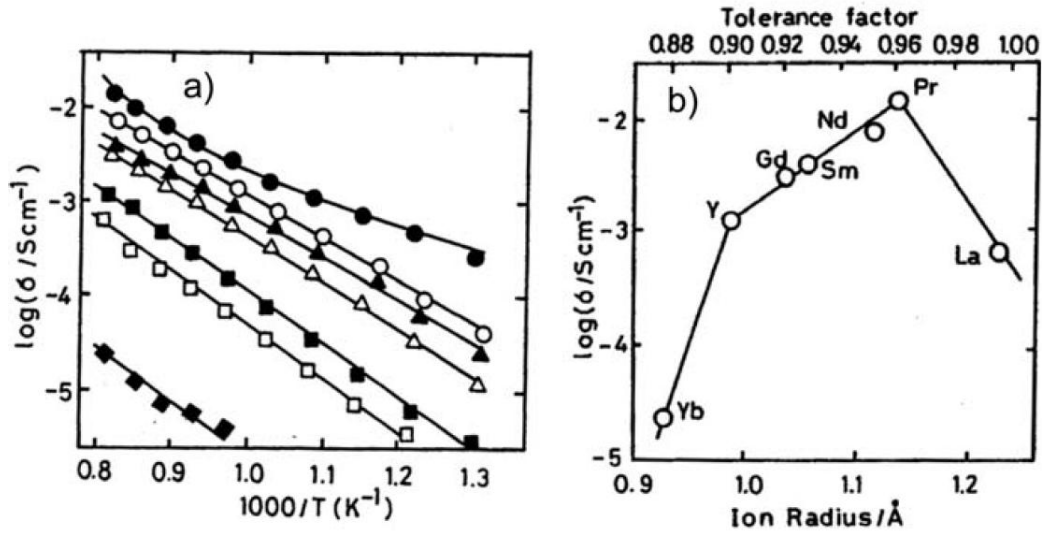
Figure 2.11 Arrhenius plot of (a) the electrical conductivity of Ca-doped $LnAlO_3$ [Ln = La (□), Pr (●), Nd (○), Sm (▲), Gd (∆), Y (■), Yb (♦)]and (b) electrical conductivity at 1223 K as a function of A-site cation size [4]

In addition to the above results, Ga-doped $LaAlO_3$ perovskite was studied in order to show the effect of cation size on the lattice structure. It was found that oxygen ion conductivity increased with increasing amount of Ga which reached a maximum when 50 mol% Ga was doped at Al sites at 1223 K. Since no oxygen vacancy was formed by

32

doping Ga^{3+} because of its identical valency to Al, higher oxygen ion conductivity is brought about by improved mobility of the oxygen ion by increasing the free volume in the unit cell. Although high ionic conductivity was obtained from such perovskite systems, the oxygen ion conductivity of these compounds is still lower than that of YSZ. However, it is of great interest that very high oxygen ion conductivity is reported for $LaGaO_3$-based perovskite oxides.

Perovskite oxides with transition elements at the B-site such as doped $LaCoO_3$ display promisingly effective mixed ionic/electronic conductivity at elevated temperatures. The electronic conductivity is a few orders of magnitudes higher than that of the oxygen ion conductivity. This kind of material is therefore a promising candidate for the SOFC electrode and ceramic membrane reactors.

2.4.2 Thermal expansion behavior and other properties

Thermal expansion is an essential property for SOFC materials. There are many reports stating that the thermal expansion increased with an increase in the dopant concentration. Thermal expansion behavior for $LaGaO_3$ and $La_{0.9}Sr_{0.1}GaO_3$ perovskite oxides were observed around 400 K and were assigned to the phase transition from orthorhombic to the rhombohedral structure. On the other hand, Sr- and Mg-doped perovskite oxides exhibit a monotonic expansion; the average thermal expansion coefficient measured was around 11.5×10^{-6} K^{-1} within the temperature range from 298 to 1273 K. Therefore, the average thermal expansion coefficient is slightly larger than that of YSZ.

Thermal conductivity of this perovskite material has also been investigated. The average thermal conductivity of LSGM is somewhat smaller than that of YSZ.

Consequently, from the point of view of uniform temperature distribution, LaGaO$_3$-based perovskites are more desirable to use as a material for several SOFC components.

In summary, several alternative anode materials display various advantages and disadvantages. Among the reviewed material systems, perovskite based oxide materials exhibit promisingly high ionic/electronic conductivity and catalytically active for various oxidation reactions which are relevant for SOFC anodes. However, the understanding of the structure-property relationship and the role of dopants in these materials are still very limited. Therefore, it is the objectives of this research to utilize various modern computational tools to systematically investigate the effect of dopants in the perovskite structure on various relevant anode properties. The fuel oxidation mechanism on the perovskite surfaces is also studied to further develop the catalytic activity of perovskite anode materials.

2.5　References

[1]　F. Nagel, Electricity from wood through the combination of gasification and solid oxide fuel cells Swiss Federal Institute of Technology Zurich, Zurich (2008).
[2]　C.W. Sun, U. Stimming, J. Power Sources 171 (2007) 247.
[3]　S. McIntosh, R.J. Gorte, Chem. Rev. 104 (2004) 4845.
[4]　W. Nernst, Verfahren zur Erzeugung von Elektrischen Glühlicht 104 (1987) 872.
[5]　E. Baur, H. Preis, Zeitung für Elektrochemie (1937) 727.
[6]　S.R. Wang, T. Kobayashi, M. Dokiya, T. Hashimoto, J. Electrochem. Soc. 147 (2000) 3606.
[7]　K.Q. Huang, R.S. Tichy, J.B. Goodenough, J. Am. Ceram. Soc. 81 (1998) 2565.
[8]　Y. Arachi, H. Sakai, O. Yamamoto, Y. Takeda, N. Imanishai, Solid State Ionics 121 (1999) 133.
[9]　J.B. Goodenough, K. Huang, Lanthanum Gallate as a New SOFC Electrolyte, *Proceedings the FuelCells'97 ReviewMeeting* (1997).
[10]　S.C. Singhal, K. Kendall, *High-temperature solid oxide fuel cells : fundamentals, design, and applicatons*, Elsevier Advanced Technology, New York 2003.
[11]　Y. Ji, J. Liu, T.M. He, L.G. Cong, J.X. Wang, W.H. Su, J. Alloys Compd. 353 (2003) 257.
[12]　M. Juhl, S. Primdahl, C. Manon, M. Mogensen, J. Power Sources 61 (1996) 173.
[13]　Z.P. Shao, S.M. Haile, Nature 431 (2004) 170.
[14]　C.R. Xia, W. Rauch, F.L. Chen, M.L. Liu, Solid State Ionics 149 (2002) 11.

[15]   H.S. Spacil, U.S. (1970).

[16]   Y. Matsuzaki, I. Yasuda, Solid State Ionics 132 (2000) 261.

[17]   X. Turrillas, A.P. Sellars, B.C.H. Steele, Solid State Ionics 28 (1988) 465.

[18]   J.B. Goodenough, Y.H. Huang, J. Power Sources 173 (2007) 1.

[19]   A. Atkinson, S. Barnett, R.J. Gorte, J.T.S. Irvine, A.J. Mcevoy, M. Mogensen, S.C. Singhal, J. Vohs, Nature Materials 3 (2004) 17.

[20]   S.P. Jiang, S.H. Chan, J. Mater. Sci. 39 (2004) 4405.

[21]   M. Mogensen, K. Kammer, Annual Review of Materials Research 33 (2003) 321.

[22]   J.W. Fergus, Solid State Ionics 177 (2006) 1529.

[23]   W.Z. Zhu, S.C. Deevi, Materials Science and Engineering a-Structural Materials Properties Microstructure and Processing 362 (2003) 228.

[24]   B.C.H. Steele, Solid State Ionics 129 (2000) 95.

[25]   S. McIntosh, J.M. Vohs, R.J. Gorte, Electrochim. Acta 47 (2002) 3815.

[26]   C. Lu, W.L. Worrell, R.J. Gorte, J.M. Vohs, J. Electrochem. Soc. 150 (2003) A354.

[27]   S.W. Tao, J.T.S. Irvine, Chemical Record 4 (2004) 83.

[28]   C.W. Sun, J. Sun, G.L. Xiao, H.R. Zhang, X.P. Qiu, H. Li, L.Q. Chen, J. Phys. Chem. B 110 (2006) 13445.

[29]   N.V. Skorodumova, S.I. Simak, B.I. Lundqvist, I.A. Abrikosov, B. Johansson, Phys. Rev. Lett. 89 (2002).

[30]   O.A. Marina, N.L. Canfield, J.W. Stevenson, Solid State Ionics 149 (2002) 21.

[31]   T. Hibino, A. Hashimoto, K. Asano, M. Yano, M. Suzuki, M. Sano, Electrochemical and Solid State Letters 5 (2002) A242.

[32]   T. Hibino, A. Hashimoto, M. Yano, M. Suzuki, M. Sano, Electrochim. Acta 48 (2003) 2531.

[33]   X.F. Ye, B. Huang, S.R. Wang, Z.R. Wang, L. Xiong, T.L. Wen, J. Power Sources 164 (2007) 203.

[34]   D. Hirabayashi, A. Hashimoto, T. Hibino, U. Harada, M. Sano, Electrochemical and Solid State Letters 7 (2004) A108.

[35]   M. Tournoux, M. Ganne, Y. Piffard, J. Solid State Chem. 96 (1992) 141.

[36]   J.L.B. A. Kaiser, P. R. Slater, J. T. S. Irvine, Solid State Ionics 135 (2000) 519.

[37]   P.R. Slater, J.T.S. Irvine, Solid State Ionics 124 (1999) 61.

[38]   P.R. Slater, J.T.S. Irvine, Solid State Ionics 120 (1999) 125.

[39]   S. Kramer, M. Spears, H.L. Tuller, Solid State Ionics 72 (1994) 59.

[40]   O. Porat, C. Heremans, H.L. Tuller, Solid State Ionics 94 (1997) 75.

[41]   B.A. Boukamp, Nature Materials 2 (2003) 294.

[42]   P.R. Slater, J.T.S. Irvine, T. Ishihara, Y. Takita, Solid State Ionics 107 (1998) 319.

[43]   T. Ishihara, H. Matsuda, Y. Takita, J. Am. Chem. Soc. 116 (1994) 3801.

[44]   T. Ishihara, H. Matsuda, Y. Takita, Solid State Ionics 79 (1995) 147.

[45]   S.W. Tao, J.T.S. Irvine, Nature Materials 2 (2003) 320.

[46]   S.W. Zha, P. Tsang, Z. Cheng, M.L. Liu, J. Solid State Chem. 178 (2005) 1844.

[47]   A. Hartley, M. Sahibzada, M. Weston, I.S. Metcalfe, D. Mantzavinos, Catal. Today 55 (2000) 197.

[48]   U. Balachandran, B. Ma, P.S. Maiya, R.L. Mieville, J.T. Dusek, J.J. Picciolo, J. Guan, S.E. Dorris, M. Liu, Solid State Ionics 108 (1998) 363.

[49] J.C. Grenier, G. Schiffmacher, P. Caro, M. Pouchard, P. Hagenmuller, J. Solid State Chem. 20 (1977) 365.

[50] Y.H. Huang, R.I. Dass, Z.L. Xing, J.B. Goodenough, Science 312 (2006) 254.

[51] Y.H. Huang, R.I. Dass, J.C. Denyszyn, J.B. Goodenough, J. Electrochem. Soc. 153 (2006) A1266.

[52] S.Q. Hui, A. Petric, J. Eur. Ceram. Soc. 22 (2002) 1673.

[53] D.P. Fagg, V.V. Kharton, A.V. Kovalevsky, A.P. Viskup, E.N. Naumovich, J.R. Frade, J. Eur. Ceram. Soc. 21 (2001) 1831.

[54] V.M. Goldschmidt, Mat.-Naturv. Kl. 2 (1926) 117.

[55] C. Schinzer, Distortion of Perovskiutes, (1997).

[56] D.M. Giaquinta, H.C. zur Loye, Chem. Mater. 6 (1994) 365.

[57] S.J. Schneider, R.S. Roth, J.L. Waring, Journal of Research of the National Bureau of Standards A 65 (1961) 345.

[58] S. Geller, V.B. Bala, Acta Crystallographica 9 (1956) 1019.

[59] A.F. Reid, A.E. Ringwood, Journal of Geophysical Research 80 (1975) 3363.

[60] R.S. Roth, S.J. Schneider, Journal of Research of the National Bureau of Standards Section a-Physics and Chemistry 64 (1960) 309.

[61] F. Bertaut, Marescha.J, Comptes Rendus Hebdomadaires Des Seances De L Academie Des Sciences 257 (1963) 867.

[62] D.M. Giaquinta, W.M. Davis, H.C. zur Loye, Acta Crystallographica Section C-Crystal Structure Communications 50 (1994) 5.

[63] S. Geller, J.B. Jeffries, P.J. Curlander, Acta Crystallographica Section B-Structural Science 31 (1975) 2770.

[64] P. Villars, Journal of the Less-Common Metals 102 (1984) 199.

[65] A.F. Reid, A.E. Ringwood, Journal of Geophysical Research 74 (1969) 3238.

[66] H. Arai, T. Yamada, K. Eguchi, T. Seiyama, Applied Catalysis 26 (1986) 265.

[67] J.C. Slater, Physical Review 78 (1950) 748.

[68] T. Ishihara, *Perovskite oxide for solid oxide fuel cells*, Springer, New York 2009.

[69] J.G. Bednorz, K.A. Muller, Zeitschrift Fur Physik B-Condensed Matter 64 (1986) 189.

[70] P.H. Hor, R.L. Meng, Y.Q. Wang, L. Gao, Z.J. Huang, J. Bechtold, K. Forster, C.W. Chu, Phys. Rev. Lett. 58 (1987) 1891.

[71] S. Shin, H. Arakawa, Y. Hatakeyama, K. Ogawa, K. Shimomura, Mater. Res. Bull. 14 (1979) 633.

[72] Y. Teraoka, T. Harada, S. Kagawa, Journal of the Chemical Society-Faraday Transactions 94 (1998) 1887.

[73] H. Yasuda, T. Nitadori, N. Mizuno, M. Misono, Bull. Chem. Soc. Jpn. 66 (1993) 3492.

[74] H. Iwakuni, Y. Shinmyou, H. Yano, H. Matsumoto, T. Ishihara, Applied Catalysis B-Environmental 74 (2007) 299.

[75] C.V. Stephenson, Bull. Am. Phys. Soc. 3 (1958) 299.

[76] T. Takahashi, H. Iwahara, Energy Conversion 11 (1971) 105.

[77] T. Ishihara, H. Matsuda, Y. Mizuhara, Y. Takita, Solid State Ionics 70 (1994) 234.

CHAPTER 3

COMPUTATIONAL METHODS

3.1 Density Functional Theory (DFT)

Density functional theory (DFT) methods are based on the Hohenberg-Kohn theorem, which states that the ground state electronic energy of an atom or molecule can be expressed as a functional of the electron density ρ of the molecule [1]. The term "functional" refers to a function of a function, which means that the energy has a functional dependence on ρ, and then ρ is the function of the coordinates of the electrons [1]. DFT has become increasingly useful for the understanding and calculation of ground state densities and energies of molecules, clusters and solids. Particularly in past three decades, DFT has been extensively used by physicists as a tool to calculate the electronic structure of solids. DFT is an alternative approach to the traditional quantum chemistry methods which are primarily based on the many-electron wave function.

3.1.1 DFT formalism

In the following, we briefly describe the fundamentals of DFT. To obtain a better understanding of the Hohenberg-Kohn theorem, the total electronic energy is defined as,

$$E = T + V_{nucl} + V_{rep} + E_{XC}, \tag{3.1}$$

where T is the electronic kinetic energy, V_{nucl} is the interaction of the electron with the nuclei, V_{rep} is the interelectronic coulomb repulsion, and E_{XC} is the exchange correlation functional. The nuclear attraction and coulomb repulsion interactions can be expressed as [1]:

$$V_{nucl} = -\sum_\propto \int \frac{Z_\propto \rho(1)}{r_{1\alpha}} d\tau_1; \tag{3.2}$$

$$V_{rep} = \frac{1}{2} \iint \frac{\rho(1)\rho(2)}{r_{12}} d\tau_1\, \tau_2. \tag{3.3}$$

Equations 3.2 and 3.3 highlight that both V_{nucl} and V_{rep} are functionals of ρ. Although the exact expression of the kinetic energy T is quite complicated and not completely known, it can also be expressed in terms of the electron density. For electrons in boxlike potentials, one can describe the kinetic energy as

$$T = \frac{3}{10}(3\pi^2)^{2/3} \int \rho^{5/3} d\tau. \tag{3.4}$$

In gradient-corrected DFT theories, the kinetic energy functional is improved by taking into account the gradient of ρ. These theories are rarely used in applications to the electronic structure of molecules. The more traditional expression involving the wavefunction is used instead.

$$T = -\frac{1}{2}\sum_i \int \psi_i \nabla^2 \psi_i d\tau \tag{3.5}$$

The exchange correlation energy, E_{XC}, includes the effects of electron exchange and correlation. There is no exact expression for E_{XC}; however, several approximate expressions have been developed in order to describe the exchange correlation energy. The simplest DFT approximation is the local density approximation (LDA), which is

$$E_{XC} = -\frac{9}{8}\left(\frac{3}{\pi}\right)^{1/5} \alpha \int \rho(1)^{4/3} d\tau_1, \qquad (3.6)$$

where α is unity when a free-electron gas model is used and values of about 0.7 are generally used for molecules [1].

In fact, for a molecular system the electron density is typically rather far from spatially uniformity, so it is believed that the LDA approach has significant limitations. To improve the correlation functional it is made not only dependent on the local value of the electron density, but also on the gradient of the density. This approach which includes a gradient correction is referred to as 'generalized gradient approximation' (GGA) [2]. Most gradient corrected functionals are constructed by adding a correction term to the LDA functional, i.e.,

$$E_{XC}^{GGA}[\rho(r)] = E_{XC}^{LSD}[\rho(r)] + \Delta E_{XC}\left[\frac{|\nabla\rho(r)|}{\rho^{\frac{4}{3}}(r)}\right]. \qquad (3.7)$$

Note that the dependence of the correction term is the dimensionless reduced gradient not the absolute gradient.

In recent years, a variety of gradient-corrected density functional methods have been developed yielding structures and energetic properties of molecules, which are significantly better than results from conventional Hartree-Fock (HF) theory. However, there is no systematic approach for achieving the exact solution to the Schrodinger equation through the use of a more accurate gradient correction.

If the Eq. 3.2 - 3.4, and 3.6 are combined and substituted into Eq. 3.1, the energy is expressed only in terms of the electron density which means that there is no need to determine the wave function. Nevertheless, it is difficult to achieve high accuracy with this approach; therefore, in practice the self consistent field approach is used to determine

the density from the wave function. Kohn and Sham [3] introduced the self consistent field calculation for DFT which involves solving the eigenvalue equation

$$F\psi = \varepsilon\psi, \tag{3.8}$$

where

$$F(1) = -\frac{1}{2}\nabla_1^2 - \sum_\infty \frac{Z_a}{r_{1a}} + \sum_j J_j(1) + V_{XC} \tag{3.9}$$

and

$$V_{XC} = \frac{\partial E_{XC}}{\partial P}. \tag{3.10}$$

The steps in the Kohn and Sham self-consistence field calculation are summarized in Fig. 3.1. These self-consistence field calculations in DFT are quite similar to those associated with Hatree-Fock calculations. However, there are some important differences; for example, the first step is to choose a basis set and from the beginning of the KS SCF procedure, there are several different basis sets involved in a calculation. The basis sets in a DFT calculation include a basis set for the KS orbitals and an auxiliary basis set. The electron density $\rho(r)$ can be expanded in an auxiliary basis set and it is computationally convenient to represent $\rho(r)$ as,

$$\rho(r) = \sum_{i=1}^M c_i\Omega_i(r) \tag{3.11}$$

where Ω is the basis function with a unit of probability density and c_i are the coefficients determined by a least-square fitting to the density that is determined from the KS orbitals [2].

After the process of choosing the basis set, a reasonable molecular geometry of the system is defined, and the overlap integrals and the kinetic energy and nuclear-attraction integrals are computed. In accordance with KS theory, all integrals can be regarded as one-electron integrals since every one reflects the interactions of each one

with external potentials. In order to evaluate the remaining integrals, an initial density must be guessed by constructing a density matrix, which is equivalent to the density matrix used in HF theory. Next, V_{XC} can be constructed from the guessed density and the fitting coefficients of the auxiliary basis sets. At this point, all integrals in each KS matrix element have been evaluated. Thereafter, the electron density is obtained from the new orbitals and compared to the density from the preceding iteration. Once convergence of this SCF procedure is achieved, the energy is computed and a geometry optimization can be performed.

The key strength of DFT methods based on the Kohn-Sham procedure is that the accuracy of the computational result is more reliable than results from HF theory. The HF method is preferable when dealing with few-atom systems, whereas DFT is preferable when the system contains more than 5-10 atoms [4]. Besides the concept of computational expense, DFT and traditional HF methods are theoretically complementary.

3.1.2   DFT + U methodology

Although the start of Kohn-Sham DFT has enabled accurate first principle simulations of many-atom systems, there still exist classes of systems or phenomena for which current forms of DFT fail. This is because of the use of approximate exchange correlation (XC) functionals. Therefore, the development of computationally efficient methods that can capture the essential physics missing in approximate XC functionals is needed [5].
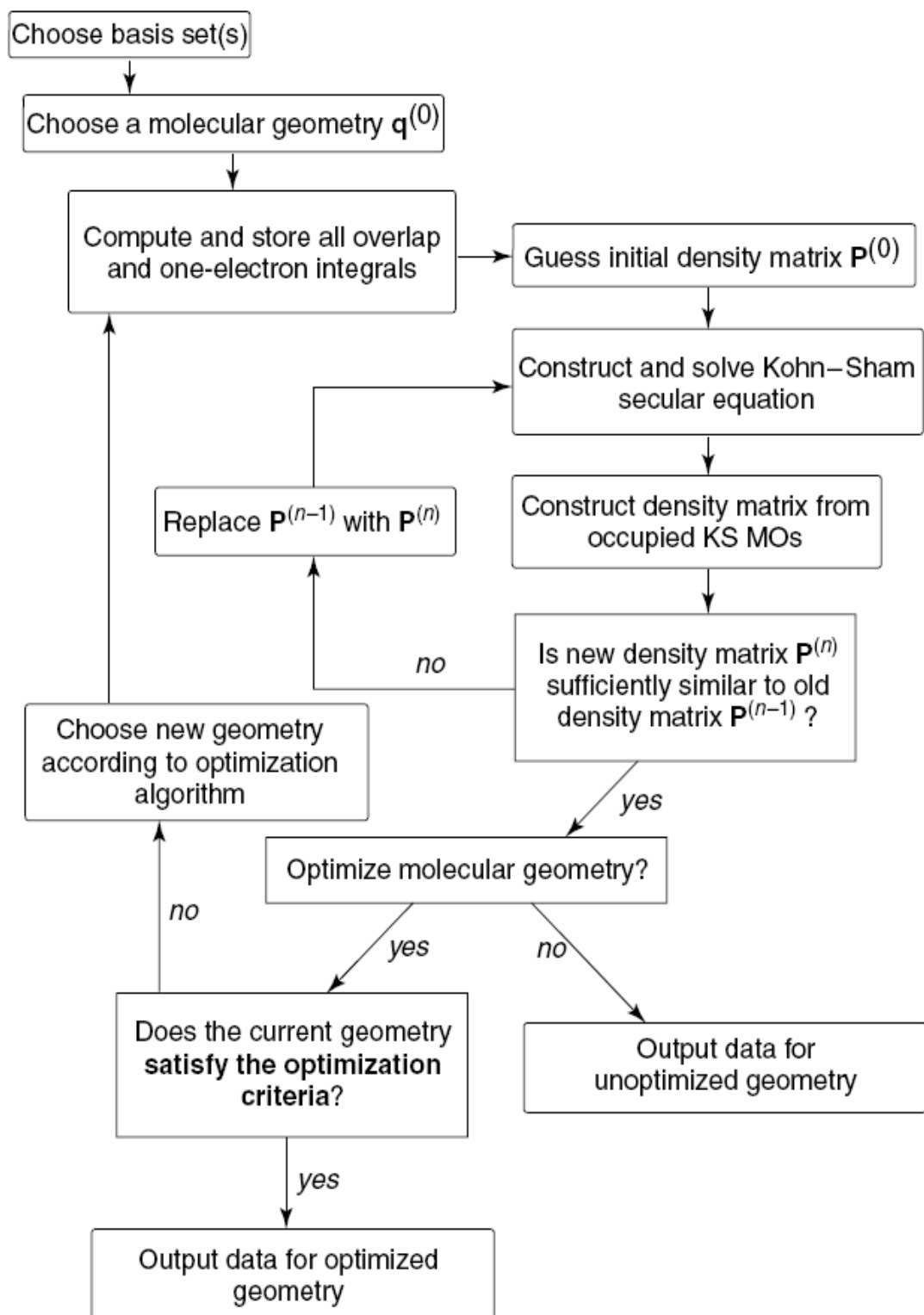
Figure 3.1 Flow chart of the KS SCF procedure [2]

Strongly correlated electron materials (SCEMs) are one of the most important classes of materials that are unsuccessfully described by conventional DFT. SCEMs include actinides and middle-to-late transition metal oxides, which have many electrons in partially filled d or f shells. These d and f electrons are naturally localized on each metal atom leading to numerous associated intra-atomic exchange and large Coulomb energy terms. The electron-electron repulsion in these systems is always predicted to be way too large because approximate exchange correlation functions implemented in conventional DFT fail to cancel out the spurious electron self-interaction. Therefore, the electrons treated by conventional DFT incorrectly delocalize to lessen the repulsion energy. This is the main reason why conventional DFT predicted a known insulator to be metallic [5].

A solution to this problem lies on the ability to accurately account for self-interaction energies that primarily occurs from d and f localized electrons. It is well known that Hatree-Fock (HF) theory can solve this problem since HF calculations contain exact exchange and are free of self-interaction. However, these methodologies are very computationally expensive and have not been implemented for extended crystals [6, 7]. Currently, DFT + U is the technique most frequently used to treat SCEM systems [8, 9]. In this approach, the electronic structure is divided into localized and delocalized states. The interactions between localized electrons on the same atomic center (on-site interactions) are treated by HF whereas the remaining interactions are treated with DFT. This is very reasonable since the errors incurred by DFT are due to the intra-atomic self-interaction error, which should be correctly treated by an HF approach. Practically, a parameterized Hamiltonian is used to evaluate the on-site interaction energy instead of

43

using an explicit HF calculation. The parameters that enter into the Hamiltonian relate to the average Coulomb (U) and exchange (J) interactions between electrons of the same angular momentum that are localized on the same atom. To perform an accurate DFT + U calculations, one needs to choose suitable values for these parameters. Generally, there are two different methods for determining the values of these parameters. In one way, one can tune the values to reproduce known properties of the system of interest. In another way, one can obtain the values of U and J parameters by performing constrained DFT calculations of the system.

The DFT + U method utilizes HF theory to evaluate the on-site interactions between localized electrons and uses DFT to compute all other electronic terms. The total energy functional can be expressed by the following [5]:

$$E^{DFT+U} = E^{DFT} + E^{on-site} - E^{dc}, \tag{3.12}$$

where E^{DFT+U} is the total energy of the system, E^{DFT} is the DFT calculated energy of the system based on the total electron density, $E^{on-site}$ is the HF energy calculated from on-site interactions between localized electrons, and E^{dc} is a double counting term which is used to correct the total energy. According to the approach proposed by Durarev et al. [10], one can rewrite the total energy form as the following;

$$E^{DFT+U} = E^{DFT} + \sum_{I,l,m,\sigma} \left(\frac{U_{Il} - J_{Il}}{2}\right) (n_{Ilm\sigma} - n_{Ilm\sigma}{}^2) \tag{3.13}$$

Note that the first term on the right hand side of this equation represents the DFT energy obtained using the total electron density (on-site interactions included). Since it is known that conventional DFT miscalculates the total energy of the system, the second term on the right hand side is used to correct this behavior. The values of U and J are always positive whereas $n_{Ilm\sigma}$ ranges from 0 to 1. Eventually, the second term acts as a penalty

function that corrects the DFT calculations and leads to an improved description of the electronic structure. In this way, the energies of the localized states will be shifted from their DFT values, which results in the increasing of band gap and insulating character of the system. The values of U and J must be provided in order to perform a DFT + U calculation. These values are system dependent and need to be determined for each particular system. Therefore, wisely selecting appropriate values for these parameters is the key challenge in performing a meaningful DFT + U calculation.

3.2   *Ab initio* Thermodynamic Simulations

The stability of metals and metal oxides at elevated temperatures has become a key challenge in several industries such as aerospace, power generation, metallurgical processing, chemical engineering, and catalysis. For example, one would question if a catalyst remain stable at reducing condition and elevated temperatures or one would want to know how the surface of a catalyst looks like under reaction conditions.

3.2.1   Stability of bulk metal oxides [11]

In atomistic studies, one can use a tool called *ab initio* thermodynamics to computationally predict the stability of the interested materials. To perform *ab initio* thermodynamic calculations, we take into account the environmental conditions (e.g. temperature and oxygen partial pressure) by combining the total energy of electronic structure calculations with a thermodynamic description of the system. The general procedure will be described in the following fashion. Let us consider the phase stability of a metal, M, in equilibrium with gas phase O_2 at specified pressure, pO_2, and temperature, T. In particular, we will determine the thermodynamic stability of Cu and Cu_2O at various oxygen partial pressures and temperatures. In this manner, we would like

to know which material minimizes the free energy of a system containing gaseous O_2 and a material at specified conditions. One useful way to perform this is to define the grand potential related to each crystal structure. We can define the grand potential of a metal oxide containing N_M metal atoms and N_o oxygen atoms by the following

$$\Omega(T,\mu_O,\mu_M) = E(N_M,N_O) - TS - \mu_O N_o - \mu_M N_M \, , \tag{3.14}$$

where E is the electronic DFT energy of the metal oxide, S is the material's entropy, and μ_a is the chemical potential of atomic species a. We can use this expression to calculate the grand potential of each material, Ω_i. We can then normalize the DFT energy of each material, E_i, so that every DFT calculation describes a material with same total number of atoms. In this way, we can compare the grand potentials of different systems. If we do this, Eq. 3.14 can be rewritten as

$$\Omega_i(T,\mu_O) = E_i - TS_i - \mu_O N_{o,i} - \Omega^M \, , \tag{3.15}$$

where Ω^M is an additive constant that is the same for every material. The chemical potential of an oxygen atom can be determined by the temperature and pressure of gaseous O_2. From ideal gas law, we can define the chemical potential of gaseous O_2 as the following

$$\mu_{O_2} = \mu_{O_2}^o(T,p^o) + kTln(p_{O_2}/p_{O_2}^o) \, , \tag{3.16}$$

where the superscript o denotes a reference pressure, usually take to be 1 atm. The chemical potential of an oxygen atom can be defined as

$$\mu_O = \frac{1}{2}\mu_{O_2}. \tag{3.17}$$

When comparing crystalline solids, the differences in the entropic contributions between different structures are usually insignificant when comparing with the contributions from electronic DFT energies. Therefore, we can treat the entropic

46

contributions as being approximately constant for all the crystal structures we consider and the grand potential becomes

$$\Omega_i(T, \mu_O) = E_i - \mu_O N_{o,i} - \Omega_S^M ,$$ (3.18)

where Ω_S^M is an additive constant that is the same for every material. Note that we can set Ω_S^M to zero without any loss of generality since we are only interested in the material that provides the lowest grand potential. Now, we can calculate the grand potential which only involves the DFT-calculated energies of the metals and metal oxides of interest and the pressure and temperature of gaseous O_2. The material that gives the lowest grand potential is the material that minimizes the free energy of the combination of gaseous O_2 and solid.

Figure 3.2 demonstrates the application of Eq. 3.18 for Cu and Ag which shows the relative stability of M and M_2O. The dotted lines in Fig. 3.2(a) show the grand potential as a function of chemical potential of gaseous O_2. The line for pure metal, M, has a slope of zero because $N_o = 0$ in this case whereas the line for metal oxide has a negative slope. The thick curves denote the structure with lowest grand potential as the chemical potential is varied. At low oxygen chemical potential, the bulk metal is thermodynamically stable whereas at high value of chemical potential the metal oxide is the favored material. This makes a lot physical sense because it is more favorable for a metal to get oxidized and become a metal oxide at high oxygen chemical potential. The schematic phase diagram of metal and its oxide is shown in Fig. 3.2(b). This phase diagram confirms that metal oxides can be reduced to metals by holding the material at high enough temperature or in a low enough oxygen partial pressure.
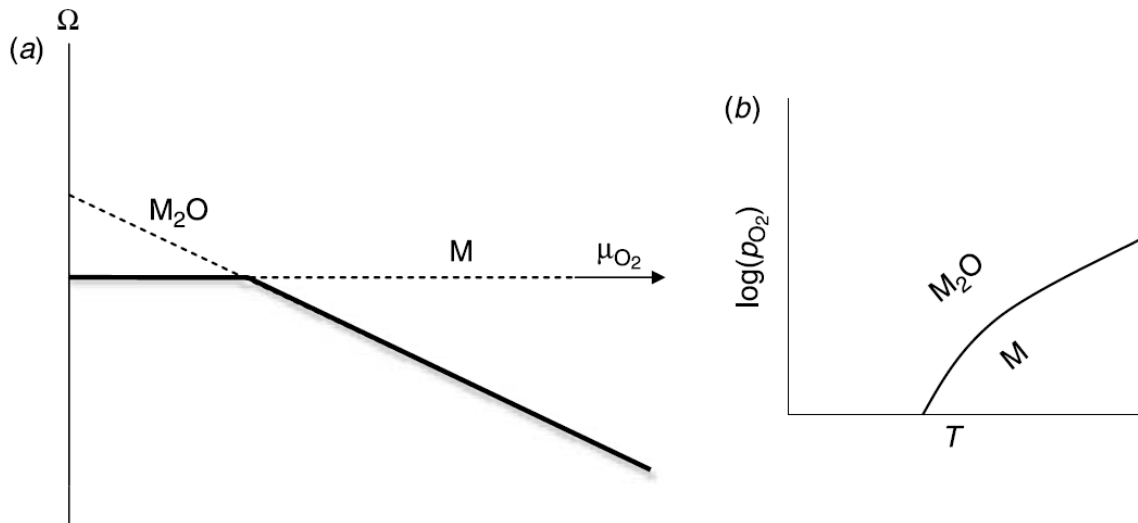
Figure 3.2 (a) Schematic grand potential diagram for oxidation of metal and its oxide and (b) the phase diagram defined by the grand potential diagram

Furthermore, we can compare more than one oxide species in *ab inito* thermodynamic calculations. Figure 3.3 shows an extension of the grand potential diagram of bulk metal, M, M_2O and M_2O_3. It can be seen from the diagram that the newly added species, M_2O_3 is not favorable since the calculated grand potential of this oxide lies above the grand potential of another oxide M_2O. This means that the phase diagram shown in Fig. 3.2(b) is still correct even when M_2O_3 is considered in addition to M and M_2O. It is noteworthy that using this method can only tell us the relative stability of materials of interest. In other words, we can only compare the thermodynamic stability of the materials that we performed DFT calculations.
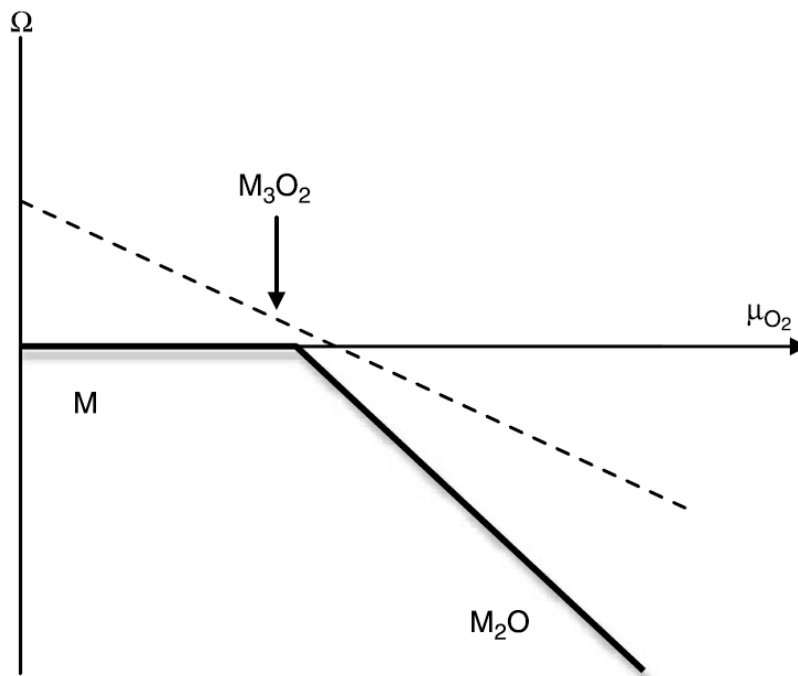
Figure 3.3 Extension of the grand potential diagram from Fig. 3.2 with the addition of a metal oxide M_2O_3

Figure 3.4 depicts the calculated phase diagram of Au and Cu and their oxides. The diagram confirms that Ag is much more resistant to oxidation than Cu. It is important to note that this phase diagram only represents the thermodynamic stability of each material; it does not provide any information about the kinetic of how fast the material can reach the equilibrium. Furthermore, it should be expected that the results from calculated phase diagram are not exact. This is because our calculations neglected the influence of vibrational contributions to the free energies of the solids. More importantly, the total energies from DFT calculations include systematic errors because of the inexact nature of DFT.
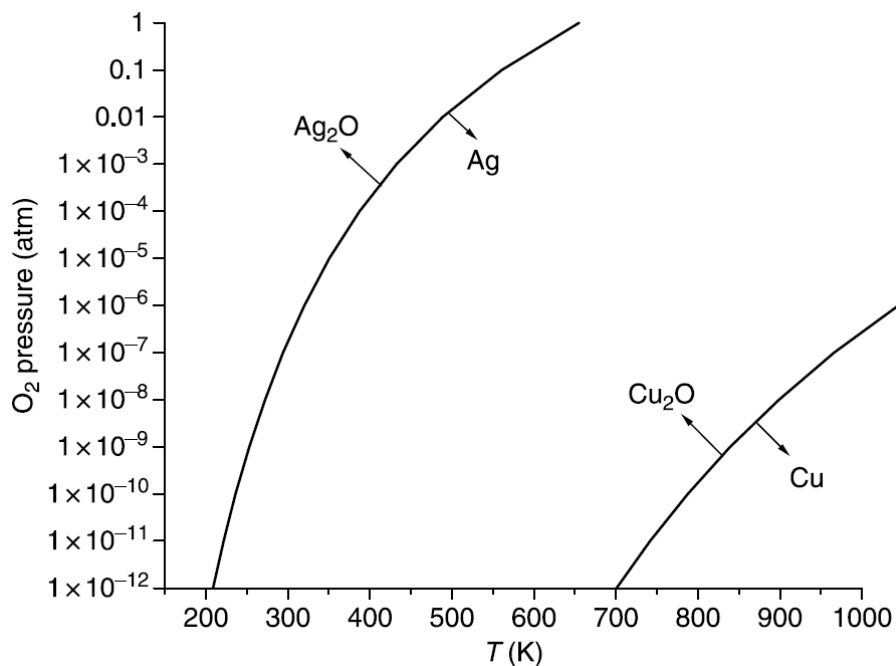
Figure 3.4 DFT-calculated phase diagram for oxidation of bulk Cu and Ag.

3.2.2 Stability of metal and metal oxide surfaces [12]

In this section, we describe in details the thermodynamic formalism used to calculate surface phase diagrams of the most stable structures of various surface terminations as a function of external environmental conditions [13-22]. A basic assumption is that the surface terminations are in thermodynamic equilibrium with separate reference phases for each atomic species i at a given temperature, T, and pressure, p. By adsorption and desorption processes, the surface allows to exchange any amount of atoms with each reference phase without changing the temperature or pressure while the total number of atoms, N_i^{tot} is held constant. Figure 3.5 illustrates the schematic of a surface in contact with a reference phase of atomic species i. Gibbs free energy is the suitable thermodynamic potential for a situation with fixed temperature,

pressure, and number of particles. Note that the total number of atoms, N_i^{tot}, are equal to sum of the number of atoms of the surface, N_i, and number of atoms in the reference phases, N_i^{ref}.

$$N_i + N_i^{ref} = N_i^{tot} \ . \tag{3.19}$$
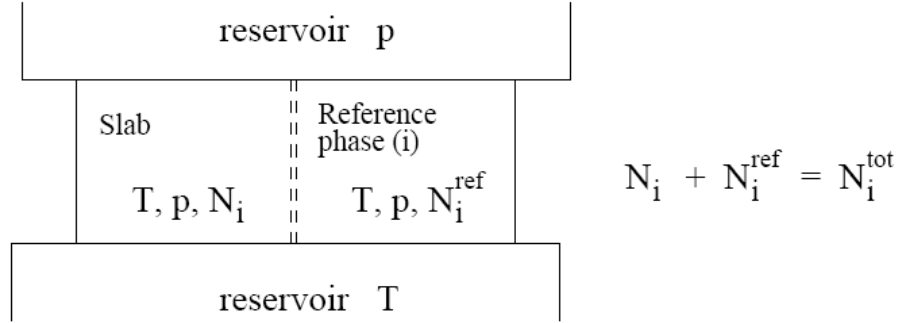
Figure 3.5 Schematic illustration of a surface in contact with a reference phase of atomic species i at particular temperature and pressure [12].

In equilibrium, the most stable structure of the surface is the one that minimizes the total Gibbs free energy of the system:

$$G_{slab}(T, p, \{N_i\}) + \sum_i G^{(i)}(T, p, N_i^{ref}) = min \ , \tag{3.20}$$

where $G_{slab}(T, p, \{N_i\})$ is the Gibbs free energy of the surface and $G^{(i)}(T, p, N_i^{ref})$ is the Gibbs free energy of the reference phases i. We can transform this equation using the Euler equation to substitute the Gibbs free energy of the reference phases by chemical potentials, $\mu_i(T, p)$;

$$G^{(i)}(T, p, N_i^{ref}) = (N_i^{tot} - N_i)\mu_i(T, p) \ . \tag{3.21}$$

Then, the Gibbs free surface energy, $\gamma(T, p)$ is defined by subtracting the total free energy of the system (Eq. 3.20) by the total free energy of the atoms, $\sum_i N_i^{tot} \mu_i(T, p)$, and normalizing the results to an energy per unit area;

$$\gamma(T, p) = \frac{1}{A}\left(G_{slab}(T, p, \{N_i\}) - \sum_i N_i \mu_i(T, p)\right).$$ (3.22)

As also shown in Eq. 3.20, the most stable surface configuration is again the one that minimizes the Gibbs free surface energy. To determine which surface configuration is the most stable in particular environmental conditions, we calculate the surface free energy of a series of surface models with different structures and compositions as a function of the chemical potentials. For a given chemical potential, the surface model that gives the lowest surface free energy is the most stable surface. Then, we can relate the chemical potentials to actual temperature and pressure by assuming that the surface is in thermodynamic equilibrium with the reference phases.

For example, let us consider a simple system with A_xB_y composition. In this particular case, there are only two chemical potentials that we have to consider, μ_A and μ_B. However, these two chemical potentials are not independent. Eventually, we can relate the chemical potentials of each atom to the Gibbs free energy of a bulk unit cell since we can assume that the surface is always in equilibrium with its own bulk.

$$\mu_A(T, p) + \mu_B(T, p) = G_{bulk}^{AB}(T, p).$$ (3.23)

Therefore, we can eliminate one of the chemical potentials in Eq. 3.22;

$$\gamma(T, p) = \frac{1}{A}\left(G_{slab}(T, p, N_A, N_B) - N_A G_{bulk}^{AB}(T, p) + (N_A - N_B)\mu_B(T, p)\right).$$ (3.24)

Since we are only interested in the relative stability of surfaces with different composition, it is useful to introduce a reference surface structure with Gibbs free energy,

$G_{slab}^o (T,p)$, and number of atoms, N_A^o, N_B^o. Then, we can relate all energies relative to the reference surface and the change of Gibbs free surface energy can be defined as follows;

$$\Delta\gamma(T,p) = \frac{1}{A}\left(G_{slab}(T,p,N_A,N_B) - G_{slab}^o(T,p) - \Delta N_A G_{bulk}^{AB}(T,p) + (\Delta N_A -\right.$$

$$\left.\Delta N_B)\mu_B(T,p)\right), \tag{3.25}$$

where the changes in number of atoms are $\Delta N_A = N_A - N_A^o$ and $\Delta N_B = N_B - N_B^o$. Note that the difference of Gibbs free surface energy is negative when a surface is more stable than the reference surface structure.

In principle, it seems like we have to calculate all Gibbs free energies of every surface and bulk species in the system. In practice, however, we can neglect all entropy and volume effects for the slabs and bulk phases since the vibrational contributions to the entropy usually cancel out when we calculate the difference of Gibbs free energies [20]. Therefore, it is quite common to replace Gibbs free energy by the internal energy as they are obtained from the total energy calculations;

$$\Delta\gamma(T,p) = \frac{1}{A}\left(E_{slab}(N_A,N_B) - E_{slab}^o - \Delta N_A E_{bulk}^{AB} + (\Delta N_A - \Delta N_B)\mu_B(T,p)\right). \tag{3.26}$$

Nevertheless, the chemical potentials are still functions of temperature and pressure which represent the effect of external environment.

3.3   Kinetic Models for Catalytic Reactions [23]

A mean-field microkinetic model [24] is an efficient tool for consolidation of fundamental information about a catalytic process. It is used to predict information about surface coverages under reaction conditions and relative rates of various elementary steps. The model used calculated DFT results such as activation energies and binding energies as initial estimates to predict the reaction behavior under a variety of different

conditions. Although, the results obtained from this model are dependent on the initial guesses of various input parameters, the model has true predictive power. In this section, we briefly describe some important concepts in microkinetic modeling and show how we can obtain a better understanding of catalytic reactions on the surface from DFT studies.

3.3.1 Rate constant

DFT calculations can be used to define the rates of chemical processes that involve energy barriers. Transition state theory is usually used to calculate the rate constant for reactions involving bond-making or bond-breaking whereas collision theory is used to determine the rate constant for the steps involving adsorption and desorption processes. In transition state theory, we assume that reactants and an activated complex are in quasi-equilibrium. Consider an elementary step A* + B* → C* + D*, where * denotes an adsorbed species, the transition state of this elementary step can be determined using nudge elastic band (NEB) or climbing image nudge elastic band (CI-NEB) methods. CI-NEB can be used to determine the minimum energy pathway (MEP) between reactants and products by optimizing several discrete intermediate images. The saddle point in this MEP represents the transition state ($AB^{\ddagger}$). As a result, we can express the elementary reaction as follows:

$$A^* + B^* \overset{k_{for}^{\ddagger}}{\longleftrightarrow} AB^{\ddagger} \overset{k_{for}}{\longrightarrow} C^* + D^* , \tag{3.27}$$

$$C^* + D^* \overset{k_{rev}^{\ddagger}}{\longleftrightarrow} AB^{\ddagger} \overset{k_{rev}}{\longrightarrow} A^* + B^* . \tag{3.28}$$
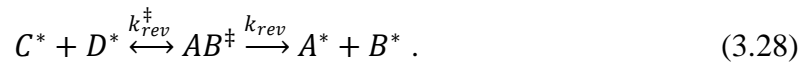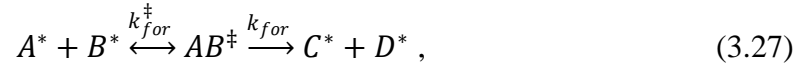
Then, we can calculate the rate of the reaction for this elementary step using the following equation:

$$r = k_{for}\theta_A\theta_B - k_{rev}\theta_C\theta_D . \tag{3.29}$$

where k_{for} and k_{rev} denote the forward and reverse rate constants and θ_A, θ_B, θ_C, and θ_D represent the surface coverages of the species A, B, C, and D, respectively. Furthermore, we can calculate the equilibrium constant using the following relation:

$$K = \frac{k_{for}}{k_{rev}}. \tag{3.30}$$

The forward rate constant is given as:

$$k_{for} = A_o \exp\left(\frac{-E_f}{k_B T}\right), \tag{3.31}$$

where k_B is the Boltzmann constant, T is the reaction temperature, E_f denotes the energy barrier of the forward reaction and A_o is the frequency factor which can be calculated using the following expression:

$$A_o = \frac{k_B T}{h} \exp\left(\frac{\Delta S_{for}^{o\ddagger}}{k_B}\right), \tag{3.32}$$

where $\Delta S_{for}^{o\ddagger} = S_{AB\ddagger}^{o\ddagger} - (S_{A*}^o + S_{B*}^o)$, is standard entropy change accompanying the formation of the transition state $AB^{\ddagger}$. To calculate the entropy of adsorbed species we can perform DFT calculations to determine the vibrational modes of each adsorbed species. The entropy contributions from vibrational modes can be evaluated using the harmonic normal mode approximation as:

$$S_{vib} = k_B \sum_i^{\# \, of \, modes} \left(\frac{x_i}{e^{x_i}-1} - \ln(1 - e^{-x_i})\right). \tag{3.33}$$

where x_i is defined in terms of the vibration frequency, v_i, as $x_i = \frac{h v_i}{k_B T}$. The same procedure can be used to calculate the entropy of the transition state, $S_{AB\ddagger}^{o\ddagger}$.

On the other hand, we used collision theory to define rate constants for adsorption-desorption processes. The rate of adsorption processes is given by [25]:

$$r_f = \frac{\sigma^o(T,\theta)P_A}{\sqrt{2\pi m_A k_B T}} \exp\left(\frac{-E_f}{k_B T}\right). \tag{3.34}$$

where r_f represents the adsorption rate, P_A is the partial pressure of adsorbing species in the gas phase, and m_A is molecular weight of the species. The sticking probability, $\sigma^o(T, \theta)$, is a function of temperature and surface coverage. The activation energies for these processes are often zero since the adsorption-desorption processes are non-activated. The rate is in units of molecules per unit surface area per time. Furthermore, the turn over frequencies (TOF) can be calculated by multiplying the rates with the area occupied by active sites (typically 10^{-15} cm^2).

3.3.2 Equilibrium constant

For an elementary reaction $A^* + B^* \rightarrow C^* + D^*$, where * denotes an adsorbed species, the equilibrium constant is given by:

$$K = \exp\left(\frac{-\Delta G^o}{k_B T}\right) = \exp\left(\frac{-\Delta S^o}{k_B}\right)\exp\left(\frac{-\Delta H^o}{k_B T}\right), \tag{3.35}$$

where ΔG^o, ΔS^o, and ΔH^o are the change in standard-state Gibbs free energy, entropy, and enthalpy, respectively. DFT calculations provide an efficient way to calculate the total electronic energy (TE) of a system, which can be used to determine the heat of the reaction at standard state, ΔH^o. For the case of adsorption of a species on a surface, we can estimate the heat of the reaction from the binding energy (BE) of the species. The BE of the adsorbed species is given as BE = TE(adsorbed configuration) – TE(clean slab) – TE(gas phase species). Thus, we can determine heat of reaction from:

$$\Delta H = \sum_{i=1}^{n} BE(Products) - \sum_{i=1}^{m} BE(Reactants) + \Delta H_{gas} . \tag{3.36}$$

where n and m denote the number of product and reactant species, respectively, and ΔH_{gas} is the heat of reaction in the gas phase. We can improve the accuracy of the heat of the reaction by correcting the binding energy using zero point energies and temperature

corrections. These parameters can be obtained from vibrational frequency calculations of each species. The entropy contributions from Eq. 3.32 can be determined using Eq. 3.30 as previously described.

3.3.3 Rate controlling step

The rate controlling step is the elementary step that provides the maximum effect to the overall rate of the reaction. We can use DFT-calculated energies and microkinetic analyses to obtain the rate controlling step of a series of elementary reactions. It has been suggested by Campbell [26] that the rate determining step of a reaction scheme can be determined by computing the relative change in the overall reaction rate upon changing the forward and reverse rate constant of the particular step, while maintaining the same value of the equilibrium constant for the step. Therefore, we can define the degree of rate control as:

$$X_{RC} = \frac{k_i}{r} \left(\frac{\delta r}{\delta k_i} \right)_{K_i, k_{j \neq i}}. \tag{3.37}$$

Note that the equilibrium constant for step i and all other rate constants are held constant.

3.3.4 Reaction orders and apparent activation energies

Another way to express the rate of overall reaction is to define it in the form of Arrhenius rate expression as follows:

$$r_{overall} = A_o \exp\left(\frac{-E_{app}}{RT} \right) \prod_i P_i^{\alpha_i} (1 - \beta), \tag{3.38}$$

where A_o denotes the frequency factor, α_i denotes the reaction orders with respect to species i, E_{app} is the apparent activation energy and β is the approach to equilibrium. Note that β can be expressed in terms of the net equilibrium constant and the partial pressure of reactants and products as follows:

$$\beta = \frac{1}{K} \frac{\prod_i^{Products} P_i^{\sigma_i}}{\prod_i^{Reactants} P_i^{\sigma_i}}, \tag{3.39}$$

where σ_i represents stoichiometric coefficients. Such kinetic expressions are very important to reactor design and optimization. Reaction orders, α_i, and apparent activation energy, E_{app} play a crucial role in determining these kinetic expressions. In this manner, we can perform a microkinetic analysis to predict how these parameters change upon reaction conditions using the following equations:

$$\alpha_i = \left(\frac{d \ln r_{overall}}{d \ln p_i} \right)_{T, p_{j \neq i}}, \tag{3.40}$$

$$E_{app} = RT^2 \left(\frac{d \ln r_{overall}}{d T} \right), \tag{3.41}$$

where p_i is the partial pressure of the gas phase species i. Once we obtain various values of reaction orders and apparent activation energies under different reaction regimes we can generate explicit rate expressions without actually performing experiments under these conditions.

3.5   References

[1]   M.A. Ratner, G.C. Schatz, *An introduction to quantum mechanics in chemistry*, Prentice Hall, Upper Saddle River, NJ 2000.
[2]   C.J. Cramer, *Essentials of computational chemistry : theories and models*, Wiley, Chichester 2004.
[3]   W. Kohn, L.J. Sham, Physical Review 140 (1965) 1133.
[4]   W. Kohn, A.D. Becke, R.G. Parr, Journal of Physical Chemistry 100 (1996) 12974.
[5]   N.J. Mosey, E.A. Carter, Phys. Rev. B 76 (2007).
[6]   P.Y. Ayala, K.N. Kudin, G.E. Scuseria, J. Chem. Phys. 115 (2001) 9698.
[7]   C. Pisani, M. Busso, G. Capecchi, S. Casassa, R. Dovesi, L. Maschio, C. Zicovich-Wilson, M. Schutz, J. Chem. Phys. 122 (2005).
[8]   S.L. Dudarev, A.I. Liechtenstein, M.R. Castell, G.A.D. Briggs, A.P. Sutton, Phys. Rev. B 56 (1997) 4900.
[9]   A. VI, F. Aryasetiawan, A.I. Lichtenstein, J. Phys.: Condens. Matter 9 (1997) 767.
[10]   S.L. Dudarev, G.A. Botton, S.Y. Savrasov, C.J. Humphreys, A.P. Sutton, Phys. Rev. B 57 (1998) 1505.
[11]   D.S. Sholl, J.A. Steckel, *Density functional theory : a practical introduction*, Wiley, Hoboken, N.J. 2009.

[12]   B. Meyer, In: S.B. J. Grotendorst, D. Marx, Editor, *Computational Nanoscience: Do It Yourself!*, John con Neumann Institute for Computing, Julich (2006), pp. 411-418.

[13]   E. Kaxiras, Y. Baryam, J.D. Joannopoulos, K.C. Pandey, Phys. Rev. B 35 (1987) 9625.

[14]   E. Kaxiras, Y. Baryam, J.D. Joannopoulos, K.C. Pandey, Phys. Rev. B 35 (1987) 9636.

[15]   E. Kaxiras, K.C. Pandey, Y. Baryam, J.D. Joannopoulos, Phys. Rev. Lett. 56 (1986) 2819.

[16]   J. Padilla, D. Vanderbilt, Phys. Rev. B 56 (1997) 1625.

[17]   A. Pojani, F. Finocchi, C. Noguera, Surf. Sci. 442 (1999) 179.

[18]   I. Batyrev, A. Alavi, M.W. Finnis, Faraday Discuss. 114 (1999) 33.

[19]   I.G. Batyrev, A. Alavi, M.W. Finnis, Phys. Rev. B 62 (2000) 4698.

[20]   K. Reuter, M. Scheffler, Surf. Sci. 490 (2001) 20.

[21]   K. Reuter, M. Scheffler, Phys. Rev. Lett. 90 (2003).

[22]   G. Kresse, O. Dulub, U. Diebold, Phys. Rev. B 68 (2003).

[23]   A.A. Gokhale, S. Kandoi, J.P. Greeley, M. Mavrikakis, J.A. Dumesic, Chem. Eng. Sci. 59 (2004) 4679.

[24]   J.A. Dumesic, *The Microkinetics of heterogeneous catalysis*, American Chemical Society, Washington, DC 1993.

[25]   R.D. Cortright, J.A. Dumesic, Advances in Catalysis, Vol 46 46 (2002) 161.

[26]   C.T. Campbell, J. Catal. 204 (2001) 520

CHAPTER 4

DFT STUDY ON THE ELECTRONIC STRUCTURE OF P- AND N-DOPED STRONTIUM TITIVATES IN A REDUCING ENVIRONMENT

4.1 Summary

The electronic conductivity and thermodynamic stability of mixed n-type and p-type doped $SrTiO_3$ have been investigated at anodic solid oxide fuel cell (SOFC) conditions using density functional theory (DFT) calculations. In particular, constrained *ab initio* thermodynamic calculations have been performed to evaluate the phase stability and reducibility of various Nb- and Ga-doped $SrTiO_3$ at synthesized and anodic SOFC conditions. The density of states of these materials was analyzed to study the effects of n- and p-doping on the electronic conductivity. In agreement with experimental observations, we find that the transformation from 20% Nb-doped Sr-deficient $SrTiO_3$ to a non Sr-deficient phase occurs at high temperature and low oxygen partial pressure which leads to a significant improvement in electronic conductivity. A mixed ionic/electronic conductor is obtained when doping 20% Nb-doped $SrTiO_3$ with small amounts of Ga (10%) in a reducing environment and high temperature. Doping with higher concentrations of Ga, e.g., 20%, diminishes the electronic conductivity of the material. These findings suggest that independent of the specific dopant, mixed

ionic/electronic conductivity can be obtained in perovskite oxides under reducing conditions and high temperatures by doping the B-site with small amounts of both n-type and p-type dopants.

4.2 Introduction

As previously described in Chapter 2, finding alternative anode materials to replace conventional Ni/YSZ electrodes is a key subject for the development of SOFC technology. Of the novel anode catalysts, perovskite based materials have been shown to satisfy most intrinsic SOFC anode requirements such as high mixed ionic/electronic conductivity, good catalytic activity, and high thermodynamic stability at anodic conditions [1-7]. Furthermore, perovskite based materials possess high resistance to sulfur impurities [8-10] and coke formation [1, 11-13] since both sulfur and carbon species can easily be oxidized at the surface of the perovskite oxide [14].

Among the numerous perovskite systems that have been explored, $SrTiO_3$ based perovskites have been widely used as alternative SOFC anode materials [3, 4, 9, 15]. Indeed, several research groups have reported that $SrTiO_3$ based perovskites exhibit some advantages over Ni/YSZ anode catalysts, such as promising mixed ionic/electronic conductivity, adequate thermodynamic stability in a wide range of oxygen partial pressure, and tolerance to sulfur impurities as well as coke formation [4, 8-10]. Moreover, it has been found that yttrium doped $SrTiO_3$ (SYT) possesses a thermal expansion coefficient compatible with that of YSZ and Lanthanum Strontium Gallium Magnesium Oxide (LSGM) based electrolytes [4].

However, stoichiometric $SrTiO_3$ is a band insulator with a band gap of 3.2 eV [16]. Therefore, various dopants have been introduced to improve the electronic

conductivity of this material. It is well known that doping the material with either n- or p-type dopants can enhance the degree of electronic conduction [17-21]. For example, the transformation from an insulating state to a metallic state has been observed when doping SrTiO$_3$ with n-type impurities such as La, Y, and Nb [9, 22-24]. In addition, theoretical studies have suggested that substituting Ti with n-type dopants can shift the Fermi level into the conduction band making the system metallic [19, 25].

It is well known that the substitution of n-type dopants in the SrTiO$_3$ lattice generates a defect with an effective positive charge in the host lattice. Overall electroneutrality of the lattice can be achieved by two different mechanisms, namely, electronic compensation and cation-vacancy compensation [26-28]. At low oxygen chemical potential, the formal charges of n-type dopants are electronically compensated by creating conduction electrons that travel along the Ti–O–Ti bridge where Ti remains mixed-valent Ti^{3+}/Ti^{4+} [29]. This electron transferring process is considered to be the origin of the electronic conductivity of the material.[30] On the other hand, at higher oxygen chemical potential the excess positive charge can be compensated by generating Sr^{2+} cation vacancies [31]. This type of electron compensation provides no conduction electrons and there is no improvement in electronic conductivity. For example, Kolodiazhnyi and Petric [24] found that TiO$_2$ and niobium oxide second phases were formed when sintering the Sr$_{1-x/2}$Ti$_{1-x}$Nb$_x$O$_3$ (x = 0.17) at low oxygen partial pressure and high temperature. This transformation can be expressed with the following equation:

$$Sr_{1-\frac{x}{2}}Ti_{1-x}Nb_xO_3 \rightarrow Sr_{1-\frac{x}{2}}Ti_{1-x-y}Nb_{x-y}O_{3-4y} + yTiO_2 + yNbO_2 \qquad (4.1)$$
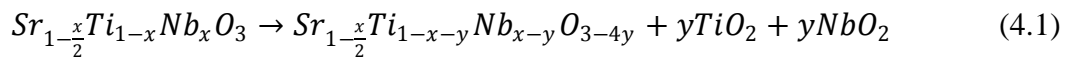
where $y < x \leq 0.2$.

Furthermore, they observed a very high electronic conductivity of $Sr_{0.9}Ti_{0.8}Nb_{0.2}O_3$ and $Sr_{0.88}Y_{0.08}TiO_3$ when these samples were sintered in forming gas [24].

In contrast to n-type doping, p-type dopants create an effective negative charge in the lattice. One way to neutralize the charge is introducing oxygen vacancies in the lattice. This mechanism of charge neutralization can take place at moderate oxygen chemical potentials and does generally not lead to improved electronic conductivity since there is no transfer of charges or electrons into the lattice. However, lowering the oxygen chemical potential can result in more oxygen vacancies, leading to an excess electron density in the lattice. The reduction reaction takes place at the surface of the material and delivers electrons to the lattice [32].

$$O_O^\times \rightleftharpoons \frac{1}{2}O_2(g) + V_O^{\circ\circ} + 2e'$$
(4.2)

These conduction electrons can often be transferred to neighboring atoms such as Ti which can be mixed-valent Ti^{3+}/Ti^{4+}. As a result, the electrical conductivity of the material is again improved.

The addition of p-type impurities not only improves the electronic conductivity but also enhances the ionic conductivity by increasing the reducibility and number of oxygen vacancies in the material. Furthermore, the amount of available oxygen vacancies plays an essential role in the enhancement of the oxide ion diffusivity (D_{O_2}) in the lattice as evidenced by the following equation [33]:

$$D_{O_2} = \beta[V_{\ddot{O}}]a^2\nu_0 e^{-\Delta H_m/RT}$$
(4.3)

where $[V_{\ddot{O}}]$ is the concentration of mobile vacancies, a is the cell parameter, ν_0 is a characteristic lattice frequency, ΔH_m is the enthalpy of vacancy migration, T is temperature, R is the ideal gas constant, and $\beta = \frac{z}{6}f e^{\Delta S_m/R}$ is a function of the number of

equivalent near-neighbor sites, z, the entropy of ion migration, ΔS_m, and a correction factor, $f\ (\approx 1)$. It is noted that the mobile vacancy concentration is usually smaller than the stoichiometric concentration due to vacancy trapping or vacancy ordering [34, 35].

Recently, various research groups reported that the catalytic activity and mixed ionic/electronic conductivity of n-type doped $SrTiO_3$ can be modified by B-site doping with p-type impurities such as Sc, Mn and Ga.[36] For example, Li et al. [37, 38] suggested that doping with Sc and Co at the B-site of $La_{0.3}Sr_{0.7}TiO_3$ can improve its ionic conductivity. Similarly, Xiao et al.[39] and Neagu and Irvine [40] proposed a similar doping strategy to improve the conductivity of n-type doped $SrTiO_3$ by enhancing bulk oxide ion mobility. In particular, they studied the effects of Ga dopants on the reducibility and conductivity of n-type doped $SrTiO_3$ systems by varying the concentration of Ga. They found that Ga doping promotes fast reduction and improves the phase stability of the material in an oxidizing environment. Impressive improvements in total conductivity were observed when doping with small amounts of Ga.

It is the objective of this theoretical study to further investigate the effect of concurrent n- and p-doping on the number of oxygen vacancies and the electronic conductivity of $SrTiO_3$ perovskites. In particular, we performed density functional theory (DFT) calculations of Nb- and Ga-doped $SrTiO_3$ and analyzed the electronic structure of the resulting materials. To evaluate the thermodynamic stability of doped $SrTiO_3$ phases at synthesized and anodic SOFC conditions, we furthermore performed constrained *ab initio* thermodynamic simulations.

4.3 Computational Details

4.3.1 Crystallographic data of SrTiO$_3$

Stoichiometric SrTiO$_3$ develops an ideal cubic perovskite structure at room temperature with *Pm3m* space group. The structural phase transition from cubic to tetragonal and to orthorhombic occurs at 110 and 65 K, respectively [41]. The cubic unit cell includes one molecular unit of SrTiO$_3$. As shown in Fig. 4.1, the structure contains 12-coordinated strontium ions occupying corner positions of the cube whereas the titanium ion, at the center of the cubic cell, is surrounded by six oxygen ions forming a TiO$_6$ octahedral unit. The octahedral units are connected by a sharing Ti-O-Ti bridge, forming a three-dimensional framework.
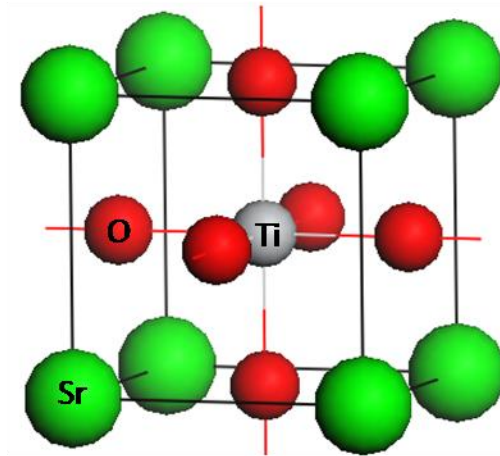
Figure 4.1 Unit cell of SrTiO$_3$ perovskite oxide

4.3.2 Computational method

To investigate the bulk electronic properties of stoichiometric and doped SrTiO$_3$, we initially optimized the lattice parameter of the SrTiO$_3$ unit cell and created a 100 atom supercell containing twenty unit cells (5×2×2). To generate doped structures we replaced

B-site cations (Ti) with various amounts of n-type (Nb) and p-type (Ga) dopants. Substitution of two Ti atoms with two dopants yields 10% B-site doped $SrTiO_3$, etc. In order to better understand the charge compensation mechanism in n- and p-type doped systems, both A-site deficient and reduced structures were created by generating strontium vacancies and oxygen vacancies, respectively. In this study, we considered up to two strontium vacancies and three oxygen vacancies in each structure. For all doped structures, we employed the lattice parameter of 20% Nb-doped $SrTiO_3$ and tried close to all ion position possibilities to identify the lowest energy structures.

All calculations performed for this study are based on the plane wave density functional theory implementation of the Vienna Ab initio Simulation Package (VASP 4.6) [42, 43]. We used the projector-augmented wave (PAW) method to represent the inner core potentials [42] and treated the Sr $4s4p5s$, Ti $3d4s$, O $2s2p$, Nb $4p5s4d$, and Ga $4s4p$ as valence electrons. The cutoff of the kinetic energy was set for all calculations to 400 eV. Exchange correlation is described within the generalized gradient approximation (GGA) with the Perdew-Burke-Ernzerhof (PBE) functional [44]. All calculations are spin-polarized and Brillouin zone integration was performed with a $2\times5\times5$ Monkhorst-Pack k-point mesh [45]. For density of state (DOS) calculations we used a $4\times10\times10$ k-mesh. In all structure optimizations, all atoms are fully relaxed until the Hellman-Feynman forces are less than 0.02 eV $Å^{-1}$.

Our calculated stoichiometric $SrTiO_3$ bulk unit cell has an optimized lattice constant of 3.948(8) Å which is in reasonable agreement to the experimental value of 3.901(1) Å [46]. The optimized supercell of 20% Nb-doped $SrTiO_3$ exhibits only a very small change in lattice parameters (3.949(4) Å) to that of stoichiometric $SrTiO_3$.

Computations predict a Sr-O and Ti-O bond distance of 2.792(2) and 1.974(4) Å, respectively. As illustrated in Fig. 4.2, the density of states of stoichiometric $SrTiO_3$ exhibits insulating behavior with a band gap of 1.80 eV. It should be noted that while DFT within the GGA approximations is known to underestimate band gaps, several studies showed excellent agreement in the predicted electronic behavior of doped oxides computed by DFT within the GGA approximation and experimental observation [47-49].
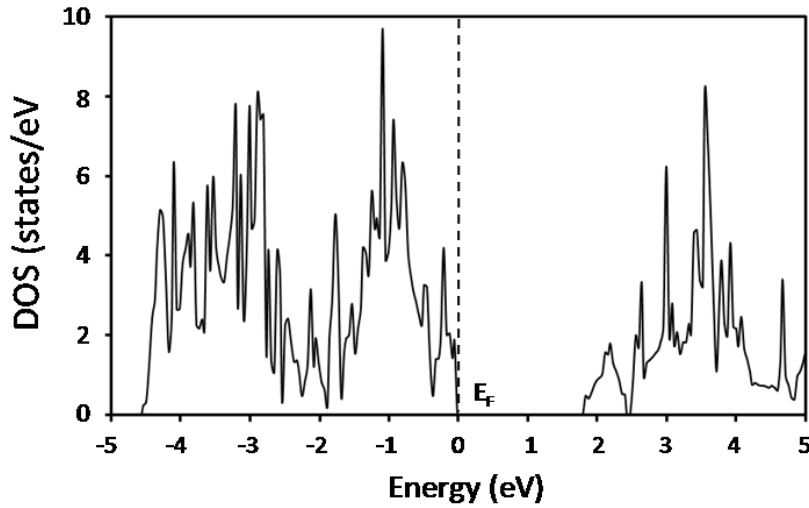
Figure 4.2 DOS of stoichiometric $SrTiO_3$ with calculated band gap of 1.80 eV

4.4   Results and Discussion

In this work, we are most interested in the electronic properties of n- and p-type doped $SrTiO_3$. Kolodiazhnyi and Petric [24] observed experimentally that $Sr_{0.9}Ti_{0.8}Nb_{0.2}O_3$ exhibits a very high conductivity at low oxygen chemical potential and Xiao et al. [39] suggested that the reducibility of this material can be promoted by doping with a certain (small) amount of p-type dopant (Ga). Therefore, we performed three different sets of calculations based on the concentration of B-site dopants, i.e., 20% Nb-doped $SrTiO_3$, 10% Ga- and 20% Nb-doped $SrTiO_3$, and 20% Ga- and 20% Nb-doped

SrTiO$_3$. In this way we can systematically study the effect of Ga (p-type) doping on Nb (n-type) doped SrTiO$_3$ on the reducibility/phase stability and electronic conductivity/density of states of the resulting materials.

For all structures we first performed constrained *ab initio* thermodynamic calculations to evaluate the relative thermodynamic stability of the systems. This *ab initio* thermodynamic approach allows us to calculate the free energy of different systems as a function of oxygen chemical potential, i.e., temperature and oxygen partial pressure, and construct phase diagrams. The reaction energies of the most dominant structures in the phase diagrams are summarized in Table 4.1. Next, the DOS related to the most dominant structures in the phase diagram were evaluated and analyzed with respect to the relative electronic conductivity.

4.4.1 Electronic structure and phase diagram of 20% Nb-doped SrTiO$_3$

In this set of calculations we substituted four Ti atoms with four Nb atoms in the 5×2×2 supercell to obtain a model for 20% Nb-doped SrTiO$_3$ (Sr$_{20}$Ti$_{16}$Nb$_4$O$_{60}$ or SrTi$_{0.8}$Nb$_{0.2}$O$_3$). In addition, we generated structures with one or two Sr vacancies to create partial (5%) A-site deficient (Sr$_{19}$Ti$_{16}$Nb$_4$O$_{60}$ or Sr$_{0.95}$Ti$_{0.8}$Nb$_{0.2}$O$_3$) and full (10%) A-site deficient 20% Nb-doped SrTiO$_3$ (Sr$_{18}$Ti$_{16}$Nb$_4$O$_{60}$ or Sr$_{0.9}$Ti$_{0.8}$Nb$_{0.2}$O$_3$) model structures, respectively. Fig. 4.3 depicts the most stable structures of 20% Nb-doped SrTiO$_3$ system. From the configuration of the most stable structures, we observe that Nb impurities prefer to be as far apart as possible due to the repulsion of the extra electrons from the Nb^{5+} cations that can be transferred to neighboring Ti atoms that are mixed-valent Ti^{3+}/Ti^{4+}. In contrast when there are Sr vacancies in the structure, Nb prefers to stay close to the vacancies since the charges originating from the Nb atoms can be

compensated by the absence of the Sr^{2+} cations. Moreover, it was found that the Sr-vacancy sites stay apart from each other in structures with more than one vacancy.
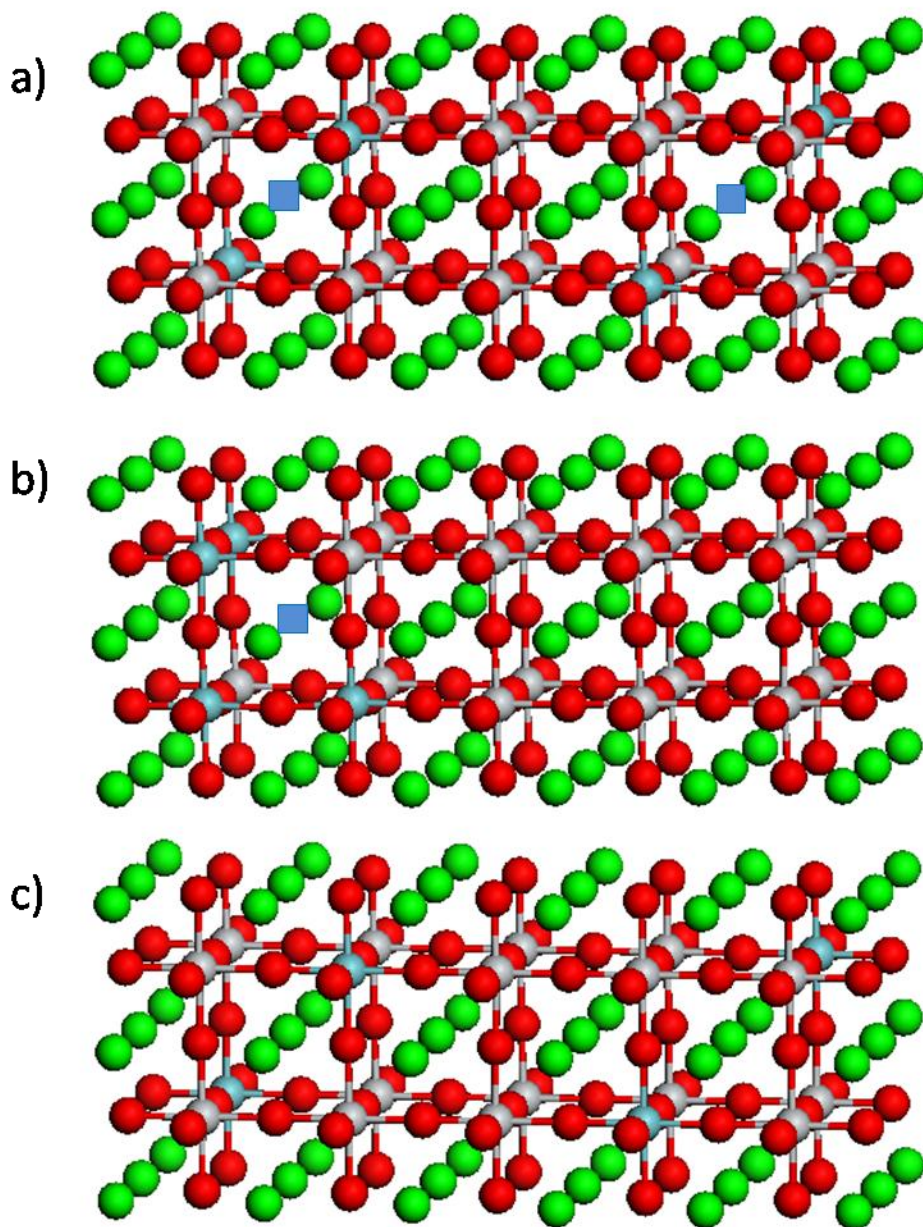
Figure 4.3 Most stable structures of 20% Nb-doped $SrTiO_3$: a) $Sr_{0.9}Ti_{0.8}Nb_{0.2}O_3$, b) $Sr_{0.95}Ti_{0.8}Nb_{0.2}O_3$ and c) $SrTi_{0.8}Nb_{0.2}O_3$. Green, gray, blue, and red spheres represent Sr, Ti, Nb, and O atoms, respectively. Blue squares represent the position of a Sr vacancy.

Table 4.1 Summary of reaction energies used in constrained *ab initio* thermodynamic calculations

Phase Diagram	Reaction	ΔE (eV)
Nb_2O_5/NbO_2	$Nb_2O_5 \rightarrow 2NbO_2 + 1/2O_2$	3.71
20% Nb-doped SrTiO$_3$ with SrO rich phase	$Sr_{20}Ti_{16}Nb_4O_{60} + 1/2O_2 \rightarrow Sr_{19}Ti_{16}Nb_4O_{60} + SrO$	-1.94
	$Sr_{20}Ti_{16}Nb_4O_{60} + O_2 \rightarrow Sr_{18}Ti_{16}Nb_4O_{60} + 2SrO$	-3.49
20% Nb-doped SrTiO$_3$ with TiO$_2$/niobium oxide rich phases	$19Sr_{18}Ti_{16}Nb_4O_{60} \rightarrow 18Sr_{19}Ti_{16}Nb_4O_{60} + 16TiO_2 + 2Nb_2O_5 + 9O_2$	2.58
	$10Sr_{18}Ti_{16}Nb_4O_{60} \rightarrow 9Sr_{20}Ti_{16}Nb_4O_{60} + 16TiO_2 + 2Nb_2O_5 + 9O_2$	5.24
	$19Sr_{18}Ti_{16}Nb_4O_{60} \rightarrow 18Sr_{19}Ti_{16}Nb_4O_{60} + 16TiO_2 + 4NbO_2 + 10O_2$	2.97
	$10Sr_{18}Ti_{16}Nb_4O_{60} \rightarrow 9Sr_{20}Ti_{16}Nb_4O_{60} + 16TiO_2 + 4NbO_2 + 10O_2$	5.98
10% Ga- and 20% Nb-doped SrTiO$_3$ with SrO rich phase	$Sr_{20}Ti_{14}Nb_4Ga_2O_{60} + 1/2O_2 \rightarrow Sr_{19}Ti_{14}Nb_4Ga_2O_{60} + SrO$	-1.74
	$Sr_{20}Ti_{14}Nb_4Ga_2O_{60} \rightarrow Sr_{20}Ti_{14}Nb_4Ga_2O_{59} + 1/2O_2$	4.54
	$Sr_{20}Ti_{14}Nb_4Ga_2O_{60} \rightarrow Sr_{20}Ti_{14}Nb_4Ga_2O_{58} + O_2$	9.01
	$Sr_{20}Ti_{14}Nb_4Ga_2O_{60} \rightarrow Sr_{20}Ti_{14}Nb_4Ga_2O_{57} + 3/2O_2$	14.16
10% Ga- and 20% Nb-doped SrTiO$_3$ with TiO$_2$/Ga$_2$O$_3$/niobium oxide rich phases	$19Sr_{18}Ti_{14}Nb_4Ga_2O_{60} \rightarrow 18Sr_{19}Ti_{14}Nb_4Ga_2O_{60} + 14TiO_2 + 2Nb_2O_5 + Ga_2O_3 + 19/2O_2$	-1.29
	$10Sr_{18}Ti_{14}Nb_4Ga_2O_{60} \rightarrow 9Sr_{20}Ti_{14}Nb_4Ga_2O_{60} + 14TiO_2 + 2Nb_2O_5 + Ga_2O_3 + 19/2O_2$	1.28
	$10Sr_{18}Ti_{14}Nb_4Ga_2O_{60} \rightarrow 9Sr_{20}Ti_{14}Nb_4Ga_2O_{59} + 14TiO_2 + 2Nb_2O_5 + Ga_2O_3 + 14O_2$	5.37
	$10Sr_{18}Ti_{14}Nb_4Ga_2O_{60} \rightarrow 9Sr_{20}Ti_{14}Nb_4Ga_2O_{58} + 14TiO_2 + 2Nb_2O_5 + Ga_2O_3 + 37/2O_2$	9.39
	$10Sr_{18}Ti_{14}Nb_4Ga_2O_{60} \rightarrow 9Sr_{20}Ti_{14}Nb_4Ga_2O_{57} + 14TiO_2 + 2Nb_2O_5 + Ga_2O_3 + 23O_2$	14.03
20% Ga- and 20% Nb-doped SrTiO$_3$	$10Sr_{18}Ti_{12}Nb_4Ga_4O_{60} \rightarrow 9Sr_{20}Ti_{12}Nb_4Ga_4O_{60} + 12TiO_2 + 2Nb_2O_5 + 2Ga_2O_3 + 10O_2$	-2.81
	$10Sr_{18}Ti_{12}Nb_4Ga_4O_{60} \rightarrow 9Sr_{20}Ti_{12}Nb_4Ga_4O_{59} + 12TiO_2 + 2Nb_2O_5 + 2Ga_2O_3 + 29/2O_2$	1.21
	$10Sr_{18}Ti_{12}Nb_4Ga_4O_{60} \rightarrow 9Sr_{20}Ti_{12}Nb_4Ga_4O_{58} + 12TiO_2 + 2Nb_2O_5 + 2Ga_2O_3 + 19O_2$	5.21
	$10Sr_{18}Ti_{12}Nb_4Ga_4O_{60} \rightarrow 9Sr_{20}Ti_{12}Nb_4Ga_4O_{57} + 12TiO_2 + 2Nb_2O_5 + 2Ga_2O_3 + 47/2O_2$	9.82

Constrained *ab initio* thermodynamic calculations of 20% Nb-doped SrTiO$_3$ systems were performed to determine the phase stability of these structures at various temperatures and oxygen partial pressures. We employed two different types of calculations based on the main products that were generated when the phase transition occurred. First, we calculated the free energies of 20% Nb-doped SrTiO$_3$ with a SrO rich second phase experimentally obtained by cooling SrTi$_{0.8}$Nb$_{0.2}$O$_3$.

$$Sr_{20}Ti_{16}Nb_4O_{60} + \frac{x}{2}O_2 \rightarrow Sr_{20-x}Ti_{16}Nb_4O_{60} + xSrO \tag{4.4}$$
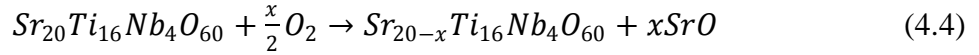
Where x represents the number of Sr-vacancy sites in the structure ($x = 1, 2$) and free energies are given by

$$\Delta G = E_{Sr-vacancy} + xE_{SrO} - E_{full} - x[E_O + \Delta\mu_O(T,P)] \tag{4.5}$$

with $E_{Sr-vacancy}$ being the DFT-calculated electronic energy of the structure with Sr-vacancy, E_{full} is the DFT-calculated electronic energy of the structure without Sr-vacancy, E_{SrO} is the DFT-calculated electronic energy of the SrO lattice, and E_O is a half of the energy of an oxygen molecule, E_{O_2}, which is obtained from the H$_2$O splitting reaction using the experimental reaction energy and calculated DFT energies of H$_2$ and H$_2$O in the gas phase [50, 51],

$$E_{O_2} = 2\left[\left(E_{H_2O}^{DFT} + E_{H_2O}^{ZPE}\right) - \left(E_{H_2}^{DFT} + E_{H_2}^{ZPE}\right) - E_{hof}\right] - E_{O_2}^{ZPE}, \tag{4.6}$$

where E^{ZPE} is the experimental zero point energy[52], E_{hof} is the experimental heat of formation of a gas-phase H$_2$O molecule[52], and E^{DFT} is the energy calculated with PBE functional. The chemical potential of O, which includes the temperature- and pressure-dependent free energy contributions of the O$_2$ molecule, is described by $\Delta\mu_O(T,P)$ and has been calculated from first principles and the rotational, translational, and vibrational partition functions of the O$_2$ molecule. We note that we neglect all zero point energies in

Eq. 4.5 and assume that entropic contributions from the solids to the free energy difference are insignificant [53-55]. Also, the pressure dependence of $\Delta\mu_O(T,P)$ is obtained assuming that the gas phase is ideal.[54]

$$\Delta\mu_O(T,P) = \frac{1}{2}\left(\Delta\mu_{O_2}(T,P^0) + k_b T ln\left(\frac{P}{P^0}\right)\right) \tag{4.7}$$

Next, we employed the same *ab initio* thermodynamic approach to investigate the thermodynamic stability of 20% Nb-doped SrTiO$_3$ with TiO$_2$ and niobium oxide rich second phases that can experimentally be obtained by heating Sr-deficient 20% Nb-doped SrTiO$_3$. Considering that Nb$_2$O$_5$ can be reduced to NbO$_2$ in a reducing environment at high temperature [56], we first performed *ab initio* thermodynamic calculations of the Nb$_2$O$_5$/NbO$_2$ system

$$Nb_2O_5 \rightarrow 2NbO_2 + \frac{1}{2}O_2 \tag{4.8}$$

and Fig. 4.4 illustrates that at low temperature Nb$_2$O$_5$ is the dominant phase whereas the NbO$_2$ phase predominates at higher temperatures.

In the following, we performed *ab initio* thermodynamic calculations of the Nb-doped SrTiO$_3$ system according to the dominant phase in the Nb$_2$O$_5$/NbO$_2$ phase diagram, i.e., whenever the Nb$_2$O$_5$ phase is preferred we calculate the free energies of the system according to Eq. 4.9,

$(20-x)Sr_{18}Ti_{16}Nb_4O_{60} \rightarrow$
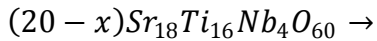
$18Sr_{20-x}Ti_{16}Nb_4O_{60} + (32-16x)TiO_2 + (4-2x)Nb_2O_5 + (18-9x)O_2$ (4.9)

and whenever NbO$_2$ is preferred, we calculate the free energies of the system according to Eq. 4.10,

$(20-x)Sr_{18}Ti_{16}Nb_4O_{60} \rightarrow$
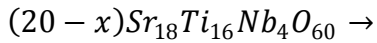
$$18Sr_{20-x}Ti_{16}Nb_4O_{60} + (32-16x)TiO_2 + (8-4x)NbO_2 + (20-10x)O_2 \quad (4.10)$$

where x is the number of Sr vacancies with $x = 0, 1$. Figure 4.5 shows the calculated phase diagrams of 20% Nb-doped SrTiO$_3$ with SrO rich second phase and TiO$_2$ and niobium oxide rich second phases. The phase transformation from 10% Sr-deficient (Sr$_{0.9}$Ti$_{0.8}$Nb$_{0.2}$O$_3$) to 5% Sr-deficient (Sr$_{0.95}$Ti$_{0.8}$Nb$_{0.2}$O$_3$) to non Sr-deficient structures (SrTi$_{0.8}$Nb$_{0.2}$O$_3$) occurs with increasing temperature and decreasing oxygen partial pressure. We note that an oxygen deficient structure is thermodynamically unstable in the considered temperature and oxygen partial pressure range.
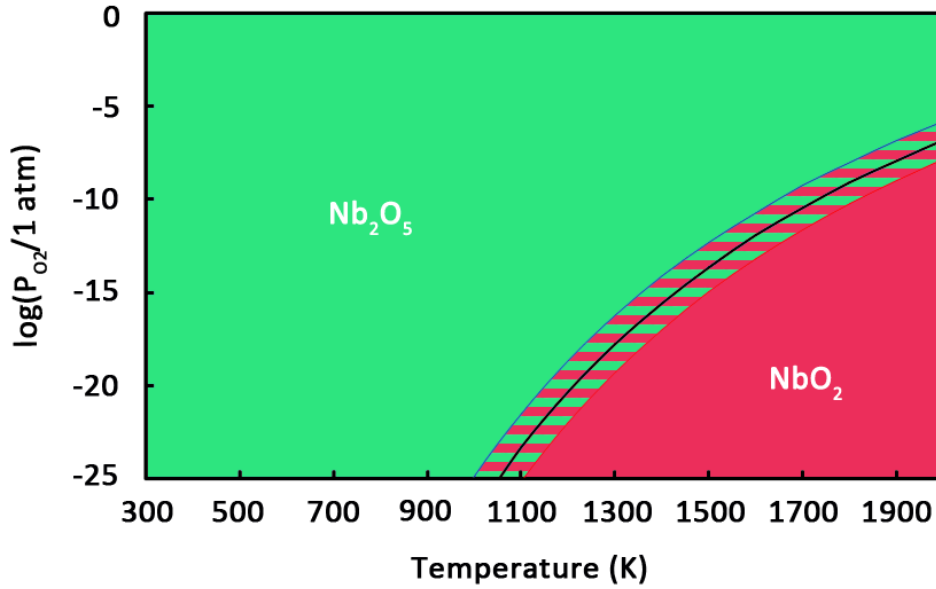
Figure 4.4 Calculated phase diagram of Nb$_2$O$_5$/NbO$_2$. Differently shaded areas mark the stability regions of various structures for a given temperature and partial pressure of oxygen. The hatched area decribes possible changes in the phase diagram if computed reaction energies shown in Table 4.1 are off by ±0.2 eV (our estimated error bar). Green and red areas symbolize stability of Nb$_2$O$_5$ and NbO$_2$, respectively.
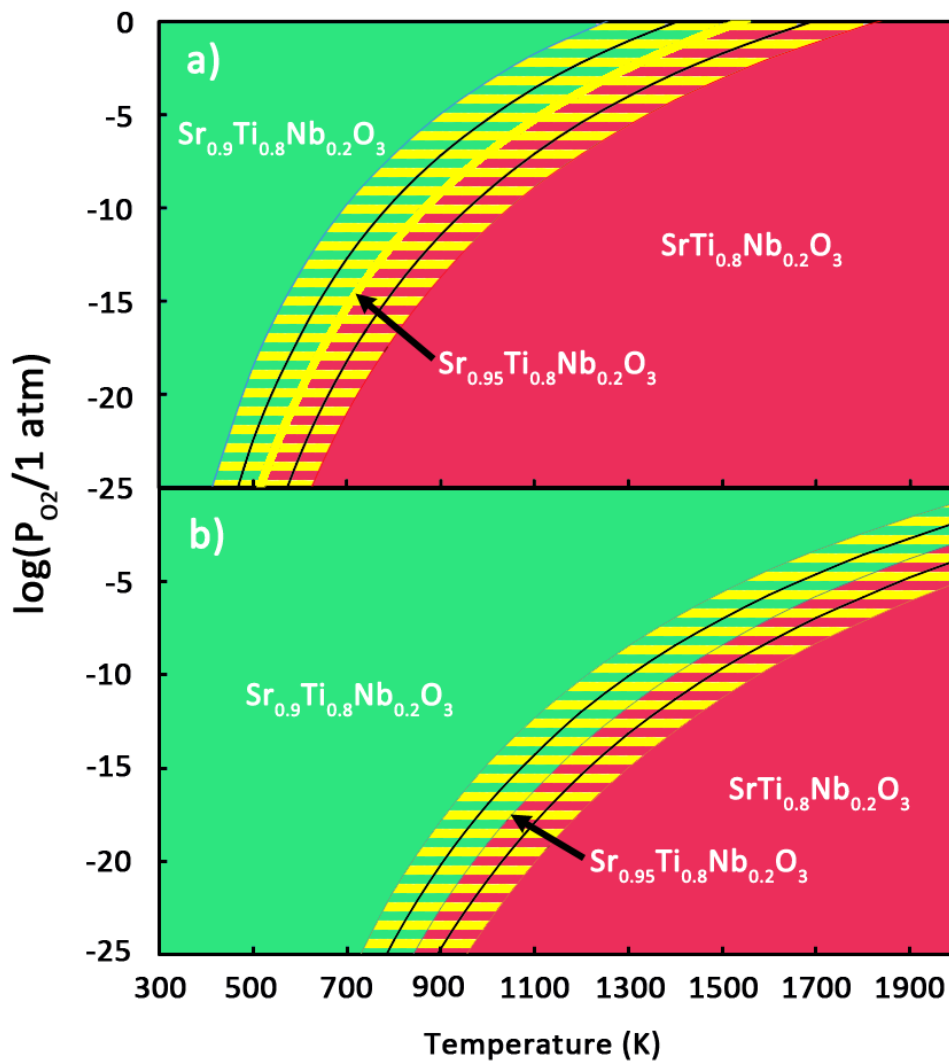
Figure 4.5 Calculated phase diagram of 20% Nb-doped $SrTiO_3$ with a) SrO rich phase and b) TiO_2/niobium oxide rich phases. Differently shaded areas mark the stability regions of various structures for a given temperature and partial pressure of oxygen. The hatched area decribes possible changes in the phase diagram if computed reaction energies shown in Table 4.1 are off by ±0.2 eV (our estimated error bar). Green, yellow, and red areas symbolize stability of $Sr_{0.9}Ti_{0.8}Nb_{0.2}O_3$, $Sr_{0.95}Ti_{0.8}Nb_{0.2}O_3$, and $SrTi_{0.8}Nb_{0.2}O_3$, respectively.

The electronic conductivity of these materials can to a first approximation be analyzed from their electronic structures. As illustrated in Fig. 4.6(a), the DOS of a 10% Sr-deficient material ($Sr_{0.9}Ti_{0.8}Nb_{0.2}O_3$) exhibits insulating behavior with a band gap of 1.80 eV. The charges from the four Nb dopants are compensated by the presence of two Sr vacancies. The DOS of the 5% Sr-deficient structure ($Sr_{0.95}Ti_{0.8}Nb_{0.2}O_3$) shows a slight improvement in electronic conductivity (Fig. 4.6(b)). The Fermi energy shifts inside the conduction band with two conduction electrons per supercell below the Fermi level. An even greater improvement in the electronic conductivity occurs when the material is fully electronically compensated. As depicted in Fig. 4.6(c), the DOS of 20% Nb-doped $SrTiO_3$ with no Sr vacancies ($SrTi_{0.8}Nb_{0.2}O_3$) exhibits metallic character with four delocalized electrons at the Fermi level. Figure 4.7 illustrates the calculated electronic band structure of $SrTi_{0.8}Nb_{0.2}O_3$ which confirms that the material is indeed metallic.

It is interesting to note that the simulation results are in agreement with experimental observations from Kolodiazhnyi and Petric [24]. They reported that the transformation of cation vacancy compensated materials to electronically compensated materials (and corresponding change in electronic conductivity) occurred when the materials were equilibrated at high temperature and low oxygen partial pressure. This condition corresponds to anodic SOFC conditions with temperatures between 1000 and 1200 K and oxygen partial pressures in the range of 10^{-20} bar.
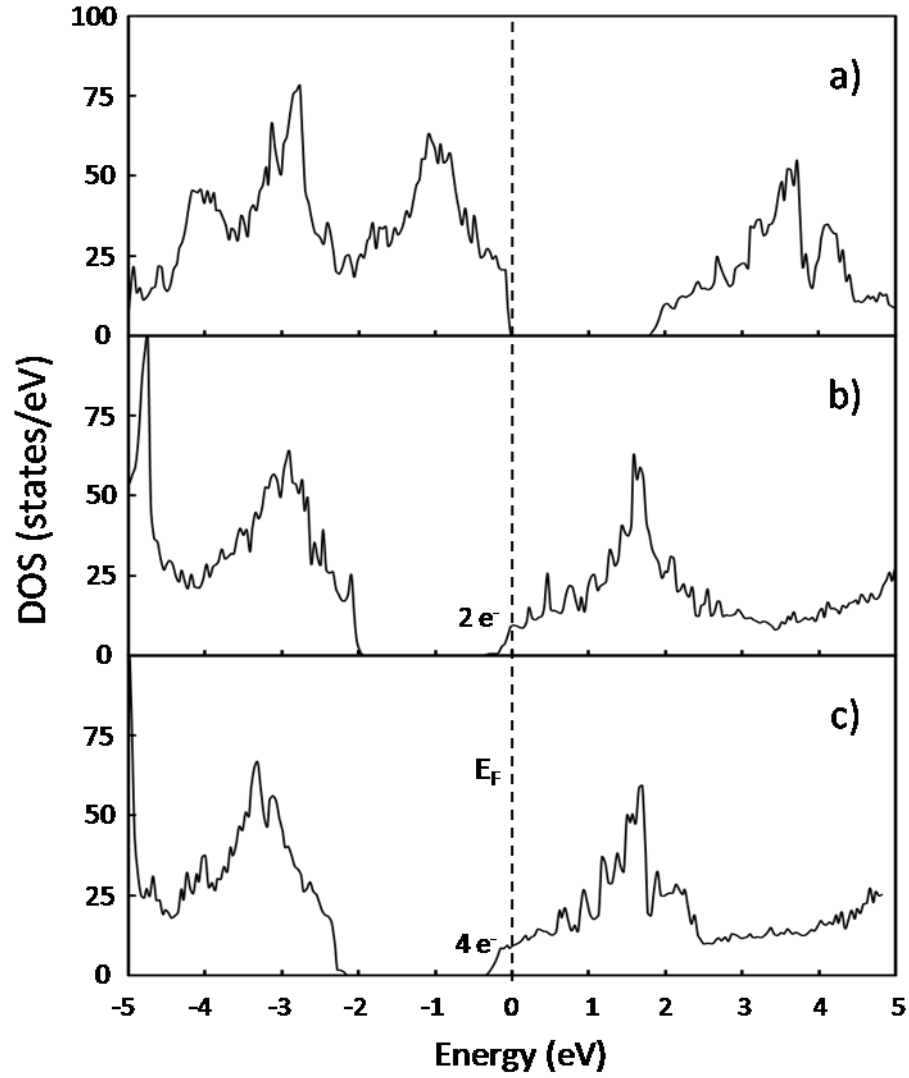
Figure 4.6 Density of states of a) $Sr_{0.9}Ti_{0.8}Nb_{0.2}O_3$`, b) $Sr_{0.95}Ti_{0.8}Nb_{0.2}O_3$ and c) $SrTi_{0.8}Nb_{0.2}O_3$. Fermi energy is set to zero on energy scale. Numbers of electrons shown in the figure indicate the integrated number of electrons per supercell for the specified DOS area, i.e., states in the band gap and states below the Fermi level.
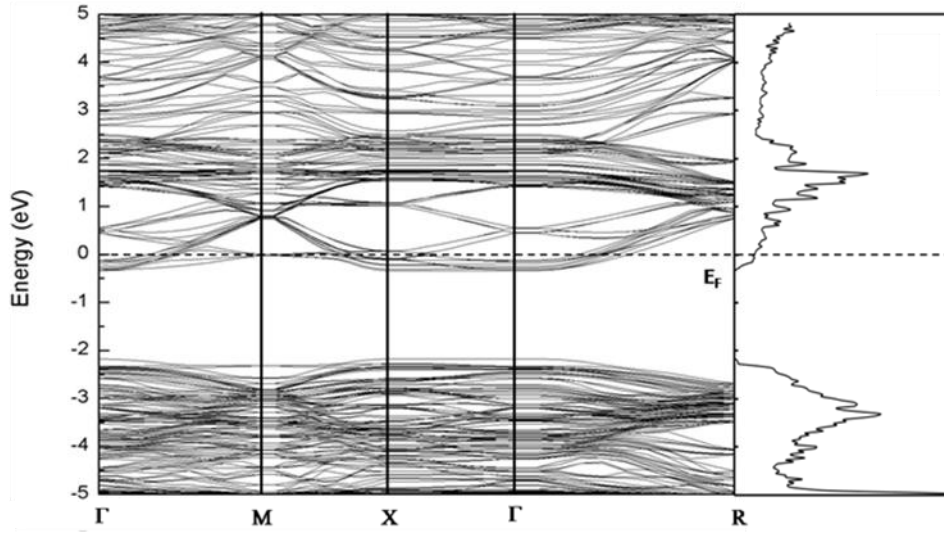
Figure 4.7 Electronic band structure and density of states of $SrTi_{0.8}Nb_{0.2}O_3$.

4.4.2 Electronic structure and phase diagram of 10% Ga- and 20% Nb-doped SrTiO$_3$

Substitution of two Ti atoms with two Ga atoms in our 20% Nb-doped SrTiO$_3$ model leads to 10% Ga- and 20% Nb-doped SrTiO$_3$. The presence of Sr and oxygen vacancies in the structure was investigated in a similar manner as described above. Figure 4.8 shows the most stable structures of 10% Ga- and 20% Nb-doped SrTiO$_3$ system. It is found that Ga atoms prefer to be next to Nb atoms since the extra electron from the Nb dopant can be compensated by the electron hole generated from the Ga dopant. At high temperatures and low oxygen partial pressures oxygen vacancies start to form. The first oxygen vacancy is created by removing an oxygen atom from the Ga-O-Ti bridge forming GaO$_5$ units whereas the second vacancy is positioned next to the same Ga atom generating a GaO$_4$ unit. Upon removal of the third oxygen atom another GaO$_5$ unit is

formed in our unit cell. It is noteworthy that we find structures with neighboring Ga atoms to be significantly less stable.
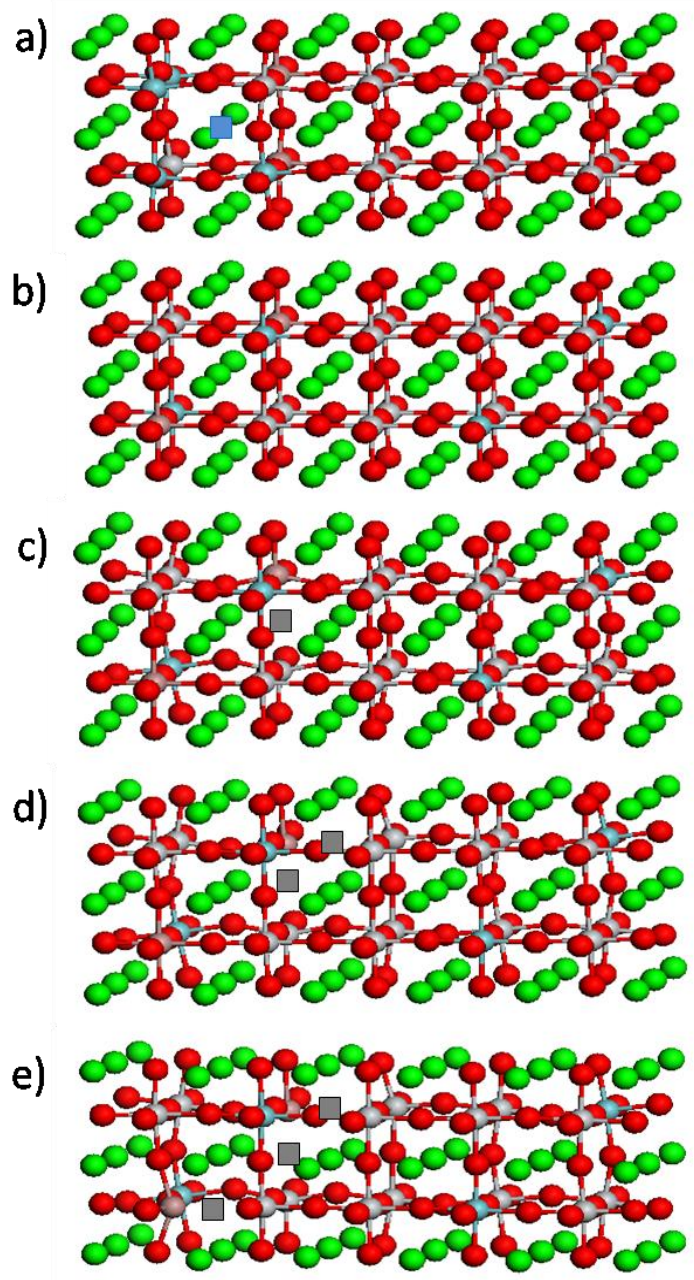
Figure 4.8 Most stable structures of 10% Ga- and 20% Nb-doped $SrTiO_3$: a) $Sr_{0.95}Ti_{0.7}Nb_{0.2}Ga_{0.1}O_3$, b) $SrTi_{0.7}Nb_{0.2}Ga_{0.1}O_3$, c) $SrTi_{0.7}Nb_{0.2}Ga_{0.1}O_{2.95}$, d) $SrTi_{0.7}Nb_{0.2}Ga_{0.1}O_{2.9}$, and e) $SrTi_{0.7}Nb_{0.2}Ga_{0.1}O_{2.85}$. Green, gray, blue, brown and red spheres represent Sr, Ti, Nb, Ga and O atoms, respectively. Blue and gray squares represent the position of a Sr and O vacancy, respectively.

Figure 4.9(a) and 4.9(b) illustrate the phase diagram for 10% Ga- and 20% Nb-doped $SrTiO_3$ as a function of temperature and partial pressure of oxygen corresponding to the formation of SrO and TiO_2/Ga_2O_3/niobium oxide rich second phases, respectively. In the presence of Ga, we find that the reduced structures ($SrTi_{0.7}Nb_{0.2}Ga_{0.1}O_{2.95}$, $SrTi_{0.7}Nb_{0.2}Ga_{0.1}O_{2.90}$, and $SrTi_{0.7}Nb_{0.2}Ga_{0.1}O_{2.85}$) are stable in the studied high temperature and low oxygen partial pressure range. The existence of a reduced structure indicates that Ga doping improves the reducibility of the materials as previously reported in Neagu and Irvine's work [40].

More interestingly, Ga and Nb dopants do not seem to compensate each other with respect to electronic conductivity. Figure 4.10 illustrates the density of states of the most important structures. While $Sr_{0.95}Ti_{0.7}Nb_{0.2}Ga_{0.1}O_3$ exhibits insulating behavior with a band gap of 1.80 eV (the charges from the Nb dopants are compensated by the Sr vacancies and Ga dopants), $SrTi_{0.7}Nb_{0.2}Ga_{0.1}O_3$, $SrTi_{0.7}Nb_{0.2}Ga_{0.1}O_{2.95}$, $SrTi_{0.7}Nb_{0.2}Ga_{0.1}O_{2.90}$, and $SrTi_{0.7}Nb_{0.2}Ga_{0.1}O_{2.85}$ exhibit metallic behavior with up to four conduction electrons at the Fermi level (the same number as in the absence of Ga). In $SrTi_{0.7}Nb_{0.2}Ga_{0.1}O_3$, the two Ga atoms in the supercell compensate for two of the Nb atoms, leaving the remaining two Nb atoms to contribute two conduction electrons at the Fermi level (Fig. 4.10(b)). In $SrTi_{0.7}Nb_{0.2}Ga_{0.1}O_{2.95}$, one oxygen atom connected to a Ga atom is removed, compensating the hole doping effect of two Ga atoms. Thus, we see the effect of 20% Nb doping in this structure (Fig. 4.10(c)). In $SrTi_{0.7}Nb_{0.2}Ga_{0.1}O_{2.9}$ and $SrTi_{0.7}Nb_{0.2}Ga_{0.1}O_{2.85}$, the electrons generated by creating further oxygen vacancies are localized mainly on the Ga atoms and an extra peak is observed in the DOS (Fig. 4.10(d) and 4.10(e)) between the valence band and the conduction band.
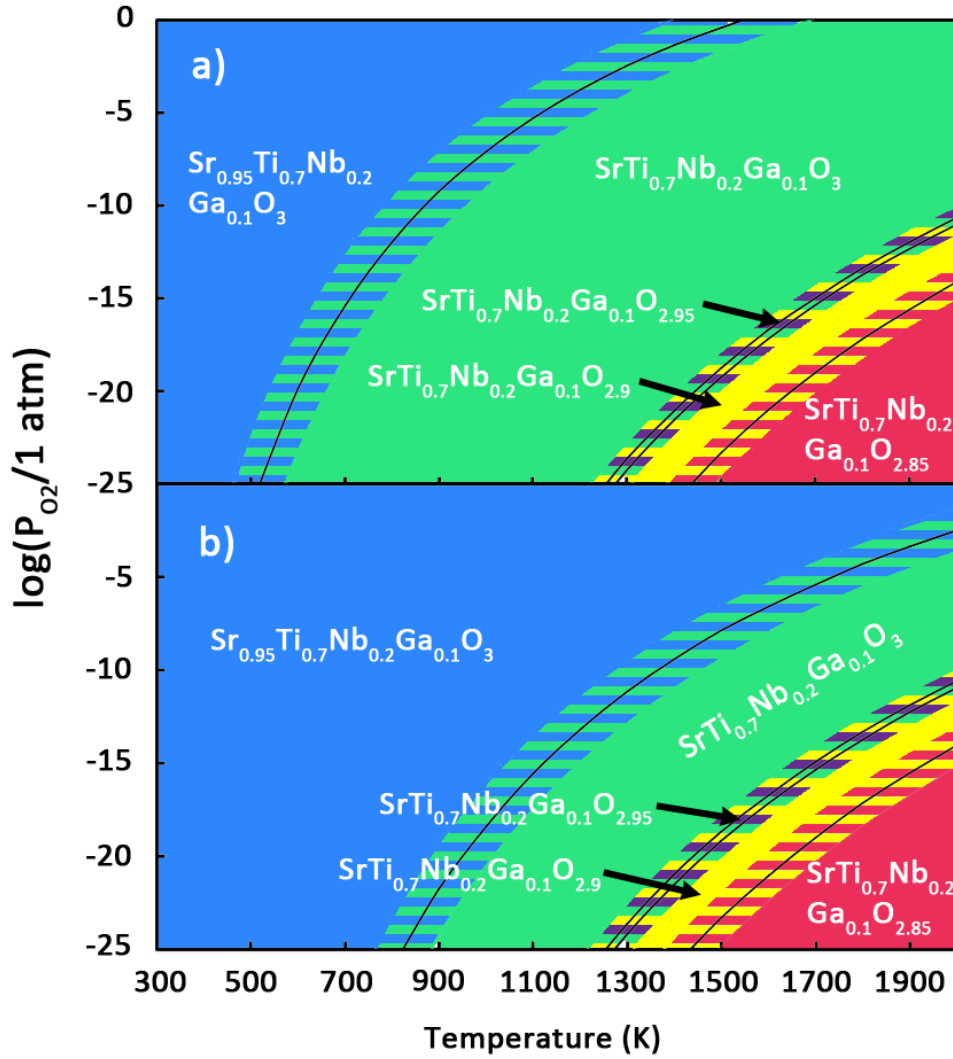
Figure 4.9 Calculated phase diagram of 10% Ga- and 20% Nb-doped $SrTiO_3$ with a) SrO rich phase and b) TiO_2/Ga_2O_3/niobium oxide rich phases. Differently shaded areas mark the stability regions of various structures for a given temperature and partial pressure of oxygen. The hatched area decribes possible changes in the phase diagram if computed reaction energies shown in Table 4.1 are off by ±0.2 eV (our estimated error bar). Blue, green, yellow, and red areas symbolize stability of $Sr_{0.95}Ti_{0.7}Nb_{0.2}Ga_{0.1}O_3$, $SrTi_{0.7}Nb_{0.2}Ga_{0.1}O_3$, $SrTi_{0.7}Nb_{0.2}Ga_{0.1}O_{2.9}$, and $SrTi_{0.7}Nb_{0.2}Ga_{0.1}O_{2.85}$, respectively. The hatched violet area symbolizes the possible stability of a $SrTi_{0.7}Nb_{0.2}Ga_{0.1}O_{2.95}$ phase.
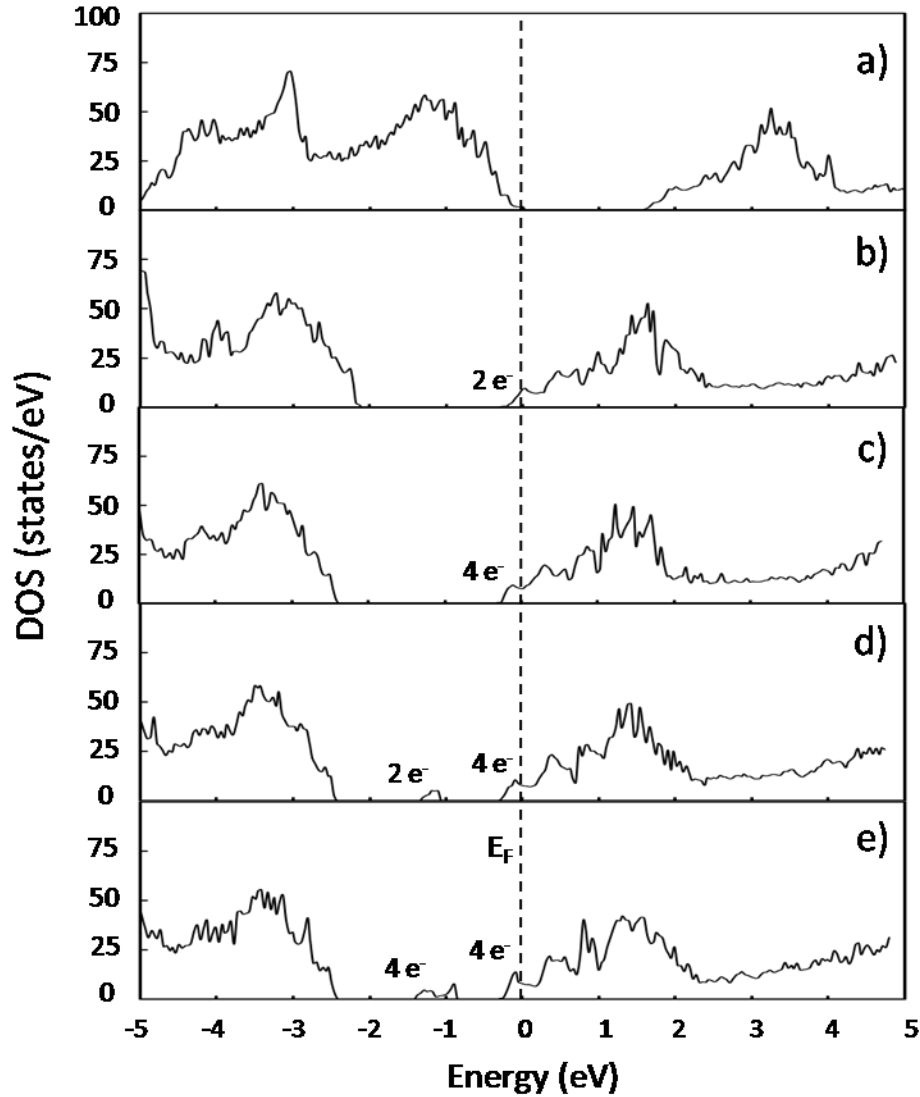
Figure 4.10 Density of states of a) $Sr_{0.95}Ti_{0.7}Nb_{0.2}Ga_{0.1}O_3$, b) $SrTi_{0.7}Nb_{0.2}Ga_{0.1}O_3$, c) $SrTi_{0.7}Nb_{0.2}Ga_{0.1}O_{2.95}$, d) $SrTi_{0.7}Nb_{0.2}Ga_{0.1}O_{2.9}$ and e) $SrTi_{0.7}Nb_{0.2}Ga_{0.1}O_{2.85}$. Fermi energy is set to zero on energy scale. Numbers of electrons shown in the figure indicate the integrated number of electrons per supercell for the specified DOS area, i.e., states in the band gap and states below the Fermi level.

A partial density of states (PDOS) analysis and electron density integration for $SrTi_{0.7}Nb_{0.2}Ga_{0.1}O_{2.9}$, as illustrated in Fig. 4.11(a), shows that there are two electrons in this peak which contains predominantly contributions from the oxygen PDOS. We see no reason for these two electrons to be delocalized and believe that these states do not

contribute to the electronic conductivity of the material. We find a qualitatively similar picture for the four electrons in the extra peak in the band gap of $SrTi_{0.7}Nb_{0.2}Ga_{0.1}O_{2.85}$. This observation is in agreement with previous computational and experimental results that the electrons from oxygen vacancies are often localized and have little contribution to the electronic conductivity of the materials [57, 58]. Next, Fig. 4.11(b) shows the PDOS of $SrTi_{0.7}Nb_{0.2}Ga_{0.1}O_{2.9}$ below the Fermi level and confirms that these states are primarily from mixed-valent Ti^{3+}/Ti^{4+} that contribute to electronic conduction. A similar behavior is observed for all structures studied with states below the Fermi level.
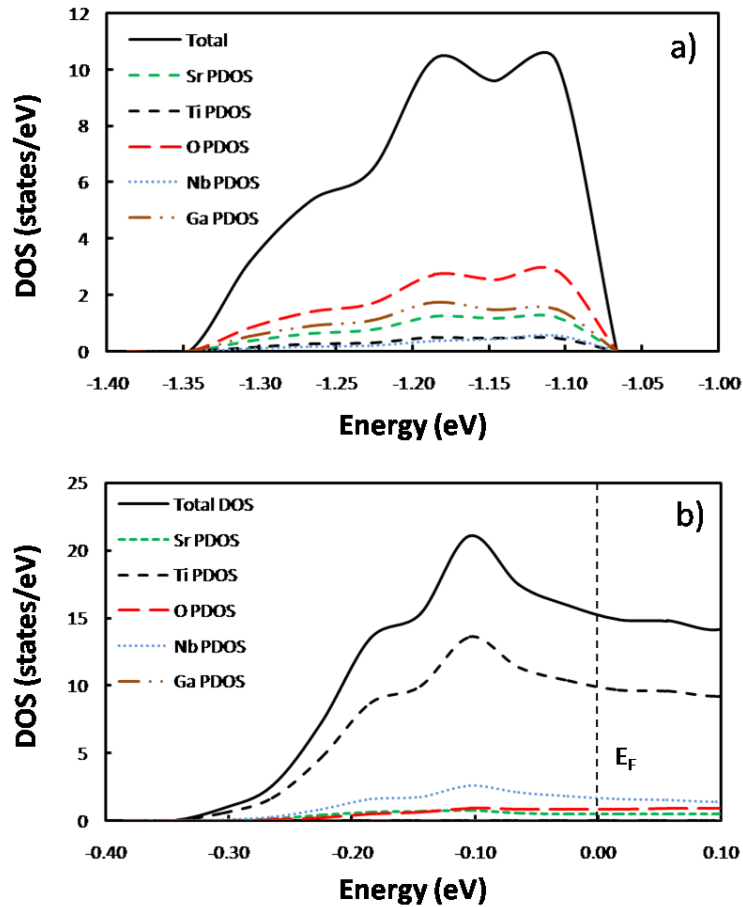
Figure 4.11 Partial density of states (PDOS) of a) the gap states between the valence and conduction band and b) the states below the Fermi level in $SrTi_{0.7}Nb_{0.2}Ga_{0.1}O_{2.9}$.

82

To conclude, further doping of 20% Nb-doped SrTiO$_3$ with 10% Ga leads to a comparable degree of electronic conductivity to that of only 20% Nb-doped SrTiO$_3$ under anodic SOFC conditions. Further, Ga promotes ionic conductivity by enhancing the reducibility of the material. These results support the experimental observations reported by several groups [39, 40] that Ga doped titanates possess a high number of oxygen vacancies and good oxide ion conduction.

4.4.3 Electronic structure and phase diagram of 20% Ga- and 20% Nb-doped SrTiO$_3$

Replacing another two Ti atoms with Ga atoms in 10% Ga- and 20% Nb-doped SrTiO$_3$ we obtain a model for 20% Ga- and 20% Nb-doped SrTiO$_3$. The most stable structures in this set of calculations are illustrated in Fig. 4.12. These structures suggest that Ga atoms prefer to position close to Nb atoms. Up to three oxygen vacancies were generated in this structure to study the effect of reducing conditions. It is preferable to create the first two oxygen vacancies at the Ga-O-Ti bridge where two vacancies share the same Ga atom forming a GaO$_4$ unit, whereas the third oxygen vacancy is again positioned at a Ga-O-Ti bridge forming a GaO$_5$ unit.

Constrained *ab initio* thermodynamic calculations of this system were carried out to determine the phase stability at various temperatures and oxygen partial pressures. In some respects, the phase transition of this system is quite similar to that of the 10% Ga doped system. In particular, the presence of a reduced phase of both the 10% and 20% Ga doped systems occurs at approximately the same temperature and oxygen partial pressure range, indicating that increasing the concentration of Ga does not significantly improve the reducibility of the material. However, the phase diagram of the 20% Ga doped system

shown in Fig. 4.13 displays no Sr-deficient phase (i.e., there are no SrO or TiO$_2$/Ga$_2$O$_3$/niobium oxide rich second phases).
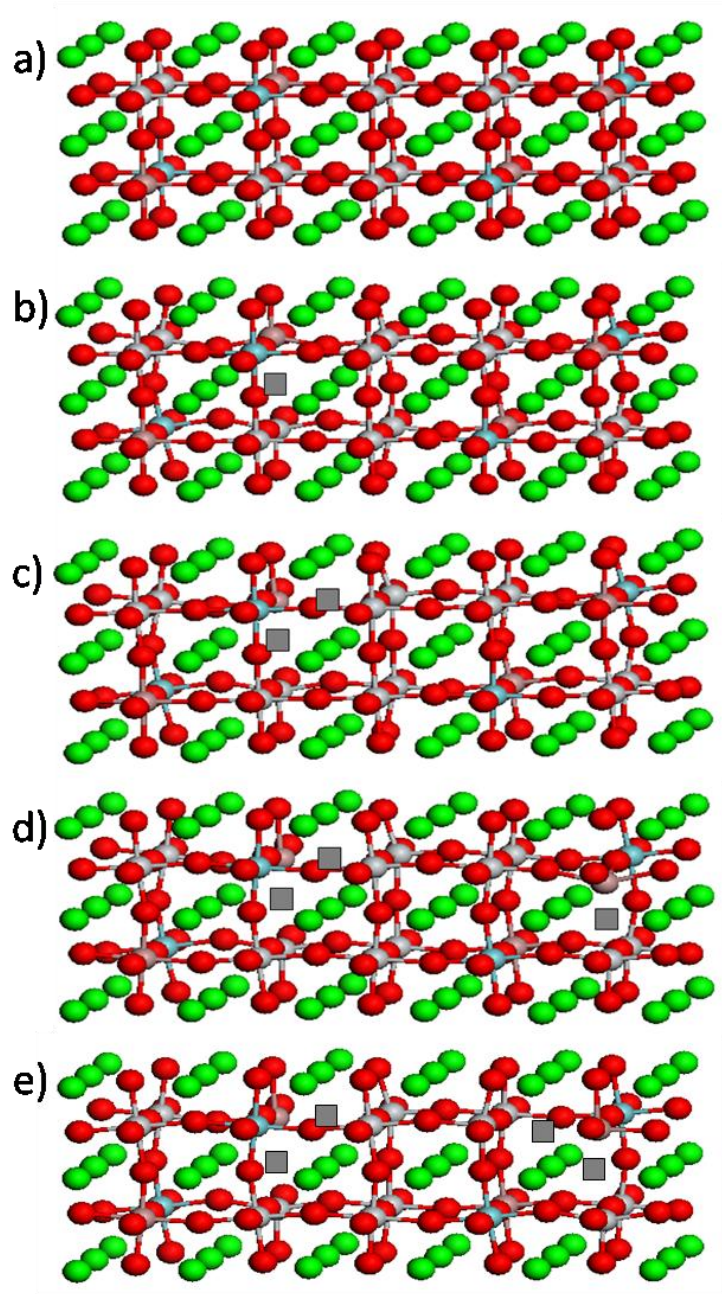
Figure 4.12 Most stable structures of 20% Ga- and 20% Nb-doped SrTiO$_3$: a) SrTi$_{0.6}$Nb$_{0.2}$Ga$_{0.2}$O$_3$, b) SrTi$_{0.6}$Nb$_{0.2}$Ga$_{0.2}$O$_{2.95}$, c) SrTi$_{0.6}$Nb$_{0.2}$Ga$_{0.2}$O$_{2.9}$, d) SrTi$_{0.6}$Nb$_{0.2}$Ga$_{0.2}$O$_{2.85}$ and e) SrTi$_{0.6}$Nb$_{0.2}$Ga$_{0.2}$O$_{2.8}$. Green, gray, blue, brown, and red spheres represent Sr, Ti, Nb, Ga, and O atoms, respectively. A gray square represents the position of an O vacancy.
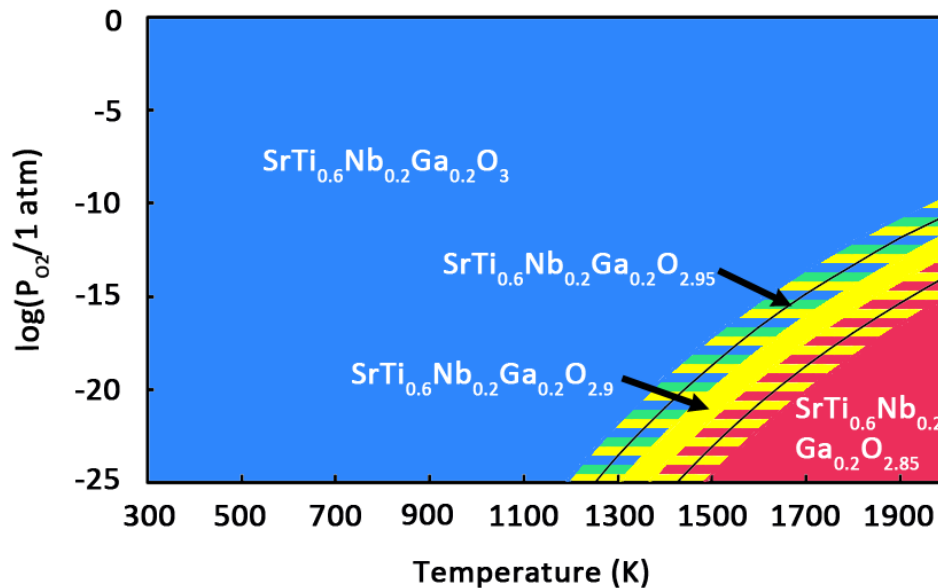
Figure 4.13 Calculated phase diagram of 20% Ga- and 20% Nb-doped $SrTiO_3$. Differently shaded areas mark the stability regions of various structures for a given temperature and partial pressure of oxygen. The hatched area decribes possible changes in the phase diagram if computed reaction energies shown in Table 4.1 are off by ±0.2 eV (our estimated error bar). Blue, yellow, and red areas symbolize stablity of $SrTi_{0.6}Nb_{0.2}Ga_{0.2}O_3$, $SrTi_{0.6}Nb_{0.2}Ga_{0.2}O_{2.9}$, and $SrTi_{0.6}Nb_{0.2}Ga_{0.2}O_{2.85}$, respectively. The hatched green area symbolizes the stability of a $SrTi_{0.6}Nb_{0.2}Ga_{0.2}O_{2.95}$ phase.

Furthermore, we observe from the DOS (Fig.4.14) a reduction in the electronic conductivity with increase in Ga doping. As shown in Fig. 4.14(c) and 4.14(d), the DOS of $SrTi_{0.6}Nb_{0.2}Ga_{0.2}O_{2.90}$ and $SrTi_{0.6}Nb_{0.2}Ga_{0.2}O_{2.85}$ exhibit only two conduction electrons at the Fermi level. It seems that doping with 20% Ga (and 20% Nb) and removing the first oxygen atom in our supercell leads to a compensation of the hole doping effect of two Ga atoms and generation of two conduction electrons from two uncompensated Nb atoms at the Fermi level (Fig. 4.14(b)). In contrast, removing one or two more oxygen atoms from the supercell leads to localized electrons observed in an extra peak in the DOS between the valence and conduction band and no compensation of the hole doping effect of the remaining two Ga atoms, and thus, no increase in charge carrier density (Fig.

4.14(c) and 4.14(d)). Interestingly, creating a fourth oxygen vacancy under very reducing conditions (usually not encountered in SOFC operation and therefore not included in the phase diagram), leads again to a full compensation of the hole doping effect of all four Ga atoms and generation of four conduction electrons from the four Nb atoms at the Fermi level (see Fig. 4.12(e)). Thus, while doping with 20% Ga improves the ionic conductivity, the electronic conductivity of the material is likely diminished under realistic fuel cell operating conditions.
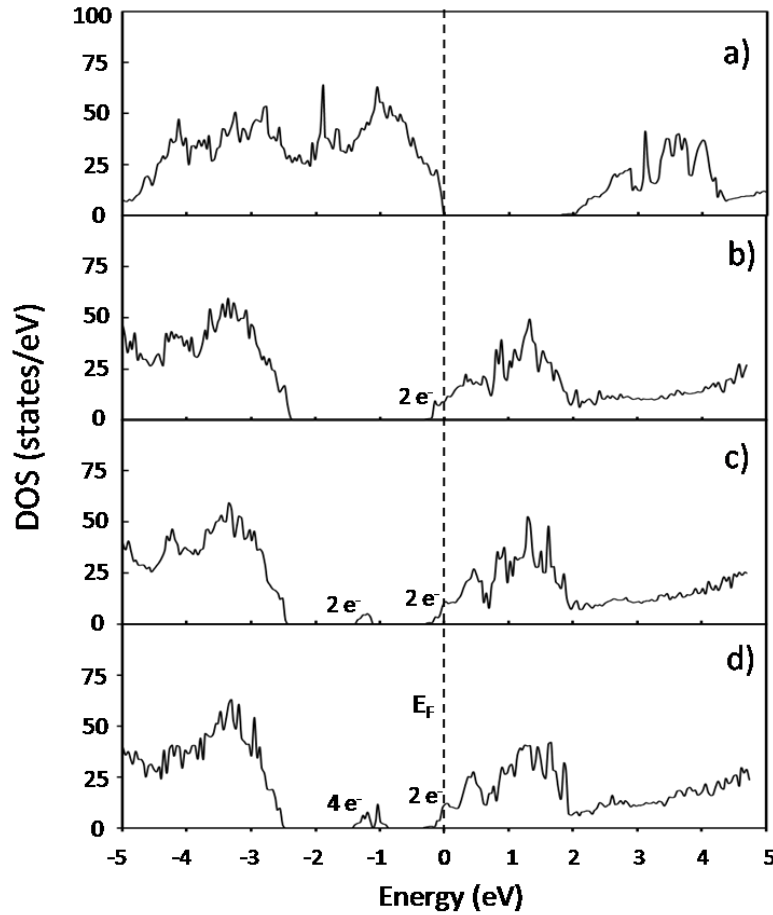
Figure 4.14 Density of states of a) $SrTi_{0.6}Nb_{0.2}Ga_{0.2}O_3$, b) $SrTi_{0.6}Nb_{0.2}Ga_{0.2}O_{2.95}$, c) $SrTi_{0.6}Nb_{0.2}Ga_{0.2}O_{2.9}$, and d) $SrTi_{0.6}Nb_{0.2}Ga_{0.2}O_{2.85}$. Fermi energy is set to zero on the energy scale. Numbers of electrons shown in the figure indicate the integrated number of electrons per supercell for the specified DOS area, i.e., states in the band gap and states below the Fermi level.

86

4.5   Conclusions

We have investigated the electronic properties and thermodynamic stability of Nb (n-type) and Ga (p-type) doped $SrTiO_3$ perovskites using density functional theory and constrained *ab initio* thermodynamic simulations. We find that cation vacancy compensated 20% Nb-doped Sr-deficient $SrTiO_3$ ($Sr_{0.9}Ti_{0.8}Nb_{0.2}O_3$) transforms to an electronically compensated non Sr-deficient phase ($SrTi_{0.8}Nb_{0.2}O_3$) at high temperature and low oxygen partial pressure which leads to a significant improvement in electronic conductivity. This result is in excellent agreement with the defect chemistry model and experimental observations reported by Kolodiazhnyi and Petric [24]. Doping 20% Nb-doped $SrTiO_3$ with 10% Ga enhances the ionic conductivity of the material by creating oxygen vacancies. The electronic conductivity is not reduced by small amounts of Ga so that a mixed ionic/electronic conductor is formed. However, doping with 20% Ga decreases the electronic conductivity of the material. This result supports the experimental observations [39, 40] that doping with a small amount of Ga improves the conductivity and promotes fast reduction of the material. From both experimental observations and our calculations, we propose that a mixed n-type and p-type doping strategy could be a general approach to obtaining mixed ionic/electronic conductivity in perovskite oxide materials.

4.6   References

[1]   S.W. Tao, J.T.S. Irvine, Nature Materials 2 (2003) 320.

[2]   Y.H. Huang, R.I. Dass, Z.L. Xing, J.B. Goodenough, Science 312 (2006) 254.

[3]   D.P. Fagg, V.V. Kharton, A.V. Kovalevsky, A.P. Viskup, E.N. Naumovich, J.R. Frade, J. Eur. Ceram. Soc. 21 (2001) 1831.

[4]   S.Q. Hui, A. Petric, J. Eur. Ceram. Soc. 22 (2002) 1673.

[5]   T. Ishihara, H. Matsuda, Y. Takita, J. Am. Chem. Soc. 116 (1994) 3801.

[6]   M. Feng, J.B. Goodenough, Eur. J. Solid State Inorg. Chem. 31 (1994) 663.

[7]   K.Q. Huang, M. Feng, J.B. Goodenough, M. Schmerling, J. Electrochem. Soc. 143 (1996) 3630.

[8]   J. Canales-Vazquez, S.W. Tao, J.T.S. Irvine, Solid State Ionics 159 (2003) 159.

[9]   O.A. Marina, N.L. Canfield, J.W. Stevenson, Solid State Ionics 149 (2002) 21.

[10]   J. Canales-Vazquez, J.C. Ruiz-Morales, J.T.S. Irvine, W.Z. Zhou, J. Electrochem. Soc. 152 (2005) A1458.

[11]   A. Sin, E. Kopnin, Y. Dubitsky, A. Zaopo, A.S. Arico, L.R. Gullo, D. La Rosa, V. Antonucci, J. Power Sources 145 (2005) 68.

[12]   P. Vernoux, E. Djurado, M. Guillodo, J. Am. Ceram. Soc. 84 (2001) 2289.

[13]   Y.B. Lin, Z.L. Zhan, S.A. Barnett, J. Power Sources 158 (2006) 1313.

[14]   L. Aguilar, S.W. Zha, Z. Cheng, J. Winnick, M.L. Liu, J. Power Sources 135 (2004) 17.

[15]   P.R. Slater, D.P. Fagg, J.T.S. Irvine, J. Mater. Chem. 7 (1997) 2495.

[16]   J.A. Noland, Physical Review 94 (1954) 724.

[17]   J.F. Schooley, W.R. Hosler, E. Ambler, J.H. Becker, M.L. Cohen, C.S. Koonce, Phys. Rev. Lett. 14 (1965) 305.

[18]   Y. Aiura, H. Bando, I. Hase, S. Nishihara, Y. Haruyama, H. Suzuki, Superlattices Microstruct. 21 (1997) 321.

[19]   N. Shanthi, D.D. Sarma, Phys. Rev. B 57 (1998) 2153.

[20]   T. Yokoya, T. Sato, H. Fujisawa, T. Takahashi, A. Chainani, M. Onoda, Phys. Rev. B 59 (1999) 1815.

[21]   T. Jarlborg, Phys. Rev. B 61 (2000) 9887.

[22]   S. Lee, G. Kim, J.M. Vohs, R.J. Gorte, J. Electrochem. Soc. 155 (2008) B1179.

[23]   H. Kurokawa, L.M. Yang, C.P. Jacobson, L.C. De Jonghe, S.J. Visco, J. Power Sources 164 (2007) 510.

[24]   T. Kolodiazhnyi, A. Petric, J. Electroceram. 15 (2005) 5.

[25]   W. Luo, W. Duan, S.G. Louie, M.L. Cohen, Phys. Rev. B 70 (2004) 214109.

[26]   U. Balachandran, N.G. Eror, J. Electrochem. Soc. 129 (1982) 1021.

[27]   A.M.J. Seuter, Philips Res. Repts (1974) 1.

[28]   R. Moos, K.H. Hardtl, J. Am. Ceram. Soc. 80 (1997) 2549.

[29]   J.B. Goodenough, Y.H. Huang, J. Power Sources 173 (2007) 1.

[30]   R. Moos, A. Gnudi, K.H. Härdtl, J. Appl. Phys. 78 (1995) 5042.

[31]   R. Moos, T. Bischoff, W. Menesklou, K.H. Hardtl, J. Mater. Sci. 32 (1997) 4247.

[32]   M.J. Akhtar, Z.U.N. Akhtar, R.A. Jackson, C.R.A. Catlow, J. Am. Ceram. Soc. 78 (1995) 421.

[33]   T. Ishihara, *Perovskite oxide for solid oxide fuel cells*, Springer, New York 2009.

[34]   K. Vidyasagar, A. Reller, J. Gopalakrishnan, C.N.R. Rao, J. Chem. Soc. Chem. Comm. (1985) 7.

[35]   J.A. Kilner, Solid State Ionics 129 (2000) 13.

[36]   J.C. Ruiz-Morales, J. Canales-Vazquez, C. Savaniu, D. Marrero-Lopez, W.Z. Zhou, J.T.S. Irvine, Nature 439 (2006) 568.

[37]   X. Li, H.L. Zhao, F. Gao, N. Chen, N.S. Xu, Electrochem. Commun. 10 (2008) 1567.

[38]   X. Li, H.L. Zhao, N.S. Xu, X. Zhou, C.J. Zhany, N. Chen, Int. J. Hydrogen Energy 34 (2009) 6407.

[39]   X. Guoliang, X. Dong, K. Huang, F. Chen, Mater. Res. Bull. 46 (2011) 57.

[40]   D. Neagu, J.T.S. Irvine, Chem. Mater. 23 (2011) 1607.
[41]   F.W. Lytle, J. Appl. Phys. 35 (1964) 2212.
[42]   G. Kresse, J. Furthmuller, Phys. Rev. B 54 (1996) 11169.
[43]   G. Kresse, D. Joubert, Phys. Rev. B 59 (1999) 1758.
[44]   J.P. Perdew, K. Burke, M. Ernzerhof, Phys. Rev. Lett. 77 (1996) 3865.
[45]   H.J. Monkhorst, J.D. Pack, Phys. Rev. B 13 (1976) 5188.
[46]   Y.A. Abramov, V.G. Tsirelson, V.E. Zavodnik, S.A. Ivanov, B.I. D., Acta Crystallogr. B 51 (1995) 942.
[47]   K. van Benthem, C. Elsasser, R.H. French, J. Appl. Phys. 90 (2001) 6156.
[48]   J. Robertson, K. Xiong, S.J. Clark, Thin Solid Films 496 (2006) 1.
[49]   C. Zhang, C.L. Wang, J.C. Li, K. Yang, Y.F. Zhang, Q.Z. Wu, Mater. Chem. Phys. 107 (2008) 215.
[50]   S.C. Ammal, A. Heyden, J. Chem. Phys. 133 (2010) 164703.
[51]   J.K. Norskov, J. Rossmeisl, A. Logadottir, L. Lindqvist, J.R. Kitchin, T. Bligaard, H. Jonsson, J. Phys. Chem. B 108 (2004) 17886.
[52]   P.W. Atkins, *Physical Chemistry*, Oxford University Press, Oxford 1998.
[53]   S. Laursen, S. Linic, PCCP 11 (2009) 11006.
[54]   S. Laursen, S. Linic, J. Phys. Chem. C 113 (2009) 6689.
[55]   J. Rogal, K. Reuter, M. Scheffler, Phys. Rev. B 75 (2007) 205433.
[56]   C.K. Gupta, A.K. Suri, *Extractive metallurgy of niobium*, CRC Press, Boca Raton 1994.
[57]   K. Kuroda, W. Sugimoto, M. Shirata, M. Takemoto, S. Hayami, Y. Sugahara, Solid State Ionics 108 (1998) 315.
[58]   J.N. Yun, Z.Y. Zhang, J.F. Yan, W. Zhao, J. Appl. Phys. 107 (2010).

CHAPTER 5

OBTAINING MIXED IONIC/ELECTRONIC CONDUCTIVITY IN PEROVSKITE OXIDES UNDER ANODIC SOLID OXIDE FUEL CELL CONDITIONS: A COMPUTATIONAL PREDICTION FOR DOPED STRONTIUM TITANATES

5.1   Summary

The electronic conductivity and thermodynamic stability of mixed p- and n-doped $SrTiO_3$ perovskites have been investigated under anodic solid oxide fuel cell conditions using density functional theory (DFT). In particular, constrained *ab initio* thermodynamic calculations have been performed to evaluate the phase stability of various Ga- and La-doped $SrTiO_3$ at synthesized and anodic SOFC conditions. The density of states (DOS) of these materials were analyzed to determine the number of charge carriers and the degree of electronic conductivity. We find that a mixed ionic/electronic conductor can be obtained when doping $SrTiO_3$ perovskite oxide with both p-type and n-type dopants. Calculations show that 10% Ga- and 20% La-doped $SrTiO_3$ exhibit mixed ionic/electronic conductivity at high temperature and low oxygen partial pressure whereas doping with higher concentrations of Ga, e.g., 20%, diminishes the electronic conductivity of the material. Furthermore, changing the n-dopant from La (A-site) to Nb (B-site) does not significantly affect the reducibility and number of charge carriers in p-

and n-doped $SrTiO_3$. However, a higher degree of oxygen vacancy clustering is observed for the La-doped material which reduces the oxygen ion diffusion rate and traps electrons. Nevertheless, our findings suggest that independent of doping site, mixed ionic/electronic conductivity can be obtained in $SrTiO_3$ perovskite oxides under reducing conditions and high temperatures when using a mixed p- and n-type doping strategy that uses a p-dopant concentration smaller than the n-dopant concentration.

5.2   Introduction

It is known that mixed ionic/electronic conductivity of perovskite based anodes plays an important role in enhancing SOFC performance. A mixed oxide ion and electron conducting perovskite has the advantage of efficiently collecting current while increasing the electrochemically active surface area for fuel oxidation [4]. As a result, several doping strategies to improve MIEC are currently being tested. In Chapter 4, we proposed that mixed p- and n-doping approach could be an efficient doing strategy to obtain mixed ionic/electronic conductivity in perovskite oxides under anodic SOFC conditions. Our calculated results suggest that ionic and electronic conductivity of doped $SrTiO_3$ perovskites are remarkably improved when doping with Ga and Nb dopants by using a Ga concentration smaller than the Nb concentration. This must be because the hole doping effect of Ga dopants are compensated by the presence of oxygen vacancies in the lattice. This result is in excellent agreement with experimental observations from Xiao et al. [2] Moreover, mixed ionic/electronic conductors with A-site and B-site co-doping have been reported. Li et al. [5, 6] and Neagu and Irvine [3] suggested that n-type (La) and p-type (Sc, Co, and Ga) co-doped $SrTiO_3$ can promote fast reduction and improve ionic and electronic conductivity of the material.

In this Chapter, we aim to show that mixed p- and n-doping is indeed an efficient strategy to obtain mixed ionic/electronic conductivity in perovskite materials. By using computational tools, we prove unambiguously that this mixed doping strategy is valid and independent of the doping site in the $SrTiO_3$ perovskite structure. In particular, we performed constrained *ab initio* thermodynamic simulations to evaluate the thermodynamic stability of Ga- and La-doped $SrTiO_3$ phases at synthesized and anodic SOFC conditions, we analyzed the electronic structure of the resulting materials, and we compared the results to our previous study of Ga- and Nb-doped $SrTiO_3$ perovskites.

5.3   Computational Details

To investigate the bulk electronic properties of stoichiometric and doped $SrTiO_3$, we initially optimized the lattice parameter of the $SrTiO_3$ unit cell and created a 100 atom supercell containing twenty unit cells ($5\times2\times2$). To generate doped structures we replaced A-site cations (Sr) with n-type dopants (La) and substituted B-site cations (Ti) with p-type dopants (Ga). Substitution of two cations on the A-site (B-site) in the host lattice with two dopants yields 10% A-site (B-site) doped $SrTiO_3$ etc. To study the charge compensation mechanism in p- and n-doped systems, both A-site deficient and reduced structures were created by generating strontium vacancies and oxygen vacancies, respectively. In this work, we considered up to two strontium vacancies and three oxygen vacancies in each structure. For all doped structures, we employed the reoptimized lattice parameters of 20% La-doped $SrTiO_3$ and tried all meaningful configurations (over one hundred configurations were tested in this study) to identify the lowest energy structures.

All calculations performed for this study are based on the plane wave density functional theory implementation of the Vienna Ab initio Simulation Package (VASP

4.6) [7, 8]. We used the projector-augmented wave (PAW) method to represent the inner core potentials [7] and treated the Sr $4s4p5s$, Ti $3d4s$, O $2s2p$, La $5s5p5d6s$, and Ga $4s4p$ as valence electrons. The cutoff of the kinetic energy was set for all calculations to 400 eV. Exchange correlation is described within the generalized gradient approximation (GGA) with the Perdew-Burke-Ernzerhof (PBE) functional [9]. All calculations are spin-polarized and Brillouin zone integration was performed with a $2\times5\times5$ Monkhorst-Pack k-point mesh [10]. For density of state (DOS) calculations we used a $4\times10\times10$ k-mesh. In all structure optimizations, all atoms are fully relaxed until the Hellman-Feynman forces are less than 0.02 eV Å^{-1}.

The optimized supercell of 20% La-doped $SrTiO_3$ exhibits only a very small change in lattice parameter (3.921 Å) to that of stoichiometric $SrTiO_3$. Computations predict a Sr-O and Ti-O bond distance of 2.792 and 1.974 Å, respectively. As shown previously, the density of states of stoichiometric $SrTiO_3$ exhibits insulating behavior with a band gap of 1.80 eV [11]. While DFT within the GGA approximation is known to underestimate band gaps, several studies showed excellent agreement in the predicted electronic behavior of doped oxides computed by DFT within the GGA approximation with the experimental observations [12-14]. Moreover, it has been shown that GGA-DFT can be used to predict formation energies and phase stabilities of several transition metal oxides [15].

5.4   Results and Discussion

As reported in Chapter 4, mixed ionic/electronic conductivity of perovskites can be obtained by introducing an optimum amount of p- and n-type dopants into the structures. DFT calculations of Ga- and Nb-doped $SrTiO_3$ systems have been performed to confirm our hypothesis [11]. Our calculated results are in excellent agreement with the experimental results reported by Xiao and co-workers [2]. In this work, we are most interested in the effect of doping site on the electronic conductivity and reducibility of the materials at sintering and anodic SOFC conditions. In order to compare the results with our previous work, we used the same computational procedure and performed three different sets of calculations of 20% La-doped $SrTiO_3$, 10% Ga- and 20% La-doped $SrTiO_3$, and 20% Ga- and 20% La-doped $SrTiO_3$. In this way, we can systematically study the effect of doping site on the mixed ionic/electronic conductivity of the resulting materials. To a first approximation, we expect the electron mobility to remain constant when changing n-type dopants in doped $SrTiO_3$ since the difference in electron mobility between Nb- and La-doped $SrTiO_3$ is insignificant [16].

For all structures we first performed constrained *ab initio* thermodynamic calculations to evaluate the relative thermodynamic stability of the systems. This *ab initio* thermodynamic approach involves the calculation of the free energy of different systems as a function of oxygen chemical potential, i.e., temperature and oxygen partial pressure, to construct a phase diagram. The reaction energies of the most dominant structures in the phase diagrams are summarized in Table 5.1. Next, the DOS related to the most dominant structures in the phase diagram has been evaluated and analyzed with respect to the relative electronic conductivity.

5.4.1 Electronic structure and phase diagram of 20% La-doped $SrTiO_3$

In this set of calculations, we replaced four Sr atoms with four La atoms in the $5 \times 2 \times 2$ supercell to obtain a model for 20% La-doped $SrTiO_3$ ($Sr_{0.8}La_{0.2}TiO_3$). In addition, we created structures with one or two Sr vacancies to form 5% A-site deficient ($Sr_{0.75}La_{0.2}TiO_3$) and 10% A-site deficient 20% La-doped $SrTiO_3$ ($Sr_{0.7}La_{0.2}TiO_3$) model structures, respectively. Substitution of Sr atoms with La atoms at an A-site does not significantly alter the lattice structure. There is no preference for the arrangement of La atoms and Sr vacancies in the lattice since the energy difference between the most stable structures are insignificant (lower than 2 meV/atom). The structures of the most stable configurations are illustrated in Fig. 5.1.

Constrained *ab initio* thermodynamic calculations of 20% La-doped $SrTiO_3$ systems were performed to determine the phase stability of these structures at various temperatures and oxygen partial pressures. We employed two different types of calculations based on the main products that are generated when a phase transition occurs, namely, SrO rich second phase and TiO_2 and La_2O_3 rich second phases. We use the approach described in Chapter 4 to calculate Gibbs free energies of reactions and construct the phase diagram. Figure 5.2 shows the calculated phase diagrams of 20% La-doped $SrTiO_3$ with SrO rich second phase and TiO_2 and La_2O_3 rich second phases. The phase transformation from 10% Sr-deficient ($Sr_{0.7}La_{0.2}TiO_3$) to a non Sr-deficient structure ($Sr_{0.8}La_{0.2}TiO_3$) occurs with increasing temperature and decreasing oxygen partial pressure. An oxygen deficient structure is thermodynamically unstable in the considered temperature and oxygen partial pressure range.

Table 5.1 Summary of reaction energies used in constrained *ab initio* thermodynamic calculations

Phase Diagram	Reaction	ΔE (eV)
20% La-doped $SrTiO_3$ with SrO rich phase	$Sr_{16}La_4Ti_{20}O_{60} + 1/2O_2 \rightarrow Sr_{15}La_4Ti_{20}O_{60} + SrO$	-1.88
	$Sr_{16}La_4Ti_{20}O_{60} + O_2 \rightarrow Sr_{14}La_4Ti_{20}O_{60} + 2SrO$	-3.78
20% La-doped $SrTiO_3$ with TiO_2/La_2O_3 rich phases	$15Sr_{14}La_4Ti_{20}O_{60} \rightarrow 14Sr_{15}La_4Ti_{20}O_{60} + 20TiO_2 + 2La_2O_3 + 7O_2$	2.98
	$8Sr_{14}La_4Ti_{20}O_{60} \rightarrow 7Sr_{16}La_4Ti_{20}O_{60} + 20TiO_2 + 2La_2O_3 + 7O_2$	5.58
10% Ga- and 20% La-doped $SrTiO_3$ with SrO rich phase	$Sr_{16}La_4Ti_{18}Ga_2O_{60} + 1/2O_2 \rightarrow Sr_{15}La_4Ti_{18}Ga_2O_{60} + SrO$	-1.59
	$Sr_{16}La_4Ti_{18}Ga_2O_{60} \rightarrow Sr_{16}La_4Ti_{18}Ga_2O_{58} + O_2$	8.86
	$Sr_{16}La_4Ti_{18}Ga_2O_{60} \rightarrow Sr_{16}La_4Ti_{18}Ga_2O_{57} + 3/2O_2$	14.07
10% Ga- and 20% La-doped $SrTiO_3$ with $TiO_2/Ga_2O_3/La_2O_3$ rich phases	$15Sr_{14}La_4Ti_{18}Ga_2O_{60} \rightarrow 14Sr_{15}La_4Ti_{18}Ga_2O_{60} + 18TiO_2 + 2La_2O_3 + Ga_2O_3 + 15/2O_2$	-1.24
	$8Sr_{14}La_4Ti_{18}Ga_2O_{60} \rightarrow 7Sr_{16}La_4Ti_{18}Ga_2O_{60} + 18TiO_2 + 2La_2O_3 + Ga_2O_3 + 15/2O_2$	1.24
	$8Sr_{14}La_4Ti_{18}Ga_2O_{60} \rightarrow 7Sr_{16}La_4Ti_{18}Ga_2O_{58} + 18TiO_2 + 2La_2O_3 + Ga_2O_3 + 29/2O_2$	8.99
	$8Sr_{14}La_4Ti_{18}Ga_2O_{60} \rightarrow 7Sr_{16}La_4Ti_{18}Ga_2O_{57} + 18TiO_2 + 2La_2O_3 + Ga_2O_3 + 18O_2$	13.55
20% Ga- and 20% La-doped $SrTiO_3$	$Sr_{16}La_4Ti_{16}Ga_4O_{60} \rightarrow Sr_{16}La_4Ti_{16}Ga_4O_{58} + O_2$	8.57
	$Sr_{16}La_4Ti_{16}Ga_4O_{60} \rightarrow Sr_{16}La_4Ti_{16}Ga_4O_{57} + 3/2O_2$	13.09
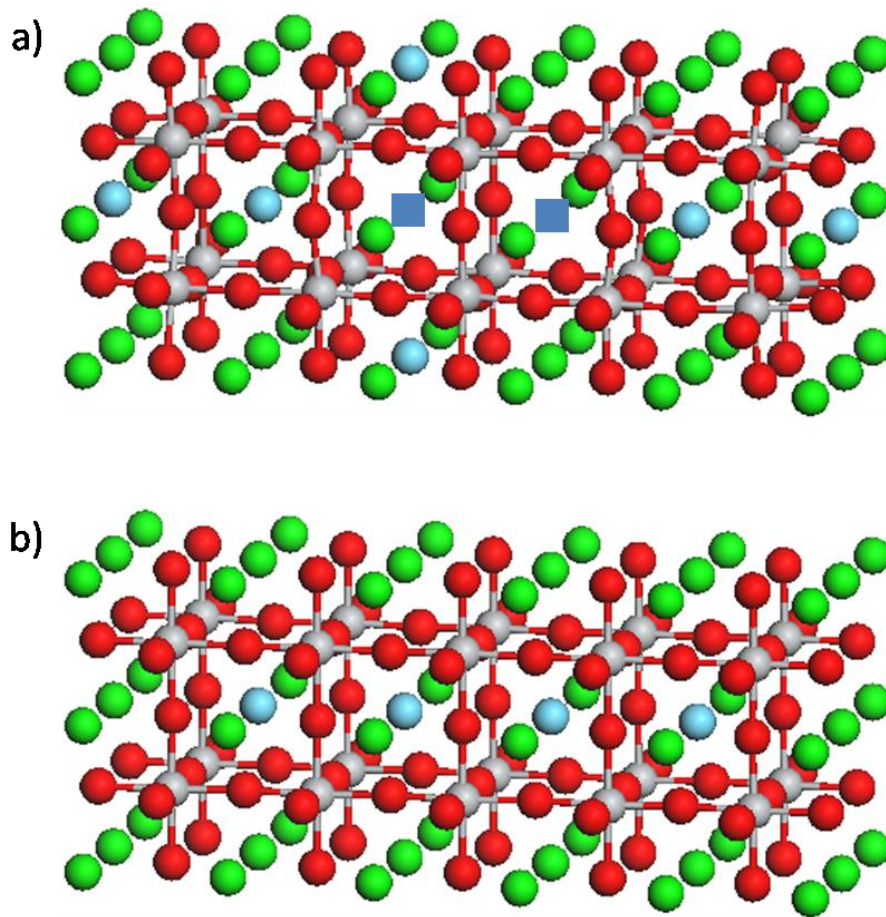
Figure 5.1 Most stable structures of 20% La-doped SrTiO$_3$: a) Sr$_{0.7}$La$_{0.2}$TiO$_3$ and b) Sr$_{0.8}$La$_{0.2}$TiO$_3$ Green, gray, blue, and red spheres represent Sr, Ti, La, and O atoms, respectively. Blue squares represent the position of Sr vacancies.

The electronic conductivity of each structure in the phase diagram can to a first approximation be analyzed from its electronic structure. We find that a very significant improvement in electronic conductivity of the materials occurs when the material is electronically compensated at high temperature and low oxygen partial pressure. As depicted in Fig. 5.3(a), the DOS of a 10% Sr-deficient phase (Sr$_{0.7}$La$_{0.2}$TiO$_3$) exhibits insulating behavior since the extra charge from La dopants are compensated by the presence of Sr vacancies. In contrast, the DOS of a non Sr-deficient phase

($Sr_{0.8}La_{0.2}TiO_3$) displays metallic character as the Fermi energy shifts inside the conduction band with four conduction electrons per supercell below the Fermi level.

Note that our simulation results are in agreement with several experimental observations. For example, it has been reported that A-site deficient n-doped $SrTiO_3$ exhibits a significant improvement in electronic conductivity when the material is pre-reduced or sintered in a reducing environment and high temperature. Neagu and Irvine found that this drastic enhancement in conductivity in La-doped $SrTiO_3$ occurs when sintering the material in H_2 atmosphere at 1650 ^{o}C [17]. Moreover, a promising conductivity of A-site deficient Y-doped $SrTiO_3$ can be achieved when the material is pre-reduced in 7% H_2/Ar at 1400 ^{o}C [18].

5.4.2 Electronic structure and phase diagram of 10% Ga- and 20% La-doped $SrTiO_3$

Substitution of two Ti atoms with two Ga atoms in our 20% La-doped $SrTiO_3$ model leads to 10% Ga- and 20% La-doped $SrTiO_3$. The presence of Sr and oxygen vacancies in the structure was investigated in a similar manner as described above. It is found that the arrangement of two Ga atoms in the stoichiometric structures is fairly random since the energy differences of the most stable structures are insignificant (lower than 2 meV/atom). At high temperatures and low oxygen partial pressures, structures with up to three oxygen vacancies are studied. In the reduced structure, the oxygen vacancies tend to cluster together. In addition, a configuration with two Ga atoms next to an oxygen vacancy is more favorable than a structure with the Ga atoms separated from the oxygen vacancies since the extra electrons from the oxygen vacancy can be partially compensated by the holes created by the Ga atoms in the structure. The configurations of

all most stable structures are shown in Fig. 5.4. Moreover, we find similar structural and electronic behavior in 3×3×3 cubic cell computations which confirms that the observed effects are not related to the rectangular cell used in this study (Fig. 5.5).
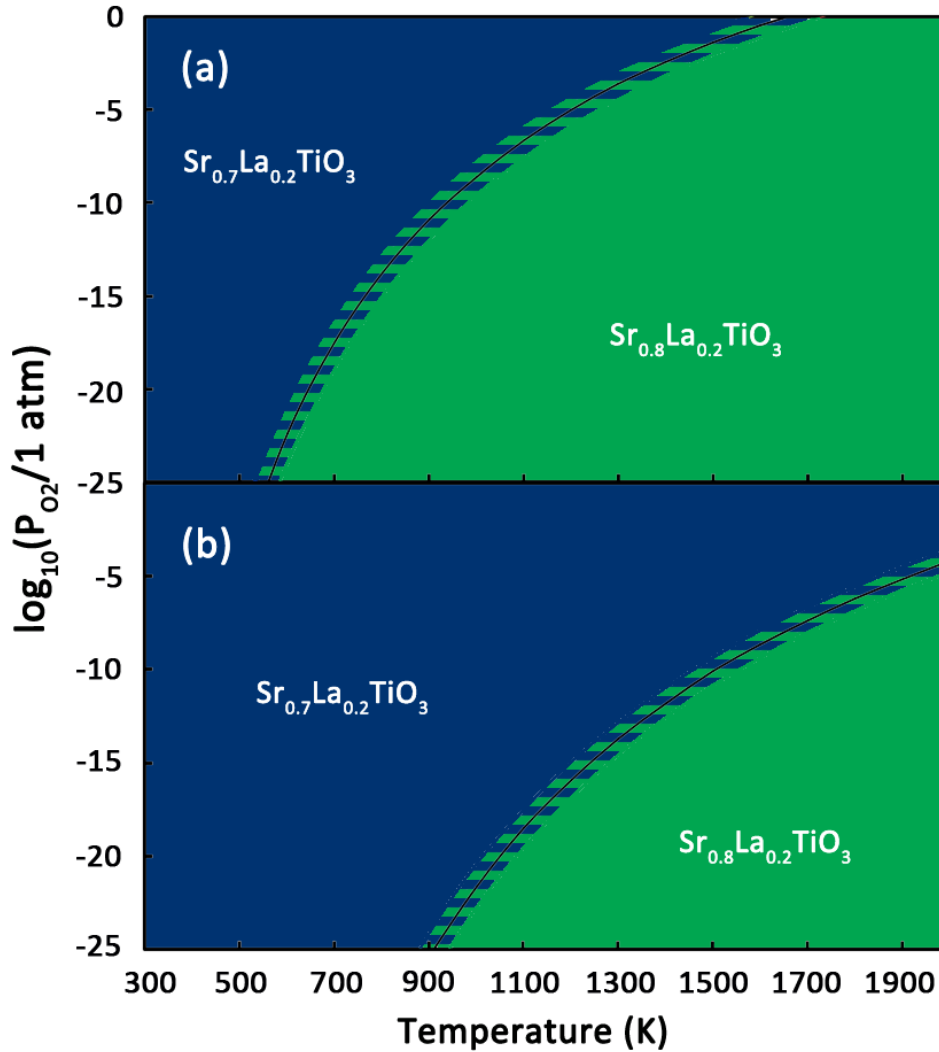
Figure 5.2 Calculated phase diagram of 20% La-doped $SrTiO_3$ with a) SrO rich phase and b) TiO_2/La_2O_3 rich phases. Differently shaded areas mark the stability regions of various structures for a given temperature and partial pressure of oxygen. The hatched area decribes possible changes in the phase diagram if computed reaction energies shown in Table 5.1 are off by ±0.2 eV (estimated error bar). Dark blue and green areas symbolize the stability of $Sr_{0.7}La_{0.2}TiO_3$ and $Sr_{0.8}La_{0.2}TiO_3$, respectively.
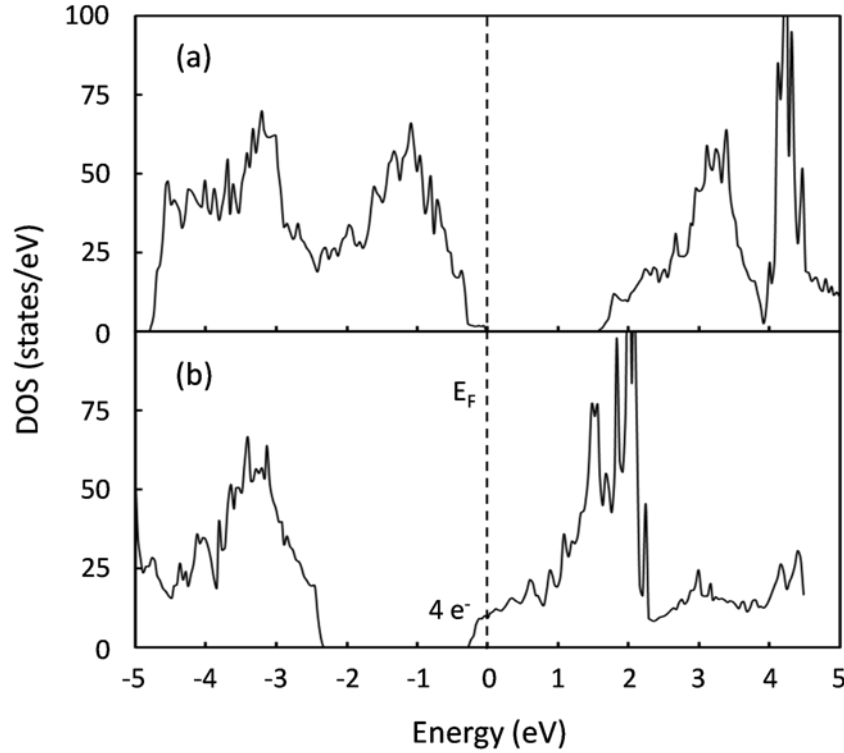
Figure 5.3 Density of states of a) $Sr_{0.7}La_{0.2}TiO_3$ and b) $Sr_{0.8}La_{0.2}TiO_3$. The Fermi energy is set to zero on the energy scale. Numbers of electrons shown in the figure indicate the integrated number of electrons per supercell for the specified DOS area, i.e., states in the band gap and states below the Fermi level.

Figure 5.6(a) and 5.6(b) illustrate the phase diagram for 10% Ga- and 20% La-doped $SrTiO_3$ as a function of temperature and partial pressure of oxygen under conditions leading to the formation of SrO and $TiO_2/Ga_2O_3/La_2O_3$ rich second phases, respectively. In the presence of Ga, we find that reduced structures ($Sr_{0.8}La_{0.2}Ti_{0.9}Ga_{0.1}O_{2.9}$ and $Sr_{0.8}La_{0.2}Ti_{0.9}Ga_{0.1}O_{2.85}$) are stable in the studied high temperature and low oxygen partial pressure range. The existence of a reduced structure indicates that Ga-doping improves the reducibility of the material as has also previously been reported by Neagu and Irvine [3]. Figure 5.7 displays the DOS of the most dominant structures in the phase diagrams. While $Sr_{0.75}La_{0.2}Ti_{0.9}Ga_{0.1}O_3$ (Fig. 5.7(a)) exhibits

insulating behavior (the charge from the La dopants are compensated by Sr vacancies and Ga dopants), $Sr_{0.8}La_{0.2}Ti_{0.9}Ga_{0.1}O_3$ (Fig. 5.7(b)), $Sr_{0.8}La_{0.2}Ti_{0.9}Ga_{0.1}O_{2.9}$ (Fig. 5.7(c)), and $Sr_{0.8}La_{0.2}Ti_{0.9}Ga_{0.1}O_{2.85}$ (Fig. 5.7(d)) exhibit metallic behavior with up to four conduction electrons at the Fermi level per supercell. It can be seen that charge compensation of the La (n-type) and Ga (p-type) dopants is absent when the material is reduced presumably because the hole doping effect of Ga is compensated by the presence of oxygen vacancies as described in our previous work [11]. More interestingly, the formation of an oxygen vacancy cluster in the structure results in localized states within the energy gap of the DOS of $Sr_{0.8}La_{0.2}Ti_{0.9}Ga_{0.1}O_{2.85}$ (Fig. 5.7(d)).
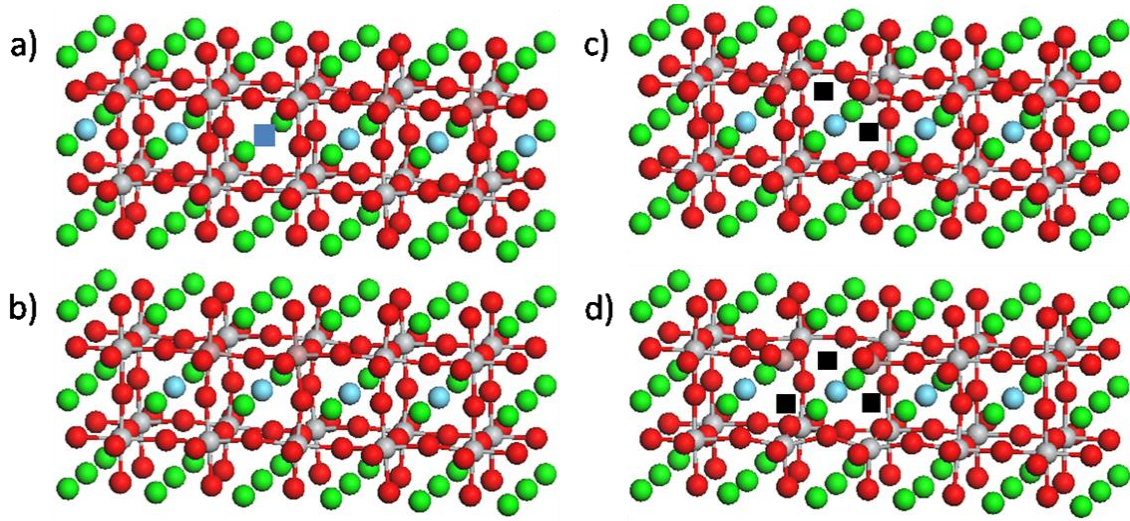
Figure 5.4 Most stable structures of 10% Ga- and 20% La-doped $SrTiO_3$: a) $Sr_{0.75}La_{0.2}Ti_{0.9}Ga_{0.1}O_3$, b) $Sr_{0.8}La_{0.2}Ti_{0.9}Ga_{0.1}O_3$, c) $Sr_{0.8}La_{0.2}Ti_{0.9}Ga_{0.1}O_{2.9}$, and d) $Sr_{0.8}La_{0.2}Ti_{0.9}Ga_{0.1}O_{2.85}$. Green, gray, blue, brown and red spheres represent Sr, Ti, La, Ga and O atoms, respectively. Blue and black squares represent the position of a Sr and O vacancy, respectively.
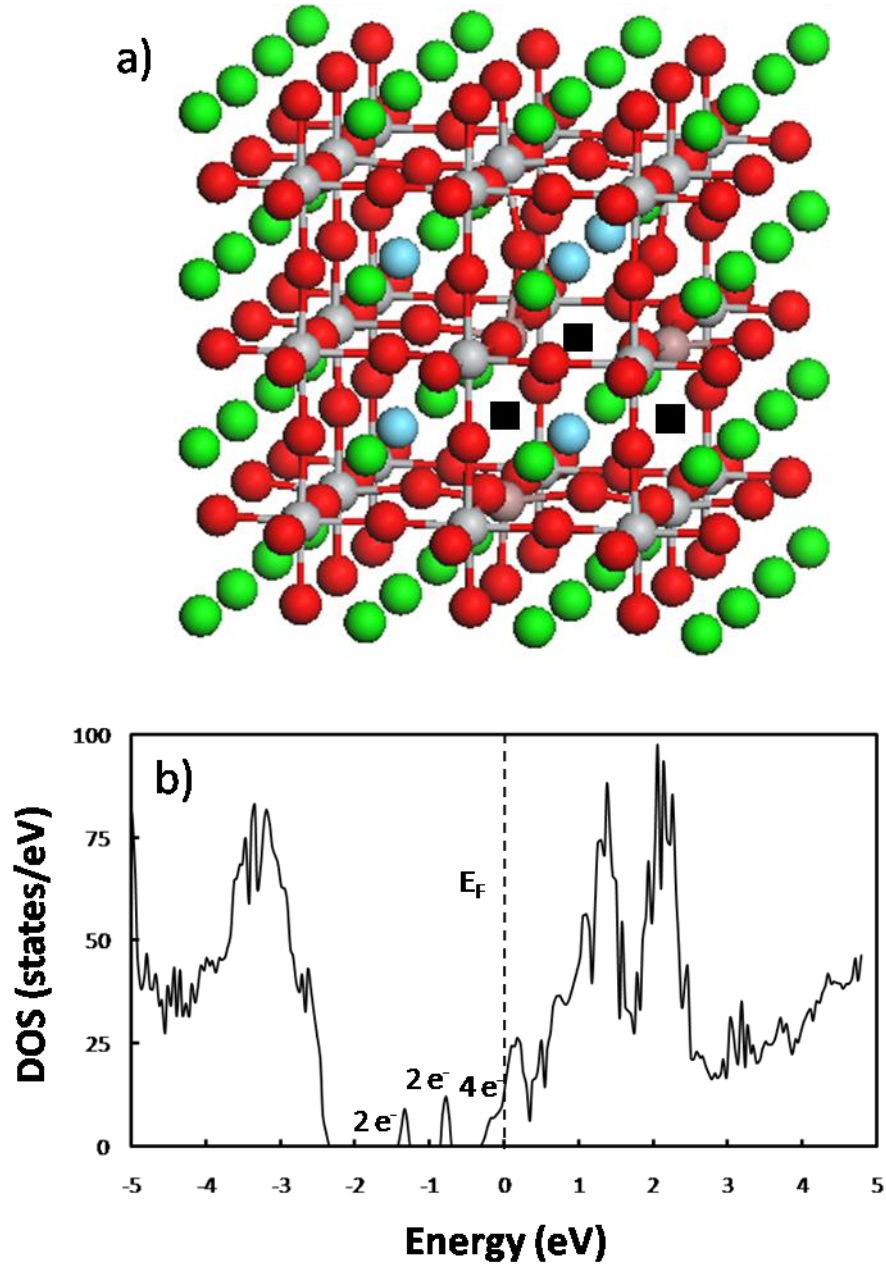
Figure 5.5 (a) The structure of $Sr_{0.81}La_{0.19}Ti_{0.89}Ga_{0.11}O_{2.89}$ with 3×3×3 supercell. Green, gray, blue, brown and red spheres represent Sr, Ti, La, Ga and O atoms, respectively. Black squares represent the position of O vacancies. (b) The DOS of $Sr_{0.81}La_{0.19}Ti_{0.89}Ga_{0.11}O_{2.89}$. Fermi energy is set to zero on the energy scale. Numbers of electrons shown in the figure indicate the integrated number of electrons per supercell for the specified DOS area, i.e., states in the band gap and states below the Fermi level.
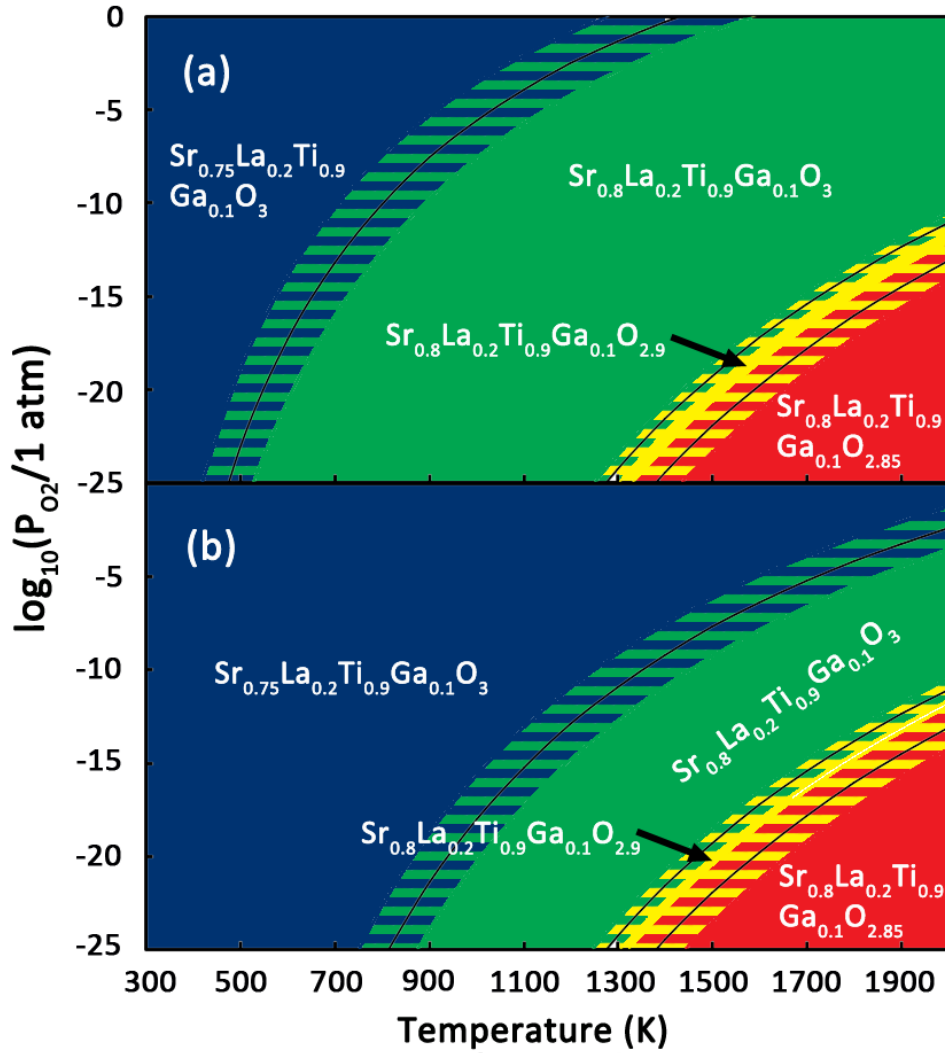
Figure 5.6 Calculated phase diagram of 10% Ga- and 20% La-doped $SrTiO_3$ with a) SrO rich phase and b) $TiO_2/Ga_2O_3/La_2O_3$ rich phases. Differently shaded areas mark the stability regions of various structures for a given temperature and partial pressure of oxygen. The hatched area decribes possible changes in the phase diagram if computed reaction energies shown in Table 5.1 are off by ± 0.2 eV (estimated error bar). Dark blue, green, yellow, and red areas symbolize the stability of $Sr_{0.75}La_{0.2}Ti_{0.9}Ga_{0.1}O_3$, $Sr_{0.8}La_{0.2}Ti_{0.9}Ga_{0.1}O_3$, $Sr_{0.8}La_{0.2}Ti_{0.9}Ga_{0.1}O_{2.9}$, and $Sr_{0.8}La_{0.2}Ti_{0.9}Ga_{0.1}O_{2.85}$, respectively.

Figure 5.7 Density of states of a) $Sr_{0.75}La_{0.2}Ti_{0.9}Ga_{0.1}O_3$, b) $Sr_{0.8}La_{0.2}Ti_{0.9}Ga_{0.1}O_3$, c) $Sr_{0.8}La_{0.2}Ti_{0.9}Ga_{0.1}O_{2.9}$, and d) $Sr_{0.8}La_{0.2}Ti_{0.9}Ga_{0.1}O_{2.85}$. The Fermi energy is set to zero on the energy scale. Numbers of electrons shown in the figure indicate the integrated number of electrons per supercell for the specified DOS area, i.e., states in the band gap and states below the Fermi level.

A partial density of states (PDOS) analysis and band decomposition charge density calculations for $Sr_{0.8}La_{0.2}Ti_{0.9}Ga_{0.1}O_{2.85}$, as illustrated in Fig. 5.8(a), show that there are two states within the gap between the valence and conduction bands. Each state contains two electrons which are mostly localized around the Ga atoms and vacancy sites. This observation is in agreement with previous computational and experimental results

that vacancy clustering can occur in perovskite oxides and that the electrons from the vacancies are often localized and do not contribute to the electronic conductivity of the material [19, 20]. Next, Fig. 5.8(b) shows the PDOS of $Sr_{0.8}La_{0.2}Ti_{0.9}Ga_{0.1}O_{2.85}$ below the Fermi level and confirms that these states are primarily from mixed-valent Ti^{3+}/Ti^{4+} that contribute to electronic conduction. A similar behavior is observed for all structures studied with states below the Fermi level.
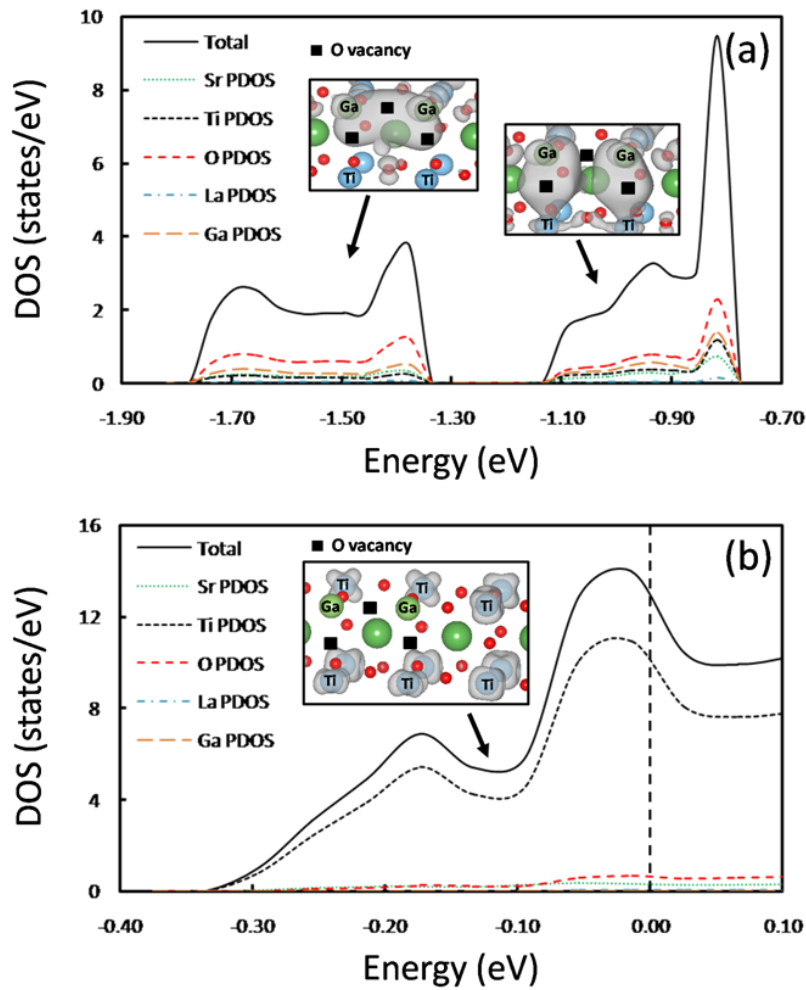
Figure 5.8 (a) Partial density of states of the gap states between the valence band and conduction band of $Sr_{0.8}La_{0.2}Ti_{0.9}Ga_{0.1}O_{2.85}$. The insets describe the charge density of the localized states which are located at the oxygen vacancy sites. (b) Partial density of states of $Sr_{0.8}La_{0.2}Ti_{0.9}Ga_{0.1}O_{2.85}$ below the Fermi level. The inset illustrates the charge density of delocalized states from mixed-valent Ti^{3+}/Ti^{4+}.

To conclude, doping of 20% La-doped $SrTiO_3$ with 10% Ga leads to a comparable degree of electronic conductivity to that of only 20% La-doped $SrTiO_3$ under anodic SOFC conditions. Furthermore, Ga promotes ionic conductivity by enhancing the reducibility of the material. These results support the experimental observations reported by several groups that Ga-doped titanates possess a high number of oxygen vacancies and good oxide ion conduction [2, 3]. However, the ordering of oxygen vacancies might reduce the ionic and electronic conductivity since the association of vacancies can impair diffusion and trap electrons.

5.4.3 Electronic structure and phase diagram of 20% Ga- and 20% La-doped $SrTiO_3$

Substitution of four Ti atoms with Ga atoms in our 20% La-doped $SrTiO_3$ model leads to a 20% Ga- and 20% La-doped $SrTiO_3$ model. Although the position of the four Ga atoms in the stoichiometric structure is nearly random, the most stable reduced structures have oxygen vacancy clusters surrounded by four Ga atoms (Fig. 5.9). Such preferred configurations confirm that the charge compensation mechanism plays an essential role in the arrangement of impurities in the structure.

Constrained *ab initio* thermodynamic calculations of this system were carried out to determine the phase stability and the reducibility of the materials at various temperatures and oxygen partial pressure. The phase transitions of this system are similar to those of the 10% Ga-doped system, i.e., the presence of a reduced phase of both the 10% Ga- and 20% Ga-doped systems occurs at approximately the same temperature and oxygen partial pressure range. This indicates that increasing the concentration of Ga does not significantly improve the reducibility of the material. However, the phase diagram of

the 20% Ga-doped system shown in Fig. 5.10 depicts the absence of a Sr-deficient phase

(i.e., there are no SrO or $TiO_2/Ga_2O_3/La_2O_3$ rich second phases).
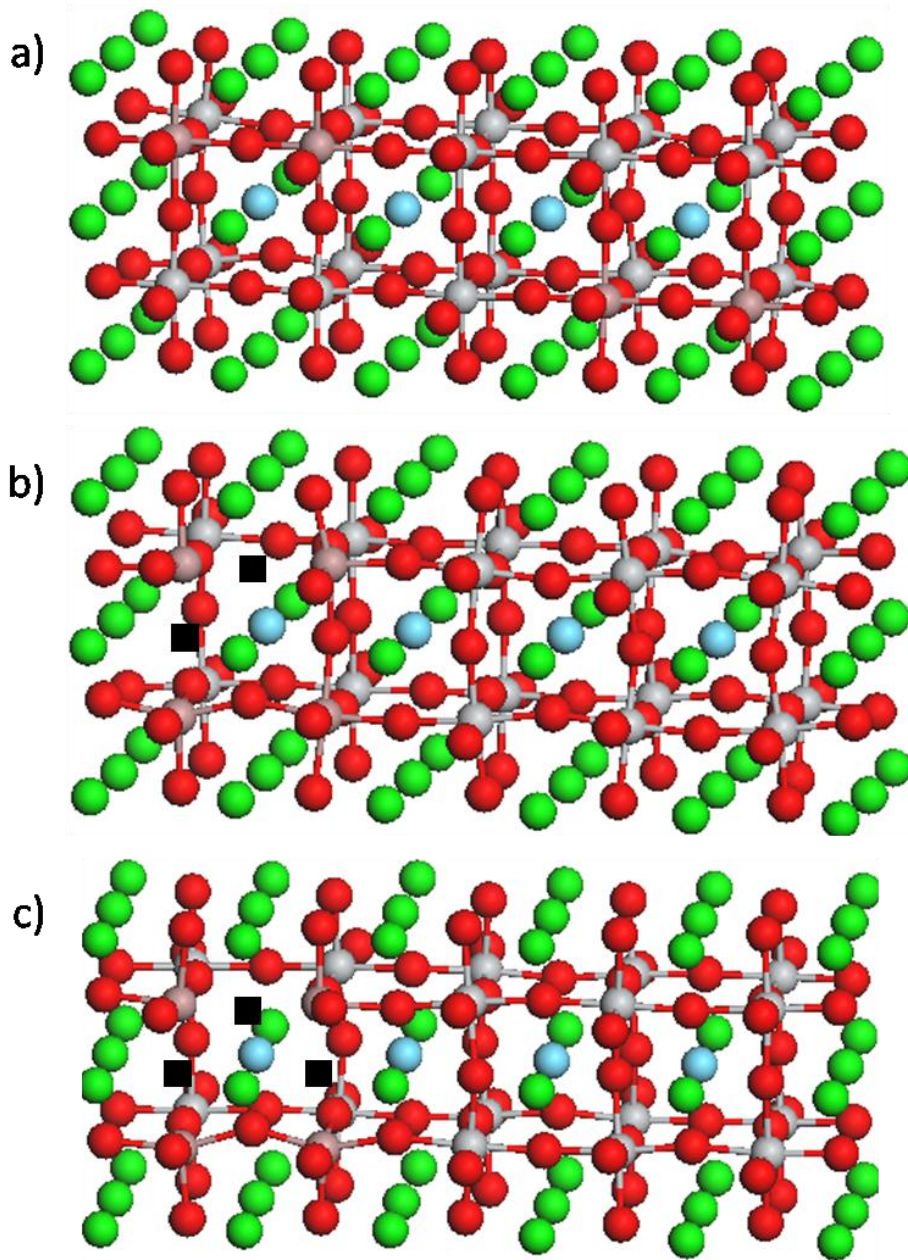
Figure 5.9 Most stable structures of 20% Ga- and 20% La-doped $SrTiO_3$: a) $Sr_{0.8}La_{0.2}Ti_{0.8}Ga_{0.2}O_3$, b) $Sr_{0.8}La_{0.2}Ti_{0.8}Ga_{0.2}O_{2.9}$, and c) $Sr_{0.8}La_{0.2}Ti_{0.8}Ga_{0.2}O_{2.85}$. Green, gray, blue, brown and red spheres represent Sr, Ti, La, Ga and O atoms, respectively. Black squares represent the position of O vacancies.
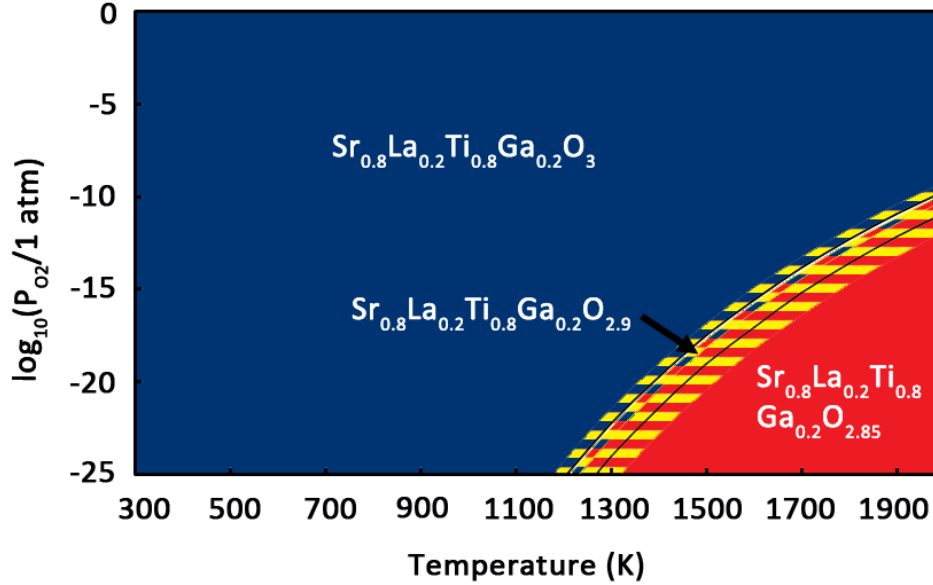
Figure 5.10 Calculated phase diagram of 20% Ga- and 20% La-doped $SrTiO_3$. Differently shaded areas mark the stability regions of various structures for a given temperature and partial pressure of oxygen. The hatched area decribes possible changes in the phase diagram if computed reaction energies shown in Table 5.1 are off by ± 0.2 eV (estimated error bar). Dark blue, yellow, and red areas symbolize stablity of $Sr_{0.8}La_{0.2}Ti_{0.8}Ga_{0.2}O_3$, $Sr_{0.8}La_{0.2}Ti_{0.8}Ga_{0.2}O_{2.9}$, and $Sr_{0.8}La_{0.2}Ti_{0.8}Ga_{0.2}O_{2.85}$, respectively.

Moreover, it can be seen from the DOS (Fig. 5.11) that increasing the Ga concentration leads to a reduction in the electronic conductivity. As shown in Fig. 5.11(b), the DOS of $Sr_{0.8}La_{0.2}Ti_{0.8}Ga_{0.2}O_{2.9}$ exhibits only two delocalized electrons in the conduction band. Although the DOS of $Sr_{0.8}La_{0.2}Ti_{0.8}Ga_{0.2}O_{2.85}$ (Fig. 5.11(c)) displays four electrons below the Fermi level in the conduction band, the PDOS and charge density shown in Fig. 5.12 reveal that there are only two electrons uniformly distributed on all Ti atoms in the supercell while the other two electrons seem to be localized on oxygen vacancy sites and Ga atoms. These localized electrons do not contribute to electronic conduction. Instead, they tend to trap electrons and could further decrease the electronic conductivity of the material. Thus, while doping with 20% Ga improves the

ionic conductivity, the electronic conductivity of the material is likely diminished under realistic fuel cell operating conditions.
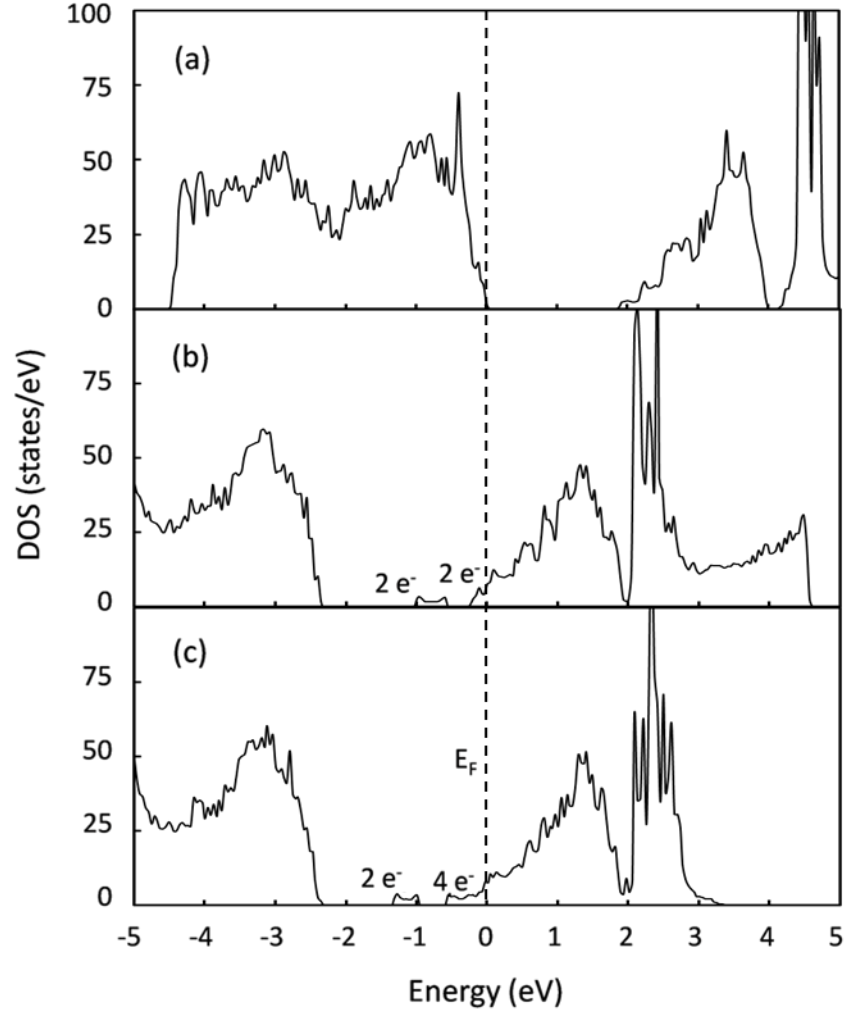
Figure 5.11 Density of states of a) $Sr_{0.8}La_{0.2}Ti_{0.8}Ga_{0.2}O_3$, b) $Sr_{0.8}La_{0.2}Ti_{0.8}Ga_{0.2}O_{2.9}$ and c) $Sr_{0.8}La_{0.2}Ti_{0.8}Ga_{0.2}O_{2.85}$. The Fermi energy is set to zero on the energy scale. Numbers of electrons shown in the figure indicate the integrated number of electrons per supercell for the specified DOS area, i.e., states in the band gap and states below the Fermi level.
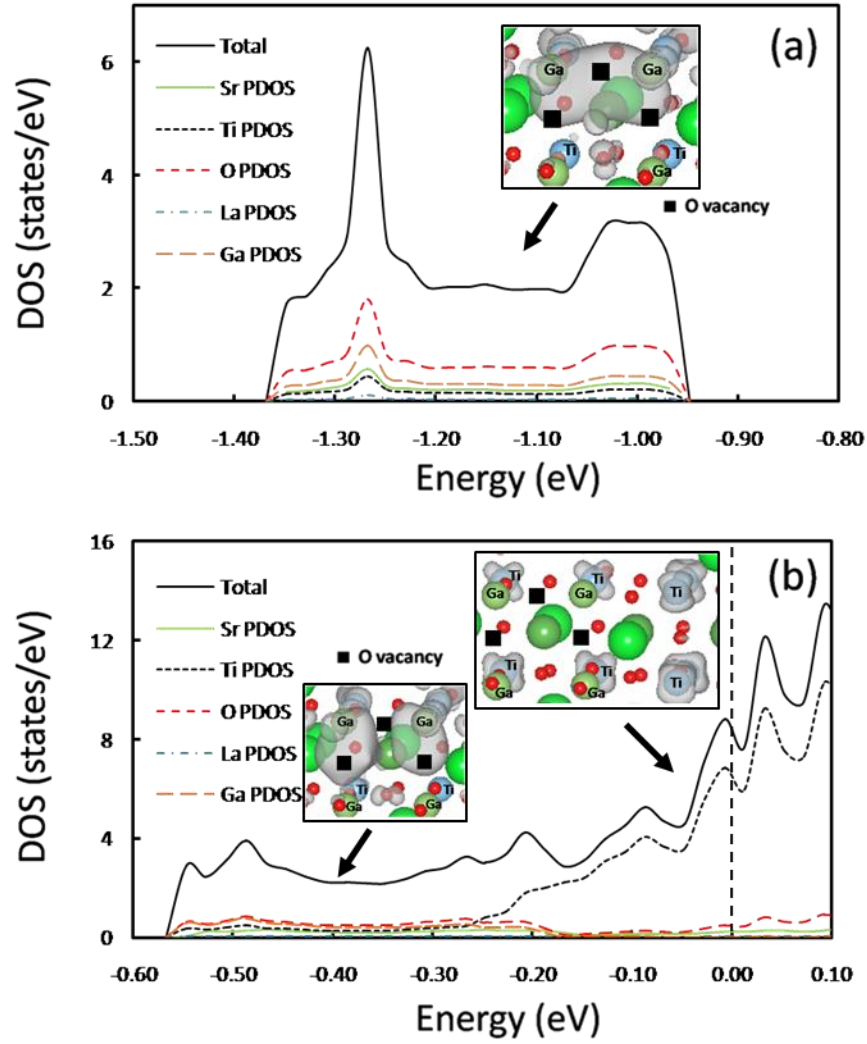
Figure 5.12 (a) Partial density of states of the gap states between the valence and conduction band of $Sr_{0.8}La_{0.2}Ti_{0.8}Ga_{0.2}O_{2.85}$. The insets describe the charge density of the localized states which are located at the oxygen vacancy sites. (b) Partial density of states of $Sr_{0.8}La_{0.2}Ti_{0.9}Ga_{0.1}O_{2.85}$ below the Fermi level. The inset illustrates the charge density of the localized states in the lower energy region and charge density of delocalized states from mixed-valent Ti^{3+}/Ti^{4+} near the Fermi level.

5.4.4 Effects of n-doping site on mixed ionic/electronic conductivity of mixed p- and n-doped $SrTiO_3$

In this section, we compare the simulation results of our previous work (Ga- and Nb-doped $SrTiO_3$) [11] with the present work (Ga- and La-doped $SrTiO_3$) to study the effects of n-doping site on the reducibility and electronic structure of mixed p- and n-doped $SrTiO_3$ perovskites. In particular, we compare the phase diagrams and DOS of the 10% Ga- and 20% Nb-doped $SrTiO_3$ and 10% Ga- and 20% La-doped $SrTiO_3$ systems since these compositions are claimed to lead to promising mixed ionic/electronic conductors. We find that altering the n-dopant from Nb (B-site) to La (A-site) does not significantly affect the phase stability and reducibility of the materials. As shown in Fig. 5.13, the presence of the reduced phases occurs in both phase diagrams, within our computational accuracy of about 0.2 eV, at the same temperature and oxygen partial pressure ranges. As a result, we expect the ionic conductivity of both systems to be comparable.

Furthermore, comparing the number of charge carriers obtained from the DOS computations, we observe that the numbers of charge carriers are equivalent in both systems (Fig. 5.14). Therefore, their electronic conductivity is expected to be similar. However, a higher degree of oxygen vacancy clustering is observed in our La-doped systems which should reduce the oxygen diffusion rate and trap electrons. Therefore, the mixed ionic/electronic conductivity of La-doped systems could be lower than that of Nb-doped systems.

Finally, in 20% Ga-doped systems, we find that the reducibility and numbers of charge carriers in 20% Ga- and 20% Nb-doped $SrTiO_3$ and 20% Ga- and 20% La-doped

111

SrTiO$_3$ are very similar. Therefore, independent of n-dopant a maximum in mixed ionic/electronic conductivity of the materials is observed when the p-dopant concentration is smaller than the n-dopant concentration.
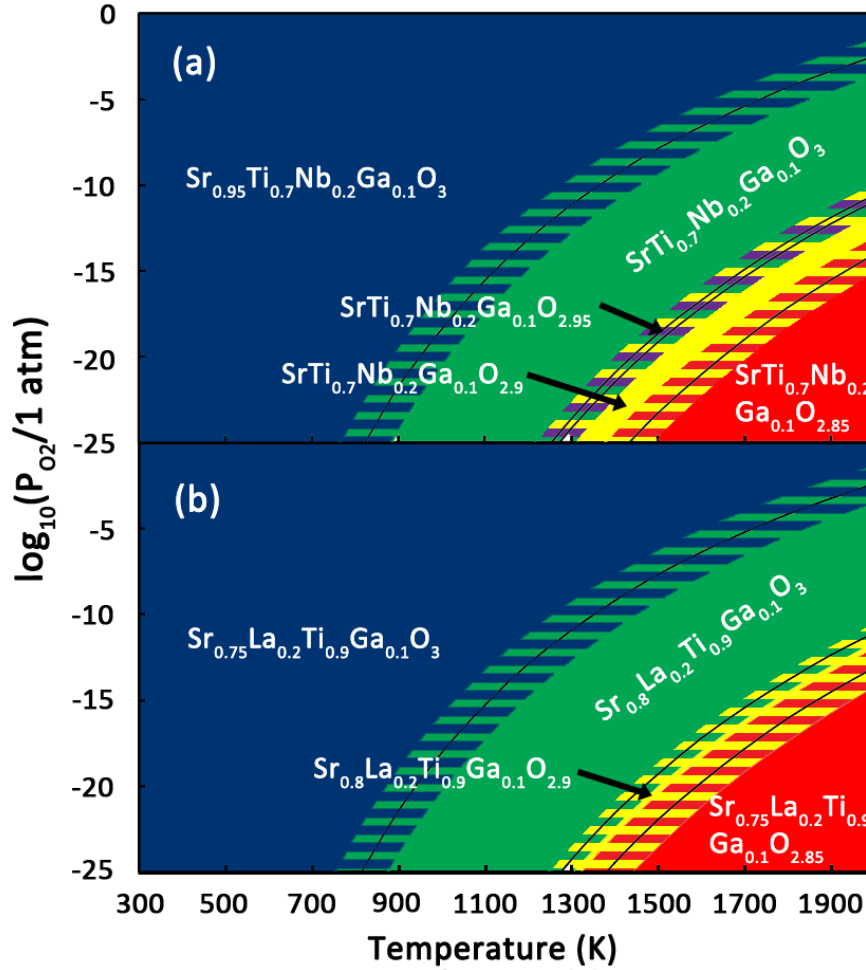
Figure 5.13 Calculated phase diagram of a) 10% Ga- and 20% Nb-doped SrTiO$_3$ and b) 10% Ga- and 20% La-doped SrTiO$_3$. Differently shaded areas mark the stability regions of various structures for a given temperature and partial pressure of oxygen. The hatched area decribes possible changes in the phase diagram if computed reaction energies shown in Table 5.1 are off by ±0.2 eV (our estimated error bar). In Fig. 5.13(a), Dark blue, green, yellow, and red areas symbolize stability of Sr$_{0.95}$Ti$_{0.7}$Nb$_{0.2}$Ga$_{0.1}$O$_3$, SrTi$_{0.7}$Nb$_{0.2}$Ga$_{0.1}$O$_3$, SrTi$_{0.7}$Nb$_{0.2}$Ga$_{0.1}$O$_{2.9}$, and SrTi$_{0.7}$Nb$_{0.2}$Ga$_{0.1}$O$_{2.85}$, respectively. The hatched violet area symbolizes the possible stability of a SrTi$_{0.7}$Nb$_{0.2}$Ga$_{0.1}$O$_{2.95}$ phase. In Fig. 5.13(b), blue, green, yellow, and red areas symbolize the stability of Sr$_{0.75}$La$_{0.2}$Ti$_{0.9}$Ga$_{0.1}$O$_3$, Sr$_{0.8}$La$_{0.2}$Ti$_{0.9}$Ga$_{0.1}$O$_3$, Sr$_{0.8}$La$_{0.2}$Ti$_{0.9}$Ga$_{0.1}$O$_{2.9}$, and Sr$_{0.8}$La$_{0.2}$Ti$_{0.9}$Ga$_{0.1}$O$_{2.85}$, respectively.

112
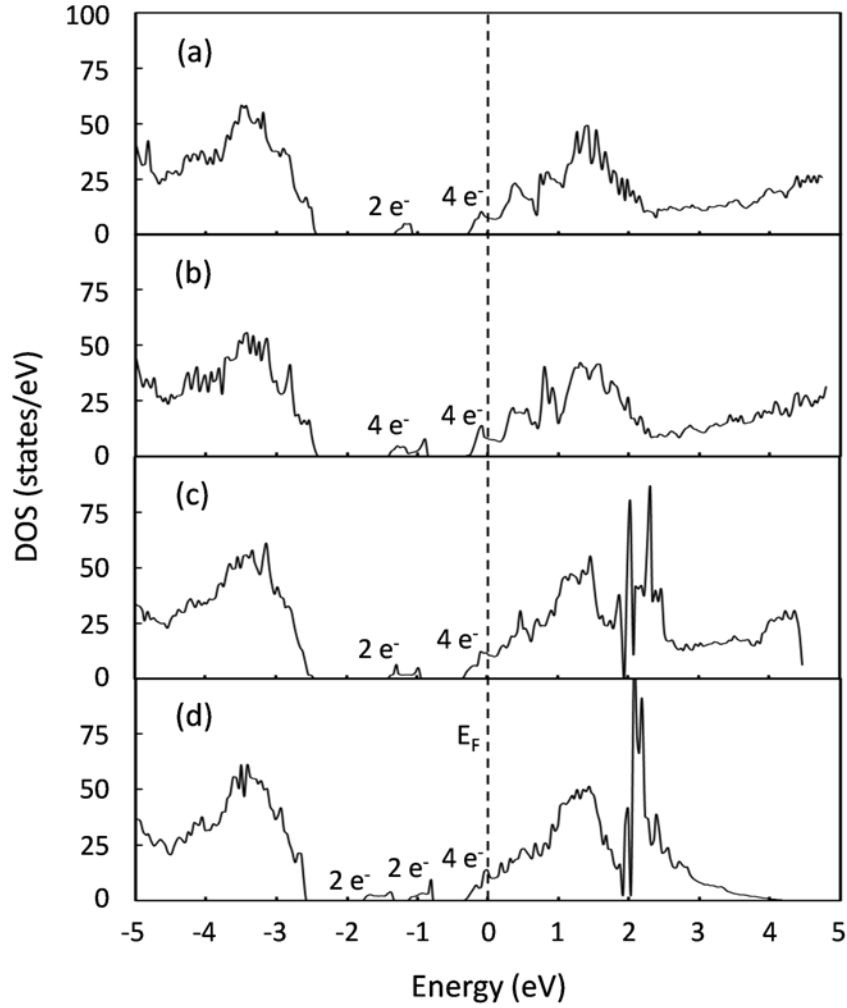
Figure 5.14 Density of states of a) $SrTi_{0.7}Nb_{0.2}Ga_{0.1}O_{2.9}$, b) $SrTi_{0.7}Nb_{0.2}Ga_{0.1}O_{2.85}$, c) $Sr_{0.8}La_{0.2}Ti_{0.9}Ga_{0.1}O_{2.9}$, and d) $Sr_{0.8}La_{0.2}Ti_{0.9}Ga_{0.1}O_{2.85}$. The Fermi energy is set to zero on the energy scale. Numbers of electrons shown in the figure indicate the integrated number of electrons per supercell for the specified DOS area, i.e., states in the band gap and states below the Fermi level.

5.5   Conclusions

In this work, the thermodynamic stability and electronic properties of Ga (p-type) and La (n-type) doped $SrTiO_3$ perovskites have been studied using density functional theory and constrained *ab initio* thermodynamic simulations. The calculations reveal that the cation vacancy compensated 20% La-doped Sr-deficient $SrTiO_3$ transforms to an

electronically compensated phase at high temperature and low oxygen partial pressure which leads to a significant improvement in electronic conductivity. This result is in agreement with the defect chemistry model and experimental observations. Doping 20% La-doped $SrTiO_3$ with 10% Ga enhances the ionic conductivity of the material by creating oxygen vacancies. The electronic conductivity is maintained since the hole doping effect is compensated by the presence of oxygen vacancies so that a mixed ionic/electronic conductor is formed. However, doping with 20% Ga decreases the electronic conductivity of the material. This result supports the experimental observation that doping with a small amount of Ga improves the conductivity and promotes fast reduction of the material. [2, 3] Altering the n-dopant from La (A-site) to Nb (B-site) has only a small effect on the ionic and electronic conductivity of the mixed p- and n-doped material. The conductivity of the La-doped systems is likely reduced due to a higher degree of oxygen vacancy ordering compared to the Nb-doped systems. Independent of doping site, mixed ionic/electronic conductivity can be achieved with a mixed p- and n-doping approach.

5.6   References

[1]   T. Kolodiazhnyi, A. Petric, J. Electroceram. 15 (2005) 5.
[2]   X. Guoliang, X. Dong, K. Huang, F. Chen, Mater. Res. Bull. 46 (2011) 57.
[3]   D. Neagu, J.T.S. Irvine, Chem. Mater. 23 (2011) 1607.
[4]   R.J. Gorte, J.M. Vohs, Current Opinion in Colloid & Interface Science 14 (2009) 236.
[5]   X. Li, H.L. Zhao, F. Gao, N. Chen, N.S. Xu, Electrochem. Commun. 10 (2008) 1567.
[6]   X. Li, H.L. Zhao, N.S. Xu, X. Zhou, C.J. Zhany, N. Chen, Int. J. Hydrogen Energy 34 (2009) 6407.
[7]   G. Kresse, J. Furthmuller, Phys. Rev. B 54 (1996) 11169.
[8]   G. Kresse, D. Joubert, Phys. Rev. B 59 (1999) 1758.
[9]   J.P. Perdew, K. Burke, M. Ernzerhof, Phys. Rev. Lett. 77 (1996) 3865.
[10]   H.J. Monkhorst, J.D. Pack, Phys. Rev. B 13 (1976) 5188.

[11]   S. Suthirakun, S.C. Ammal, G. Xiao, F. Chen, H.C. zur Loye, A. Heyden, Phys. Rev. B 84 (2011).

[12]   K. van Benthem, C. Elsasser, R.H. French, J. Appl. Phys. 90 (2001) 6156.

[13]   J. Robertson, K. Xiong, S.J. Clark, Thin Solid Films 496 (2006) 1.

[14]   C. Zhang, C.L. Wang, J.C. Li, K. Yang, Y.F. Zhang, Q.Z. Wu, Mater. Chem. Phys. 107 (2008) 215.

[15]   G. Hautier, S.P. Ong, A. Jain, C.J. Moore, G. Ceder, Phys. Rev. B 85 (2012) 155208.

[16]   S. Ohta, T. Nomura, H. Ohta, K. Koumoto, J. Appl. Phys. 97 (2005) 034106.

[17]   D. Neagu, J.T.S. Irvine, Chem. Mater. 22 (2010) 5042.

[18]   S.Q. Hui, A. Petric, J. Eur. Ceram. Soc. 22 (2002) 1673.

[19]   K. Kuroda, W. Sugimoto, M. Shirata, M. Takemoto, S. Hayami, Y. Sugahara, Solid State Ionics 108 (1998) 315.

[20]   J.N. Yun, Z.Y. Zhang, J.F. Yan, W. Zhao, J. Appl. Phys. 107 (2010).

CHAPTER 6

RATIONAL DESIGN OF MIXED IONIC AND ELECTRONIC CONDUCTING PEROVSKITE OXIDES FOR SOLID OXIDE FUEL CELL ANODE MATERIALS: A CASE STUDY FOR DOPED STRONTIUM TITANATES

6.1 Summary

The effect of p- and n-type dopants on ionic and electronic conductivity of $SrTiO_3$ based perovskites were investigated both computationally and experimentally. Specifically, we performed density functional theory (DFT) calculations of Na- and La-doped $SrTiO_3$ and Na- and Nb-doped $SrTiO_3$ systems. Constrained *ab initio* thermodynamic calculations were used to evaluate the phase stability and reducibility of doped $SrTiO_3$ under both oxidizing and reducing synthesis conditions, as well as under anodic solid oxide fuel cell (SOFC) conditions. The density of states (DOS) of these materials was analyzed to study the effects of p- and n-doping on the electronic conductivity. Furthermore, Na- and La-doped $SrTiO_3$ and Na- and Nb-doped $SrTiO_3$ samples were experimentally prepared and the conductivity was measured to confirm our computational predictions. The experimental observations are in very good agreement with the theoretical predictions that doping n-doped $SrTiO_3$ with small amounts of p-type dopants promotes both the ionic and electronic conductivity of the material. This doping

strategy is valid independent of p- and n-doping site and permits the synthesis of perovskite based mixed ionic/electronic conductors.

6.2   Introduction

Since the Ni metal in Ni-based electrodes is the component that exhibits instability and low tolerance to sulfur impurities and coking, it has been suggested to remove the Ni metal and use only ceramic components for electron transport and fuel oxidation [1]. Furthermore, to maximize the electrochemically active surface area for fuel oxidation, the anode electrode should consist of only mixed ionic/electronic conducting materials. Among the ceramic anode materials, perovskite based oxides (ABO_3) are of great interest because they can accommodate various dopants and incorporate cations with multiple oxidation states, which permits tuning the electro-catalytic activity and provides a mechanism for tailoring electronic and ionic conductivity [2]. In addition, perovskite oxides have been shown to satisfy most intrinsic SOFC anode requirements such as high thermodynamic stability under anodic conditions [3-9] and strong resistance to carbon deposition [3, 10-12] and sulfur poisoning [13-15].

In Chapter 4 and 5, we have shown that a mixed p- and n-doping approach can be used to improve mixed ionic/electronic conductivity in perovskite oxides. This doping strategy is efficient when doping with p-type dopants at the B-site and n-type dopants at either the A- or B-site of $SrTiO_3$ perovskites [16, 17]. In this Chapter, we used computational and experimental tools to we illustrate that mixed p- and n-doping is indeed an efficient strategy independent of doping site in the $SrTiO_3$ perovskite structure. In particular, we performed constrained *ab initio* thermodynamic calculations to evaluate the thermodynamic stability of Na- and La-doped $SrTiO_3$ and Na- and Nb-doped $SrTiO_3$

117

phases at synthesized under oxidizing and under reducing anodic SOFC conditions. We analyzed the electronic structure of the resulting materials and compared the results to our previous study of Ga- and La-doped $SrTiO_3$ and Ga- and Nb-doped $SrTiO_3$. Finally, we synthesized several compositions of Na- and La-doped $SrTiO_3$ and Na- and Nb-doped $SrTiO_3$ perovskites and measured their conductivities to confirm our computational predictions.

6.3 Methods

6.3.1 Computational approach

To investigate the bulk electronic properties of stoichiometric and doped $SrTiO_3$, we initially optimized the lattice parameter of the $SrTiO_3$ unit cell and created a 100 atom supercell containing twenty unit cells (5×2×2). Doped structures were generated by substituting A- or B-site cations with various amount of n-type (La, Nb) and p-type (Na) dopants. Substitution of two Ti atoms with two dopants yields 10% B-site doped $SrTiO_3$, etc. In order to better understand the charge compensation mechanism in the p- and n-doped systems, both A-site deficient and reduced structures were created by generating Sr vacancies and oxygen vacancies, respectively. In this study, we considered up to two Sr vacancies and three oxygen vacancies in each structure. The reoptimized lattice parameters of the 20% La-doped $SrTiO_3$ and 20% Nb-doped $SrTiO_3$ were employed for all La-doped and Nb-doped structures, respectively. We tried all meaningful configurations (over one hundred configurations were tested in this study) to identify the lowest energy structures.

Spin-polarized density functional theory was employed in this study using the projector-augmented wave approach [18] with Perdew-Burke-Ernzerhof (PBE) functional

[19]. All calculations were performed with the VASP 5.2 code [18, 20]. We use a kinetic energy cutoff of 400 eV for the planewave basis and a 2×5×5 Monkhorst-Pack k-point mesh for Brillouin zone integration [21]. For density of state (DOS) calculations we used a 4×10×10 k-mesh. In all structure optimizations, all atoms are fully relaxed until the Hellman-Feynman forces are less than 0.02 eV Å^{-1}.

6.3.2 Experimental approach

$Sr_{1-x}Na_xTi_{0.8}Nb_{0.2}O_3$ (x = 0, 0.05, 0.10, 0.20) and $Sr_{0.8-x}Na_xLa_{0.2}TiO_3$ (x = 0, 0.10, 0.20) powders were synthesized by standard solid state reactions. The starting materials include $SrCO_3$ (99%), TiO_2 (99.9%), Nb_2O_5 (99.9%, for Nb-doped samples), La_2O_3 (99%, for La-doped samples), and Na_2CO_3 (99%). The chemical constituents were carefully weighed according to the stoichiometry and mixed in a mortar. The mixed powder was calcined at 900 °C for 6 h in air. The powder was then ground, pressed into pellets and calcined at 1250 °C in air for 20 h. This step was repeated to improve the phase purity. The obtained powder was finally pressed into bar samples and sintered in 5% H_2/N_2 at 1400 °C for 10 h.

All samples were characterized by powder X-ray diffraction using a D/MAX-3C X-ray diffractometer with graphite-monochromatized Cu Kα radiation in the 2θ range of 20-80°. Resistance of all bar samples with dimension of 35×5×1 mm^3 was recorded using a multimeter (Keithley model 2001 7-1/2 DDM) in a standard four probe configuration in H_2 with a flow rate of 80 mL/min. The samples were held at each temperature for 1 h before the data was collected.

6.4   Results and Discussion

Previous theoretical studies performed by us [16, 17] suggest that independent of n-doping site, mixed ionic/electronic conductivity of perovskites can be obtained when using a mixed p- and n-doping approach that uses a p-dopant concentration smaller than the n-dopant concentration. In this work, we aim to further prove that this doping strategy can be employed independent of p-doping site. Therefore, we performed DFT calculations of Na- and La-doped $SrTiO_3$ and Na- and Nb-doped $SrTiO_3$. We used the same computational procedure as in our previous studies which permits us to systematically investigate the effects of doping site on the electronic conductivity and reducibility of the resulting structures at synthesized and anodic SOFC conditions. To a first approximation, we expect the electron mobility to remain constant when changing n-type dopants in doped $SrTiO_3$ since the difference in electron mobility between Nb- and La-doped $SrTiO_3$ is insignificant [22].

We first investigated the relative thermodynamic stability of all doped structures in each system using constrained *ab initio* thermodynamic simulations. The phase diagrams were constructed by calculating the free energy of different systems as a function of oxygen chemical potential, i.e., temperature and oxygen partial pressure. We neglect entropic contributions from the solids to the free energy differences and note that a reasonable estimate of the error in the calculated phase diagram is 0.2 eV considering that phonon contributions and configurational entropy likely only change on the order of 0.1 to 0.2 eV [23-25]. The reaction energies of the most dominant structures in the phase diagrams are summarized in Table 6.1. Next, the DOS related to the most dominant

structures in the phase diagram were evaluated and analyzed with respect to relative electronic conductivity.

Table 6.1 Summary of reaction energies used in constrained *ab initio* thermodynamic calculations.

Phase diagram	Reaction	ΔE (eV)
10% Na and 20% Nb-doped $SrTiO_3$ with SrO rich second phase	$Sr_{18}Na_2Ti_{16}Nb_4O_{60} + 1/2O_2 \rightarrow Sr_{17}Na_2Ti_{16}Nb_4O_{60} + SrO$	-2.08
	$Sr_{18}Na_2Ti_{16}Nb_4O_{60} \rightarrow Sr_{18}Na_2Ti_{16}Nb_4O_{59} + 1/2O_2$	4.84
	$Sr_{18}Na_2Ti_{16}Nb_4O_{60} \rightarrow Sr_{18}Na_2Ti_{16}Nb_4O_{58} + O_2$	10.00
	$Sr_{18}Na_2Ti_{16}Nb_4O_{60} \rightarrow Sr_{18}Na_2Ti_{16}Nb_4O_{57} + 3/2O_2$	15.36
10% Na and 20% Nb-doped $SrTiO_3$ with TiO_2/Na_2O/Nb_2O_5 rich second phases	$17Sr_{16}Na_2Ti_{16}Nb_4O_{60} \rightarrow 16Sr_{17}Na_2Ti_{16}Nb_4O_{60} + 16TiO_2 + 2Nb_2O_5 + Na_2O + 17/2O_2$	-1.53
	$9Sr_{16}Na_2Ti_{16}Nb_4O_{60} \rightarrow 8Sr_{18}Na_2Ti_{16}Nb_4O_{60} + 16TiO_2 + 2Nb_2O_5 + Na_2O + 17/2O_2$	1.51
	$9Sr_{16}Na_2Ti_{16}Nb_4O_{60} \rightarrow 8Sr_{18}Na_2Ti_{16}Nb_4O_{59} + 16TiO_2 + 2Nb_2O_5 + Na_2O + 25/2O_2$	5.81
	$9Sr_{16}Na_2Ti_{16}Nb_4O_{60} \rightarrow 8Sr_{18}Na_2Ti_{16}Nb_4O_{58} + 16TiO_2 + 2Nb_2O_5 + Na_2O + 33/2O_2$	10.40
	$9Sr_{16}Na_2Ti_{16}Nb_4O_{60} \rightarrow 8Sr_{18}Na_2Ti_{16}Nb_4O_{57} + 16TiO_2 + 2Nb_2O_5 + Na_2O + 41/2O_2$	15.17
20% Na and 20% Nb-doped $SrTiO_3$	$Sr_{16}Na_4Ti_{16}Nb_4O_{60} \rightarrow Sr_{16}Na_4Ti_{16}Nb_4O_{59} + 1/2O_2$	4.06
	$Sr_{16}Na_4Ti_{16}Nb_4O_{60} \rightarrow Sr_{16}Na_4Ti_{16}Nb_4O_{58} + O_2$	9.07
	$Sr_{16}Na_4Ti_{16}Nb_4O_{60} \rightarrow Sr_{16}Na_4Ti_{16}Nb_4O_{57} + 3/2O_2$	14.26
10% Na and 20% La-doped $SrTiO_3$ with SrO rich second phase	$Sr_{14}La_4Na_2Ti_{20}O_{60} + 1/2O_2 \rightarrow Sr_{13}La_4Na_2Ti_{20}O_{60} + SrO$	-1.46
	$Sr_{14}La_4Na_2Ti_{20}O_{60} \rightarrow Sr_{14}La_4Na_2Ti_{20}O_{58} + O_2$	10.03
	$Sr_{14}La_4Na_2Ti_{20}O_{60} \rightarrow Sr_{14}La_4Na_2Ti_{20}O_{57} + 3/2O_2$	15.39
10% Na and 20% La-doped $SrTiO_3$ with TiO_2/Na_2O/La_2O_3 rich second phases	$13Sr_{12}La_4Na_2Ti_{20}O_{60} \rightarrow 12Sr_{13}La_4Na_2Ti_{20}O_{60} + 20TiO_2 + 2La_2O_3 + Na_2O + 13/2O_2$	0.57
	$7Sr_{12}La_4Na_2Ti_{20}O_{60} \rightarrow 6Sr_{14}La_4Na_2Ti_{20}O_{60} + 20TiO_2 + 2La_2O_3 + Na_2O + 13/2O_2$	4.68
	$7Sr_{12}La_4Na_2Ti_{20}O_{60} \rightarrow 6Sr_{14}La_4Na_2Ti_{20}O_{58} + 20TiO_2 + 2La_2O_3 + Na_2O + 25/2O_2$	13.46
	$7Sr_{12}La_4Na_2Ti_{20}O_{60} \rightarrow 6Sr_{14}La_4Na_2Ti_{20}O_{57} + 20TiO_2 + 2La_2O_3 + Na_2O + 31/2O_2$	18.15
20% Na and 20% La-doped $SrTiO_3$	$Sr_{12}La_4Na_4Ti_{20}O_{60} \rightarrow Sr_{12}La_4Na_4Ti_{20}O_{59} + 1/2O_2$	4.46
	$Sr_{12}La_4Na_4Ti_{20}O_{60} \rightarrow Sr_{12}La_4Na_4Ti_{20}O_{58} + O_2$	9.43
	$Sr_{12}La_4Na_4Ti_{20}O_{60} \rightarrow Sr_{12}La_4Na_4Ti_{20}O_{57} + 3/2O_2$	14.54

6.4.1   Electronic structures and phase diagrams of 10% Na- and 20% La-doped SrTiO$_3$.

To obtain a model of 10% Na- and 20% La-doped SrTiO$_3$, we first replaced four Sr atoms with four La atoms in the 5×2×2 supercell to create a structure of 20% La-doped SrTiO$_3$. Next, we substituted another two Sr atoms with two Na atoms to generate a 10% Na- and 20% La-doped SrTiO$_3$ model. Furthermore, we removed one or two Sr atoms to create partial (5%) A-site deficient and full (10%) A-site deficient model structures, respectively. From the configuration of the most stable structures, we conclude that there is no long-range site preference for any Sr cation substitution with La or Na atoms since the energy differences of the most stable structures are insignificant (lower than 2 meV/atom). Only in the Sr-deficient structures do La atoms prefer to be close to Sr vacancies since the charge of the La dopants can be compensated by the presence of Sr vacancies. In an environment of low oxygen chemical potential (anodic SOFC conditions), the materials are reduced and oxygen vacancies start to form. We find that under these reducing conditions there is a tendency for oxygen vacancies to cluster close to nearby Na atoms. The extra electrons from the oxygen vacancies can be partially compensated by the holes created by the Na atoms in the structure. The configurations of all most stable structures are shown in Fig. 6.1
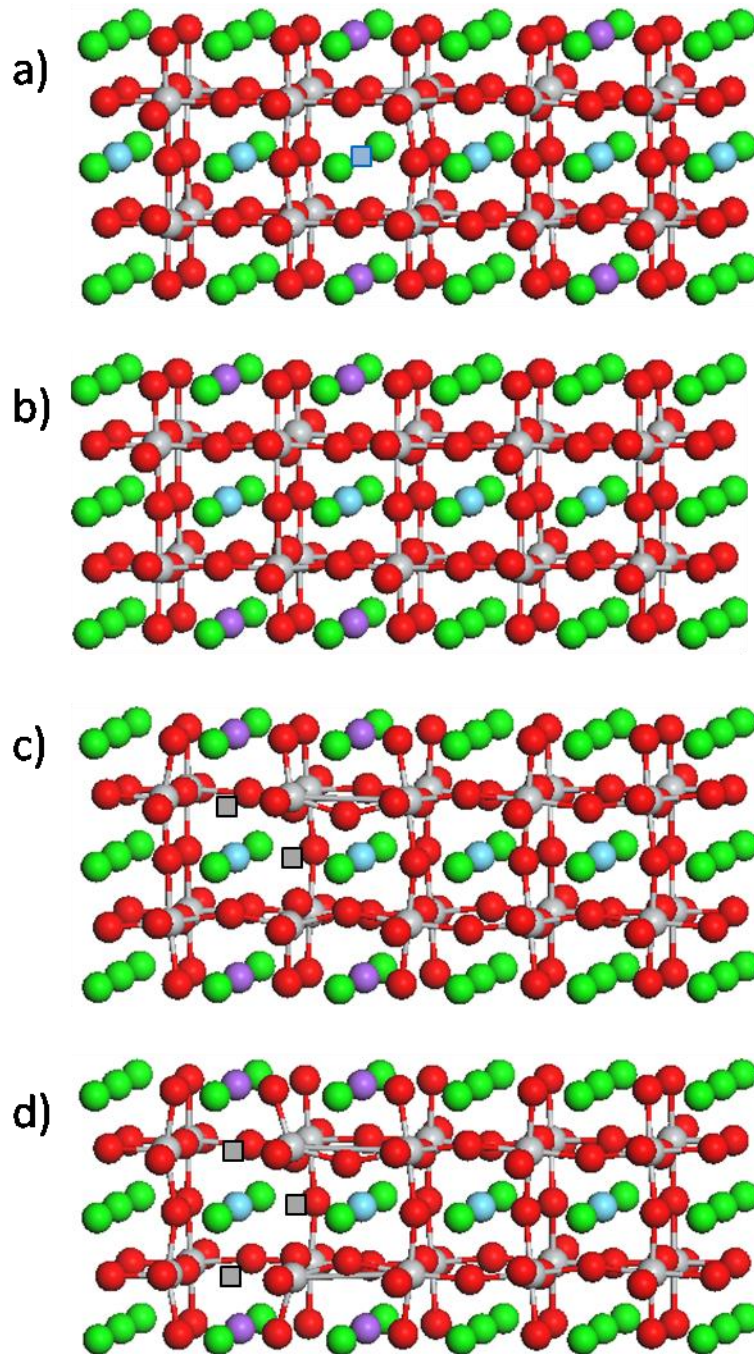
Figure 6.1 Most stable structures of 10% Na- and 20% La-doped $SrTiO_3$: a) $Sr_{0.65}La_{0.2}Na_{0.1}O_3$, b) $Sr_{0.7}La_{0.2}Na_{0.1}O_3$, c) $Sr_{0.7}La_{0.2}Na_{0.1}O_{2.9}$, and d) $Sr_{0.7}La_{0.2}Na_{0.1}O_{2.85}$. Green, gray, blue, purple and red spheres represent Sr, Ti, La, Na and O atoms, respectively. Blue and gray squares represent the position of a Sr and O vacancy, respectively.

Constrained *ab initio* thermodynamic calculations were performed to determine the approximate phase stability and reducibility of these structures at various temperatures and oxygen partial pressures. We employed two different types of calculations based on the main products that were generated upon the phase transition, i.e., a SrO rich second phase or $TiO_2/Na_2O/La_2O_3$ rich second phases. The details of these calculations can be found in our previous publication [16, 17]. As shown in Fig. 6.2, the calculated phase diagrams of 10% Na- and 20% La-doped $SrTiO_3$ with SrO rich second phase and $TiO_2/Na_2O/La_2O_3$ rich second phases illustrate a phase transformation from 5% Sr-deficient structure to non Sr-deficient phase with increasing temperature and decreasing oxygen partial pressure. Further reduced structures are formed at high temperature and low oxygen partial pressure typical of SOFCs. The existence of a reduced structure indicates that Na-doping improves the reducibility of the material since in the absence of Na dopants only very few oxygen vacancies are observed [16].

The electronic conductivity of the most dominant structures in the phase diagram can to a first approximation be analyzed from their electronic structures. In particular, we performed DOS calculations and calculated the number of charge carriers per supercell to determine the degree of electronic conduction of the material. As illustrated in Fig. 6.3(a), the DOS of a 5% Sr-deficient phase exhibits insulating behavior since the charges from the four La dopants of the supercell are compensated by the presence of a Sr vacancy and electron holes generated from two Na dopants. A dramatic improvement in electronic conductivity is observed when the material is reduced. The DOS of the reduced structures exhibit metallic character as the Fermi energy shifts inside the conduction band with up to six electrons per supercell in the conduction band below the Fermi energy.

124
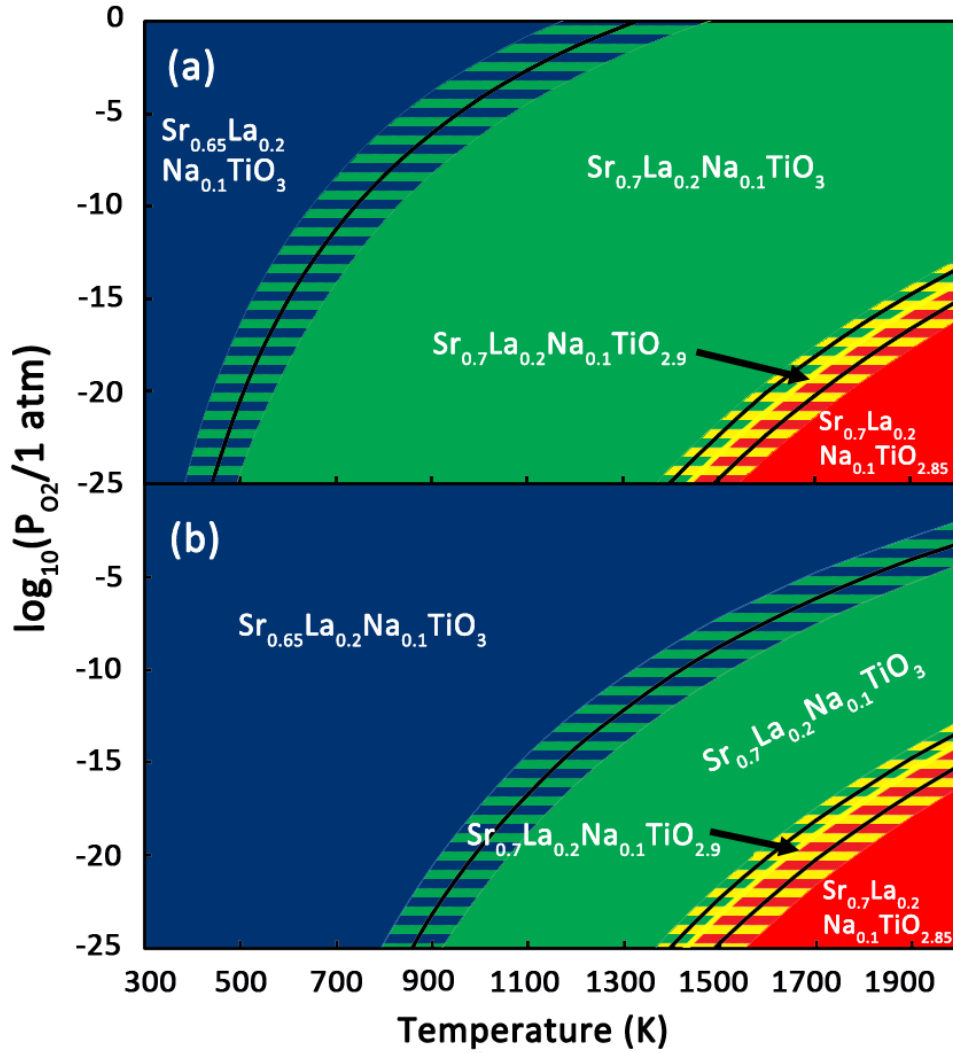
Figure 6.2 Calculated phase diagram of 10% Na- and 20% La-doped $SrTiO_3$ with a) SrO rich phase and b) $TiO_2/La_2O_3/Na_2O$ rich phases. Differently shaded areas mark the stability region of various structures for a given temperature and partial pressure of oxygen. The hatched areas describe possible changes in the phase diagram if computed reaction energies shown in Table 6.1 are off by ±0.2 eV (estimated error bar). Dark blue, green, yellow and red areas symbolize the stability of $Sr_{0.65}La_{0.2}Na_{0.1}TiO_3$, $Sr_{0.7}La_{0.2}Na_{0.1}TiO_3$, $Sr_{0.7}La_{0.2}Na_{0.1}TiO_{2.9}$, and $Sr_{0.7}La_{0.2}Na_{0.1}TiO_{2.85}$, respectively.

Furthermore, partial density of states (PDOS) analyses were performed to evaluate the behavior of the electrons below the Fermi level in the conduction band and in the gap state. As reported in our previous studies, electrons in the gap state are mostly localized around the oxygen vacancies and thus do not contribute to the electronic conductivity of the material [16, 17]. More interestingly, we observe that not all electrons below the Fermi energy in the conduction band are conductive. Figure 6.4 depicts the PDOS and their respective charge densies obtained from band decomposition charge density calculations of $Sr_{0.7}La_{0.2}Na_{0.1}TiO_{2.9}$. It can be seen that the electrons act differently in the two different energy regions. In the lower energy range (-0.3 to -0.2 eV), the electrons are mostly localized around oxygen vacancies and surrounded atoms whereas the electrons in the higher energy range (-0.2 to 0 eV) are delocalized throughout the Ti atoms in the lattice. These localized electrons in the low energy region do not contribute to the electronic conductivity of the material and therefore, we do not take these electrons into account when we calculate the number of charge carriers. Hence, the exact number of charge carriers can be calculated by considering only the states on the Ti atoms and the calculated number of charge carriers for the $Sr_{0.7}La_{0.2}Na_{0.1}TiO_{2.9}$ and $Sr_{0.7}La_{0.2}Na_{0.1}TiO_{2.85}$ structures are 4.03 and 4.35, respectively. The calculated number of charge carriers for all p- and n-doped $SrTiO_3$ structures considered in this work are summarized in Table 6.2.
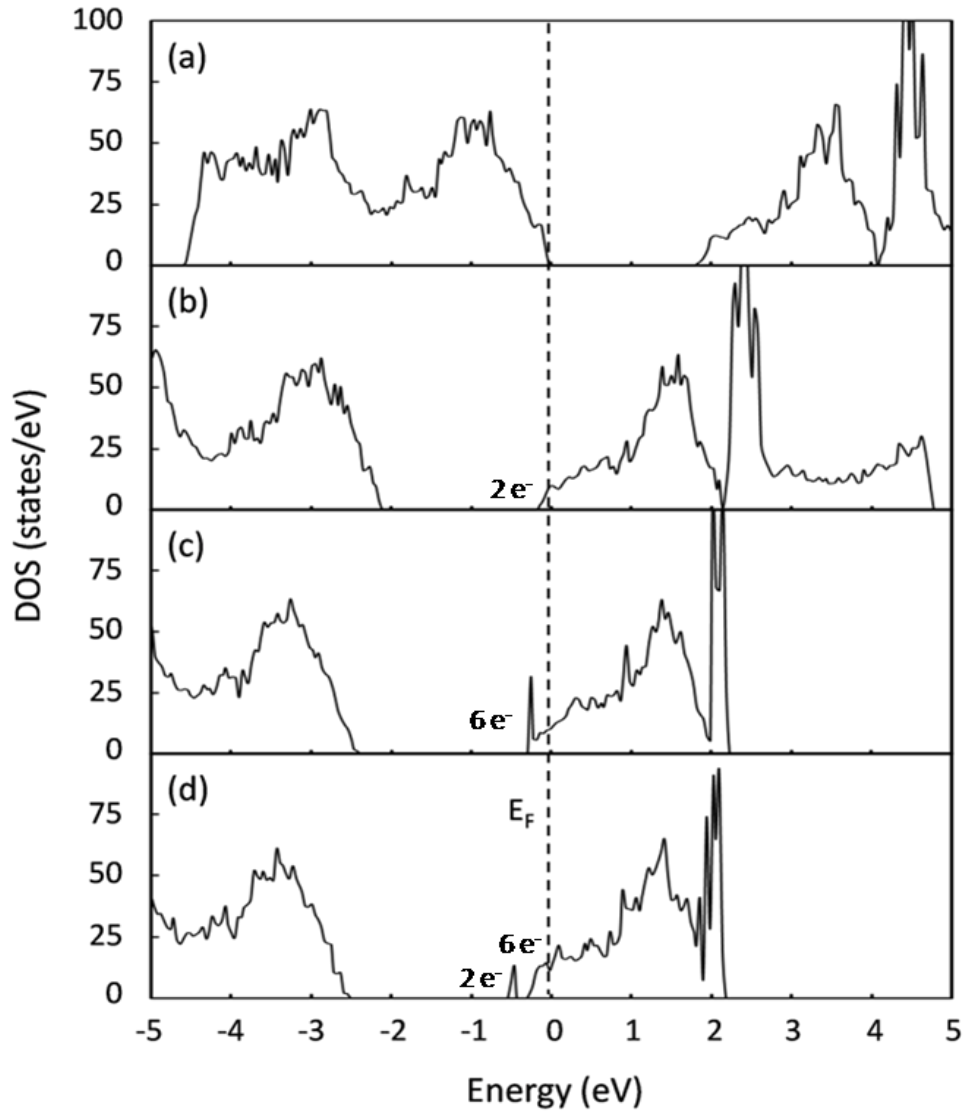
Figure 6.3 Density of states of a) $Sr_{0.65}La_{0.2}Na_{0.1}TiO_3$, b) $Sr_{0.7}La_{0.2}Na_{0.1}TiO_3$, c) $Sr_{0.7}La_{0.2}Na_{0.1}TiO_{2.9}$, and d) $Sr_{0.7}La_{0.2}Na_{0.1}TiO_{2.85}$. The Fermi level is set to zero on the energy scale. Numbers of electrons shown in the figure indicate that integrated number of electrons per supercell for the specified DOS area, i.e., states in the band gap and states below the Fermi level.

Figure 6.4 Partial density of states of $Sr_{0.7}La_{0.2}Na_{0.1}TiO_{2.9}$ below the Fermi level in the conduction band. The left inset illustrates the charge density of the localized states which are located at the oxygen vacancy (energy ranges between -0.3 and -0.2 eV). The right inset describes the charge density of delocalized states from mixed-valent Ti^{3+}/Ti^{4+} found in the energy range between -0.2 to 0 eV.

6.4.2 Electronic structures and phase diagrams of 20% Na- and 20% La-doped SrTiO$_3$.

Substitution of four Sr atoms with four Na atoms in 20% La-doped structures leads to 20% Na- and 20% La-doped SrTiO$_3$. The presence of Sr and oxygen vacancies in the structure was investigated in a similar manner as described above. The most dominant structures display a random configuration of La and Na atoms since the energy difference of the lowest energy structures is insignificant (lower than 2 meV/atom). On the other hand, the most stable reduced structures have oxygen vacancies surrounded by the four Na atoms of the supercell (see supporting information for structures). Such preferred configurations confirm that the charge compensation mechanism plays an essential role

in the arrangement of impurities in the structure. The structures found most stable of 20% Na- and 20% La-doped $SrTiO_3$ are illustrated in Fig. 6.5
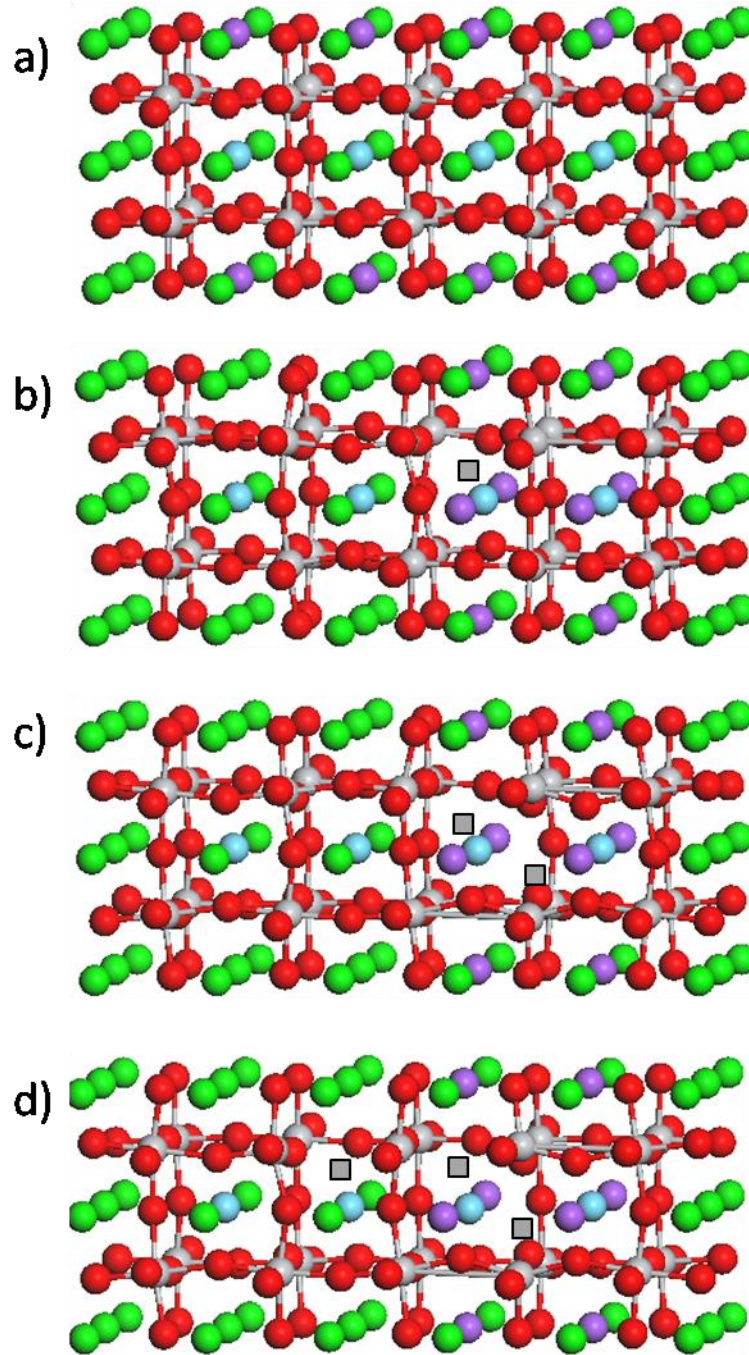
Figure 6.5 Most stable structures of 20% Na- and 20% La-doped $SrTiO_3$: a) $Sr_{0.6}La_{0.2}Na_{0.2}TiO_3$, b) $Sr_{0.6}La_{0.2}Na_{0.2}TiO_{2.95}$, c) $Sr_{0.6}La_{0.2}Na_{0.2}TiO_{2.9}$, and d) $Sr_{0.6}La_{0.2}Na_{0.2}TiO_{2.85}$. Green, gray, blue, purple, and red spheres represent Sr, Ti, La, Na, and O atoms, respectively. A gray square represents the position of an O vacancy.

Table 6.2 Summary of integrated number of electrons below the Fermi level in the conduction band computed from partial density of states (PDOS) of various p- and n-doped $SrTiO_3$ structures. Mobile charge carriers are assumed to originate only from Ti and Nb.

Structure	Integrated number of electrons below Fermi level in conduction band (#/supercell)					Number of mobile charge carriers (#/supercell)
	Sr	Ti	O	Nb/La	Ga/Na	
20% Nb-doped $SrTiO_3$	0.17	2.62	0.15	0.48	-	3.10
10% Ga- and 20% Nb-doped $SrTiO_3$						
$SrTi_{0.7}Nb_{0.2}Ga_{0.1}O_{2.95}$	0.14	2.56	0.18	0.51	0.00	3.08
$SrTi_{0.7}Nb_{0.2}Ga_{0.1}O_{2.90}$	0.16	2.59	0.18	0.55	0.00	3.14
$SrTi_{0.7}Nb_{0.2}Ga_{0.1}O_{2.85}$	0.16	2.61	0.18	0.54	0.00	3.14
20% Ga- and 20% Nb-doped $SrTiO_3$						
$SrTi_{0.6}Nb_{0.2}Ga_{0.2}O_{2.95}$	0.08	1.24	0.13	0.25	0.00	1.50
$SrTi_{0.6}Nb_{0.2}Ga_{0.2}O_{2.90}$	0.09	1.26	0.13	0.24	0.00	1.49
$SrTi_{0.6}Nb_{0.2}Ga_{0.2}O_{2.85}$	0.09	1.26	0.13	0.23	0.00	1.50
10% Na- and 20% Nb-doped $SrTiO_3$						
$Sr_{0.9}Na_{0.1}Ti_{0.8}Nb_{0.2}O_{2.95}$	0.14	2.69	0.19	0.68	0.00	3.37
$Sr_{0.9}Na_{0.1}Ti_{0.8}Nb_{0.2}O_{2.90}$	0.15	2.69	0.19	0.68	0.00	3.38
$Sr_{0.9}Na_{0.1}Ti_{0.8}Nb_{0.2}O_{2.85}$	0.37	3.56	0.32	0.71	0.00	4.27
20% Na- and 20% Nb-doped $SrTiO_3$						
$Sr_{0.8}Na_{0.2}Ti_{0.8}Nb_{0.2}O_{2.95}$	0.07	1.26	0.07	0.30	0.00	1.56
$Sr_{0.8}Na_{0.2}Ti_{0.8}Nb_{0.2}O_{2.90}$	0.13	2.56	0.17	0.55	0.00	3.10
$Sr_{0.8}Na_{0.2}Ti_{0.8}Nb_{0.2}O_{2.85}$	0.13	2.56	0.17	0.54	0.00	3.11
20% La-doped $SrTiO_3$	0.14	3.15	0.14	0.02	-	3.15
10% Ga- and 20% La-doped $SrTiO_3$						
$Sr_{0.8}La_{0.2}Ti_{0.9}Ga_{0.1}O_{2.90}$	0.13	3.14	0.17	0.02	0.00	3.14
$Sr_{0.8}La_{0.2}Ti_{0.9}Ga_{0.1}O_{2.85}$	0.13	3.15	0.16	0.02	0.00	3.15
20% Ga- and 20% La-doped $SrTiO_3$						
$Sr_{0.8}La_{0.2}Ti_{0.8}Ga_{0.2}O_{2.90}$	0.06	1.81	0.10	0.01	0.00	1.81
$Sr_{0.8}La_{0.2}Ti_{0.8}Ga_{0.2}O_{2.85}$	0.23	1.84	0.54	0.04	0.37	1.84
10% Na- and 20% La-doped $SrTiO_3$						
$Sr_{0.7}La_{0.2}Na_{0.1}TiO_{2.90}$	0.28	4.03	0.33	0.07	0.00	4.03
$Sr_{0.7}La_{0.2}Na_{0.1}TiO_{2.85}$	0.21	4.35	0.29	0.05	0.00	4.35
20% Na- and 20% La-doped $SrTiO_3$						
$Sr_{0.6}La_{0.2}Na_{0.2}TiO_{2.95}$	0.05	1.61	0.07	0.01	0.00	1.61
$Sr_{0.6}La_{0.2}Na_{0.2}TiO_{2.90}$	0.09	2.90	0.20	0.03	0.00	2.90
$Sr_{0.6}La_{0.2}Na_{0.2}TiO_{2.85}$	0.11	3.00	0.18	0.03	0.00	3.00

The calculated phase diagram of this system obtained from constrained *ab initio* thermodynamic simulations is illustrated in Fig. 6.6. Since the Sr-deficient structures are not stable in this system, there are no SrO or $TiO_2/Na_2O/La_2O_3$ rich second phases. Interestingly, increasing the Na content from 10% to 20% in 20% La-doped $SrTiO_3$ does not lead to a significant improvement of the reducibility of the material. Moreover, the number of charge carriers obtained from DOS and PDOS analyses reveal that increasing the amount of Na dopants leads to a reduction in the electronic conductivity. As shown in Fig. 6.7, the states below the Fermi level in the conduction band of the reduced structures contain up to four electrons and PDOS analyses show that the exact number of delocalized electrons are 1.61, 2.90, and 3.00 per supercell for $Sr_{0.6}La_{0.2}Na_{0.2}TiO_{2.95}$, $Sr_{0.6}La_{0.2}Na_{0.2}TiO_{2.90}$, and $Sr_{0.6}La_{0.2}Na_{0.2}TiO_{2.85}$, respectively (see also Table 6.2). Thus, while doping with 20% Na improves the ionic conductivity (though not significantly more than 10% Na doping), the electronic conductivity is likely diminished under realistic fuel cell operating conditions.
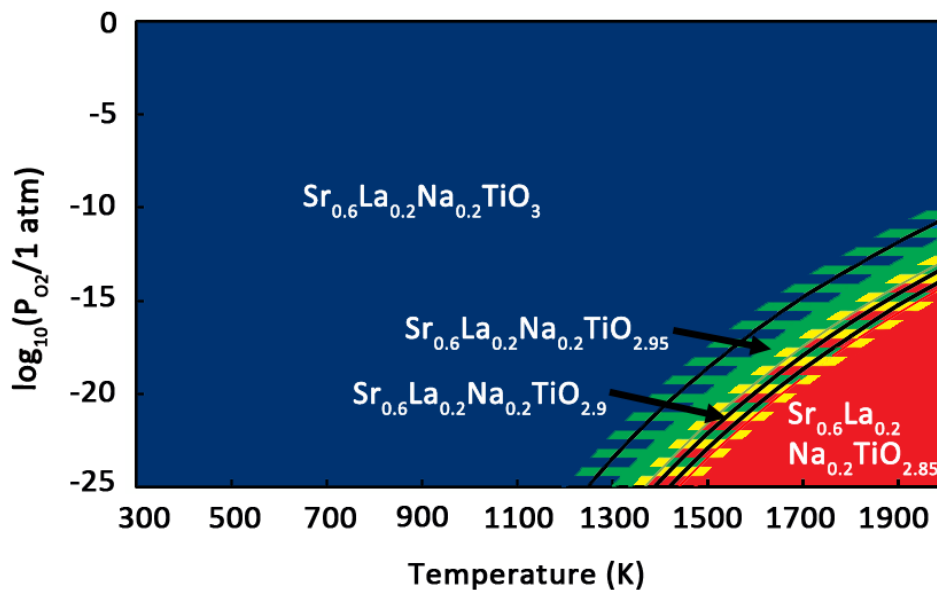
Figure 6.6 Calculated phase diagram of 20% Na- and 20% La-doped SrTiO₃. Differently shaded areas mark the stability region of various structures for a given temperature and partial pressure of oxygen. The hatched areas describe possible changes in the phase diagram if computed reaction energies shown in Table 6.1 are off by ±0.2 eV (estimated error bar). Dark blue, green, yellow, and red areas symbolize the stability of Sr₀.₆La₀.₂Na₀.₂TiO₃, Sr₀.₆La₀.₂Na₀.₂TiO₂.₉₅, Sr₀.₆La₀.₂Na₀.₂TiO₂.₉, and Sr₀.₆La₀.₂Na₀.₂TiO₂.₈₅, respectively.
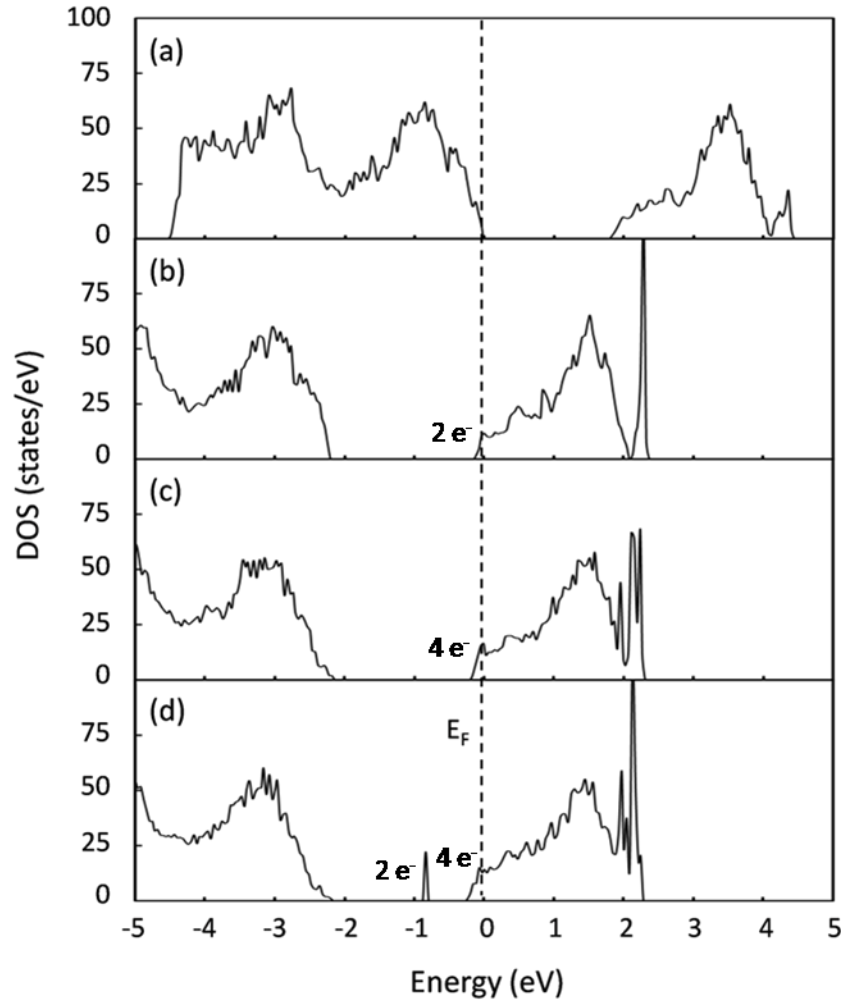
Figure 6.7 Density of states of a) $Sr_{0.6}La_{0.2}Na_{0.2}TiO_3$, b) $Sr_{0.6}La_{0.2}Na_{0.2}TiO_{2.95}$, c) $Sr_{0.6}La_{0.2}Na_{0.2}TiO_{2.9}$, and d) $Sr_{0.6}La_{0.2}Na_{0.2}TiO_{2.85}$. The Fermi level is set to zero on the energy scale. Numbers of electrons shown in the figure indicate the integrated number of electrons per supercell for the specified DOS area, i.e., states in the band gap and states below the Fermi level.

6.4.3   Electronic structures and phase diagrams of 10% Na- and 20% Nb-

doped $SrTiO_3$.

In this set of calculations, we first created a 20% Nb-doped $SrTiO_3$ structure by

replacing four Ti atoms with four Nb atoms in the 5×2×2 supercell. Next, we substituted

two Sr atoms with two Na atoms in the 20% Nb-doped $SrTiO_3$ structure to obtain a model

of 10% Na- and 20% Nb-doped $SrTiO_3$. To study the cation vacancy compensation mechanism, we created up to two Sr vacancies in the lattice to obtain Sr-deficient structures as described previously. As shown in Fig. 6.8, the most stable structures reveal that Nb and Na impurities prefer to be in close proximity since the extra electron from the Nb dopants can be compensated by the electron holes generated from the Na dopants. This preferred configuration is also observed in the presence of Sr vacancies. Up to three oxygen vacancies were generated in the structure to study the effect of a reducing environment typical of anodic SOFC conditions. The most stable first vacancy is created by removing an oxygen atom from a Ti-O-Ti bridge close to Na dopants whereas the second oxygen vacancy is positioned next to the same Ti atom. Upon removal of the third oxygen, a row of oxygen vacancies is formed along the TiO_6 octahedra framework.

Figure 6.9 displays the calculated phase diagrams of 10% Na- and 20% Nb-doped $SrTiO_3$ under synthesized and anodic SOFC conditions leading to the formation of a SrO rich second phase (Fig. 7(a)) and $TiO_2/Nb_2O_5/NaO$ rich second phases (Fig 7(b)). It can be seen from the phase diagrams that the phase transitions of this system are very similar to those of the 10% Na- and 20% La-doped system, i.e., the presence of 5% Sr-deficient, non Sr-deficient, and reduced phases of both systems occur at approximately the same temperature and oxygen partial pressure. Again, the presence of the reduced phases in this system confirms that Na facilitates oxide ion conduction as the reducibility of the material has been improved. The electronic structures of the reduced phases exhibit up to six electrons per supercell below the Fermi energy in the conduction band. As shown in Fig. 6.10, the DOS of 10% Na- and 20% Nb-doped $SrTiO_3$ reveal that the electronic conductivity is remarkably improved when the material is reduced under anodic SOFC

conditions. The electronic conductivity of these reduced structures are comparable to those of 10% Na- and 20% La-doped $SrTiO_3$ since the number of conduction electrons are up to 4.27 per supercell (Table 6.2). It is noteworthy that mixed valent $Nb^{4+/5+}$ can also play a role in the electron conduction process and contributes to the electronic conductivity of the material; therefore, electronic states on both Ti and Nb atoms are taken into account when calculating the number of charge carriers.
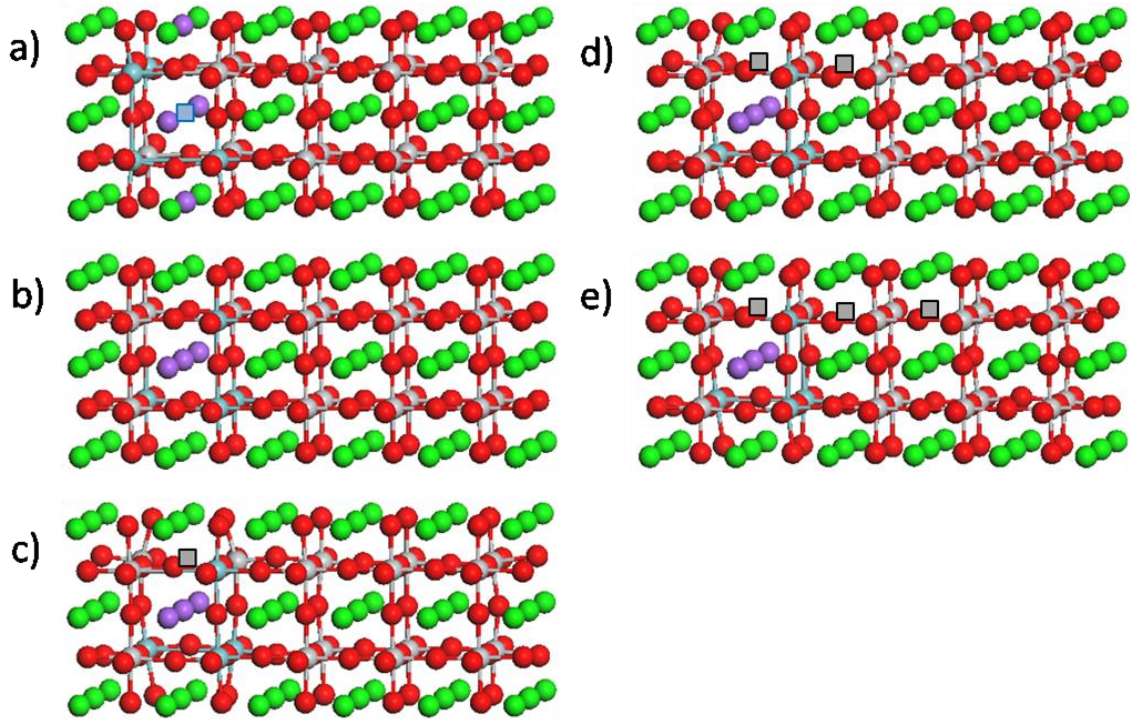
Figure 6.8 Most stable structures of 10% Na- and 20% Nb-doped $SrTiO_3$: a) $Sr_{0.85}Na_{0.1}Ti_{0.8}Nb_{0.2}O_3$, b) $Sr_{0.9}Na_{0.1}Ti_{0.8}Nb_{0.2}O_3$, c) $Sr_{0.9}Na_{0.1}Ti_{0.8}Nb_{0.2}O_{2.95}$, d) $Sr_{0.9}Na_{0.1}Ti_{0.8}Nb_{0.2}O_{2.90}$ and e) $Sr_{0.9}Na_{0.1}Ti_{0.8}Nb_{0.2}O_{2.85}$. Green, gray, blue, purple and red spheres represent Sr, Ti, Nb, Na and O atoms, respectively. Blue and gray squares represent the position of a Sr and O vacancy, respectively.
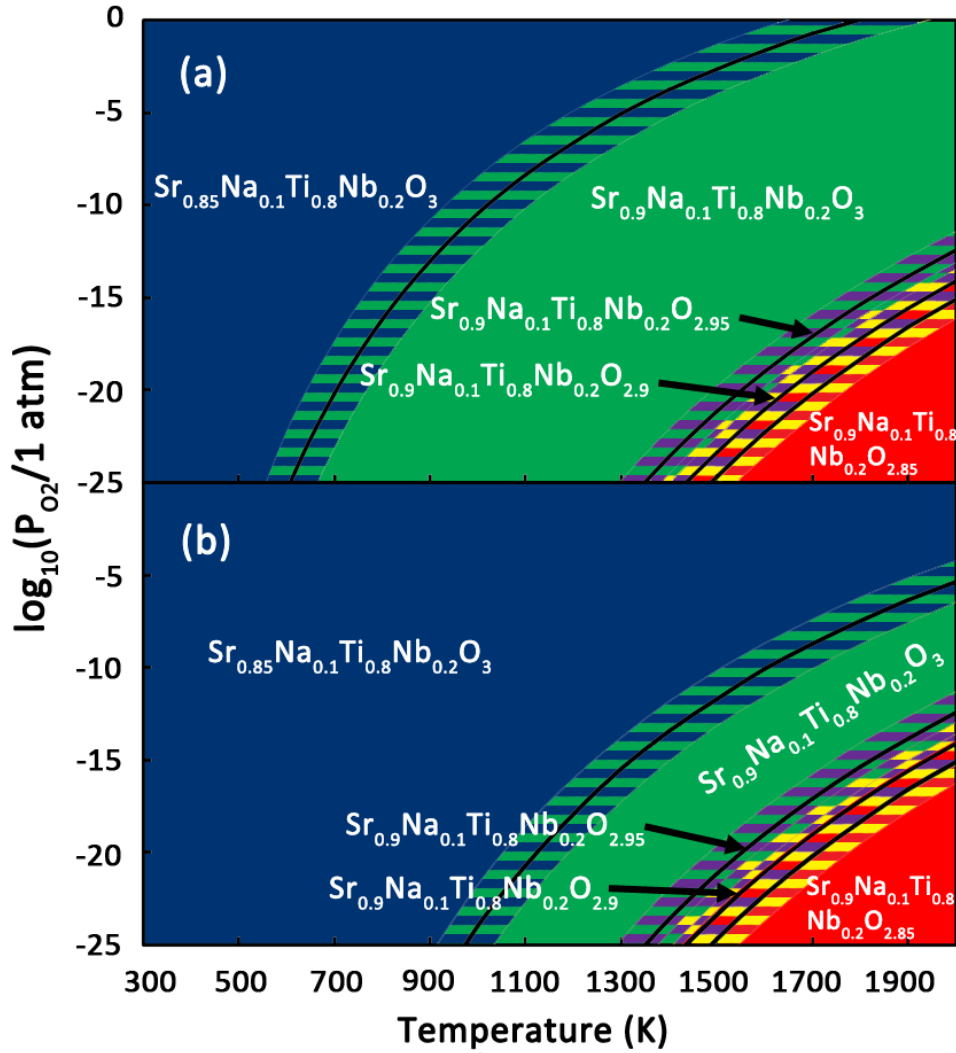
Figure 6.9 Calculated phase diagram of 10% Na- and 20% Nb-doped SrTiO$_3$ with a) SrO rich phase and b) TiO$_2$/NbO$_2$/Na$_2$O rich phases. Differently shaded areas mark the stability region of various structures for a given temperature and partial pressure of oxygen. The hatched areas describe possible changes in the phase diagram if computed reaction energies shown in Table 6.1 are off by ±0.2 eV (estimated error bar). Dark blue, green, purple, yellow and red areas symbolize the stability of Sr$_{0.85}$Na$_{0.1}$Ti$_{0.8}$Nb$_{0.2}$O$_3$, Sr$_{0.9}$Na$_{0.1}$Ti$_{0.8}$Nb$_{0.2}$O$_3$, Sr$_{0.9}$Na$_{0.1}$Ti$_{0.8}$Nb$_{0.2}$O$_{2.95,}$ Sr$_{0.9}$Na$_{0.1}$Ti$_{0.8}$Nb$_{0.2}$O$_{2.9,}$ and Sr$_{0.9}$Na$_{0.1}$Ti$_{0.8}$Nb$_{0.2}$O$_{2.85}$, respectively.
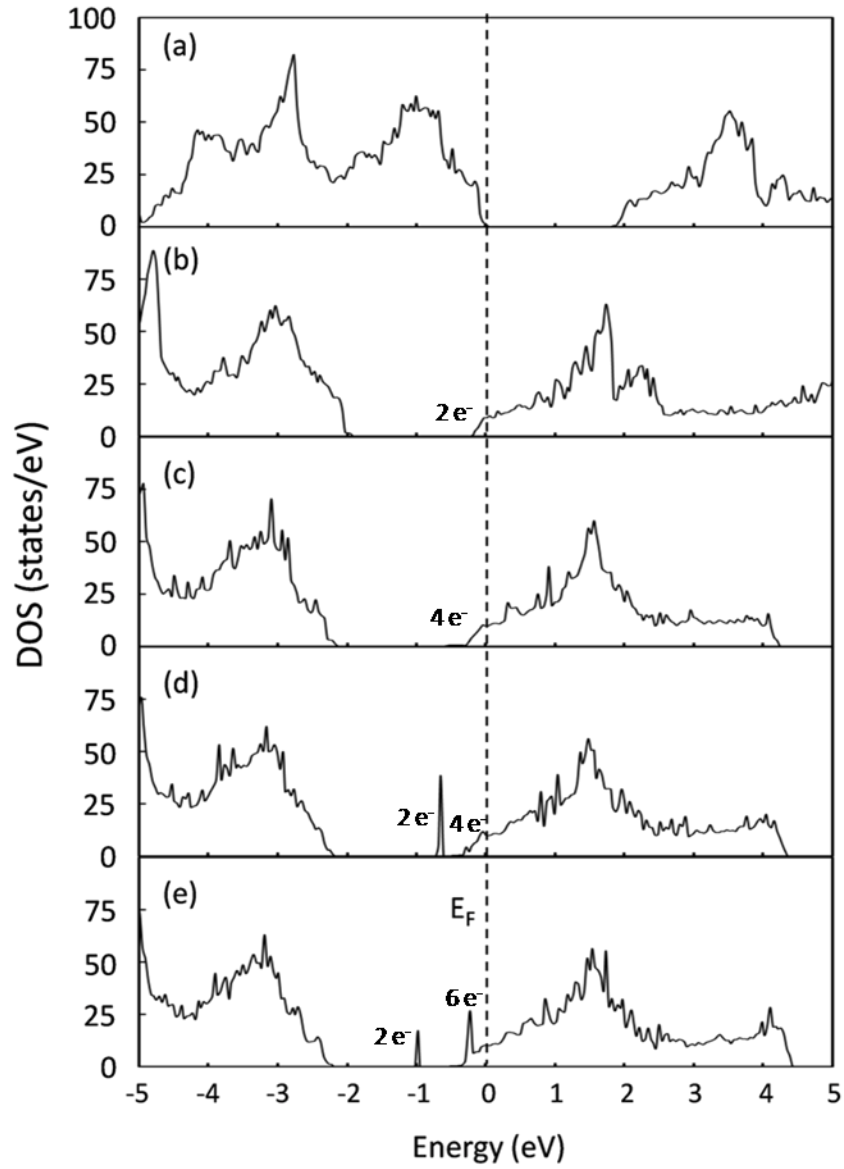
Figure 6.10 Density of states of a) $Sr_{0.85}Na_{0.1}Ti_{0.8}Nb_{0.2}O_3$, b) $Sr_{0.9}Na_{0.1}Ti_{0.8}Nb_{0.2}O_3$, c) $Sr_{0.9}Na_{0.1}Ti_{0.8}Nb_{0.2}O_{2.95}$, d) $Sr_{0.9}Na_{0.1}Ti_{0.8}Nb_{0.2}O_{2.90}$ and e) $Sr_{0.9}Na_{0.1}Ti_{0.8}Nb_{0.2}O_{2.85}$. The Fermi level is set to zero on the energy scale. Numbers of electrons shown in the figure indicate the integrated number of electrons per supercell for the specified DOS area, i.e., states in the band gap and states below the Fermi level.
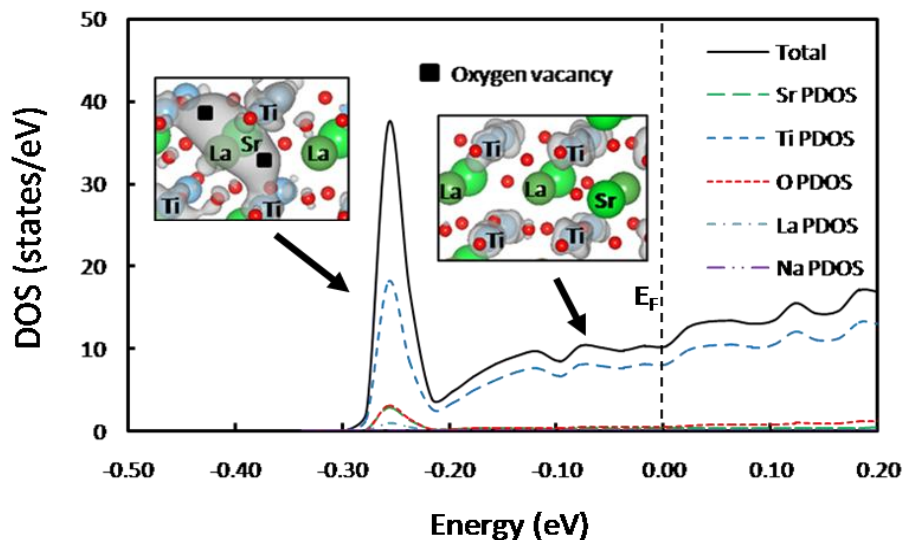
137

6.4.4   Electronic structures and phase diagrams of 20% Na- and 20% Nb-doped SrTiO$_3$.

Substitution of four Sr atoms with four Na atoms in the 20% Nb-doped SrTiO$_3$ structure yields a model of 20% Na- and 20% Nb-doped SrTiO$_3$. Sr-deficient and reduced structures were created to investigate the charge compensation mechanism in the presence of Sr vacancies and oxygen vacancies. The most stable structures (Fig. 6.11) in this set of calculations have Na atoms close to Nb atoms. Again, it is preferable to create the first and second oxygen vacancies at the Ti-O-Ti bridge where two oxygen vacancies share the same Ti atom forming a TiO$_4$ unit, whereas the third oxygen vacancy is positioned at another Ti-O-Ti bridge nearby generating a TiO$_5$ unit. These three oxygen vacancies are close to the Na atoms, which confirms that electrons from oxygen vacancies are partially compensated by holes generated from the Na dopants.

Figure 6.12 illustrates the phase diagram for 20% Na- and 20% Nb-doped SrTiO$_3$ as a function of temperature and oxygen partial pressure. Unlike Na- and La-doped SrTiO$_3$, increasing the Na concentration in this system does improve the reducibility of the material. As seen in the phase diagram, at an oxygen partial pressure of 10^{-20} atm the reduced phases of 20% Na- and 20% Nb-doped SrTiO$_3$ start to develop 200 K below when those are formed for the 10% Na-doped system. However, adding too much Na results in a decreasing electronic conductivity. The DOS of the reduced structures of this system (Fig. 6.13) exhibit states below the Fermi level in the conduction band that contain up to four electrons per supercell. Nevertheless, PDOS calculations show that the degree of electronic conductivity of this system is generally lower than that of the 10%

Na-doped system (Table 6.2). The concentration of conduction electrons in the lattice is reduced by the large amounts of electron holes from the Na dopants.
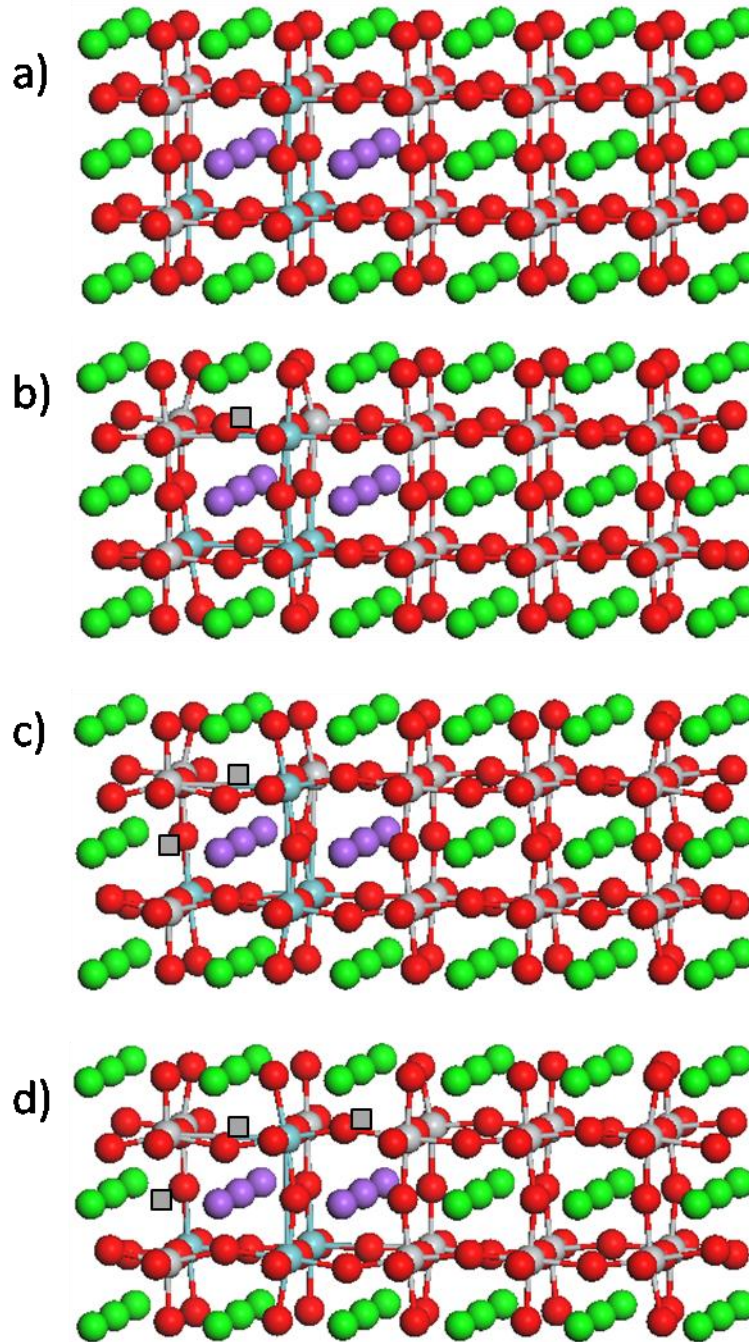
Figure 6.11 Most stable structures of 20% Na- and 20% Nb-doped $SrTiO_3$: a) $Sr_{0.8}Na_{0.2}Ti_{0.8}Nb_{0.2}O_3$, b) $Sr_{0.8}Na_{0.2}Ti_{0.8}Nb_{0.2}O_{2.95}$, c) $Sr_{0.8}Na_{0.2}Ti_{0.8}Nb_{0.2}O_{2.9}$, and d) $Sr_{0.8}Na_{0.2}Ti_{0.8}Nb_{0.2}O_{2.85}$. Green, gray, blue, purple and red spheres represent Sr, Ti, Nb, Na and O atoms, respectively. A gray square represent the position of an O vacancy.
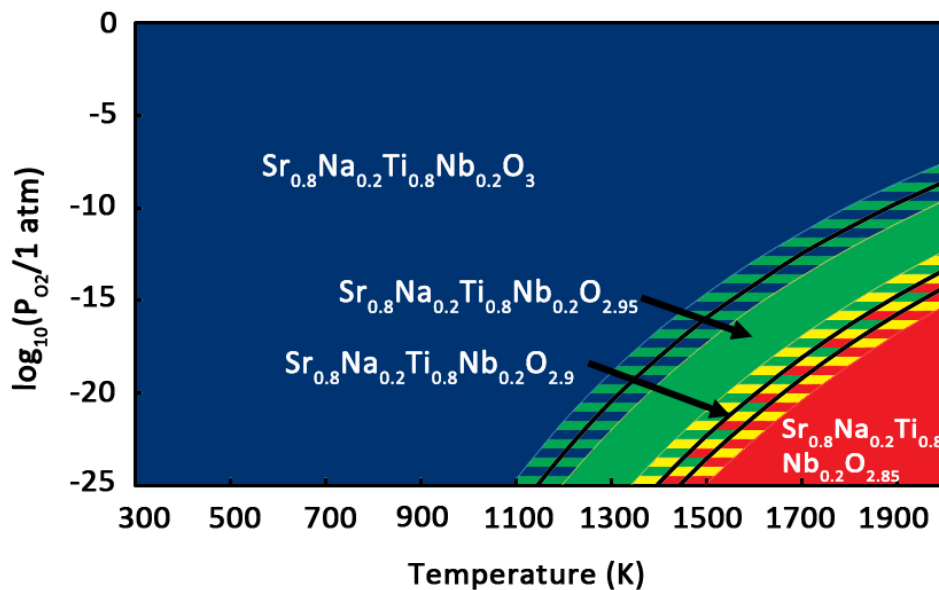
Figure 6.12 Calculated phase diagram of 20% Na- and 20% Nb-doped SrTiO₃. Differently shaded areas mark the stability region of various structures for a given temperature and partial pressure of oxygen. The hatched areas describe possible changes in the phase diagram if computed reaction energies shown in Table 6.1 are off by ± 0.2 eV (estimated error bar). Dark blue, green, yellow, and red areas symbolize the stability of $Sr_{0.8}Na_{0.2}Ti_{0.8}Nb_{0.2}O_3$, $Sr_{0.8}Na_{0.2}Ti_{0.8}Nb_{0.2}O_{2.95}$, $Sr_{0.8}Na_{0.2}Ti_{0.8}Nb_{0.2}O_{2.9}$, and $Sr_{0.8}Na_{0.2}Ti_{0.8}Nb_{0.2}O_{2.85}$, respectively.

6.4.5 Experimental verification of computational predictions

To study the effect of p-doping on the mixed ionic/electronic conductivity and to confirm our computational predictions, Na- and Nb-doped SrTiO₃ and Na- and La-doped SrTiO₃ samples were prepared at 1250 $^{\circ}$C in air and reduced in 5% H₂/N₂ at 1400 $^{\circ}$C. Powder X-ray diffraction (PXRD) patterns of $Sr_{1-x}Na_xTi_{0.8}Nb_{0.2}O_3$ (where x = 0, 0.05, 0.10, 0.20) and $Sr_{0.8-x}Na_xLa_{0.2}Ti_{0.8}Nb_{0.2}O_3$ (where x = 0, 0.10, 0.20) calcined under oxidizing conditions are depicted in Fig. 6.14(a) and 6.14(b), respectively. The presence of impurity peaks for all samples other than $Sr_{0.8}Na_{0.2}Ti_{0.8}Nb_{0.2}O_3$ indicates that due to a lack of charge compensation, these compositions cannot form under oxidizing conditions

where titanium and niobium are in their highest oxidation states. Since the extra charges

from the n-type dopants (Nb or La) cannot be electronically compensated under oxidizing
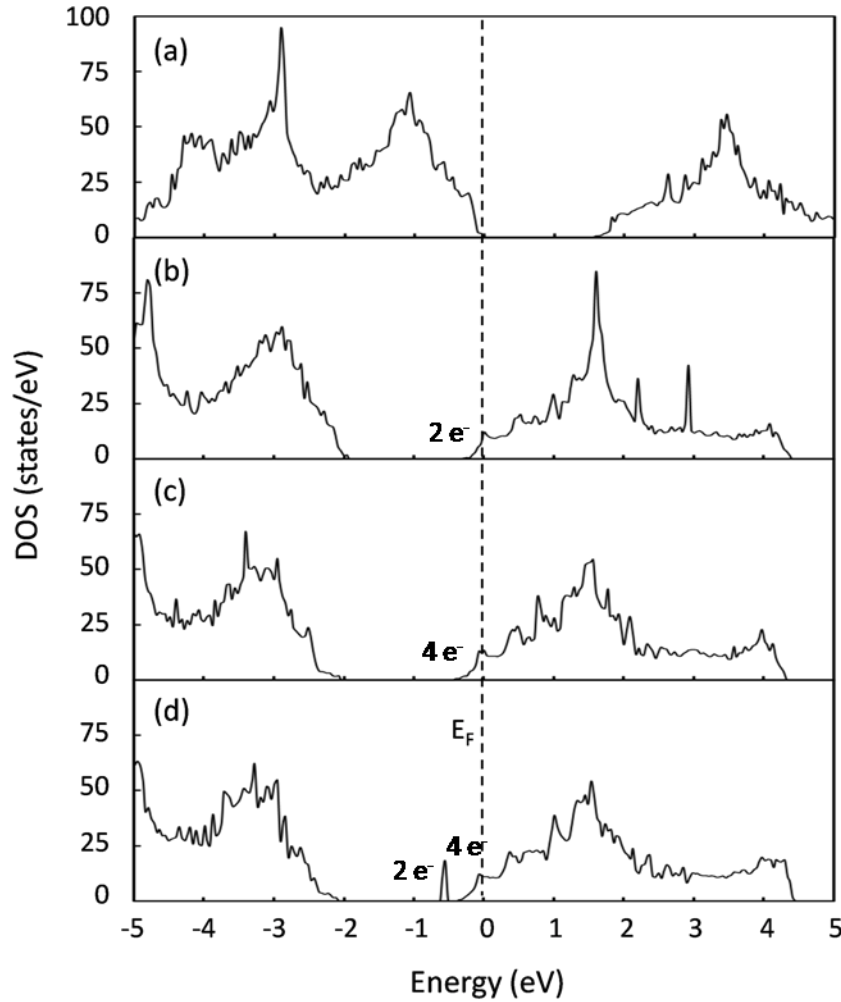
Figure 6.13 Density of states of a) $Sr_{0.8}Na_{0.2}Ti_{0.8}Nb_{0.2}O_3$, b) $Sr_{0.8}Na_{0.2}Ti_{0.8}Nb_{0.2}O_{2.95}$, c) $Sr_{0.8}Na_{0.2}Ti_{0.8}Nb_{0.2}O_{2.9}$, and d) $Sr_{0.8}Na_{0.2}Ti_{0.8}Nb_{0.2}O_{2.85}$. The Fermi level is set to zero on the energy scale. Numbers of electrons shown in the figure indicate the integrated number of electrons per supercell for the specified DOS area, i.e., states below the Fermi level.

conditions, these extra electrons are instead neutralized by creating Sr vacancies in the

lattice (cation vacancy compensation), which creates Sr rich impurity phases. The main

impurity phase in Fig. 6.14(a) can be attributed to $Sr_5Nb_4O_{15}$ (JCPDS file no. 48-0421).

In La-doped SrTiO$_3$, it has been reported that under oxidizing conditions the extra oxygen can be accommodated by La$_2$Ti$_2$O$_7$-type layers. No cation vacancy is required in this mechanism. At low doping concentrations, for example 20% in our work, the impurity peaks in XRD are less evident [26]. Increasing the concentration of Na (p-type) dopants leads eventually to charge compensation and stable phases since now the extra electrons from the n-type dopants are compensated by electron holes generated from the Na dopants. In agreement with this observation, it has been reported that p-type doping significantly promotes oxygen loss from the structure and enhances oxygen diffusion in the materials [27, 28]. These experimental findings are in an excellent agreement with our theoretical predictions, suggesting that p-doping (Na or Ga) improves the reducibility of the materials [28].

To perform conductivity measurements, all samples were pressed into bar samples and sintered in reducing atmosphere at 1400 ^{o}C. The conductivities of the doped SrTiO$_3$ samples were then measured under reducing conditions. We find that p-type doping allows not only for the formation of a stable, reduced phase, but also enhances the electrical conductivity of the samples. Figure 6.15 illustrates the electrical conductivity of Na- and Nb-doped SrTiO$_3$ as a function of Na concentration at different temperatures. In a reducing atmosphere at high temperatures, Na- and Nb-doped SrTiO$_3$ samples exhibit metallic behavior as their conductivity decreases when the temperature increases. The conductivity shows a maximum at 5% Na concentration and decreases abruptly when increasing the doping concentration to 10% and 20%. At high Na concentration the conduction electrons from the Nb dopants seem to be mostly compensated by the hole doping effect of Na leading to a reduction in the electronic conductivity, in excellent

qualitative agreement with our calculations that doping with only small amounts of Na

significantly improves the electronic conductivity since a small concentration of electron

holes can be compensated by the presence of oxygen vacancies in the lattice.
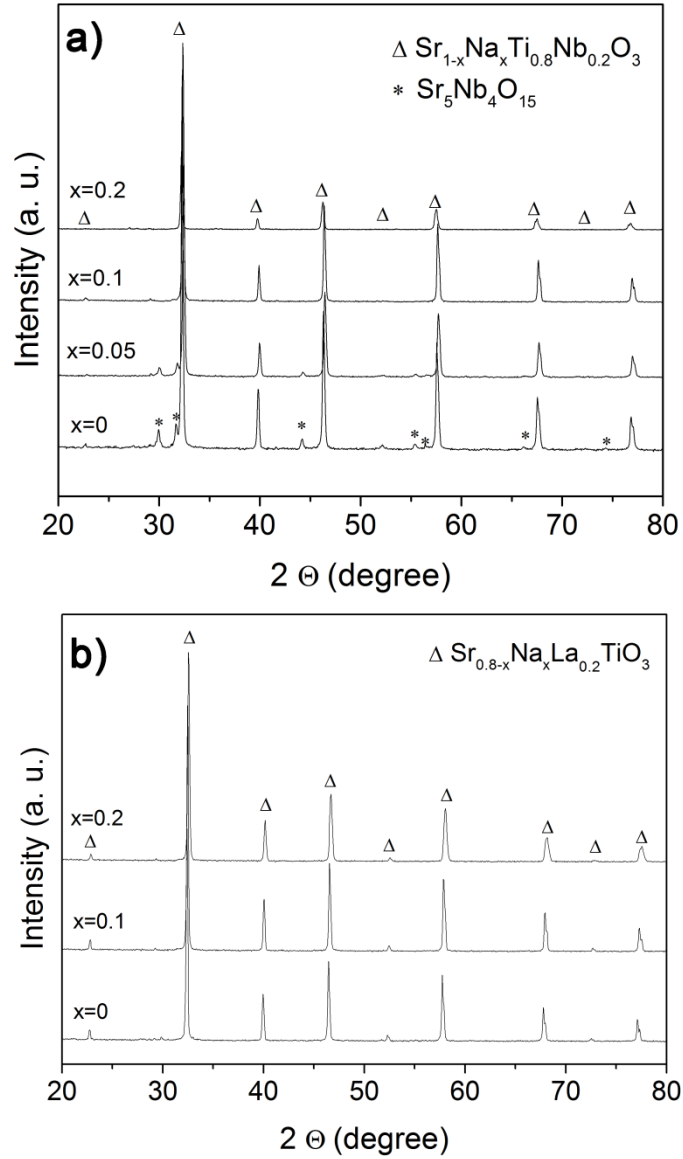
Figure 6.14 XRD pattern of a) $Sr_{1-x}Na_xTi_{0.8}Nb_{0.2}O_3$ powder and b) $Sr_{0.8-x}Na_xLa_{0.2}TiO_3$ powder after solid state reactions at 1250 ^{o}C in air.

It is interesting to note that stoichiometric and A-site deficient 20% La-doped $SrTiO_3$ samples do not exhibit metallic behavior as expected. Instead, these samples show semiconducting behavior with low conductivity as shown in Fig. 6.15. We believe this behavior can be explained by the poor phase stability of the La-doped $SrTiO_3$ samples [26] which leads to the low incorporation of La in the samples even when these samples were exposed to a reducing atmosphere at high temperatures. Since the concentration of conduction electrons depends strongly on the level of La dopants in the lattice, the samples with low La concentration exhibit a small concentration of conduction electrons. According to Mott's theory [26, 29], a transition from semiconducting to metallic behavior may occur if the concentration of conduction electrons exceeds a critical value. In this particular case, the number of conduction electrons that 20% La-doped $SrTiO_3$ samples possess may not surpass this value and we observe semiconducting behavior and low conductivity for these samples. This semiconducting behavior has also been reported in Y-doped $SrTiO_3$ systems [26].

We want to emphasize that Na-doping improves the formation, reducibility, and mixed ionic/electronic conductivity of the materials. Figure 6.16 shows that doping 20% La-doped $SrTiO_3$ with small amounts of Na remarkably increases the conductivity of the materials. The improvement in conductivity originates from the improved reducibility and increased number of charge carriers (as discussed above) of the Na-doped materials. Note that small amounts of Na do not diminish the electronic conductivity of the materials since the hole doping effect from Na dopants is compensated by the presence of oxygen vacancies in the material.
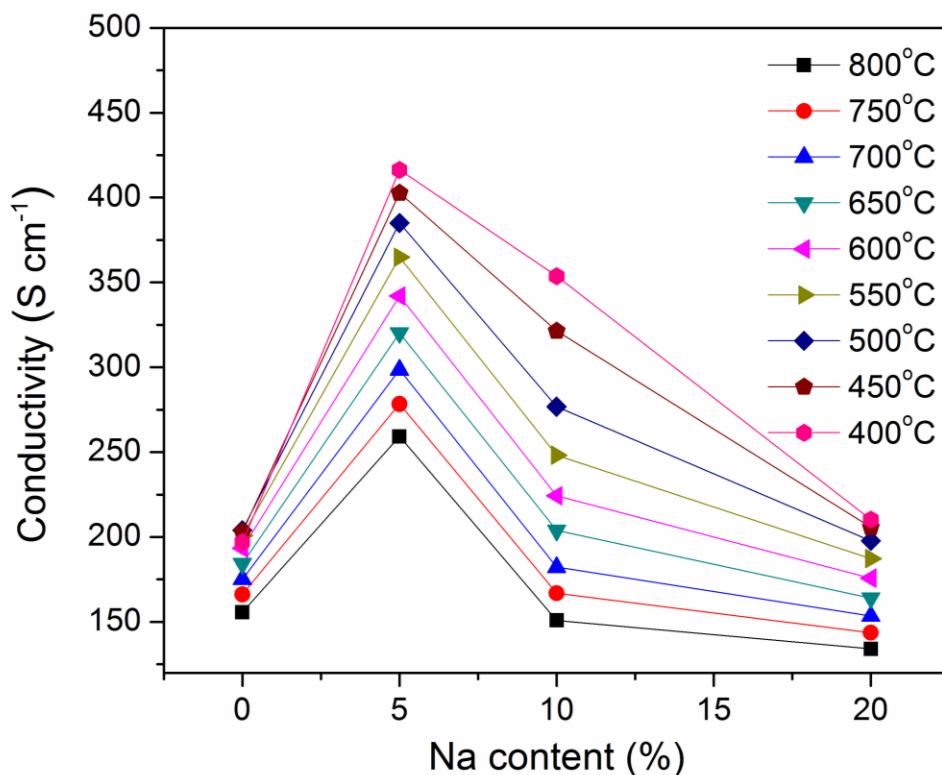
Figure 6.15 Electrical conductivity of $Sr_{1-x}Na_xTi_{0.8}Nb_{0.2}O_3$ samples sintered in 5% H_2/N_2 ($pO_2\sim10^{-22}$ bar at 800^oC) at 1400^oC as a function of temperature and Na content. The conductivity was measured in H_2 with a flow rate of 80 ml min^{-1} ($pO_2\sim10^{-26}$ bar at 800^oC).

Furthermore, the number of oxygen vacancies produced in the lattice could support oxide ion conductivity of the material. As a result, the materials become mixed ionic/electronic conductors. However, as predicted above adding too much Na diminishes the electronic conductivity because the concentration of charge carriers in the lattice is reduced by the effects of electron-hole compensation due to the large amount of Na dopants in the materials. As can be seen from Fig. 6.16, the conductivity drops by a half when increasing the concentration of Na from 10% to 20%. Moreover, using Na as a p-type dopant in p- and n-doped $SrTiO_3$ results in a higher conductivity than using Ga [16, 17]. As shown in Table 6.2, the calculated number of charge carriers in Na- and n- (La or

145

Nb) doped $SrTiO_3$ perovskites are generally higher than those of Ga- and n- (La or Nb) doped $SrTiO_3$ perovskites. The computational predictions are in excellent agreement with the experimental results [27, 28].

To conclude, p- (Na or Ga) and n- (La or Nb) doped $SrTiO_3$ perovskites are promising mixed ionic/electronic conductors. Computations predict that doping n-doped $SrTiO_3$ with small amounts of p-type dopants significantly improves the ionic and electronic conductivity. Experimental observations confirm that introducing small amounts of p-type dopants into the lattice promotes reducibility and conductivity; however, the introduction of too large amounts of p-type dopants in an n-doped material reduces the electronic conductivity.
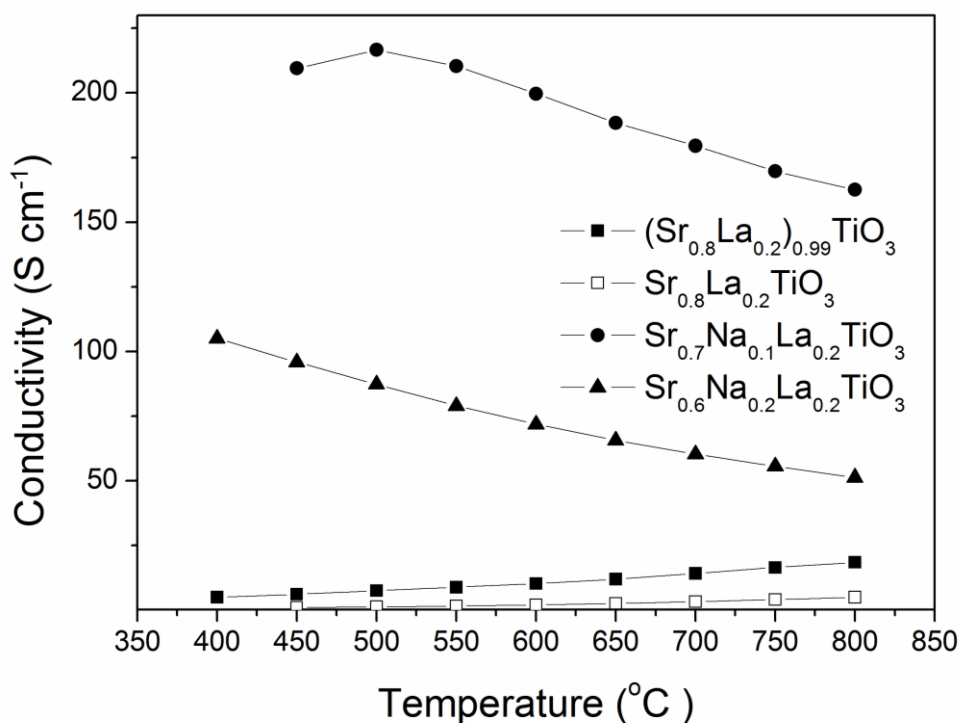
Figure 6.16 Temperature dependence of the conductivity of $Sr_{0.8-x}Na_xLa_{0.2}TiO_3$ samples sintered in 5% H_2/N_2 at 1400^oC. The conductivity was measured in H_2 with a flow rate of 80 ml min^{-1}.

6.5   Conclusions

We utilized computational and experimental tools to develop a mixed p- and n-type doping strategy to obtain mixed ionic/electronic conductivity in $SrTiO_3$ based perovskite oxides. First, we performed DFT calculations of various Na- and Nb-doped $SrTiO_3$ and Na- and La-doped $SrTiO_3$ systems. In particular, we performed constrained *ab initio* thermodynamic simulations to determine the phase stability and reducibility of doped $SrTiO_3$ under synthesized and anodic SOFC conditions. Then, we analyzed the DOS of the most dominant structures in the phase diagrams to compute the number of charge carriers per supercell. The calculations reveal that doping 20% n- (La or Nb) doped $SrTiO_3$ with small amounts of Na (e.g. 10%) enhances the ionic conductivity of the material by creating oxygen vacancies. The electronic conductivity is improved since the hole doping effect is compensated by the presence of oxygen vacancies such that a mixed ionic/electronic conductor is formed. However, increasing the Na concentration further (e.g. 20%) diminishes the electronic conductivity of the material because the concentration of conduction electrons is reduced by excessive electron holes from the Na dopants. These theoretical predictions are confirmed by experimental observations. Experimentally, we find that introducing small amounts of Na in n-doped $SrTiO_3$ dramatically enhances the total conductivity. In addition to the reasons suggested theoretically, we also observe an improved stability of the materials. From computational predictions and experimental observations we confirm that a mixed p- and n-doping approach is an efficient doping strategy to obtain mixed ionic/electronic conductivity in perovskite oxides; which could be one of the reasons why a large number of elements can be found in most high performance perovskite electrodes for SOFCs. We note that this

doping approach is valid independent of p- and n-doping site since either altering the n-type dopant from La (A-site) to Nb (B-site) or changing the p-type dopant from Ga (B-site) to Na (A-site) does not significantly affect the ionic and electronic conductivity of the doped material.

6.6   References

[1]   R.J. Gorte, J.M. Vohs, Current Opinion in Colloid & Interface Science 14 (2009) 236.
[2]   D. Neagu, J.T.S. Irvine, Chem. Mater. 22 (2010) 5042.
[3]   S.W. Tao, J.T.S. Irvine, Nature Materials 2 (2003) 320.
[4]   Y.H. Huang, R.I. Dass, Z.L. Xing, J.B. Goodenough, Science 312 (2006) 254.
[5]   D.P. Fagg, V.V. Kharton, A.V. Kovalevsky, A.P. Viskup, E.N. Naumovich, J.R. Frade, J. Eur. Ceram. Soc. 21 (2001) 1831.
[6]   S.Q. Hui, A. Petric, J. Eur. Ceram. Soc. 22 (2002) 1673.
[7]   T. Ishihara, H. Matsuda, Y. Takita, J. Am. Chem. Soc. 116 (1994) 3801.
[8]   M. Feng, J.B. Goodenough, Eur. J. Solid State Inorg. Chem. 31 (1994) 663.
[9]   K.Q. Huang, M. Feng, J.B. Goodenough, M. Schmerling, J. Electrochem. Soc. 143 (1996) 3630.
[10]   Y.B. Lin, Z.L. Zhan, S.A. Barnett, J. Power Sources 158 (2006) 1313.
[11]   A. Sin, E. Kopnin, Y. Dubitsky, A. Zaopo, A.S. Arico, L.R. Gullo, D. La Rosa, V. Antonucci, J. Power Sources 145 (2005) 68.
[12]   P. Vernoux, E. Djurado, M. Guillodo, J. Am. Ceram. Soc. 84 (2001) 2289.
[13]   J. Canales-Vazquez, S.W. Tao, J.T.S. Irvine, Solid State Ionics 159 (2003) 159.
[14]   O.A. Marina, N.L. Canfield, J.W. Stevenson, Solid State Ionics 149 (2002) 21.
[15]   J. Canales-Vazquez, J.C. Ruiz-Morales, J.T.S. Irvine, W.Z. Zhou, J. Electrochem. Soc. 152 (2005) A1458.
[16]   S. Suthirakun, S.C. Ammal, G.L. Xiao, F.L. Chen, K.V. Huang, H.C. zur Loye, A. Heyden, Solid State Ionics 228 (2012) 37.
[17]   S. Suthirakun, S.C. Ammal, G.L. Xiao, F.L. Chen, H.C. zur Loye, A. Heyden, Phys. Rev. B 84 (2011) 205102.
[18]   G. Kresse, J. Furthmuller, Phys. Rev. B 54 (1996) 11169.
[19]   J.P. Perdew, K. Burke, M. Ernzerhof, Phys. Rev. Lett. 77 (1996) 3865.
[20]   G. Kresse, D. Joubert, Phys. Rev. B 59 (1999) 1758.
[21]   H.J. Monkhorst, J.D. Pack, Phys. Rev. B 13 (1976) 5188.
[22]   S. Ohta, T. Nomura, H. Ohta, K. Koumoto, J. Appl. Phys. 97 (2005) 034106.
[23]   S. Laursen, S. Linic, PCCP 11 (2009) 11006.
[24]   S. Laursen, S. Linic, J. Phys. Chem. C 113 (2009) 6689.
[25]   J. Rogal, K. Reuter, M. Scheffler, Phys. Rev. B 75 (2007) 205433.
[26]   Q.L. Ma, F. Tietz, D. Stover, Solid State Ionics 192 (2011) 535.
[27]   G. Xiao, X. Dong, K. Huang, F. Chen, Mater. Res. Bull. 46 (2011) 57.
[28]   D. Neagu, J.T.S. Irvine, Chem. Mater. 23 (2011) 1607.
[29]   N.F. Mott, Reviews of Modern Physics 40 (1968) 677.

CHAPTER 7

THEORETICAL INVESTIGATION OF HYDROGEN OXIDATION ON THE

$Sr_2Fe_{1.5}Mo_{0.5}O_{6-\delta}$ (001) PEROVSKITE SURFACE UNDER

ANODIC SOLID OXIDE FUEL CELL CONDITIONS

7.1   Summary

In this work, we used density functional theory and microkinetic modeling to investigate the oxidation mechanism of H_2 fuel on the (001) surface of the $Sr_2Fe_{1.5}Mo_{0.5}O_{6-\delta}$ (SFM) perovskite under anodic solid oxide fuel cell conditions. The model predicts that in the absence of a bias potential H_2 dissociation and H transfer are the rate limiting steps for H_2 oxidation on Mo and Fe sites on the SFM surface, respectively. However, the rate determining step for H_2 oxidation on both Mo and Fe sites become the H transfer when the anode bias potential is included in the model. The overall rates and apparent activation barriers are computed under the assumption of a fast cathode reaction. The model predictions are in a very good agreement with experimental observations that adding a transition metal on the SFM surface improves the electrochemical performance of the anode catalyst. The presence of a transition metal on the surface facilitates the H transfer process and leads to a dramatic improvement in SOFC performance.

7.2 Introduction

$Sr_2Fe_{1+x}Mo_{1-x}O_{6-\delta}$ (SFM) based perovskites [1, 2] have been proposed as promising anode materials for SOFCs since they exhibit high mixed ionic and electronic conductivity under SOFC operating conditions. The mixed valence Mo^{6+}/Mo^{5+} and Fe^{4+}/Fe^{3+} provide electronic conductivity whereas their characteristic of oxygen deficiency leads to high ionic conductivity in the material. Experiments have shown that this material can be used with H_2 fuel and natural gas with high thermodynamic stability and tolerance to sulfur. Furthermore, it was reported that SFM displayed good thermal compatibility with $La_{0.9}Sr_{0.1}Ga_{0.8}Mg_{0.2}O_{3-\delta}$ (LSGM) electrolyte [1]. Although SFM perovskite anode materials display several advantages over conventional Ni/YSZ cermets, their electrochemical activity is not satisfactory. Relatively low electrochemical activity of $Sr_2Fe_{1.5}Mo_{0.5}O_{6-\delta}$ has been reported when using H_2 or methane as a fuel. The 2 wt.% Ni content in the anode was necessary to obtain good performance, indicating that a small amount of Ni provides a significant electrocatalytic effect while not causing coking [1].

Despite the considerable experimental work cited above, the oxidation of H_2 on the SFM surface has not been treated theoretically. Understanding the mechanism of H_2 oxidation is crucial for aiding the development of SFM perovskite anode catalysts. In this Chapter, we aim at illustrating how a combination of density functional theory (DFT) and mean-field microkinetic modeling [3] can be used to gain insight into the catalytic reaction mechanism of H_2 oxidation on the SFM surfaces. First, constrained *ab initio* thermodynamic calculations were carried out to create surface models at realistic SOFC conditions. Then, we used the obtained realistic surface model to perform a mechanistic

study of H_2 oxidation using DFT. A microkinetic analysis was conducted to predict reaction behavior under anodic SOFC conditions. To compare our calculated results to experimental SOFC performance we considered the effect of the anode potential bias to the free energies of surface intermediates and activation free energies of charge transfer steps along the reaction pathway.

7.3   Computational Details

All calculations performed for this study are based on the plane wave DFT + U implementation of the Vienna Ab initio Simulation Package (VASP 5.2) [4, 5]. We used the projector-augmented wave (PAW) method [4] to represent the inner core potentials and treated the Sr $4s4p5s$, Fe $3p4s3d$, Mo $4p5s4d$, and O $2s2p$ electrons as valence . The cutoff of the kinetic energy was set for all calculations to 800 eV. Exchange correlation is described within the generalized gradient approximation (GGA) with the Perdew-Burke-Ernzerhof (PBE) functional [6]. Spin-polarized calculations have been used throughout. The Hubbard U parameter were employed to correct for the self-interaction error inherent in pure DFT when applied to mid-to-late first row transition metal oxides with tightly localized d-electrons. The U-J value for Fe was set to 4 eV and as previously reported by Carter, it is not necessary to assign a U-J value for Mo [2].

The SFM (001) perovskite surface was constructed using a slab model of a 2×2 supercell configuration of ideal cubic simple ABO_3 perovskite with eight atomic layers depth ($Sr_{16}Fe_{12}Mo_4O_{48}$). The bottom layer was fixed in all calculations. A vacuum gap of 15 Å was used to minimize the interaction between images along the z-axis. The Monkhorst-Pack method [7] was used to generate k-point sets with 4×4×1 k-points. By increasing the number of k-points to 5×5×1, we observed a negligibly small change in

oxygen vacancy formation energy (<0.01 eV) suggesting a very good convergence of reaction energies with respect to k-point density. The contribution of dipole interactions along the z-axis is subtracted from the total energy. Test calculations on a symmetric slab display a negligible difference of less than 0.07 eV in oxygen vacancy formation energy which indicates that the dipole correction scheme implemented in VASP can be used to adjust dipole interactions in our asymmetric system and i.e., it confirms that our asymmetric slab model with dipole correction scheme can be used to accurately predict energies of redox reactions on the surface.

Transition states (TS) and minimum energy reaction paths of various elementary steps were studied using the climbing image nudge-elastic band (CI-NEB) [8] and Dimer method [9]. The DFT-derived parameters were employed in a microkinetic model to calculate the surface coverage of adsorbed species under anodic SOFC conditions to determine the rate limiting step. A detailed description of the microkinetic modeling approach is described in the results and discussion section.

7.4   Results and Discussion

7.4.1   Surface model development

It has previously been shown that the BO_2 terminated (001) surface of simple cubic ABO_3 perovskite is the most stable of the various surfaces under reducing conditions [10, 11]. As a result, we considered the $(Fe/Mo)O_2$ terminated (001) surface to be a starting point for the examination of the baseline activity of fuel oxidation on SFM surfaces. The possibilities of Fe and Mo distribution in the 3-dimentional space contribute to differences in surface configurations. Figure 7.1 illustrates three different surface configurations that are considered in this study, namely, Plane-Mo (Fig. 7.1(a)),

Diagonal-Mo (Fig. 7.1(b)), and FeO_2-terminated surfaces (Fig. 7.1(c)). Our preliminary study revealed that the Plane-Mo surface exhibits the lowest surface energy among the other surfaces. Therefore, we chose this surface configuration to be our surface model for the mechanistic H_2 oxidation.
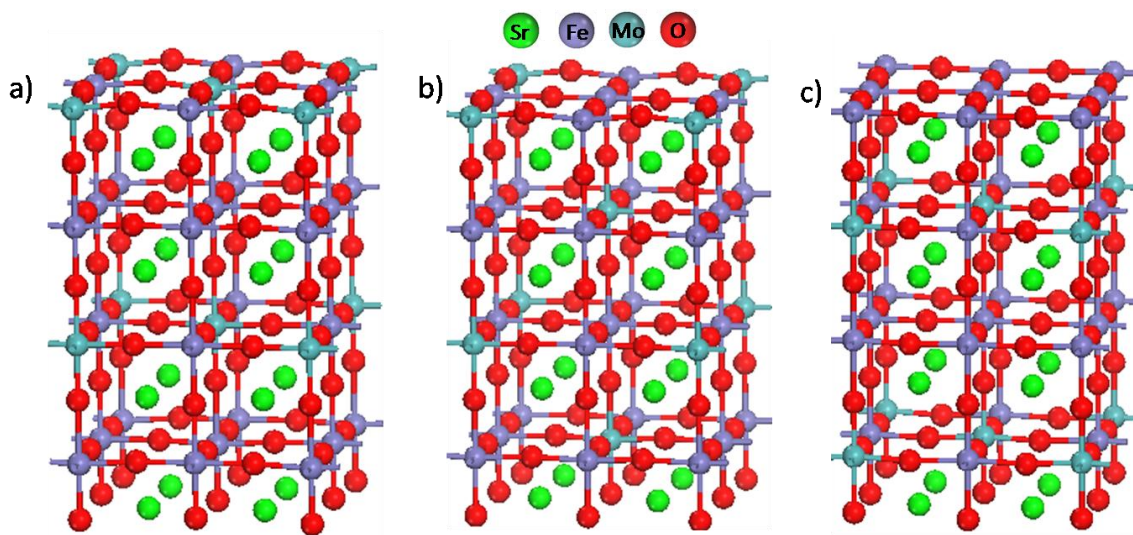
Figure 7.1 Surface models with different Fe/Mo configurations a) Plane-Mo surface, b) Diagonal-Mo surface, and c) Fe-terminated surface

To obtain a realistic surface model under anodic SOFC conditions we build a reduced slab model by creating up to six oxygen vacancies in the stoichiometric slab model. Figure 7.2 depicts the reduced slab model with six oxygen vacancies. The first two oxygen vacancies are positioned on the top-most layer, which allow a significant surface reconstruction in the top two layers of the model. The third and fourth oxygen vacancies are located in the second bottom layer between Fe atoms generating a row of vacancies. It is preferred to create the fifth oxygen vacancy in the $(Fe/Mo)O_2$ layer between Fe and Mo atoms whereas the sixth oxygen vacancy is positioned on the top most layer of the surface model. It is important to note that since SFM exhibits

153

antiferromagetic behavior we need to perform an optimization of the magnetic configuration of Fe spins to minimize the energy. This can be done by manually assign a spin configuration (up or down) on every Fe atoms in the surface model. We tried up to twelve different configurations and the one that minimizes the total electronic energy exhibits the most stable magnetic configuration. This approach was applied to optimize the magnetic configuration of all stoichiometric and reduced surface models.
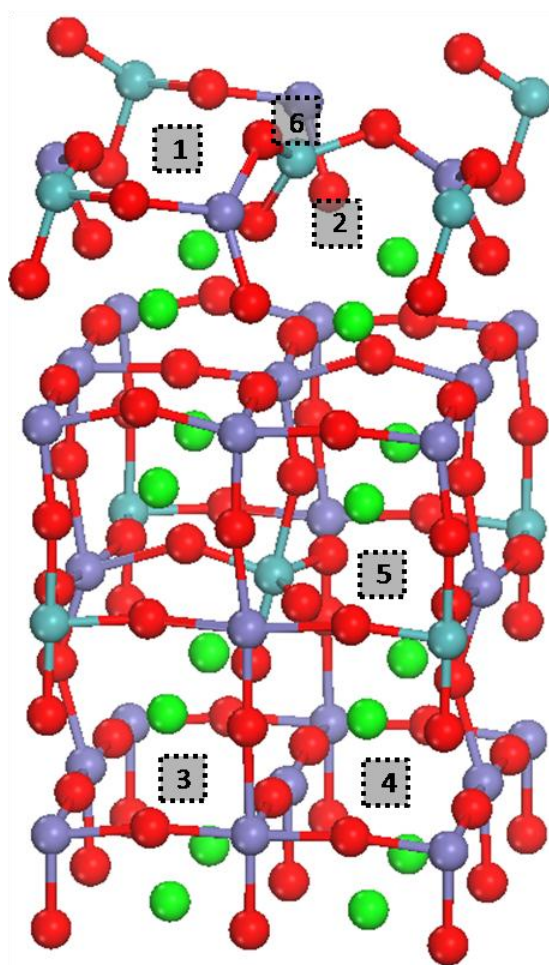
Figure 7.2 The Plane-Mo surface model with six oxygen vacancies. The dotted squares represent the position of oxygen vacancies and the order the oxygen vacancy were generated are labeled the number in the square.

We further employed constrained *ab initio* thermodynamic calculations to determine the relevant surface model under realistic SOFC conditions. The *ab initio* thermodynamic approach allows us to calculate the free energies of different compositions as a function of oxygen chemical potential. The phase diagram was constructed using the free energies from the calculations. Free energies of the stoichiometric and reduced slab were calculated using the following reaction:

$$Sr_{16}Fe_{12}Mo_4O_{48} \rightarrow Sr_{16}Fe_{12}Mo_4O_{48-\delta} + \frac{\delta}{2}O_2, \tag{7.1}$$
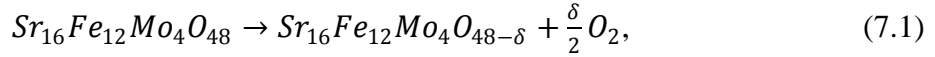
where δ represents the number of oxygen vacancy sites in the structure ($\delta = 1 - 6$). The Gibbs free energy of the reaction can be computed as:

$$\Delta G = E_{red} + \delta[E_O + \Delta\mu_O(T, P)] - E_{full}, \tag{7.2}$$

where E_{red} denotes the DFT-calculated electronic energy of the structure with oxygen vacancy(ies), E_{full} is the DFT-calculated electronic energy of the stoichiometric slab, and E_O is a half of the energy of an oxygen molecule, E_{O_2}, which is obtained from the H_2O splitting reaction using the experimental reaction energy and calculated DFT energies of H_2 and H_2O in the gas phase,[10, 11]

$$E_{O_2} = 2\left[\left(E_{H_2O}^{DFT} + E_{H_2O}^{ZPE}\right) - \left(E_{H_2}^{DFT} + E_{H_2}^{ZPE}\right) - E_{hof}\right] - E_{O_2}^{ZPE}, \tag{7.3}$$

where E^{ZPE} is the experimental zero point energy [12], E_{hof} is the experimental heat of formation of a gas-phase H_2O molecule [12], and E^{DFT} is the energy calculated with PBE functional. The chemical potential of O, which includes the temperature- and pressure-dependent free energy contributions of the O_2 molecule, is described by $\Delta\mu_O(T, P)$ and has been calculated from first principles and the rotational, translational, and vibrational partition functions of the O_2 molecule. We note that we neglect all zero point energies in Eq. 7.2 and assume that entropic contributions from the solids to the free energy

difference are insignificant [13-15]. Also, the pressure dependence of $\Delta\mu_O(T, P)$ is obtained assuming that the gas phase is ideal [14].

$$\Delta\mu_O(T, P) = \frac{1}{2}\left(\Delta\mu_{O_2}(T, P^0) + k_b T ln\left(\frac{P}{P^0}\right)\right) \quad (7.4)$$

Figure 7.3(a) shows the calculated phase diagram of the reduced slab model. It can be seen that the reduced slab model consists of five oxygen vacancies under anodic SOFC conditions ($pO_2 \sim 10^{-20}$ atm, 1000 K). This reduced slab model (Fig. 7.3(b)) was then used as our surface model to study the oxidation of H_2.
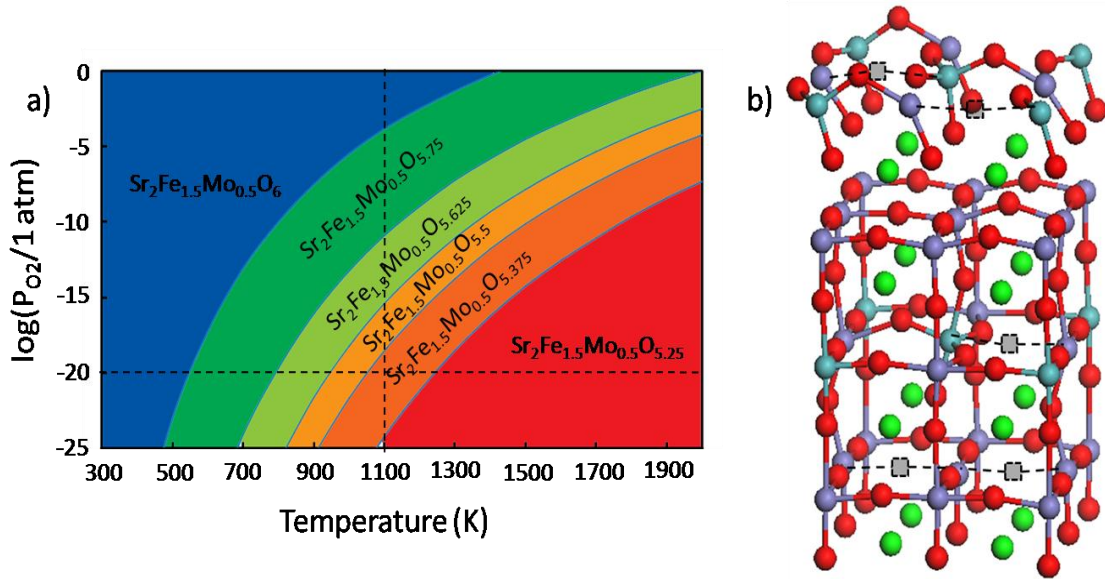
Figure 7.3 a) Calculated phase diagram of the Plane-Mo surface model b) Plane-Mo surface model with five oxygen vacancies. The dotted squares represent the position of oxygen vacancies.

7.4.2 Reaction pathways

In this section, we describe the catalytic mechanism of H_2 oxidation on the SFM anode surface. The overall electrochemical oxidation of H_2 at the anode can be expressed as:

156

$$H_{2(g)} + O_O^{2-} \rightarrow H_2O_{(g)} + 2e_{SFM}^- + V_O^{2+} \,, \tag{7.5}$$
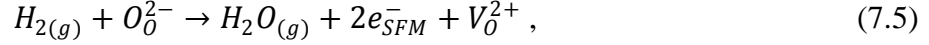
where V_O^{2+} denotes a doubly charged oxygen vacancy on the SFM surface and the two electrons of O_O^{2-} (oxygen on the surface) are transferred through the M-O-M (M = Fe, Mo) bridge to the current collector. Figure 7.4 illustrates our proposed reaction scheme. First, a H_2 molecule in the feed gas adsorbs dissociatively on a metal site and an oxygen site on the surface.

$$SFM + H_{2(g)} \rightarrow SFM_{H-H} \tag{step I}$$

where SFM and SFM_{H-H} denote the SFM surface model and the surface with two H atoms adsorbed on the surface. Then, the H atom on the metal site is transferred to the hydroxyl species (-OH) leading to a formation of a water molecule on the surface.

$$SFM_{H-H} \rightarrow SFM_{OH_2} \tag{step II}$$

where SFM_{OH_2} represents the surface with a water molecule. After that, the desorption of the water molecule takes place creating an oxygen vacancy on the surface.

$$SFM_{OH_2} \rightarrow SFM_{VS} \tag{step III}$$

where SFM_{VS} denotes the surface model with an oxygen vacancy on the top most layer. Next, oxygen ions from the SFM bulk (anode) are transferred to the anode surface:

$$SFM_{VS} \rightarrow SFM_{VB} \tag{step IV}$$

where SFM_{VB} represents the surface model with an oxygen vacancy in the second top most layer. The electrochemical reaction of step IV can be written as:

$$O_{SFM}^{2-} + V_O^{2+} \rightarrow O_O^{2-} + V_{SFM}^{2+}, \tag{7.6}$$

where O_{SFM}^{2-} and V_{SFM}^{2+} represent the doubly charged oxygen and the vacancy in the SFM bulk. Finally, the SFM bulk vacancies are filled by oxygen ions from the cathode which are obtained by the reduction of oxygen at the cathode side:

$$SFM_{\text{VB}} + \frac{1}{2}O_{2(g)}(cathode) \rightarrow SFM. \qquad \text{(step V)}$$
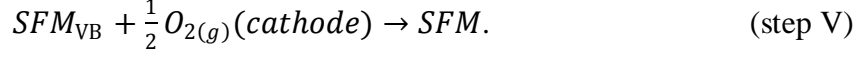
This process consists of two elementary steps. First, the replenishment of the SFM bulk vacancies by oxygen ions from cathode:

$$O_{cat}^{2-} + V_{SFM}^{2+} \rightarrow O_{SFM}^{2-} + V_{cat}^{2+} , \qquad (7.7)$$
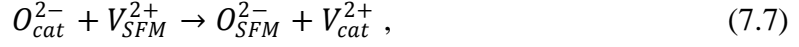
where O_{cat}^{2-} and V_{cat}^{2+} denote the doubly charged oxygen and vacancy in the cathode. Then, the oxygen vacancies at the cathode are filled by the reduction of oxygen at the cathode side:

$$\frac{1}{2}O_{2(g)} + V_{cat}^{2+} + 2e^-(cathode) \rightarrow O_{cat}^{2-} . \qquad (7.8)$$
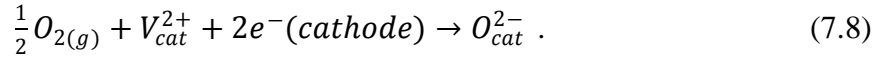
In this study, we explicitly calculated the oxygen migration from the SFM bulk to the anode surface (step IV) and we used the literature value for bulk oxygen diffusion in SFM (step V). To a first approximation, we assume that the current collection and oxygen reduction reaction at the cathode are fast which is the case at high temperatures.

7.4.3   Reaction intermediates and energy barriers

To investigate the most favorable pathway of H_2 oxidation on the surface, all possible reaction intermediates were considered. We assume that the spin configuration of Fe atoms in our surface model does not change along the reaction coordinate and we used the optimized spin configuration of our surface model to describe the magnetic behavior of all intermediates. All structural configurations of $SFM_{\text{H}-\text{H}}$ and SFM_{OH_2} intermediates are illustrated in Fig 7.5.
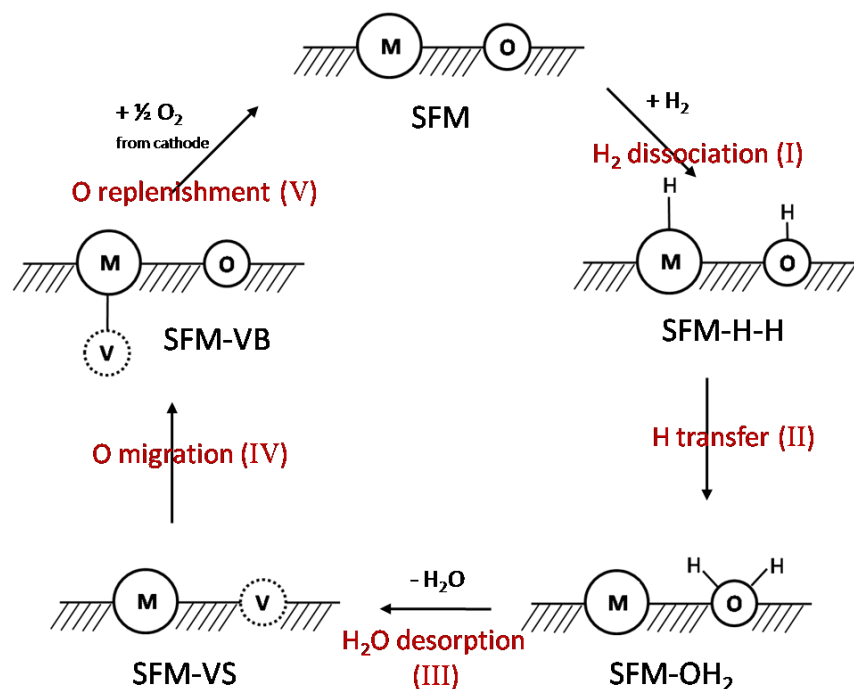
Figure 7.4 Proposed pathway for H_2 oxidation mechanism on the SFM surface

Geometric and energetic information for the reaction intermediates resulting from the H_2 dissociation and water formation on the surface are listed in Table 7.1 and Table 7.2, respectively. It can be seen that the active sites of the SFM surface involve a metal (Fe or Mo) site and an oxygen site. Note that the dissociative adsorption of H_2 is not stable on the Fe1-2 site and we did not include these intermediates in this study. The SFM_{H-H} intermediates exhibit an average bond distance of Mo-H of 1.73 Å which is similar to that of Fe-H (1.81 Å) whereas the average bond distance of O-H is 0.98 Å. The H atom from the metal site is transferred to the hydroxyl site forming a water molecule on the surface, SFM_{OH_2}. The SFM_{OH_2} intermediates display an average bond distance of O-H (H_2O) of 0.99 Å and an average bond angle of 106.85 degree. We notice that the O atom of the water molecule on the surface model is preferred to be connected to an Fe

atom rather than a Mo atom. Upon the process of water desorption, it is easier to break the Fe-O bond than Mo-O bond since the bond strength of Fe-O bond is lower. Figure 7.6 depicts the position of oxygen vacancies created to form SFM_{VS} (Fig 7.6(a)) and SFM_{VB} (Fig 7.6(b)) intermediates and the energies of oxygen vacancy formation of these intermediates are listed in Table 7.3.

Table 7.1 Geometric and energetic parameters for intermediates resulting from H_2 dissociation (SFM_{H-H}), $H_2(g) + SFM \rightleftharpoons SFM_{H-H}$

Species	Binding Energy (eV)	Bondlength (Å)	
		M-H	O-H
Mo1	-0.34	1.74	0.98
Mo2	-0.34	1.74	0.97
Mo3	0.08	1.72	1.00
Fe1-1	-0.16	1.83	0.99
Fe2-1	0.67	1.86	0.97
Fe2-2	0.63	1.75	0.98

Table 7.2 Geometric and energetic parameters for intermediates resulting from H-transfer (SFM_{OH2}), $H_2(g) + SFM \rightleftharpoons SFM_{OH2}$

Species	Binding Energy (eV)	Bondlength(Å)		Angle (H^a-O-H^b, degrees)
		O-H^a	O-H^b	
Mo1	-0.47	0.98	1.00	106.23
Mo2	0.06	0.98	1.00	105.68
Mo3	0.06	1.01	0.97	107.61
Fe1-1	-0.03	1.00	0.99	104.53
Fe2-1	0.10	0.98	1.00	109.66
Fe2-2	0.13	1.00	0.99	107.38

Table 7.3 Energies of oxygen vacancy formation of SFM_{VS} and SFM_{VB} intermediates

Intermediates	Position of oxygen vacancy wrt Fig. 7.6	E_{VF} (eV)
SFM_{VS}	1	4.53
	2	3.95
	3	3.95
	4	4.56
	5	4.14
	6	4.14
SFM_{VB}	1	4.02
	2	4.46
	3	4.00
	4	4.46

The TS of the H_2 dissociation process (step I) and H-transfer (step II) were located using the CI-NEB method and the reaction energy barriers of selected pathway were calculated. We calculated the energy barriers for the Mo1, Mo2, Mo3, and Fe1-1 pathways to determine the most favorable pathway of H_2 oxidation on the SFM surface. The energy barriers of Fe2-1 and Fe2-2 were not computed because the energies of their SFM_{H-H} intermediates are less stable than the most stable one by 1.02 and 0.98 eV, respectively, and it is expected that H_2 dissociation on these sites is not preferred. Figure 7.7 illustrates the one-dimensional potential energy surface (PES) for the H_2 oxidation mechanism on the SFM surface which was constructed using the DFT calculated energies of all stable intermediates. The PES shows that the H_2 oxidation on Mo1 and Fe1-1 are competitive and could be energetically favorable; therefore, we performed dimer calculations to determine a more accurate TS structure and energy. The calculated energy barriers of Mo1 and Fe1-1 are 0.58 and 0.06 for step I and 0.74 and 0.86 for step II, respectively. Furthermore, since Mo1 and Fe1-1 involve the same oxygen site, only one

TS of the oxygen migration process (step IV) is calculated. The NEB calculation did not identify any TS for this process, suggesting that the TS is product-like and the energy barrier is similar to the energy of reaction.
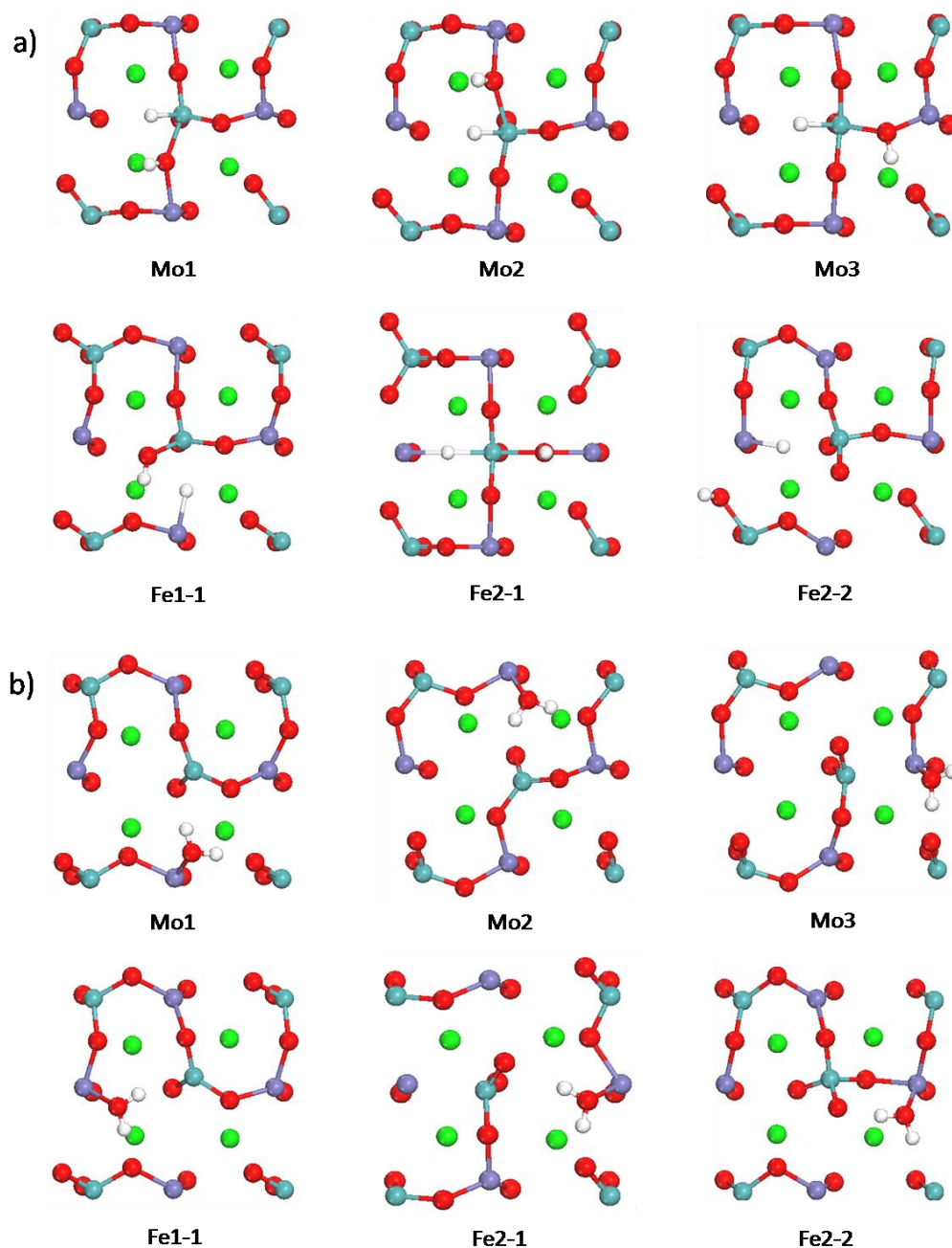
Figure 7.5 Top view of surface intermediates resulting from a) H_2 dissociation (SFM_{H-H}) and b) H transfer (SFM_{OH2})
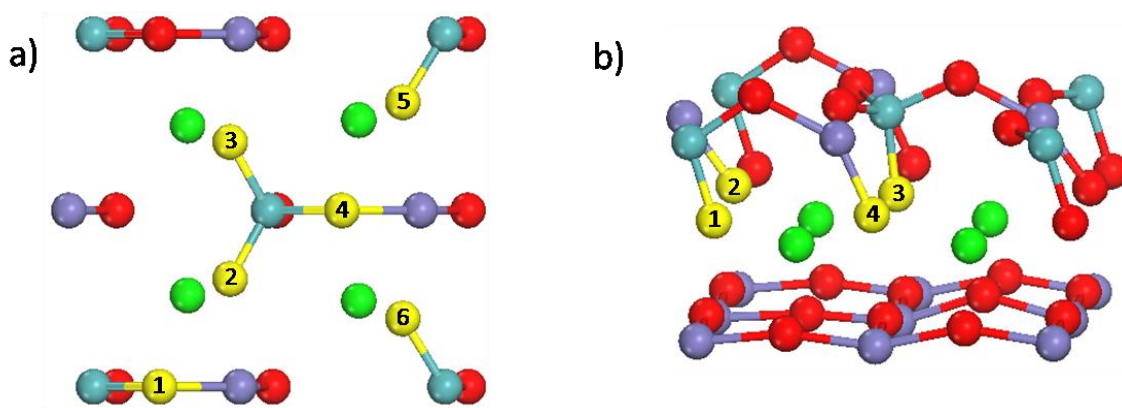
Figure 7.6 All possible positions of oxygen vacancies that can be generated in the slab model to create a) *SFM*$_{VS}$ intermediates and b) *SFM*$_{VB}$ intermediates. The yellow oxygen atoms indicate the possible positions of oxygen vacancies that were created with the labeled numbers with respect to E$_{VF}$ listed in Table 7.2
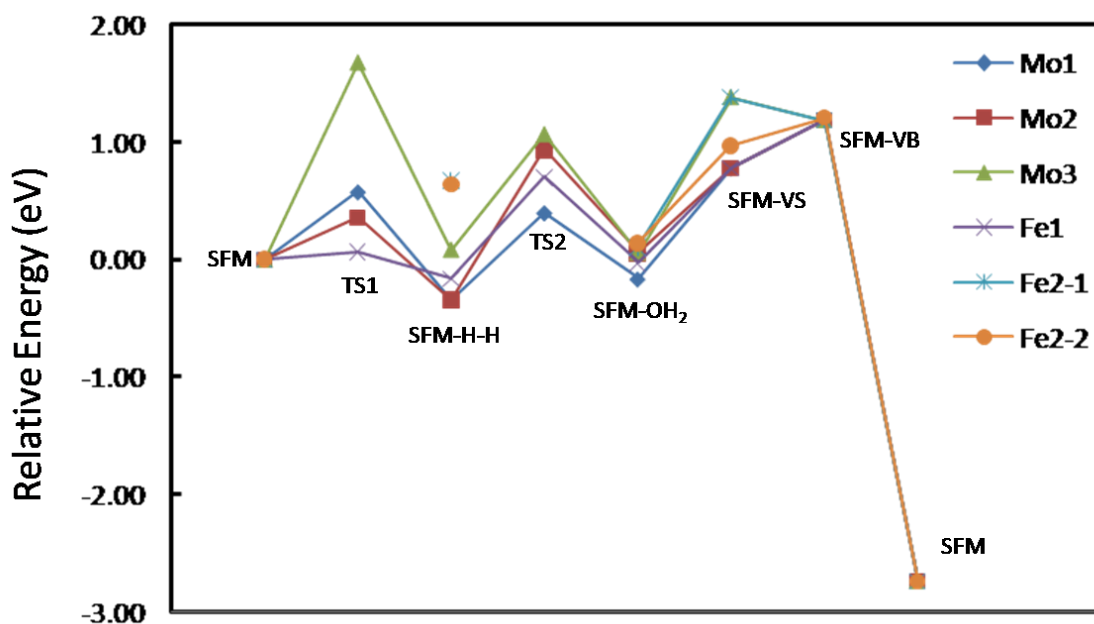
Figure 7.7 One-dimensional potential energy surface (PES) for H$_2$ oxidation on the SFM surface (zero-point energy effects not included).

163

7.4.4   Microkinetic modeling

The thermochemical data and activation barriers for the elementary steps suggest that H_2 oxidation on Mo1 or Fe1-1 could be the most favorable pathway. However, we cannot deduce the most favorable pathway from DFT calculations alone since the relative rates of these pathways depend on reaction conditions. Therefore, we continue to conduct the microkinetic analysis for the H_2 oxidation mechanism on Mo1 and Fe1-1 sites to further investigate the reaction behavior under realistic SOFC conditions. We used the results from the DFT calculations as initial estimates for the parameters of the microkinetic model. Zero-point corrected reaction energies and zero-point corrected energy barriers (calculated using DFT frequencies) for all elementary steps of Mo1 and Fe1-1 pathways are given in Table 7.4. The zero point energy (ZPE) is calculated as $ZPE = \sum \frac{1}{2} h v_i$, where v_i denotes the different vibrational modes of the species.

Figure 7.8 depicts the free energy profile of H_2 oxidation on Mo1 and Fe1-1 sites on the SFM surface model. In this free energy profile, we take into account the contributions from ZPE, temperature, and pressure of the environmental conditions to correct the calculated DFT energies. The free energy profile of the two possible pathways indicates that the H_2 oxidation on Mo1 site seems to be less favorable since it exhibits the highest TS energy (Mo1-TS1) which is 0.24 eV higher than the highest TS energy of Fe1-1 (TS2).

Table 7.4 Zero-point energy corrected reaction energies and forward activation barriers for the elementary steps considered in the Mo1 and Fe1-1 pathways of the H_2 oxidation mechanism.

Elementary step	Mo1 Pathway		Fe1-1 Pathway	
	ΔE_{ZPE} (eV)	ΔE_{ZPE}^{act} (eV)	ΔE_{ZPE} (eV)	ΔE_{ZPE}^{act} (eV)
SFM + H₂ --> SFM_{H-H}	-0.10	0.76	-0.04	0.16
SFM_{H-H} --> SFM_{OH2}	-0.05	0.68	0.32	0.88
SFM_{OH2} --> SFM_{VS} + H₂O	1.13	0.00	0.71	0.00
SFM_{VS} --> SFM_{VB}	0.37	0.00	0.37	0.00
SFM_{VB} + 1/2O₂ --> SFM	-3.83	0.33	-3.83	0.33
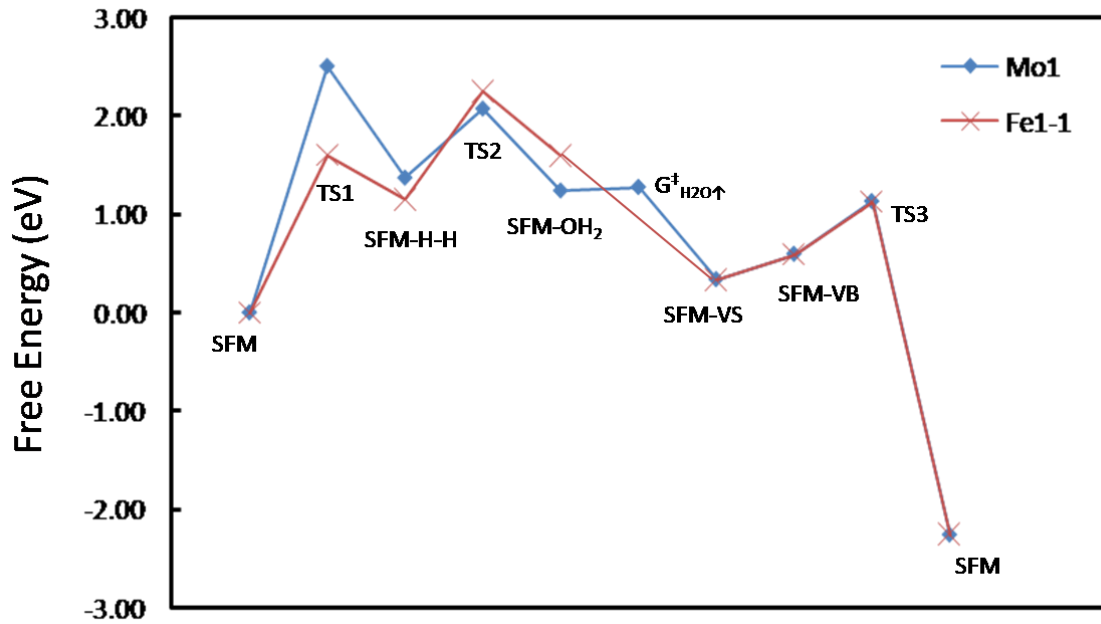
Figure 7.8 Free energy profile (in eV) for Mo1 and Fe1-1 pathways of H_2 oxidation under reaction conditions (T = 1100 K, $pH_2 = pO_2 = 1$ atm, and $pH_2O = 0.03$ atm). All energies are with reference to the sum of the energies of the initial state and the reactant gas molecules. TS1, TS2, and TS3 denote the TS energies of TS of H_2 dissociation, H transfer, and bulk oxygen migration, respectively. $G^{\ddagger}_{H2O\uparrow}$ represents the TS free energy of the water desorption process.

The set of 5 steps described in section 7.4.2 constitutes the backbone of the microkinetic model. The reaction energies (calculated from binding energies), activation barriers, entropies of surface intermediates, and frequency factors are the parameters required for describing the model. Collision and transition state theories have been used to calculate the forward and reverse rate constants for these elementary steps. Table 7.5 lists the calculated forward rate and equilibrium constants of all elementary steps. These calculated rate constants are used to solve the steady-state equations which give the fractional surface coverages of all adsorbed species and the fraction of free sites. The temperature range used in this model is between 900 and 1300 K, and the partial pressure of the feed gas at the anode are typical experimental conditions of $pH_2 = 1$ atm, and $pH_2O = 0.03$ atm whereas the oxygen partial pressure at the cathode is 1 atm. The calculated rates and other insights obtained from the microkinetic model at a representative temperature of 1100 K are summarized in Table 7.6. The model predicts that under the SOFC anodic conditions the Fe1-1 pathway exhibits a significantly higher reaction rate than that of Mo1 pathway. Campbell's degree of rate control analysis indicates that the H_2 dissociation is the rate-determining process for the Mo1 pathway whereas the H transfer process is rate-limiting for the Fe1-1 pathway. Furthermore, Campbell's degree of thermodynamic rate control analysis reveals that the overall rate is sensitive mostly to the stability of the reactant structure (SFM) for both Mo1 and Fe1-1 pathways. The apparent activation energy for H_2 oxidation on Mo1 and Fe1-1 sites are calculated to be 0.66 and 0.83 eV, respectively.

Table 7.5 Forward rate constants (k_{for}) and equilibrium constants (K) calculated at 1100 K for the elementary steps considered in the Mo1 and Fe1-1 pathways of the H_2 oxidation mechanism.

Elementary step	Mo1 Pathway		Fe1-1 Pathway	
	k_{for} (s^{-1})	K	k_{for} (s^{-1})	K
$SFM + H_2 \rightarrow SFM_{H-H}$	7.76×10^{1}	5.30×10^{-7}	1.02×10^{6}	5.25×10^{-6}
$SFM_{H-H} \rightarrow SFM_{OH2}$	1.40×10^{10}	3.98×10^{0}	1.95×10^{8}	9.04×10^{-3}
$SFM_{OH2} \rightarrow SFM_{VS} + H_2O$	1.57×10^{13}	1.35×10^{4}	6.98×10^{14}	6.02×10^{5}
$SFM_{VS} \rightarrow SFM_{VB}$	1.51×10^{12}	6.59×10^{-2}	1.51×10^{12}	6.59×10^{-2}
$SFM_{VB} + 1/2O_2 \rightarrow SFM$	7.99×10^{10}	1.19×10^{13}	7.99×10^{10}	1.19×10^{13}

Table 7.6 Calculated rates for H_2 oxidation on Mo1 and Fe1-1 sites on the SFM surface, apparent activation barriers, degree of rate control (X_{RC}), and degree of thermodynamic rate control (X_{TRC}) obtained from microkinetic analysis at 1100 K.

Pathway	Overall rate (s^{-1})	E_{app} (eV)	X_{RC}		X_{TRC}
			H_2 dissociation	H transfer	SFM
Mo1	76.77	0.66	0.99	0.01	-1.00
Fe1-1	1024.73	0.83	0.00	1.00	-1.00

7.4.5   Effects of anode bias potential

It is noteworthy that the microkinetic analysis performed in the previous section neglects the presence of an electric field (electrochemical double layer) that is induced by the potential drop across the anode/electrolyte interface. It has been shown by Linic and coworkers [18, 19] that the applied electric field interacts with the surface intermediates

and changes their adsorption energies. Their calculations reveal that the field effect on the binding energies of O and OH on Ni is less than 0.15 eV and there is no effect on the adsorption energy of H in the presence of typical electric field strengths expected in SOFCs. In addition to the effect of electric fields to the adsorption energies, the free energy of surface intermediates is also influenced by the anode potential bias. The reaction free energies of elementary steps that involve charge species are directly affected by the potential bias. It has been reported that the chemical potential of the charged species is shifted by the amount of charge multiplied by the electrical potential [19]. For example, for the H_2 dissociation process (step I) $[H_2 + * \rightarrow [\text{H-H*}]^{2+} + 2e^-]$, where a H_2 molecule in the feed gas dissociatively adsorbs on the surface and gives 2 electrons to the metal, the Gibbs free energy is calculated as;

$$\Delta G_{stepI} = G_{\text{H-H}*} + 2e\Delta V - G_{H2} - G_* , \qquad (7.9)$$

where $G_{\text{H-H}*}$ is the free energy of the H-H* adsorbed species, G_{H2} is the free energy of a H_2 molecule in the gas phase, e is the magnitude of charge of an electron (1.6×10^{-19} C), and ΔV is the cell voltage which is the difference between the cathode potential (fixed to be at 1.16 V) and the anode potential ($\Delta V = V_{cathode} - V_{anode}$). From Eq. 7.9, we can see that an increase in the anode potential lowers the free energy of the elementary step that involved charge species (ions or electrons). Furthermore, the activation barrier of the charge transfer step is influenced by the anode bias potential. Increasing the anode potential, V_{anode}, lowers the cell voltage, ΔV, and the free energy of activation, $\Delta G^{\ddagger}$ is calculated as:

$$\Delta G^{\ddagger} = \Delta G^{0,\ddagger} + n_i \beta \Delta V , \qquad (7.10)$$

where $\Delta G^{0,\ddagger}$ is the free energy of activation of the elementary step at short circuit conditions (without the effect of bias potential), n_i represents the number of transferring electrons in the charge transfer step, and β denotes the symmetry coefficient (range from 0 to 1, in this study $\beta = 0.5$). The forward, k_f, and reverse k_b rate constant of the charge transfer step are then calculated as:

$$k_f = A_f \exp\left(\frac{-\Delta G_f^{0,\ddagger} - n_i \beta \Delta V}{RT}\right),$$
(7.11)

$$k_b = A_b \exp\left(\frac{-\Delta G_b^{0,\ddagger} - n_i(1-\beta)\Delta V}{RT}\right),$$
(7.12)

where A_f and A_b denote the frequency factors of the forward and reverse rates, respectively. Figure 7.9 illustrates the free energy profile of H_2 oxidation on Mo1 and Fe1-1 sites in the presence of bias potential at a cell voltage of 0.7 V.
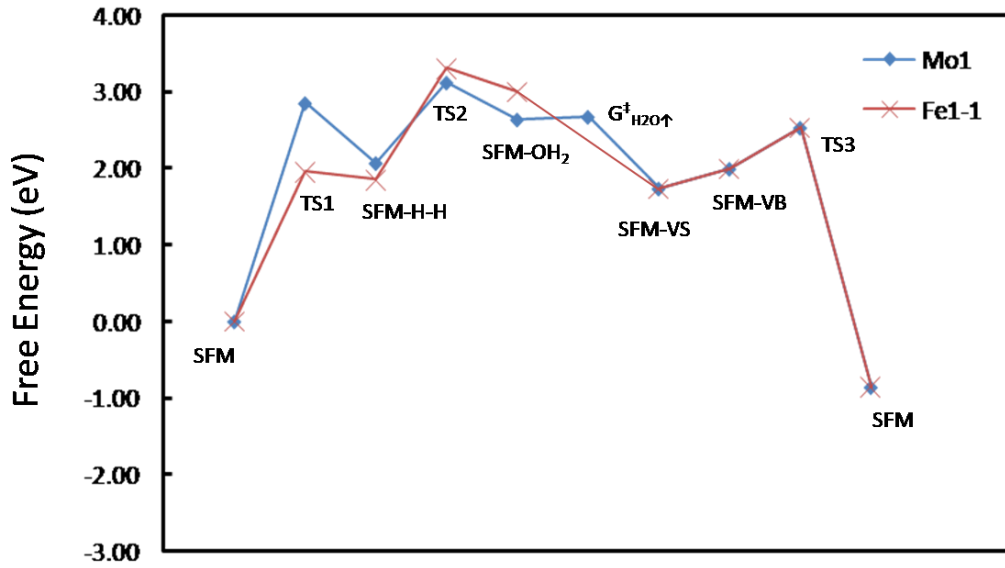
Figure 7.9 Free energy profile (in eV) for Mo1 and Fe1-1 pathways of H_2 oxidation under operating voltage ($\Delta V = 0.7$ V) in the reaction conditions (T = 1100 K, $pH_2 = pO_2$ = 1 atm, and $pH_2O = 0.03$ atm). All energies are with reference to the sum of the energies of the initial state and the reactant gas molecules. TS1, TS2, and TS3 denote the TS energies of TS of H_2 dissociation, H transfer, and bulk oxygen migration, respectively. $G^{\ddagger}_{H2O\uparrow}$ represents the TS free energy of the water desorption process.

Under operating voltage ($\Delta V = 0.7$ V), the bias potential shifts the free energies of all charge transfer steps upwards by $0.7n$ where n is the number of charges involving in the elementary steps (Eq. 7.9). We employed Bader charge analysis to identify the charge transfer steps and we find that an electron is transferred from the H_2 molecule to the adsorbed oxygen site when it dissociatively adsorbs on the surface (step I). Another electron is transfer from the adsorbed H atom to the metal site when this H migrates to the hydroxyl site to from a water molecule (step II). The change of free energy of activation of the charge transfer step is then calculated using Eq. 7.10. Unlike the free energy profiles at short circuit, the free energy profiles at operating voltage indicate that the highest energy TS is TS2 of the Fe1-1 pathway.

Next, we used the parameters obtained from the updated free energy profiles to conduct a microkinetic analysis. The model was constructed to further investigate the effect of anode bias potential to the reaction behavior. The rate-controlling step, apparent activation energy, and overall rate of reaction in the presence of a cell potential of $\Delta V = 0.7$ V are given in Table 7.7. The overall rate and apparent activation energy are clearly more favorable for Mo1 than for Fe1-1 which suggested that H_2 oxidation on Mo1 site is indeed the most favorable pathway under operating voltage. Campbell's degree of rate control analysis indicates that the reaction behavior of the Mo1 pathway depends strongly on the operating voltage and temperature. As shown in Fig. 7.10, the degree of rate control of the Mo1 pathway changes when operating voltage or temperatures are varied. In contrast, the degree of rate control of Fe1-1 pathway is exactly unity for the H-transfer process within the considered temperature and operating voltage. Overall, at relevant operating conditions ($\Delta V = 0.7$ V and T = 1100 K) the H-transferring process is the

performance limiting step for both Mo and Fe1-1 pathways. The computational predictions are in a very good agreement with experimental observations. As shown in Fig. 7.11, the electrochemical performance of the anode catalyst is dramatically improved when depositing a small amount of Ni on the electrode surface [1]. Adding a transition metal to the SFM surface (e.g. Ni) facilitates H_2 dissociation and H transfer and therefore improves the overall cell performance.
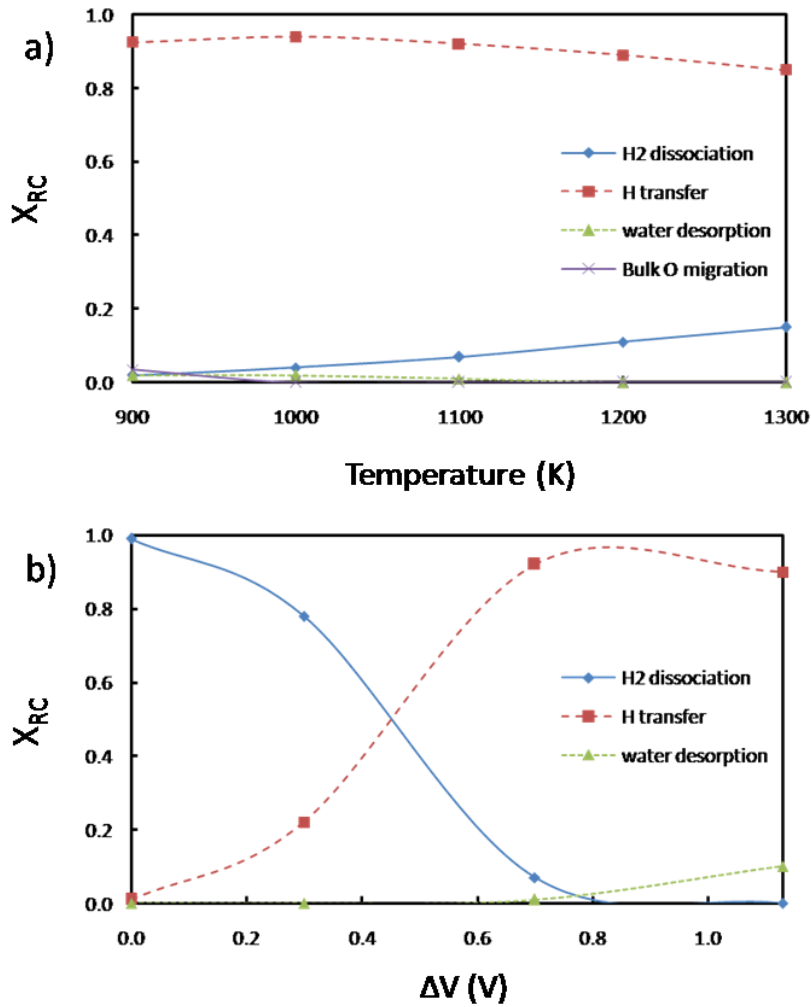
Figure 7.10 Campbell's degree of rate control a) as a function of temperature at 0.7 V and b) as a function of operating voltage at 1100 K.

171

Table 7.7 Calculated rates for H_2 oxidation on Mo1 and Fe1-1 sites on the SFM surface, apparent activation barriers, and degree of rate control (X_{RC}) obtained from microkinetic analysis at operating voltage of 0.7 V and 1100 K.

Pathway	Overall rate (s^{-1})	E_{app} (eV)	X_{RC}		
			H_2 dissociation	H transfer	water desorption
Mo1	0.11	1.56	0.07	0.92	0.01
Fe1-1	0.02	2.40	0.00	1.00	0.00
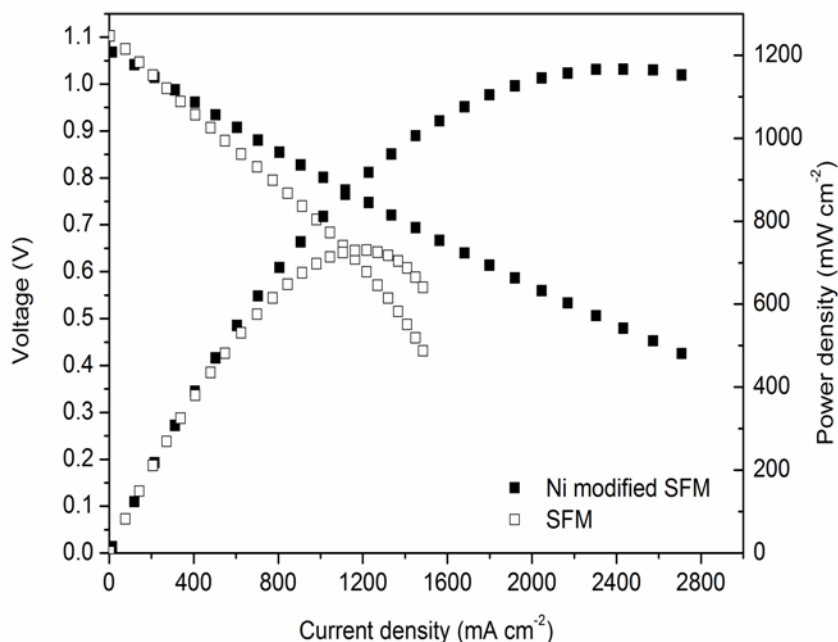
Figure 7.11 Polarization curve of SFM and Ni modified SFM anode electrode [1]

7.5   Conclusions

Our microkinetic model based on DFT-derived parameters was able to accurately predict the experimentally observed reaction behavior and provide significant insights into the rate-limiting process of the H_2 oxidation on the SFM (001) surface. We employed constrained *ab initio* thermodynamic calculations to construct a surface model

172

under realistic reaction conditions. The surface model was used to investigate the thermochemistry and reaction barriers of the elementary steps leading to H_2 oxidation on the anode surface. The H_2 oxidation mechanism involved the H_2 dissociation, H-transfer, water desorption, bulk-to-surface oxygen migration, and oxygen replenishment process. A microkinetic analysis was conducted to include the effect of reaction conditions. In addition, the anode bias potential is included in the model to study the effect of the bias potential to the reaction behavior. Overall, the model predicts that at relevant operating voltage and realistic SOFC conditions the H-transfer is the performance limiting process. The calculated results agree very well with the experimental observations that the electrochemical performance of the SFM anode can be improved when adding small amounts of Ni on the catalyst surface. Adding a transition metal to the SFM surface (e.g. Ni) facilitates the H transfer process and therefore improves the overall cell performance.

7.6   References

[1]   G.L. Xiao, F.L. Chen, Electrochem. Commun. 13 (2011) 57.
[2]   A.B. Munoz-Garcia, D.E. Bugaris, M. Pavone, J.P. Hodges, A. Huq, F.L. Chen, H.C. zur Loye, E.A. Carter, J. Am. Chem. Soc. 134 (2012) 6826.
[3]   J.A. Dumesic, *The Microkinetics of heterogeneous catalysis*, American Chemical Society, Washington, DC 1993.
[4]   G. Kresse, J. Furthmuller, Phys. Rev. B 54 (1996) 11169.
[5]   G. Kresse, D. Joubert, Phys. Rev. B 59 (1999) 1758.
[6]   J.P. Perdew, K. Burke, M. Ernzerhof, Phys. Rev. Lett. 77 (1996) 3865.
[7]   H.J. Monkhorst, J.D. Pack, Phys. Rev. B 13 (1976) 5188.
[8]   G. Henkelman, B.P. Uberuaga, H. Jonsson, J. Chem. Phys. 113 (2000) 9901.
[9]   A. Heyden, A.T. Bell, F.J. Keil, J. Chem. Phys. 123 (2005).
[10]   R.I. Eglitis, Integrated Ferroelectrics 108 (2009) 11.
[11]   Y.F. Zhukovskii, E.A. Kotomin, S. Piskunov, D.E. Ellis, Solid State Commun. 149 (2009) 1359.
[12]   S.C. Ammal, A. Heyden, J. Chem. Phys. 133 (2010) 164703.
[13]   J.K. Norskov, J. Rossmeisl, A. Logadottir, L. Lindqvist, J.R. Kitchin, T. Bligaard, H. Jonsson, J. Phys. Chem. B 108 (2004) 17886.
[14]   P.W. Atkins, *Physical Chemistry*, Oxford University Press, Oxford 1998.
[15]   S. Laursen, S. Linic, PCCP 11 (2009) 11006.
[16]   S. Laursen, S. Linic, J. Phys. Chem. C 113 (2009) 6689.

[17]   J. Rogal, K. Reuter, M. Scheffler, Phys. Rev. B 75 (2007) 205433.
[18]   D.B. Ingram, S. Linic, J. Electrochem. Soc. 156 (2009) B1457.
[19]   J. Mukherjee, S. Linic, J. Electrochem. Soc. 154 (2007) B919.

CHAPTER 8

CONCLUSIONS AND FUTURE OUTLOOK

8.1   Conclusions

This work presents a case study for the application of density functional theory calculations to the rational design of heterogeneous functional materials. Specifically, the design of alternative perovskite-based SOFC anode materials has been the focus of this research. Obtaining ionic conductivity, electronic conductivity, and catalytic activity in perovskite based anode materials has been a major challenge for the development of SOFC technology. The main conclusions derived from this work are:

- The effects of p- and n-type dopants to the mixed ionic/electronic conductivity of $SrTiO_3$ based perovskite oxides were investigated using density functional theory calculations. We find that n-doping generates effective positive charges to the lattice. These extra charges can be electronically compensated by introducing conduction electrons which travel through the Ti-O-Ti bridge in the $SrTiO_3$ perovskites. This electron transferring process contributes to an improvement in electronic conductivity.

- We find that p-doping generates negative charges to the lattice. Oxygen vacancies were created to neutralize the extra negative charges at moderate and low oxygen

chemical potential. Increasing the number of oxygen vacancies in the structure leads to an enhanced ionic conductivity.

- A mixed p- and n-dope strategy was used to obtain mixed ionic/electronic conductivity in perovskite anode materials. This doping approach is efficient and completely independent of doping site. The concentration of p-type dopant should be lower than n-type dopant so that the hole doping effect from the p-type dopants can be compensated by the presence of oxygen vacancies in the structure and as such do not lead to a decrease in electronic conductivity.

- The electro-catalytic mechanism of the H_2 fuel oxidation on the SFM surface was investigated using a combination of DFT and microkinetic analysis. The derived DFT parameters were used to construct a microkinetic model. The model predicts that at relevant operating voltage in anodic SOFC conditions H transfer is the performance limiting step. The calculated results are in a very good agreement with experimental observations that the electrochemical performance of the anode catalyst is remarkably improved when adding small amounts of a transition metal like Ni on the catalyst surface.

The work presented in this thesis is significant to the field of high temperature electro-catalysis since it demonstrates the value of DFT as a predictive tool in the design of electrodes. The application of DFT did not only explain experimentally observed phenomena but also permitted the generation of fundamental understanding regarding an electrochemical process that led to the development of novel electro-catalysts.

8.2   Future Research Directions

In this dissertation, we have mainly focused on the investigation of the H_2 oxidation on the SFM surface under anodic SOFC conditions. Another challenging problem for SOFCs is the syngas fuel oxidation where CO oxidation occurs on the anode surface. A similar approach to the one utilized in this dissertation, combined DFT and microkinetic modeling, can be used to predict the reaction behavior of CO on the SFM anode surface.

Another extension of the work presented in this dissertation would be to utilize the tools employed herein to investigate the oxidation mechanism of more complex fuels (e.g. CH_4) on the SFM anode surface. The surface model description could be very similar to the one used in the present work. However, the challenge of this study could be the complexity of the reaction network and the numbers of possibilities to abstract the H from a CH_4 molecule. Again, a microkinetic model would have to be developed to predict the reaction behavior under reaction conditions.

Finally, sulfur poisoning of the anode electrocatalysts is another important problem that has been considered for the past few years [1]. It has been shown that small amounts of sulfur impurities in the feed gas can dramatically deactivate the anode catalyst [2-4]. Future research should focus on identifying the SFM surface model under the presence of various amounts of sulfur impurities. This can be done by using constrained *ab initio* thermodynamic simulations. The effects of sulfur impurities can thus be included in the surface model which can then be used to study the fuel oxidation mechanism with a combination of DFT and microkinetic modeling. The results from the

model predictions can be utilized to identify ways to improve the electrochemical activity

of the anode catalyst under the environment of sulfur impurities.

8.3 References

[1]   Y. Matsuzaki, I. Yasuda, Solid State Ionics 132 (2000) 261.
[2]   K. Sasaki, K. Susuki, A. Iyoshi, M. Uchimura, N. Imamura, H. Kusaba, Y. Teraoka, H. Fuchino, K. Tsujimoto, Y. Uchida, N. Jingo, J. Electrochem. Soc. 153 (2006) A2023.
[3]   S.W. Zha, Z. Cheng, M.L. Liu, J. Electrochem. Soc. 154 (2007) B201.
[4]   S.W. Zha, P. Tsang, Z. Cheng, M.L. Liu, Journal of Solid State Chemistry 178 (2005) 1844.

REFERENCES

A. Kaiser, J. L. B., P. R. Slater, J. T. S. Irvine (2000). "Tetragonal tungsten bronze type phases $(Sr_{1-x}Ba_x)_{0.6}Ti_{0.2}Nb_{0.8}O_{3-\delta}$: Material characterisation and performance as SOFC anodes " *Solid State Ionics* **135**: 519.

Abramov, Y. A., V. G. Tsirelson, et al. (1995). "The chemical bond and atomic displacements in $SrTiO_3$ from X-ray diffraction analysis." *Acta Crystallographica Section B* **51**: 942-951.

Aguilar, L., S. W. Zha, et al. (2004). "A solid oxide fuel cell operating on hydrogen sulfide (H_2S) and sulfur-containing fuels." *Journal of Power Sources* **135**(1-2): 17-24.

Aiura, Y., H. Bando, et al. (1997). "Effects of doping on the electronic structure of $La_xSr_{1-x}TiO_3$." *Superlattices and Microstructures* **21**(3): 321-324.

Akhtar, M. J., Z. U. N. Akhtar, et al. (1995). "Computer-Simulation Studies of Strontium-Titanate." *Journal of the American Ceramic Society* **78**(2): 421-428.

Ammal, S. C. and A. Heyden (2010). "Modeling the noble metal/TiO_2 (110) interface with hybrid DFT functionals: A periodic electrostatic embedded cluster model study." *Journal of Chemical Physics* **133**(16): 164703.

Arachi, Y., H. Sakai, et al. (1999). "Electrical conductivity of the ZrO_2-Ln_2O_3 (Ln = lanthanides) system." *Solid State Ionics* **121**(1-4): 133-139.

Arai, H., T. Yamada, et al. (1986). "Catalytic Combustion of Methane over Various Perovskite-Type Oxides." *Applied Catalysis* **26**(1-2): 265-276.

Atkins, P. W. (1998). "Physical Chemistry". Oxford, Oxford University Press.

Atkinson, A., S. Barnett, et al. (2004). "Advanced anodes for high-temperature fuel cells." *Nature Materials* **3**(1): 17-27.

Ayala, P. Y., K. N. Kudin, et al. (2001). "Atomic orbital Laplace-transformed second-order Moller-Plesset theory for periodic systems." *Journal of Chemical Physics* **115**(21): 9698-9707.

Balachandran, U. and N. G. Eror (1982). "Electrical-Conductivity in Lanthanum-Doped Strontium-Titanate." *Journal of the Electrochemical Society* **129**(5): 1021-1026.

179

Balachandran, U., B. Ma, et al. (1998). "Development of mixed-conducting oxides for gas separation." *Solid State Ionics* **108**(1-4): 363-370.

Batyrev, I., A. Alavi, et al. (1999). "Ab initio calculations on the $Al_2O_3(0001)$ surface." *Faraday Discussions* **114**: 33-43.

Batyrev, I. G., A. Alavi, et al. (2000). "Equilibrium and adhesion of Nb/sapphire: The effect of oxygen partial pressure." *Physical Review B* **62**(7): 4698-4706.

Baur, E., H. Preis (1937). *Zeitung für Elektrochemie*: 727.

Bednorz, J. G. and K. A. Muller (1986). "Possible High-Tc Superconductivity in the Ba-La-Cu-O System." *Zeitschrift Fur Physik B-Condensed Matter* **64**(2): 189-193.

Boukamp, B. A. (2003). "The amazing Perovskite anode." *Nature Materials* **2**(5): 294-296.

Campbell, C. T. (2001). "Finding the rate-determining step in a mechanism - Comparing DeDonder relations with the "degree of rate control"." *Journal of Catalysis* **204**(2): 520-524.

Canales-Vazquez, J., J. C. Ruiz-Morales, et al. (2005). "Sc-substituted oxygen excess titanates as fuel electrodes for SOFCs." *Journal of the Electrochemical Society* **152**(7): A1458-A1465.

Canales-Vazquez, J., S. W. Tao, et al. (2003). "Electrical properties in $La_2Sr_4Ti_6O_{19-delta}$: a potential anode for high temperature fuel cells." *Solid State Ionics* **159**(1-2): 159-165.

Cortright, R. D. and J. A. Dumesic (2002). "Kinetics of heterogeneous catalytic reactions: Analysis of reaction schemes." *Advances in Catalysis, Vol 46* **46**: 161-264.

Cramer, C. J. (2004). "Essentials of computational chemistry : theories and models". Chichester, Wiley.

D. P. Fagg, V. V. K., A. V. Kovalevsky, A. P. Viskup, E. N. Naumovich, J. R. Frade (2001). "The stability and mixed conductivity in La and Fe doped $SrTiO_3$ in the search for potential SOFC anode materials " *Journal of the European Ceramic Society* **21**: 1831.

Dresselhaus, M. S. and I. L. Thomas (2001). "Alternative energy technologies." *Nature* **414**(6861): 332-337.

Dudarev, S. L., G. A. Botton, et al. (1998). "Electron-energy-loss spectra and the structural stability of nickel oxide: An LSDA+U study." *Physical Review B* **57**(3): 1505-1509.

Dudarev, S. L., A. I. Liechtenstein, et al. (1997). "Surface states on NiO (100) and the origin of the contrast reversal in atomically resolved scanning tunneling microscope images." *Physical Review B* **56**(8): 4900-4908.

Dumesic, J. A. (1993). "The Microkinetics of heterogeneous catalysis". Washington, DC, American Chemical Society.

Eglitis, R. I. (2009). "Ab Initio Calculations of $SrTiO_3$, $BaTiO_3$, $PbTiO_3$, $CaTiO_3$ and BaZrO3 (001) and (011) Surfaces." *Integrated Ferroelectrics* **108**: 11-20.

Fagg, D. P., V. V. Kharton, et al. (2001). "The stability and mixed conductivity in La and Fe doped SrTiO3 in the search for potential SOFC anode materials." *Journal of the European Ceramic Society* **21**(10-11): 1831-1835.

Feng, M. and J. B. Goodenough (1994). "A Superior Oxide-Ion Electrolyte." *European Journal of Solid State and Inorganic Chemistry* **31**(8-9): 663-672.

Fergus, J. W. (2006). "Oxide anode materials for solid oxide fuel cells." *Solid State Ionics* **177**(17-18): 1529-1541.

Gokhale, A. A., S. Kandoi, et al. (2004). "Molecular-level descriptions of surface chemistry in kinetic models using density functional theory." *Chemical Engineering Science* **59**(22-23): 4679-4691.

Goodenough, J. B. and Y. H. Huang (2007). "Alternative anode materials for solid oxide fuel cells." *Journal of Power Sources* **173**(1): 1-10.

Goodenough, J. B., K. Huang (1997). "Lanthanum Gallate as a New SOFC Electrolyte". Proceedings the FuelCells'97 ReviewMeeting.

Gorte, R. J. and J. M. Vohs (2009). "Nanostructured anodes for solid oxide fuel cells." *Current Opinion in Colloid & Interface Science* **14**(4): 236-244.

Grenier, J. C., G. Schiffmacher, et al. (1977). "X-Ray-Diffraction Study and Electron-Microscopy of System $CaTiO_3$-$Ca_2Fe_2O_5$." *Journal of Solid State Chemistry* **20**(4): 365-379.

Guoliang, X., X. Dong, et al. (2011). "Synthesis and characterizations of A-site deficient perovskite." *Materials Research Bulletin* **46**: 57-61.

Gupta, C. K. and A. K. Suri (1994). "Extractive metallurgy of niobium". Boca Raton, CRC Press.

Hartley, A., M. Sahibzada, et al. (2000). "$La_{0.6}Sr_{0.4}Co_{0.2}Fe_{0.8}O_3$ as the anode and cathode for intermediate temperature solid oxide fuel cells." *Catalysis Today* **55**(1-2): 197-204.

Hautier, G., S. P. Ong, et al. (2012). "Accuracy of density functional theory in predicting formation energies of ternary oxides from binary oxides and its implication on phase stability." *Physical Review B* **85**(15): 155208.

Henkelman, G., B. P. Uberuaga, et al. (2000). "A climbing image nudged elastic band method for finding saddle points and minimum energy paths." *Journal of Chemical Physics* **113**(22): 9901-9904.

Heyden, A., A. T. Bell, et al. (2005). "Efficient methods for finding transition states in chemical reactions: Comparison of improved dimer method and partitioned rational function optimization method." *Journal of Chemical Physics* **123**(22).

Hibino, T., A. Hashimoto, et al. (2002). "An intermediate-temperature solid oxide fuel cell providing higher performance with hydrocarbons than with hydrogen." *Electrochemical and Solid State Letters* **5**(11): A242-A244.

Hibino, T., A. Hashimoto, et al. (2003). "Ru-catalyzed anode materials for direct hydrocarbon SOFCs." *Electrochimica Acta* **48**(17): 2531-2537.

Hirabayashi, D., A. Hashimoto, et al. (2004). "Bi-based oxide anodes for direct hydrocarbon SOFCs at intermediate temperatures." *Electrochemical and Solid State Letters* **7**(5): A108-A110.

Hor, P. H., R. L. Meng, et al. (1987). "Superconductivity above 90 K in the Square-Planar Compound System $A_2Cu_3O_{6+x}$ with a = Y, La, Nd, Sm, Eu, Gd, Ho, Er, and Lu." *Physical Review Letters* **58**(18): 1891-1894.

Huang, K. Q., M. Feng, et al. (1996). "Characterization of Sr-doped $LaMnO_3$ and $LaCoO_3$ as cathode materials for a doped $LaGaO_3$ ceramic fuel cell." *Journal of the Electrochemical Society* **143**(11): 3630-3636.

Huang, K. Q., R. S. Tichy, et al. (1998). "Superior perovskite oxide-ion conductor; strontium- and magnesium-doped $LaGaO_3$: I, phase relationships and electrical properties." *Journal of the American Ceramic Society* **81**(10): 2565-2575.

Huang, Y. H., R. I. Dass, et al. (2006). "Synthesis and characterization of $Sr_2MgMoO_{6-delta}$ - An anode material for the solid oxide fuel cell." *Journal of the Electrochemical Society* **153**(7): A1266-A1272.

Huang, Y. H., R. I. Dass, et al. (2006). "Double perovskites as anode materials for solid-oxide fuel cells." *Science* **312**(5771): 254-257.

Hui, S. Q. and A. Petric (2002). "Evaluation of yttrium-doped $SrTiO_3$ as an anode for solid oxide fuel cells." *Journal of the European Ceramic Society* **22**(9-10): 1673-1681.

Ingram, D. B. and S. Linic (2009). "First-Principles Analysis of the Activity of Transition and Noble Metals in the Direct Utilization of Hydrocarbon Fuels at Solid Oxide Fuel Cell Operating Conditions." *Journal of the Electrochemical Society* **156**(12): B1457-B1465.

Ishihara, T. (2009). "Perovskite oxide for solid oxide fuel cells". New York, Springer.

Ishihara, T., H. Matsuda, et al. (1994). "Improved Oxygen-Ion Conductivity of NdAlO$_3$ Perovskite-Type Oxide by Doping with Ga." *Solid State Ionics* **70**: 234-238.

Ishihara, T., H. Matsuda, et al. (1994). "Doped LaGaO$_3$ Perovskite-Type Oxide as a New Oxide Ionic Conductor." *Journal of the American Chemical Society* **116**(9): 3801-3803.

Ishihara, T., H. Matsuda, et al. (1995). "Effects of Rare-Earth Cations Doped for La Site on the Oxide Ionic-Conductivity of LaGaO$_3$-Based Perovskite-Type Oxide." *Solid State Ionics* **79**: 147-151.

Iwakuni, H., Y. Shinmyou, et al. (2007). "Direct decomposition of NO into N$_2$ and O$_2$ on BaMnO$_3$-based perovskite oxides." *Applied Catalysis B-Environmental* **74**(3-4): 299-306.

Jarlborg, T. (2000). "Tuning of the electronic screening and electron-phonon coupling in doped SrTiO$_3$ and WO$_3$." *Physical Review B* **61**(15): 9887-9890.

Ji, Y., J. Liu, et al. (2003). "Single intermediate-temperature SOFC prepared by glycine-nitrate process." *Journal of Alloys and Compounds* **353**(1-2): 257-262.

Jiang, S. P. and S. H. Chan (2004). "A review of anode materials development in solid oxide fuel cells." *Journal of Materials Science* **39**(14): 4405-4439.

Juhl, M., S. Primdahl, et al. (1996). "Performance/structure correlation for composite SOFC cathodes." *Journal of Power Sources* **61**(1-2): 173-181.

Kanamura, F. (1997). "Perovskite Related Compound." *Kikan Kagaku Sosetsu* **32**: 9.

Kaxiras, E., Y. Baryam, et al. (1987). "Abinitio Theory of Polar Semiconductor Surfaces .1. Methodology and the (2x2) Reconstructions of Gaas(111)." *Physical Review B* **35**(18): 9625-9635.

Kaxiras, E., Y. Baryam, et al. (1987). "Ab initio Theory of Polar Semiconductor Surfaces .2. (2x2) Reconstructions and Related Phase-Transitions of GaAs(111)." *Physical Review B* **35**(18): 9636-9643.

Kaxiras, E., K. C. Pandey, et al. (1986). "Role of Chemical-Potentials in Surface Reconstruction - a New Model and Phase-Transition on GaAs(111)2x2." *Physical Review Letters* **56**(26): 2819-2822.

Kee, R. J., H. Y. Zhu, et al. (2005). "Solid-oxide fuel cells with hydrocarbon fuels." *Proceedings of the Combustion Institute* **30**: 2379-2404.

Kilner, J. A. (2000). "Fast oxygen transport in acceptor doped oxides." *Solid State Ionics* **129**(1-4): 13-23.

Kohn, W., A. D. Becke, et al. (1996). "Density functional theory of electronic structure." *Journal of Physical Chemistry* **100**(31): 12974-12980.

Kohn, W. and L. J. Sham (1965). "Self-Consistent Equations Including Exchange and Correlation Effects." *Physical Review* **140**(4A): 1133-&.

Kolodiazhnyi, T. and A. Petric (2005). "The applicability of Sr-deficient n-type $SrTiO_3$ for SOFC anodes." *Journal of Electroceramics* **15**(1): 5-11.

Kramer, S., M. Spears, et al. (1994). "Conduction in Titanate Pyrochlores - Role of Dopants." *Solid State Ionics* **72**: 59-66.

Kresse, G., O. Dulub, et al. (2003). "Competing stabilization mechanism for the polar ZnO(0001)-Zn surface." *Physical Review B* **68**(24).

Kresse, G. and J. Furthmuller (1996). "Efficient iterative schemes for ab initio total-energy calculations using a plane-wave basis set." *Physical Review B* **54**(16): 11169-11186.

Kresse, G. and D. Joubert (1999). "From ultrasoft pseudopotentials to the projector augmented-wave method." *Physical Review B* **59**(3): 1758-1775.

Kuroda, K., W. Sugimoto, et al. (1998). "Synthesis and structures of carrier doped titanates with the Ruddlesden-Popper structure $(Sr_{0.95}La_{0.05})_{(n+1)}Ti_nO_{3n+1}$ (n = 1, 2)." *Solid State Ionics* **108**(1-4): 315-319.

Kurokawa, H., L. M. Yang, et al. (2007). "Y-doped SrTiO3 based sulfur tolerant anode for solid oxide fuel cells." *Journal of Power Sources* **164**(2): 510-518.

Laursen, S. and S. Linic (2009). "Geometric and electronic characteristics of active sites on TiO_2-supported Au nano-catalysts: insights from first principles." *Physical Chemistry Chemical Physics* **11**(46): 11006-11012.

Laursen, S. and S. Linic (2009). "Strong Chemical Interactions Between Au and Off-Stoichiometric Defects on TiO_2 as a Possible Source of Chemical Activity of Nanosized Au Supported on the Oxide." *Journal of Physical Chemistry C* **113**(16): 6689-6693.

Lee, S., G. Kim, et al. (2008). "SOFC anodes based on infiltration of $La_{0.3}Sr_{0.7}TiO_3$." *Journal of the Electrochemical Society* **155**(11): B1179-B1183.

Li, X., H. L. Zhao, et al. (2008). "La and Sc co-doped $SrTiO_3$ as novel anode materials for solid oxide fuel cells." *Electrochemistry Communications* **10**(10): 1567-1570.

Li, X., H. L. Zhao, et al. (2009). "Electrical conduction behavior of La, Co co-doped $SrTiO_3$ perovskite as anode material for solid oxide fuel cells." *International Journal of Hydrogen Energy* **34**(15): 6407-6414.

Lin, Y. B., Z. L. Zhan, et al. (2006). "Improving the stability of direct-methane solid oxide fuel cells using anode barrier layers." *Journal of Power Sources* **158**(2): 1313-1316.

Lu, C., W. L. Worrell, et al. (2003). "SOFCs for direct oxidation of hydrocarbon fuels with samaria-doped ceria electrolyte." *Journal of the Electrochemical Society* **150**(3): A354-A358.

Luo, W., W. Duan, et al. (2004). "Structural and electronic properties of n-doped and p-doped $SrTiO_3$." *Physical Review B* **70**: 214109.

Lytle, F. W. (1964). "X-Ray Diffractometry of Low-Temperature Phase Transformations in Strontium Titanate." *Journal of Applied Physics* **35**(7): 2212-&.

Ma, Q. L., F. Tietz, et al. (2011). "Nonstoichiometric Y-substituted $SrTiO_3$ materials as anodes for solid oxide fuel cells." *Solid State Ionics* **192**(1): 535-539.

Marina, O. A, N. L. Canfield, et al. (2002). "Thermal, electrical, and electrocatalytical properties of lanthanum-doped strontium titanate." *Solid State Ionics* **149**(1-2): 21-28.

Marina, O. A. and M. Mogensen (1999). "High-temperature conversion of methane on a composite gadolinia-doped ceria-gold electrode." *Applied Catalysis a-General* **189**(1): 117-126.

Matsuzaki, Y. and I. Yasuda (2000). "The poisoning effect of sulfur-containing impurity gas on a SOFC anode: Part I. Dependence on temperature, time, and impurity concentration." *Solid State Ionics* **132**(3-4): 261-269.

McIntosh, S. and R. J. Gorte (2004). "Direct hydrocarbon solid oxide fuel cells." *Chemical Reviews* **104**(10): 4845-4865.

McIntosh, S., J. M. Vohs, et al. (2002). "An examination of lanthanide additives on the performance of Cu-YSZ cermet anodes." *Electrochimica Acta* **47**(22-23): 3815-3821.

Meyer, B. (2006). Surface Phase Diagrams from Ab Initio Thermodynamics. Computational Nanoscience: Do It Yourself! S. B. J. Grotendorst, D. Marx. Julich, John con Neumann Institute for Computing. **31:** 411-418.

Minh, N. Q. (1993). "Ceramic Fuel-Cells." *Journal of the American Ceramic Society* **76**(3): 563-588.

Minh, N. Q. (2004). "Solid oxide fuel cell technology—features and applications." *Solid State Ionics* **174**(1-4): 271.

Mogensen, M. and K. Kammer (2003). "Conversion of hydrocarbons in solid oxide fuel cells." *Annual Review of Materials Research* **33**: 321-331.

Monkhorst, H. J. and J. D. Pack (1976). "Special Points for Brillouin-Zone Integrations." *Physical Review B* **13**(12): 5188-5192.

Moos, R., T. Bischoff, et al. (1997). "Solubility of lanthanum in strontium titanate in oxygen-rich atmospheres." *Journal of Materials Science* **32**(16): 4247-4252.

Moos, R., A. Gnudi, et al. (1995). "Thermopower of $Sr_{1-x}La_xTiO_3$ ceramics." *Journal of Applied Physics* **78**(8): 5042.

Moos, R. and K. H. Hardtl (1997). "Defect chemistry of donor-doped and undoped strontium titanate ceramics between 1000 degrees and 1400 degrees C." *Journal of the American Ceramic Society* **80**(10): 2549-2562.

Mosey, N. J. and E. A. Carter (2007). "Ab initio evaluation of Coulomb and exchange parameters for DFT+U calculations." *Physical Review B* **76**(15).

Mott, N. F. (1968). "Metal-Insulator Transition." *Reviews of Modern Physics* **40**(4): 677

Mukherjee, J. and S. Linic (2007). "First-principles investigations of electrochemical oxidation of hydrogen at solid oxide fuel cell operating conditions." *Journal of the Electrochemical Society* **154**(9): B919-B924.

Munoz-Garcia, A. B., D. E. Bugaris, et al. (2012). "Unveiling Structure-Property Relationships in Sr2Fe1.5Mo0.5O6-delta, an Electrode Material for Symmetric Solid Oxide Fuel Cells." *Journal of the American Chemical Society* **134**(15): 6826-6833.

Nagel, F. (2008). Electricity from wood through the combination of gasification and solid oxide fuel cells. Zurich, Swiss Federal Institute of Technology Zurich. **Ph.D.** .

Neagu, D. and J. T. S. Irvine (2010). "Structure and Properties of $La_{0.4}Sr_{0.4}TiO_3$ Ceramics for Use as Anode Materials in Solid Oxide Fuel Cells." *Chemistry of Materials* **22**(17): 5042-5053.

Neagu, D. and J. T. S. Irvine (2011). "Enhancing Electronic Conductivity in Strontium Titanates through Correlated A and B-Site Doping." *Chemistry of materials* **23**(6): 1607.

Nernst, W. (1987). *Verfahren zur Erzeugung von Elektrischen Glühlicht* **104**: 872.

Nguyen, Q. M. and T. Takahashi (1995). "Science and technology of ceramic fuel cells". Amsterdam ; New York, Elsevier Science.

Noland, J. A. (1954). "Optical Absorption of Single-Crystal Strontium Titanate." *Physical Review* **94**(3): 724-724.

Norskov, J. K., J. Rossmeisl, et al. (2004). "Origin of the overpotential for oxygen reduction at a fuel-cell cathode." *Journal of Physical Chemistry B* **108**(46): 17886-17892.

Ohta, S., T. Nomura, et al. (2005). "High-temperature carrier transport and thermoelectric properties of heavily La- or Nb-doped $SrTiO_3$ single crystals." *Journal of Applied Physics* **97**(3): 034106.

Padilla, J. and D. Vanderbilt (1997). "Ab initio study of $BaTiO_3$ surfaces." *Physical Review B* **56**(3): 1625-1631.

Perdew, J. P., K. Burke, et al. (1996). "Generalized gradient approximation made simple." *Physical Review Letters* **77**(18): 3865-3868.

Pisani, C., M. Busso, et al. (2005). "Local-MP2 electron correlation method for nonconducting crystals." *Journal of Chemical Physics* **122**(9).

Pojani, A., F. Finocchi, et al. (1999). "Polarity on the SrTiO3 (111) and (110) surfaces." *Surface Science* **442**(2): 179-198.

Porat, O., C. Heremans, et al. (1997). "Stability and mixed ionic electronic conduction in Gd-2(Ti1-xMox)(2)O-7 under anodic conditions." *Solid State Ionics* **94**(1-4): 75-83.

Ratner, M. A. and G. C. Schatz (2000). "An introduction to quantum mechanics in chemistry". Upper Saddle River, NJ, Prentice Hall.

Reuter, K. and M. Scheffler (2001). "Surface core-level shifts at an oxygen-rich Ru surface: O/Ru(0001) vs. RuO2(110)." *Surface Science* **490**(1-2): 20-28.

Reuter, K. and M. Scheffler (2003). "First-principles atomistic thermodynamics for oxidation catalysis: Surface phase diagrams and catalytically interesting regions." *Physical Review Letters* **90**(4).

Robertson, J., K. Xiong, et al. (2006). "Band gaps and defect levels in functional oxides." *Thin Solid Films* **496**(1): 1-7.

Rogal, J., K. Reuter, et al. (2007). "CO oxidation at Pd(100): A first-principles constrained thermodynamics study." *Physical Review B* **75**(20): 205433.

Ruiz-Morales, J. C., J. Canales-Vazquez, et al. (2006). "Disruption of extended defects in solid oxide fuel cell anodes for methane oxidation." *Nature* **439**(7076): 568-571.

Sasaki, K., K. Susuki, et al. (2006). "H2S poisoning of solid oxide fuel cells." *Journal of the Electrochemical Society* **153**(11): A2023-A2029.

Schooley, J. F., W. R. Hosler, et al. (1965). "Dependence of Superconducting Transition Temperature on Carrier Concentration in Semiconducting $SrTiO_3$." *Physical Review Letters* **14**(9): 305-&.

Seuter, A. M. J. (1974). "Defect Chemistry and Electrical Transport Properties of Barium-Titanate." *Philips Research Reports*: 1-84.

Shanthi, N. and D. D. Sarma (1998). "Electronic structure of electron doped $SrTiO_3$: $SrTiO_{3-delta}$ and $Sr_{1-x}La_xTiO_3$." *Physical Review B* **57**(4): 2153-2158.

Shao, Z. P. and S. M. Haile (2004). "A high-performance cathode for the next generation of solid-oxide fuel cells." *Nature* **431**(7005): 170-173.

Shin, S., H. Arakawa, et al. (1979). "Absorption of No in the Lattice of an Oxygen-Deficient Perovskite Srfeo3-X and the Infrared Spectroscopic Study of the System No - Srfeo3-X." *Materials Research Bulletin* **14**(5): 633-639.

Shiqiang Hui, A. P. (2002). "Evaluation of yttrium-doped $SrTiO_3$ as an anode for solid oxide fuel cells " *Shiqiang Hui and Anthony Petric*(22): 1673.

Sholl, D. S. and J. A. Steckel (2009). "Density functional theory : a practical introduction". Hoboken, N.J., Wiley.

Sin, A., E. Kopnin, et al. (2005). "Stabilisation of composite LSFCO-CGO based anodes for methane oxidation in solid oxide fuel cells." *Journal of Power Sources* **145**(1): 68-73.

Singh, P. and N. Q. Minh (2004). "Solid Oxide Fuel Cells: Technology Status." *International Journal of Applied Ceramic Technology* **1**(1): 5.

Singhal, S. C. and K. Kendall (2003). "High-temperature solid oxide fuel cells : fundamentals, design, and applicatons". New York, Elsevier Advanced Technology.

Skorodumova, N. V., S. I. Simak, et al. (2002). "Quantum origin of the oxygen storage capability of ceria." *Physical Review Letters* **89**(16): -.

Slater, J. C. (1950). "The Lorentz Correction in Barium Titanate." *Physical Review* **78**(6): 748-761.

Slater, P. R., D. P. Fagg, et al. (1997). "Synthesis and electrical characterisation of doped perovskite titanates as potential anode materials for solid oxide fuel cells." *Journal of Materials Chemistry* **7**(12): 2495-2498.

Slater, P. R. and J. T. S. Irvine (1999). "Niobium based tetragonal tungsten bronzes as potential anodes for solid oxide fuel cells: synthesis and electrical characterisation." *Solid State Ionics* **120**(1-4): 125-134.

Slater, P. R. and J. T. S. Irvine (1999). "Synthesis and electrical characterisation of the tetragonal tungsten bronze type phases, $(Ba/Sr/Ca/La)_{0\ 6}M_xNb_{1-x}O_{3-delta}$ (M = Mg, Ni, Mn, Cr, Fe, In, Sn): evaluation as potential anode materials for solid oxide fuel cells." *Solid State Ionics* **124**(1-2): 61-72.

Slater, P. R., J. T. S. Irvine, et al. (1998). "The structure of the oxide ion conductor $La_{0.9}Sr_{0.1}Ga_{0.8}Mg_{0.2}O_{2.85}$ by powder neutron diffraction." *Solid State Ionics* **107**(3-4): 319-323.

Steele, B. C. H. (2000). "Appraisal of $Ce_{1-y}Gd_yO_{2-y/2}$ electrolytes for IT-SOFC operation at 500 degrees C." *Solid State Ionics* **129**(1-4): 95-110.

Sun, C. W. and U. Stimming (2007). "Recent anode advances in solid oxide fuel cells." *Journal of Power Sources* **171**(2): 247-260.

Sun, C. W., J. Sun, et al. (2006). "Mesoscale organization of nearly monodisperse flowerlike ceria microspheres." *Journal of Physical Chemistry B* **110**(27): 13445-13452.

Suthirakun, S., S. C. Ammal, et al. (2011). "Density functional theory study on the electronic structure of n- and p-type doped $SrTiO_3$ at anodic solid oxide fuel cell conditions." *Physical Review B* **84**(20).

Suthirakun, S., S. C. Ammal, et al. (2012). "Obtaining mixed ionic/electronic conductivity in perovskite oxides in a reducing environment: A computational prediction for doped $SrTiO_3$." *Solid State Ionics* **228**: 37-45.

Suthirakun, S., S. C. Ammal, et al. (2011). "Density functional theory study on the electronic structure of n- and p-type doped SrTiO3 at anodic solid oxide fuel cell conditions." *Physical Review B* **84**(20): 205102.

Takahash.T and H. Iwahara (1971). "Ionic Conduction in Perovskite-Type Oxide Solid Solution and Its Application to Solid Electrolyte Fuel Cell." *Energy Conversion* **11**(3): 105-&.

Tao, S. W. and J. T. S. Irvine (2003). "A redox-stable efficient anode for solid-oxide fuel cells." *Nature Materials* **2**(5): 320-323.

Tao, S. W. and J. T. S. Irvine (2004). "Discovery and characterization of novel oxide anodes for solid oxide fuel cells." *Chemical Record* **4**(2): 83-95.

Teraoka, Y., T. Harada, et al. (1998). "Reaction mechanism of direct decomposition of nitric oxide over Co- and Mn-based perovskite-type oxides." *Journal of the Chemical Society-Faraday Transactions* **94**(13): 1887-1891.

Tournoux, M., M. Ganne, et al. (1992). "Htb-Like 6-Membered Rings of Octahedra in Some New Oxides - Structural Aspects and Related Properties." *Journal of Solid State Chemistry* **96**(1): 141-153.

Turrillas, X., A. P. Sellars, et al. (1988). "Oxygen Ion Conductivity in Selected Ceramic Oxide Materials." *Solid State Ionics* **28**: 465-469.

Van Benthem, K., C. Elsasser, et al. (2001). "Bulk electronic structure of $SrTiO_3$: Experiment and theory." *Journal of Applied Physics* **90**(12): 6156-6164.

Vernoux, P., E. Djurado, et al. (2001). "Catalytic and electrochemical properties of doped lanthanum chromites as new anode materials for solid oxide fuel cells." *Journal of the American Ceramic Society* **84**(10): 2289-2295.

VI, A., F. Aryasetiawan, et al. (1997). "First-principles calculations of the electronic structure and spectra of strongly correlated systems: The LDA+U method." *Journal of Physics-Condensed Matter* **9**(4): 767-808.

Vidyasagar, K., A. Reller, et al. (1985). "Oxygen Vacancy Ordering in Superlattices of the 2 Novel Oxides, $La_2Ni_2O_5$ and $La_2Co_2O_5$, Prepared by Low-Temperature Reduction of the Parent Perovskites." *Journal of the Chemical Society-Chemical Communications*(1): 7-8.

Wang, S. R., T. Kobayashi, et al. (2000). "Electrical and ionic conductivity of Gd-doped ceria." *Journal of the Electrochemical Society* **147**(10): 3606-3609.

Xia, C. R., W. Rauch, et al. (2002). "$Sm_{0.5}Sr_{0.5}CoO_3$ cathodes for low-temperature SOFCs." *Solid State Ionics* **149**(1-2): 11-19.

Xiao, G., X. Dong, et al. (2011). "Synthesis and characterizations of A-site deficient perovskite $Sr_{0.9}Ti_{0.8-x}Ga_xNb_{0.2}O_3$." *Materials Research Bulletin* **46**(1): 57-61.

Xiao, G. L. and F. L. Chen (2011). "Ni modified ceramic anodes for direct-methane solid oxide fuel cells." *Electrochemistry Communications* **13**(1): 57-59.

Yasuda, H., T. Nitadori, et al. (1993). "Catalytic Decomposition of Nitrogen Monoxide over Valency-Controlled La_2CuO_4-Based Mixed Oxides." *Bulletin of the Chemical Society of Japan* **66**(11): 3492-3502.

Ye, X. F., B. Huang, et al. (2007). "Preparation and performance of a $Cu-CeO_2$-ScSZ composite anode for SOFCs running on ethanol fuel." *Journal of Power Sources* **164**(1): 203-209.

Yokoya, T., T. Sato, et al. (1999). "Electronic structure of $Ce_{1-x}Sr_xTiO_3$: Comparison between substitutional and vacancy doping." *Physical Review B* **59**(3): 1815-1818.

Yun, J. N., Z. Y. Zhang, et al. (2010). "First-principles study of structural stability and electronic structure of La-doped $Sr_{1.9375}La_{0.0625}TiO_{3.968}$ (75)." *Journal of Applied Physics* **107**(10).

Zha, S. W., Z. Cheng, et al. (2007). "Sulfur poisoning and regeneration of Ni-based anodes in solid oxide fuel cells." *Journal of the Electrochemical Society* **154**(2): B201-B206.

Zha, S. W., P. Tsang, et al. (2005). "Electrical properties and sulfur tolerance of $La_{0.75}Sr_{0.25}Cr_{1-x}Mn_xO_3$ under anodic conditions." *Journal of Solid State Chemistry* **178**(6): 1844-1850.

Zhang, C., C. L. Wang, et al. (2008). "Substitutional position and insulator-to-metal transition in Nb-doped $SrTiO_3$." *Materials Chemistry and Physics* **107**(2-3): 215-219.

Zhu, W. Z. and S. C. Deevi (2003). "A review on the status of anode materials for solid oxide fuel cells." *Materials Science and Engineering a-Structural Materials Properties Microstructure and Processing* **362**(1-2): 228-239.

Zhukovskii, Y. F., E. A. Kotomin, et al. (2009). "A comparative ab initio study of bulk and surface oxygen vacancies in $PbTiO_3$, $PbZrO_3$ and $SrTiO_3$ perovskites." *Solid State Communications* **149**(33-34): 1359-1362.